EARLY AGE RESPONSE OF JOINTED PLAIN CONCRETE PAVEMENTS TO ENVIRONMENTAL LOADS

by

Steven A. Wells

B.S. in Civil Engineering, Pennsylvania State University, 2003

Submitted to the Graduate Faculty of

School of Engineering in partial fulfillment

of the requirements for the degree of

Master of Science

University of Pittsburgh

2005

UNIVERSITY OF PITTSBURGH

SCHOOL OF ENGINEERING

This thesis was presented

by

Steven A. Wells

It was defended on

July 27, 2005

and approved by

Christopher J. Earls, Ph.D., Associate Professor and Chairman,
Department of Civil and Environmental Engineering

Kent A. Harries, Ph.D., Assistant Professor,
Department of Civil and Environmental Engineering

Amir Koubaa, Ph.D., Assistant Professor and Academic Coordinator,
Department of Civil and Environmental Engineering

Julie M. Vandenbossche, Ph.D., Assistant Professor,
Department of Civil and Environmental Engineering
Thesis Advisor

EARLY AGE RESPONSE OF JOINTED PLAIN CONCRETE PAVEMENTS TO ENVIRONMENTAL LOADS

Steven A. Wells, M.S.

University of Pittsburgh, 2005

The behavior of jointed plain concrete pavements during the initial time period following paving provides vital information concerning how the pavement structure will perform throughout its intended life. A primary contributor to the development of stresses in pavements following paving comes from environmental conditions, particularly from differential thermal and moisture gradients throughout the pavement depth.

The following study analyzes the response of a jointed plain concrete pavement structure during the period of initial concrete strength gain (first 72 hours after paving) and throughout a full cycle of seasonal conditions (first ten months after paving). The response of the pavement structure is characterized through the analysis of on-site climatic conditions, analysis of embedded strain, temperature, and moisture gages, as well as through manual field data collection.

The field data collection effort conducted for this study is described in terms of an overview of the site conditions, construction parameters, instrumentation utilized and data acquisition employed. The climatic response of the pavement structure was analyzed, with particular emphasis on curling and warping.

This study investigated the strain response of the pavement structure with respect to the parameters influencing strain location and magnitude. Both the early-age (the first 72-hours after

paving) and the seasonal strain response with respect to spatial characteristics and level of restraint were analyzed.

Based on the results from this study, the built-in construction gradient was found to be 0.7 °F/in. at the edge of the slab and negligible at midpanel. In general, the measured curvature tended to be 7 percent larger for unrestrained slabs when compared to restrained slabs. The tie and dowel bars produced a reduction in strain with changes in temperature of approximately 0.34 to 0.41 microstrain/°F at locations near the joints. The strains measured in the restrained slabs also tended to be more uniform than for the unrestrained slabs. A couple of seasonal observations were also made. The average strain at midslab was -450 microstrain in the fall and -600 microstrain in the winter with diurnal strain fluctuations being the lowest in the winter. This study also evaluated the drying shrinkage that occurred in the slab. Drying shrinkage increased drastically during the first 50 days after construction and continued through the winter but began to decrease during the spring when rain events occur more frequently.

TABLE OF CONTENTS

LIST OF TABLES

LIST OF FIGURES

ACKNOWLEDGEMENTS

I would first like to thank the Pennsylvania Department of Transportation and the Federal Highway Administration for their financial support and, along with Mascaro Construction, their cooperation and assistance throughout the instrumentation and data collection efforts of this project.

I would also like to express my gratitude to the graduate and undergraduate students who offered their assistance for this project. Their hard work in the field instrumentation, data collection, and material testing aspects of this research project is greatly appreciated.

I would like to thank my advisor, Dr. Julie Vandenbossche, for her guidance and encouragement throughout my graduate studies. Her dedication to education and commitment to excellence in research has been inspirational and it has been a great privilege to have studied under her.

Finally, I would like to thank my parents, Dennis and Karol Wells, for their support and encouragement during my years of engineering education and throughout life. This thesis is dedicated to them.

1.0 INTRODUCTION

1.1 BACKGROUND

The mechanisms leading to pavement failure can be better understood by developing a better understanding of how rigid pavements respond to load. Stresses in jointed plain concrete pavements (JPCP) occur as the result of three separate phenomena:

1. curling and warping due to temperature and moisture differences, respectively, between the top and bottom of the slab;
2. restraint of thermal expansion and contraction of the slab due to friction between the Portland cement concrete (PCC) pavement and underlying support layer;
3. external vehicle load.

The first two of these phenomena are environmentally related and will be addressed in this study.

Cracking can develop in concrete pavements even when an external load has never been applied. This emphasizes the magnitude of the stresses that can develop as a result of thermal and moisture loads. The environmental conditions under which the slabs were paved will have an influence on the performance life of the structure. It is therefore important to be able to characterize this influence if the life of the pavement is to be accurately predicted. The focus of this study will be to characterize the early-age response of the slab to environmental loads.

1.2 OBJECTIVES

The primary objective of this research is to characterize the early-age response of restrained and unrestrained JPCP pavements subject to seasonal and diurnal environmental loadings. Strain response during the first 72 hours after paving was investigated in addition to seasonal behavior for the first year after construction. The effects of dowel and tie bars on strain response were characterized.

1.3 RESEARCH APPROACH

This research effort consists of the construction of an instrumented JPCP. This highly instrumented pavement section contains a variety of environmental, static, and dynamic strain sensors. The focus here will be on the environmental and static strain sensors. In particular, the data collected from thermocouples, moisture sensors, static strain gages, and weather monitoring equipment from the first 10 months after paving will be analyzed. The slab profile was measured continuously for the first 72 hours after paving to also assist in characterizing early-age slab response.

This early-age analysis provides in-site into how the pavement responds to environmental factors during the time period in which the concrete is developing strength and stiffness. This study is part of a larger study that also included a substantial laboratory component for characterizing the materials properties of the concrete. The measured material properties, along with the measured moisture and temperature conditions within the slab, will be used to help explain the slab response measured in the field.

A literature review of work previously performed is provided in Chapter 2. Chapter 3 contains a detailed description of the instrumented test section, referred to as the Smart Pavement, the sensors selected for installation, the data acquisition system developed to read the sensors, and the layout of the test section. Chapter 4 provides a discussion on the analysis of the temperature and moisture data while Chapter 5 discusses the measured effects of the temperature and moisture profiles throughout the depth of the slab on slab shape. A detailed discussion of the analysis of the static strain data is provided in Chapter 6. Finally, a comprehensive summary of research findings and recommendations are provided in Chapter 8.

2.0 LITERATURE REVIEW

2.1 SOURCES OF STRESS IN PCC PAVMENTS

One of the fundamental principles of rigid pavement design is to ensure that the combined stresses induced on the slabs do not exceed the flexural strength of the PCC. An understanding of rigid pavement stress mechanisms is vital to achieving this task. Sources of stress in rigid pavements are categorized into several broad categories. Yoder and Witzcak identified the following stress-inducing mechanisms:

1. restrained temperature and moisture deformations
2. externally applied loads
3. volume changes of supporting material, including frost heave
4. continuity of subgrade support as affected by permanent deformations of the subgrade or loss of support through pumping. (Yoder and Witzcak, 1975)

Stresses due to temperature and moisture may occur as the result of two separate phenomena. When non-uniform temperature or moisture gradients exist within a slab, the differential strain response throughout the slab depth leads to curvature, a condition known as curling or warping. When uniform temperature changes occur within a slab, the entire slab tends to contract or expand horizontally. This slab movement is resisted by friction at the PCC/base interface, creating tensile stresses on the underside of the slab.

2.2 CURLING AND WARPING

Curling is slab curvature produced by a temperature gradient throughout the depth of the slab and warping is moisture-induced slab curvature produced by a temperature gradient. As shown in figure 2.1, a positive gradient occurs when temperature and/or moisture levels at the top of a PCC slab are higher than that at the bottom of the PCC slab, resulting in downward curvature.

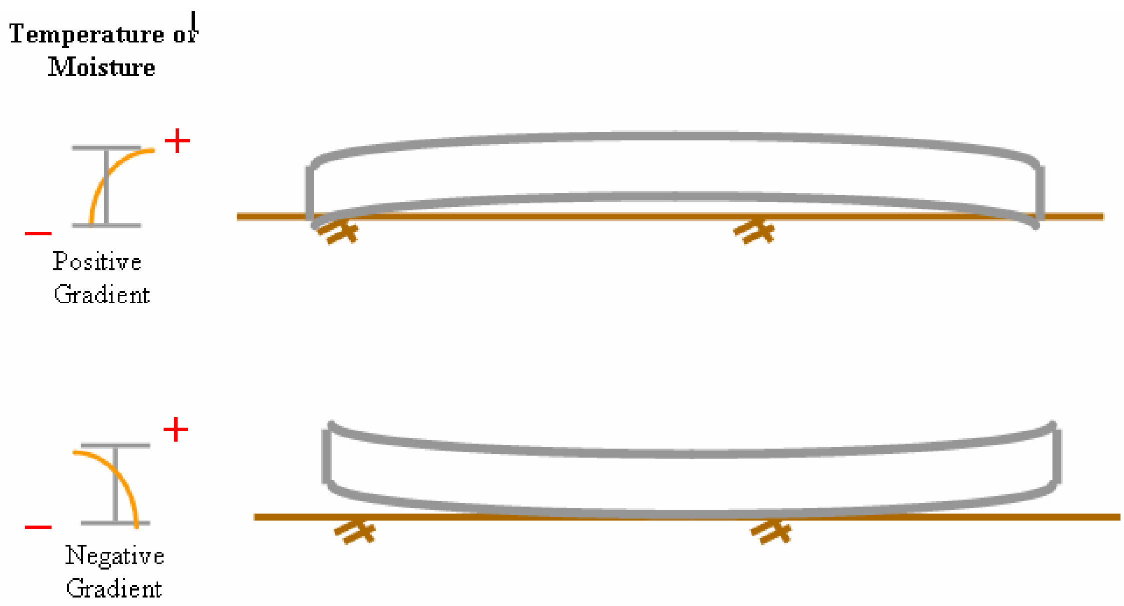

Figure 2.1 Curling and warping in PCC slabs.

In contrast, negative gradients occur when the temperature and moisture in the slab are greater at the bottom, resulting in upward slab curvature. Gradients, as shown in Figure 2.1, are primarily non-linear in nature.

Figure 2.2, shows the locations of critical tensile stresses that occur as the result of upward and downward slab curvature, respectively. The slab on the left side of Figure 2.2 is undergoing upward curvature as the result of a negative temperature or moisture gradient. Support is lost near the ends of the slab, and hence, the self weight of the slab exerts tensile stresses near the top of the PCC. The slab on the right side of Figure 2.2 is undergoing downward curvature as the result of a positive temperature or moisture gradient. In this case, support is lost near the center of the slab and the self weight of the slab exerts tensile stresses near the bottom of the slab. Curling and warping-induced tensile stresses are further magnified under vehicle loading. The repetitive stresses induced by curling and warping, particularly when combined with vehicle loading, can often lead to transverse cracking.

Figure 2.2 Locations of critical curling and warping stresses.

2.2.1 Factors Influencing Curling and Warping

The magnitude of thermal and moisture gradients within a pavement is influenced by factors including daily temperature and relative humidity conditions, base layer type, slab geometry, shrinkage characteristics, and concrete mixture characteristics (Vandenbossche et al., 2002). The magnitude of curling and warping is dependent upon these factors as well as the degree of built-in slab curvature, creep, and drying shrinkage (Rao and Roesler, 2005). Thermal gradients are dependent upon heat transfer to and from the slab, a process that is primarily a function of solar radiation and thermal irradiation, convection and heat conduction (Mirambell, 1990). Aside from the heat of hydration experienced in newly placed concrete, the most significant environmental contribution to heat within the pavement is from solar radiation, a factor influenced by cloud cover. The key characteristics of PCC mixtures that influence pavement response to thermal gradients are coefficient of thermal expansion, thermal conductivity, and specific heat (Vandenbossche et al., 2002).

2.2.2 Built-in Curling and Warping

Construction curling and warping is a built-in curvature, which takes place as the result of changes in temperature and moisture that occur prior to hardening of the PCC. Construction curling typically involves an upward curvature of the slab caused by a built-in negative gradient. Slabs that are constructed during the daytime gain a significant amount of heat energy from solar radiation and heat of hydration during the day. At night, as the ambient temperature drops and both moisture and heat energy are lost near the surface of the PCC, resulting in a negative built-in temperature gradient. Wet curing of the concrete helps to mitigate the effects of early age negative gradients by reducing the surface temperature and preventing surface moisture loss (Vandenbossche et al., 2002).

Thermal and moisture gradients present at the time the concrete sets, as well as creep, are factors which influence the level of built-in curl. Over time, creep tends to reduce the effects of built-in curl. Slabs that experience construction curling have a built-in temperature gradient, meaning that in order for the slab to reach a condition of flatness an equivalent but opposite temperature gradient must exist (Vandenbossche et al., 2002).

The built-in construction curling and warping that a slab undergoes shortly after the concrete sets can substantially affect the long term performance of the pavement structure. Tensile stresses generated by this phenomenon, particular when augmented with stresses generated by truck loading, can lead to premature distresses in the pavement structure. As these conditions worsen, the performance life of the pavement diminishes. The development of early-age strength in rigid pavements is vital to preventing early-age distress, which are amplified over the performance life of the pavement.

Until recently, the phenomenon of construction curling has not been considered in the design of concrete pavements even though it is a parameter known to be critical to the performance of a pavement. The importance of construction curling is indicated by its inclusion in the 2002 Mechanistic Empirical Pavement Design and Analysis Guide. The design procedure is very sensitive to this parameter, as would be expected. Unfortunately very little information is available on appropriate inputs for this parameter. This study includes a method for identifying how this value can be determined and quantifies the value for the instrumented section included in the study.

2.2.3 Daily and Seasonal Effects on Curling and Warping

The effects of seasonal variations on curling and warping were studied extensively by Vandenbossche at the Mn/Road research facility. The following seasonal observations were obtained:

- The top of the pavement is affected predominantly by daily environmental changes while the bottom varies more seasonally.

- Maximum positive temperature gradients typically occurred during the afternoon in the spring and summer months. Despite higher ambient temperatures in the summer, the thermal gradients experienced in the spring were greater overall due to the fact that the base layer was significantly cooler.
- Larger negative gradients occurred during the summer and winter months. The largest negative gradients in the summer occurred periodically when rain events occurred on hot afternoons. The large negative gradient was generated when the rain rapidly cooled the surface of the pavement. During the winter months, the average maximum negative gradients were higher than for any other season, a fact which might explain the findings of Guo and Marsey, who based on the results of Heavy Weight Deflectometer (HWD) data, discovered a significant increase in the upward curling of slabs form the summer to the winter (Guo and Marsey, 2001).
- The overall gradients were less in the winter than those observed in the spring, summer, and fall.
- The fall months experienced lower gradients and zero gradient conditions more than any other season.

Data from the Mn/ROAD site also indicated that during the afternoon hours positive gradients are prevalent; however, temperature and moisture gradients are typically counteractive, with temperature gradients being largely positive and moisture gradients being almost always negative. In the early morning, during times of high negative gradients, thermal and moisture gradients are typically additive (Vandenbossche 2003).

2.3 RESTRAINT IN SLAB DEFORMATION

As previously stated, thermal- and moisture-related deformation in the slab does not induce stress. It is the restraint of this deformation that induces the stress. This deformation is restrained by the self-weight of the slab, friction between the bottom of the slab and the underlying base, tie bars and dowel devices. Each of these components are discussed below.

2.3.1 Friction at Slab/Base Interface

PCC slabs experiencing a uniform decrease in temperature will contract. A tensile stress will then develop at midpanel on the bottom of the slab, particularly for longer slabs. As pointed out by Huang, stress in concrete due to friction is proportional to the slab length, unit weight, and frictional coefficient but independent of slab thickness (Huang, 1993). Slabs constructed on open-graded stabilized materials will result in larger tensile stresses compared to more densely graded unstabilized base materials. The concrete will penetrate into an open-graded base course during paving, thereby creating a strong mechanical interlocking bond. Little to no penetration will occur on the more densely-graded base materials.

2.3.2 Restraint Along the Transverse Joint

Load transfer across the transverse joint is achieved primarily through the individual or combined contributions of aggregate interlock and dowel bar reinforcement, and less-seldom used keyways. Maintaining a high degree of load transfer efficiency across a discontinuity diminishes the potential for pumping and associated distresses, particularly faulting. The goal of traditional load transfer mechanisms has been to provide shear transfer and continuity at the joint. The residual effect is the restraint it provides against curling and warping and the resulting stresses generated.

The shear transfer mechanism of aggregate interlock is dependant upon crack width as well the size, strength, durability, and angularity of aggregate particles in the PCC mixture (Kelleher and Larson, 1989). The greater the degree of aggregate interlock across the fractured faces of a PCC slab, the greater the load transfer efficiency. Aggregate interlock provides a pure-shear load transfer mechanism that does not significantly restrain curling and warping.

Dowel bars are the most commonly used method to insure load transfer across the joint. Dowels primarily transfer shear forces and, to a lesser extent, bending forces. Dowels bars are commonly placed at transverse joints such that one end of the bar is permitted to slide in the longitudinal direction by means of a bond breaking coating such as grease. The dowel thus acts primarily as a shear transfer devices rather than a reinforcing bar (Kelleher and Larson 1998). The debonding agent also reduces stresses brought upon by thermal curling and moisture-related warping of the PCC slabs (Kelleher and Larson, 1998). Expansion caps are often placed at the ends of dowels to prevent excessive stresses on the PCC upon thermal expansion of the slabs.

The role of the dowel bar as a mechanism of restraining curvature in PCC slabs undergoing curling and warping has been recognized in a number of research investigations. Three dimensional finite element models produced by William and Shoukry revealed that dowel bars tend to obstruct slab deflections near transverse joints. (William and Shoukry, 2001). Vandenbossche found that the curvature response of undoweled slabs, relying on only aggregate interlock, was more sensitive to slab temperature than doweled slabs (Vandenbossche, 2003). Battelle and Everhart used finite element modeling to show that the degree of upward displacement of transverse joints is restricted by dowels in slabs undergoing negative (colder on top than the bottom) thermal gradients (Battelle and Everhart, 1998). Finite element analysis work performed by Davids shown that such stresses may not be sufficient to significantly affect the potential for damage to the PCC surrounding the dowel (Davids, 2000) although stresses generated within the panel are sufficiently high to affect the performance life of the slab.

Dowel bars also affect the magnitude of the built-in curl. As the concrete gains strength and stiffness, the slab will begin to curl and warp based on the gradients present. This deformation will be restrained by the dowel bars. This is supported by work peformed by Rao and Roesler who found that slabs restrained by dowels and tied concrete shoulders experienced less built in curl than unrestrained slabs (Rao and Roesler, 2005).

While dowels may reduce stresses inherent to curling and warping by reducing the associated degree of curvature, it has been proposed by several researchers (Vandenbossche et al., 2002) that this curvature restraint leads to increased levels of stress in the surrounding concrete.

2.3.3 Restraint Along the Longitudinal Joint

The primary function of tie bars is to hold faces of adjacent slabs in close contact with one another so that load can be transferred by aggregate interlock (Huang, 1993). By maintaining tight contact between adjacent slabs, tie bars also help to prevent moisture infiltration through joints and cracks. The ability of the tie bar to transfer shear forces or “dowel action”, however, is small compared to that provided by dowel bars (Hammons and Ioannides, 1996). It is believed however, that tie bars do play a role in the restraint of slabs undergoing curling and warping.

2.3.4 Self-Weight of the Slab

As mentioned in Section 2.2, JPCP slabs undergoing curling and warping will experience stress as the result slab self-weight. For upward curvature, the self-weight of the slab produces maximum tensile stresses at the top near midpanel, and for downward curvature, the slab self-weight produces maximum tensile stresses at the bottom of the slab near midpanel. The magnitude of self-weight contribution to curling and warping stresses is significantly influenced by slab length. Generally, the shorter the slab length, the lower the curling stresses in the slab. In a study conducted by Vandenbosshe, it was found that slab length was a significant parameter for predicting curvature in un-doweled slabs. This was found not the case for doweled slabs. The support across transverse joints provided by dowel bars causes the slab to behave more like a continuous slab, making slab length less of a factor with respect to curling behavior (Vandenbossche, 2003).

2.4 EFFECT OF CONCRETE MATERIAL PROPERTIES ON CURLING AND WARPING

Concrete material properties also have a significant influence on curling and warping of JPCP slabs. Parameters including thermal coefficient of expansion, elastic modulus, and drying shrinkage influence the level of curling and warping stress within a slab. The thermal coefficient of expansion is a measure of strain per change in temperature. This parameter is primarily a function of the aggregate used in the concrete mixture. The thermal coefficient of the concrete is generally similar to that of its constituent aggregate particles. When materials of varying thermal coefficients come in contact, such as when a PCC slab rests on an asphalt stabilized base, the difference in strain response to temperature between the two materials generates stress. Drying shrinkage, or the reduction of concrete volume due to loss of water, also leads to warping related stresses. Generally, the top of the slab loses moisture, and therefore reduces in volume, at a greater rate than the bottom of the slab, a phenomenon leading to warping. The elastic modulus also plays vital role in concrete deformations related to curling and warping stresses. Concrete slabs with a higher elastic modulus will produce higher stress for any given level of strain.

3.0 FIELD DATA COLLECTION

The following section provides an overview of the field instrumentation and data acquisition effort carried out to capture the curling, warping, and strain response of JPCP to environmental loading. Environmental conditions were monitored using an on site weather station as well as embedded temperature and moisture sensors. The response of the pavement was monitored using embedded static strain sensors, pressure plates, and surface profile measurements.

The following chapter provides a description of the site location characteristics, physical aspects of the instrumented pavement sections, curling and warping-related measurement approach, and the data acquisition system used to collect the data.

3.1 SITE LOCATION AND PROJECT DESCRIPTION

The site location for the instrumented test sections was selected based on a number of criteria including construction schedule, roadway grade, subgrade support characteristics, and traffic patterns. After careful consideration, a section of highway along construction Section B01 of U.S. Route 22 was chosen. The majority of Section B01 runs through the municipality of Murrysville in Westmoreland County. Murrysville, a suburb of Pittsburgh, is located approximately 20 miles east of the city, as shown in Figure 3.1.

Figure 3.1 Map of the area of Pittsburgh, (www.mappoint.msn.com, June 2005).

Section B01 is a 3.4 mile stretch of highway running from stations 513+45.144 to 0+08.573 in Allegheny County and from stations 0+08.573 to 166+99.475 in Westmoreland County. It is one of ten designated construction sections (B01 through B10) that are part of the Pennsylvania Department of Transportation (PENNDOT) Renew 22 reconstruction project, that runs primarily through Westmoreland County between the Allegheny and Indiana County lines. A map of the Renew 22 construction sections, including Section B01, is shown in Figure 3.2.

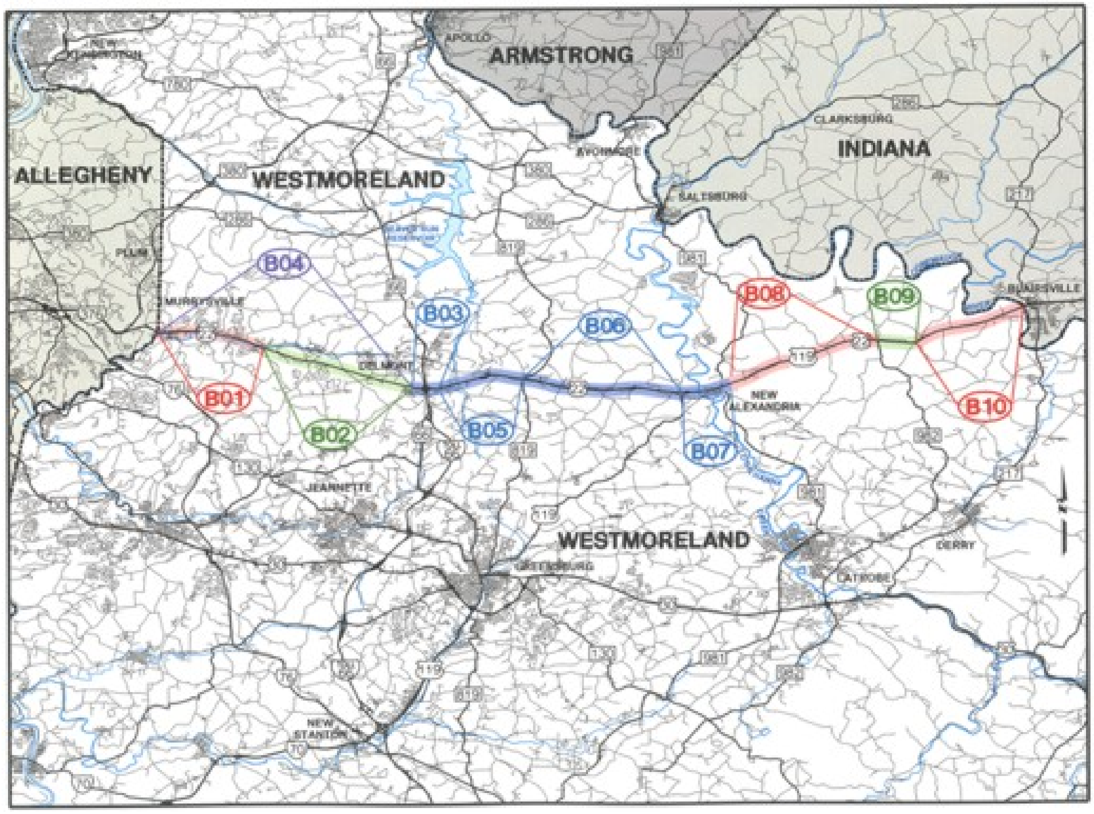

Figure 3.2 Renew 22 project construction sections, (www.renew22.com, June 2005).

Section B01 consists of eleven major intersections. The Smart Pavement research section is located in the westbound truck lane between intersection 7 (Tarr Hollow Road) and intersection 8 (School Road). Figure 3.3, shows the general location of these intersections, with respect to nearby roads and businesses.

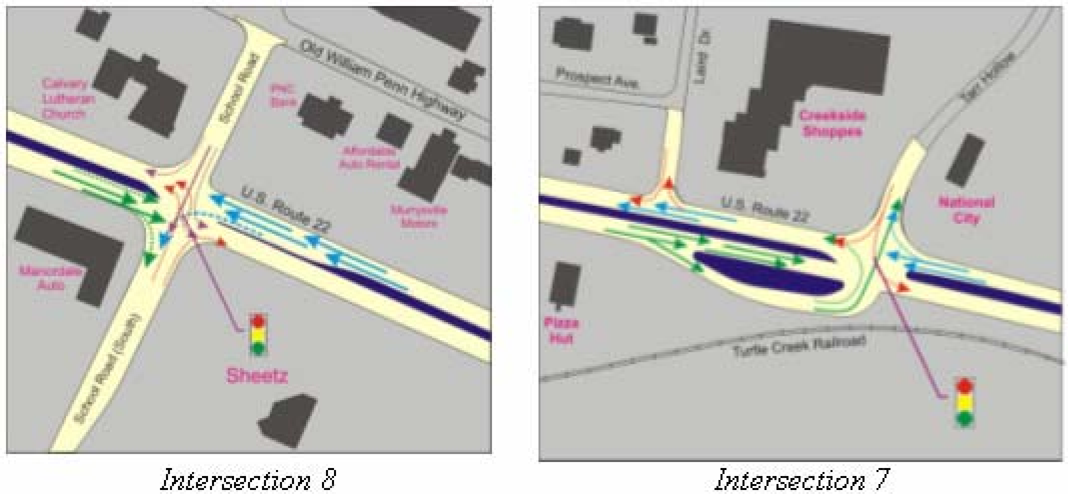

Figure 3.3 Locations of intersections 7 and 8, (www.renew22.com/B01/int7.htm, June 2005 and www.renew22.com/B01/int8.htm, June 2005, respectively).

The Smart Pavement test section consists of fourteen PCC slabs running from station 94+82 to station 96+92. The test section is located in front of a shopping plaza (Franklin Plaza) on the westbound side of the highway and a manufacturing facility (Beckwith Machinery Company) on the eastbound side. Figure 3.4 shows the location of PCC slabs that were instrumented.

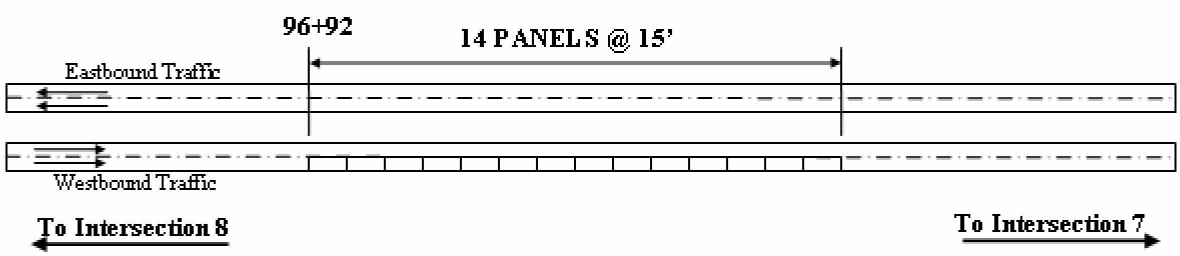

Figure 3.4 Layout of Smart Pavement test section.

The newly constructed roadway is a four-lane urban major arterial divided by a concrete median. At the time of design in June 2002, the two-way average daily traffic (ADT) volume was 26,950 vehicles with 5% being truck traffic. The projected ADT at the end of the design life in 2022 is 36,780 vehicles. The design hourly volume in June 2002 was 3,678 vehicles with a directional split of 60% in the predominate direction of travel. The posted speed limit is 35 miles per hour, with several traffic signals and businesses entrances occurring along the roadway.

3.2 SITE GEOMETRY

The new pavement structure is a JPCP with 15-ft transverse joints and 12-ft lanes. This section of roadway is crowned with a 2.0% transverse slope. The longitudinal slope along the research section is approximately 2.4%. The concrete medians vary in width from 14.4 ft to 2.0 ft with concrete mountable curbs. The Smart Pavement section contains 2.6-ft wide concrete curb-and-gutter-type shoulders at an 8% transverse slope, as shown in Figure 3.5.

Figure 3.5 Test section in the westbound lanes.

A description of the layers and layer thicknesses of the pavement structure are provided in Figure 3.6. Originally, the pavement was to be constructed directly on the subgrade but the poor soil conditions required the removal of a portion of the subgrade material Additional details are on the support conditions are provided in Section 3.3.1 of this chapter.

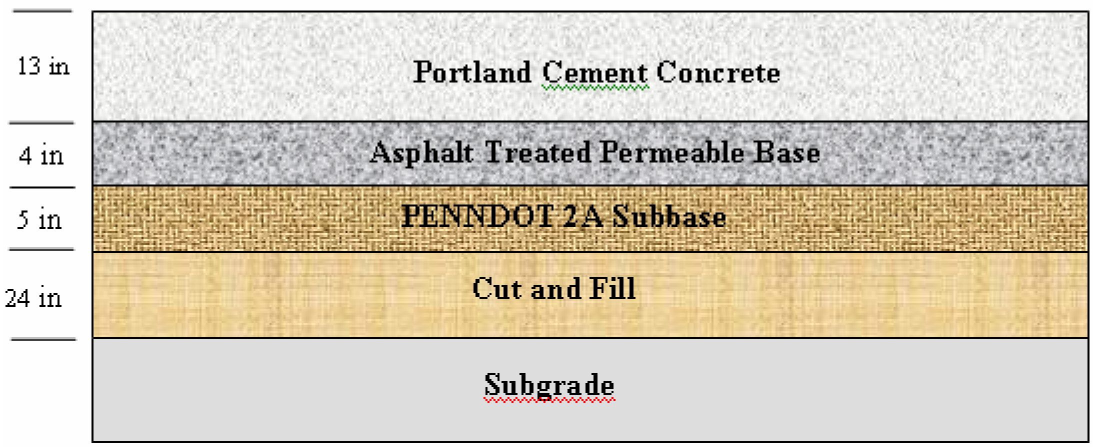

Figure 3.6 Design thicknesses of the pavement layers.

No. 5 epoxy-coated tie bars, were placed every 2.5 ft along both the lane/shoulder (l/s) and centerline joints. Epoxy coated 1.5-in dowel bars are spaced every 12" along transverse joints. The dowel and tie bar layout are depicted in Figure 3.7.

Figure 3.7 Dowel and tie bar configuration on SR-22.

Six-inch corrugated, polyvinyl chloride (PVC), longitudinal edge drains are present beneath the curb at a depth of approximately 8 inches below the bottom of the subgrade. The longitudinal drainage trenches are lined with a geotextile and filled with a American Association of State Highway Officials (AASHTO) No. 57 coarse aggregate. The drainage inlets are spaced at approximately 260 ft.

3.3 PAVEMENT CONSTRUCTION OVERVIEW

Construction conditions can have a significant influence on early-age strength development of concrete pavements. It is therefore important to characterize these conditions accurately. The construction conditions of each layer in the pavement structure were carefully documented at the Smart Pavement site. The following section provides an overview of these conditions, beginning with the subgrade and moving upwards towards the PCC surface.

3.3.1 Subgrade

An important aspect to consider during the design and analysis of a concrete pavement is to identify the depth to a rigid layer or a water table that might be present. The presence of either of these within 10 ft of the surface of the subgrade will influence the response of the slab to applied loads. The depths to the water table and the rigid layer were identified from the results of the soil borings pulled near the test section. These results are summarized in Table 3.1. These borings indicate the depth to rigid rock layers and the water table. For some of the borings, rock layers and water tables were not detected. For this case, the layers are assumed to be at least the depth of the boring. Note that in the vicinity of the Smart Pavement section (stations 96+92 to 94+82) at stations 95+145 and 97+11, the depth to either a layer of bedrock or a water table is at least 10 ft. These values are subject to a certain degree of error due to the fact that the final roadway elevations are located at the roadway centerline, while the borings were taken at an offset from the centerline.

Following a geotechnical analysis of the original subgrade, it was determined that the existing soil lacked the strength to adequately support the overlying pavement structure. PENNDOT discourages the construction of a pavement on a subgrade with a resilient modulus (MR) less than 7,500 psi (equivalent to a CBR value of approximately 5). Soils not meeting this criterion are to be undercut and backfilled with a more suitable material. Table 3.2 shows estimated resilient modulus values for soils at various stationing along Section B01. Note that at station 95+14, a station located within the Smart Pavement section, the MR value is 4,482 psi, indicating the need for an undercut in this section. The particle size distribution of the subgrade material shown in Table 3.3 is based on a Shelby Tube sample taken at station 97+11 at an offset of 49 ft to the right and at a depth of 5.9 to 7.9 ft below the original ground elevation of 923.56

ft. The sample contained a significant amount of fines with 77% of the material passing the #200 sieve. The AASHTO classification for this soil is an A-6, which generally performs fair to poor as a subgrade material, as shown in Figure 3.8.

Table 3.1 Field borings taken near the Smart Pavement test section.

Station	Distance From CL	Boring No.	Original Ground El. (ft)	New Ground El. at Given Station (ft)	Bedrock El. (ft)	Water Table El. (ft)	Bedrock Depth (ft)	Water Table Depth (ft)
66+60	16.4 ft RT	R-28	931.46	931.91	901.80	910.79	30.10	21.12
66+60	52.5 ft RT	R-29	917.39	931.91	901.05	910.01	30.86	21.90
69+16	16.4 ft RT	R-30	930.15	930.63	900.33	912.43	30.30	18.20
73+16	32.8 ft RT	R-31	926.67	928.63	NA	NA	NA	NA
76+12	105 ft LT	R-32	959.94	927.15	955.51	< 917.13	-28.36	> 10.02
80+05	85.3 ft LT	R-33	946.46	925.18	940.16	< 916.54	-14.97	> 8.64
82+35	55.8 ft LT	R-34	938.94	924.04	< 914.96	< 914.96	> 9.08	> 9.08
85+30	72.2 ft RT	R-35	922.54	923.26	< 912.20	< 912.20	> 11.06	> 11.06
85+96	26.2 ft LT	R-36	922.74	923.27	< 918.31	< 918.31	> 4.96	> 4.96
86+88	98.4 ft LT	R-37	937.34	923.42	< 927.00	< 927.00	> -3.58	> -3.58
90+88	27.9 ft RT	R-38	924.61	925.55	< 914.30	< 914.30	> 11.25	> 11.25
95+14	14.8 ft LT	R-39	930.71	930.60	< 920.37	< 920.37	> 10.23	> 10.23
97+11	49.2 ft RT	R-40	923.39	933.91	912.40	< 902.49	21.51	> 31.42
103+67	62.3 ft LT	R-41	957.48	948.64	< 934.84	939.76	> 13.80	8.87
105+81	37.7 ft RT	R-43	951.31	953.71	< 942.55	< 942.55	> 11.16	> 11.16
106+56	213.3 ft LT	R-44	969.23	955.33	< 959.97	< 959.97	> -4.64	> -4.64
112+20	24.6 ft LT	R-45	960.47	961.05	< 951.35	< 951.35	> 9.70	> 9.70
118+77	21.3 ft RT	R-46	952.95	953.45	< 943.34	< 943.34	> 10.11	> 10.11
122+34	55.8 ft LT	R-47	943.86	944.55	< 933.53	< 933.53	> 11.02	> 11.02

Table 3.2 Estimated resilient modulus values along section B01.

Station	Distance From CL	Estimated Field MR Value (psi)
66+60	16 ft RT	4482
69+16	16 ft RT	>8963
73+16	33 ft RT	8963
85+30	72 ft RT	8963
85+96	26 ft LT	>8963
86+88	98 ft LT	5976
90+88	28 ft RT	4482
95+14	15 ft LT	4482
106+56	213 ft LT	2988
112+20	25 ft LT	>8963
118+77	21 ft RT	5976
122+34	56 ft LT	2988

Table 3.3 Gradation of existing subgrade.

Sieve Size	Percent Passing
#4	100
#10	99
#20	99
#40	98
#60	95
#100	89
#200	77
0.787 mils	65
0.079 mils	33
0.039 mils	29

TABLE A CLASSIFICATION OF SOILS AND SOIL-AGGREGATE MIXTURES											
General Classification	Granular Materials (35% or less passing 75μm) [No. 200]							Silt-Clay Materials (More than 35% passing 75μm) [No. 200]			
Group Classification	A-1		A-3*	A-2				A-4	A-5	A-6	A-7
	A-1-a	A-1-b		A-2-4	A-2-5	A-2-6	A-2-7				A-7-5 A-7-6
Sieve Analysis:											
Percent passing:											
2mm (No. 10)	50 max.	---	---	---	---		---	---	---	---	---
425μm (No. 40)	30 max.	50 max.	51 min.	---	---	---	---	---	---	---	---
75μm (No. 200)	15 max.	25 max.	10 max.	35 max.	35 max.	35 max.	35 max.	36 min.	36 min.	36 min.	36 min.
Characteristics of fraction passing No. 425μm (No. 40):											
Liquid Limit	---		---	40 max.	41 min.	40 max.	41 min.	40 max.	41 min.	40 max.	41 min.
Plasticity Index	6 max.		N.P.	10 max.	10 max.	11 min.	11 min.	10 max.	10 max.	11 min.	11 min**
Usual Types of Significant Constituent Materials	Stone Fragments Gravel and Sand		Fine Sand	Silty or Clayey Gravel and Sand				Silty Soils		Clayey Soils	
General Rating as Subgrade	Excellent to Good							Fair to Poor			

The placing of A-3 before A-2 is necessary in the "left to right elimination process" and does not indicate superiority of A-3 over A-2.
**Plasticity Index of A-7-5 subgroup is equal to or less than LL minus 30. Plasticity Index of A-7-6 subgroup is greater than LL minus 30.

Figure 3.8 AASHTO soil classification chart, (www.mrr.dot.state.mn.us, July 2005).

In order to provide a more suitable material, the existing material in the area of the Smart Pavement section was undercut to a depth of approximately 2 ft. The cut began approximately 4 to 5 ft off from the edge of the existing eastbound lane and extended the width of the lane and the curb and gutter in the westbound direction, as shown in Figure 3.9. During the site selection phase, a section for the test site was selected in a region that a cut/ fill was not originally planned. It was determined that the subgrade materials should be removed and replaced with more suitable material after the existing pavement structure was removed. However, due to project constraints, the location of the instrumentation could not be moved to an alternate location after this was discovered.

Figure 3.9 Excavation of existing subgrade.

After the 2-ft cut was made, this area was then backfilled with a gap-graded soil and aggregate mixture, containing a significant amount of 206 rock. The fill material included large stone with diameters as large as 22 inches and greater as pictured in Figure 3.10.

Figure 3.10 Backfill material containing large boulders.

During installation of sensors in the subgrade, it was discovered that a 4-inch diameter gas line, running approximately parallel with the proposed roadway, existed approximately two feet below the surface of the 2A subbase and approximately 6 inches from the edge of the proposed PCC roadway surface as shown in Figure 3.11. Per contractor protocol, the trench (approximately 4 ft long by 2 ft wide) surrounding this exposed gas line was backfilled with a fine, granular sand-like material.

Figure 3.11 Gas utility running through subgrade.

3.3.2 Subbase

A 5-in slag subbase meeting PENNDOT Class 2A material was placed on top of the fill material. See Figure 3.12. The material was obtained from International Mill Service, located in Patton, PA.

Aside from providing economical protection from subgrade deformation, the 2A material is intended to act as a separator layer to prevent intrusion of subgrade fines into the asphalt treated permeable base, provide frost protection and provide a platform for subsequent construction.

Gradation specifications for this material were obtained from PENNDOT Publication 408 and are given in Table 3.4.

Figure 3.12 Slag subbase placed on top of the fill material.

Table 3.4 Gradation of the subbase.

PENNDOT 2A Subbase	
Sieve Size	**Percent Passing**
2"	100
3/4"	52 - 100
3/8"	36 - 70
No. 4	24 - 50
No. 8	16 - 38
No. 16	10 - 30
No. 200	$\leq$ 10

3.3.3 Permeable Asphalt Stabilized Base

A 4-in layer of asphalt treated permeable base (ATPB) was placed on top of the subbase. The mixture design is provided in Table 3.5. The maximum specific gravity of the hot mix asphalt was 2.57.

The gradation of the open-graded aggregate used for the ATPB is shown in Table 3.6. As of 2003, PENNDOT increased the allowable fines from 12% to 20% to help stabilized this very open-graded mix. The asphalt mixture used on SR-22 contained 9.7% sand, 85.8% coarse aggregate and 2.5% PG 64-22 binder.

The mixture used, shown in Figure 3.13, is highly permeable since only 9.7% sand was added. Prior to placement of the PCC layer, it was noted that a 5 gallon bucket dumped on this layer would flow freely through the layer without ponding on the surface.

Table 3.5 Mixture design for the ATPB.

Material Type	Material Specification	Proportion of Total Mixture	Bulk Specific Gravity	Absorption
Coarse Aggregate	PENNDOT A57	87.8 %	2.661	0.44 %
Fine Aggregate	PENNDOT B3	9.7 %	2.631	0.89 %
Binder	PG 64-22	2.5 %	1.030	-

Table 3.6 Gradation of the aggregate used in the ATPB.

Asphalt-Treated Permeable Base	
Sieve Size	**Percent Passing**
1 ½”	100
1”	99
½”	45
No. 4	16
No. 16	11
No. 200	3

Figure 3.13 Close up of the ATPB prior to placement of the concrete.

The hot mix asphalt was plant-mixed by Better Materials Corporation located in Adamsburg, Pennsylvania and was delivered by dump truck to the project site. A photograph of the paving operation is shown in Figure 3.14.

Figure 3.14 Placement of the ATPB.

A few difficulties were encountered with the construction of the base layer. First, prior to construction of the PCC, the ATPB was used as a platform for subsequent construction. Significant rutting (up to 1-in) caused by construction vehicles was observed throughout the instrumentation section prior to construction, particularly at the east end near station 96+92.

Furthermore, paving of the PCC was accidentally performed in the area of stations 94+82 to 95+42 prior to the installation of the sensors. The PCC was removed in this region. However, many of the voids near the surface of the ATPB were filled by the concrete debris created during the removal of the slabs, resulting in a less permeable base. These conditions also result in a lower degree of friction between the base and a newly placed pavement. Since these conditions would not be representative of those throughout the remaining portion of the test section, most of the ATBP in this area was removed and replaced. Some of the ATPB in an area that would not contain instrumentation was left in place, as pictured in Figure 3.15.

Figure 3.15 Region PCC slabs were removed and a portion of the ATPB was replaced.

Falling Weight Deflectometer (FWD) data was used to evaluate uniformity of support along the test section and to backcalculate layer stiffness in terms of resilient modulus (modulus of subgrade reaction). The resilient modulus of the ATPB was backcalculated using FWD testing performed on October 11, 2004 on top of the PCC layer. Calculations were based on slab on dense-liquid models and the AREA method-based procedure (Hall and et al., 1997). The slab and the ATPB were modeled as bonded plates (Ioannides and et al., 1992). See Figure 3.16 for the results of the analysis. The 5 inches of 2A subbase and 24 inches of backfill material have similar stiffness properties based on their soil classifications so they were modeled as one layer. Deflection data from the FWD testing performed on the ATPB prior to the placement of the PCC was then used with the known resilient modulus of the subgrade (provided in the soils report) and ATPB (backcalculated with FWD deflections measured on top of the PCC slab and corrected for temperature) to backcalulate the resilient modulus of the combined layers. The pavement structure was modeled using linear elastic layered analysis to perform the backcalculation.

The measured deflection basins and the resulting backcalculated effective resilient moduli of the subbase and fill along the Smart Pavement section are provided in Figures 3.17 and 3.18, respectively.

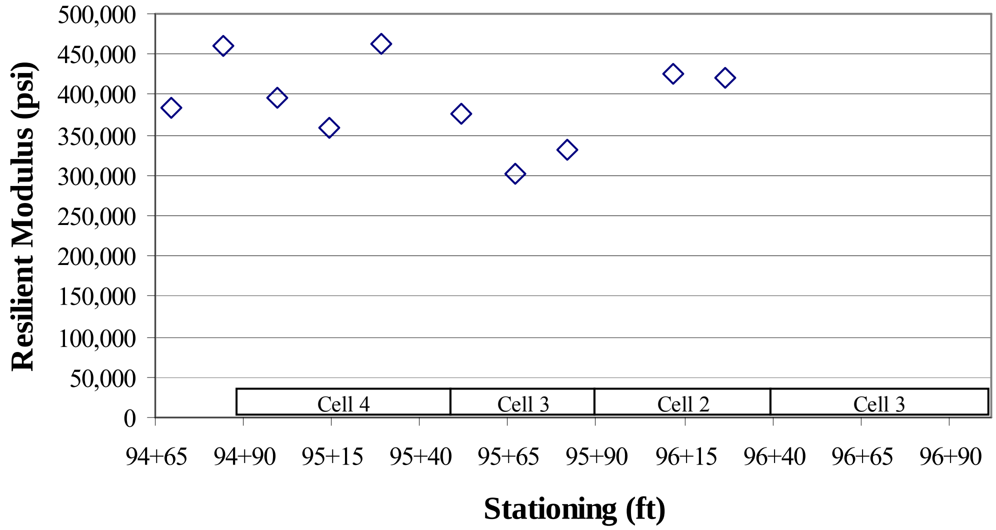

Figure 3.16 Backcalculated resilient moduli for the ATPB.

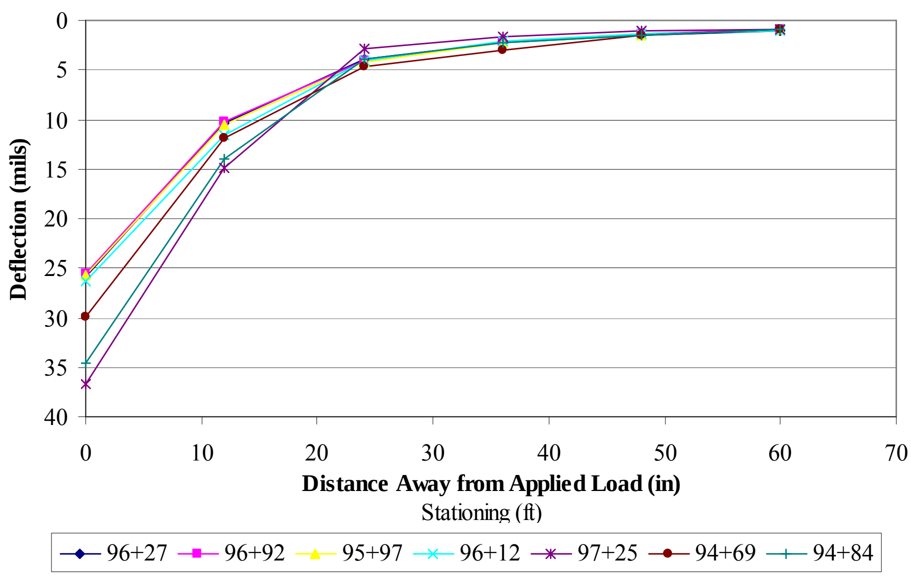

Figure 3.17 FWD deflection basins measured on top of the ATPB.

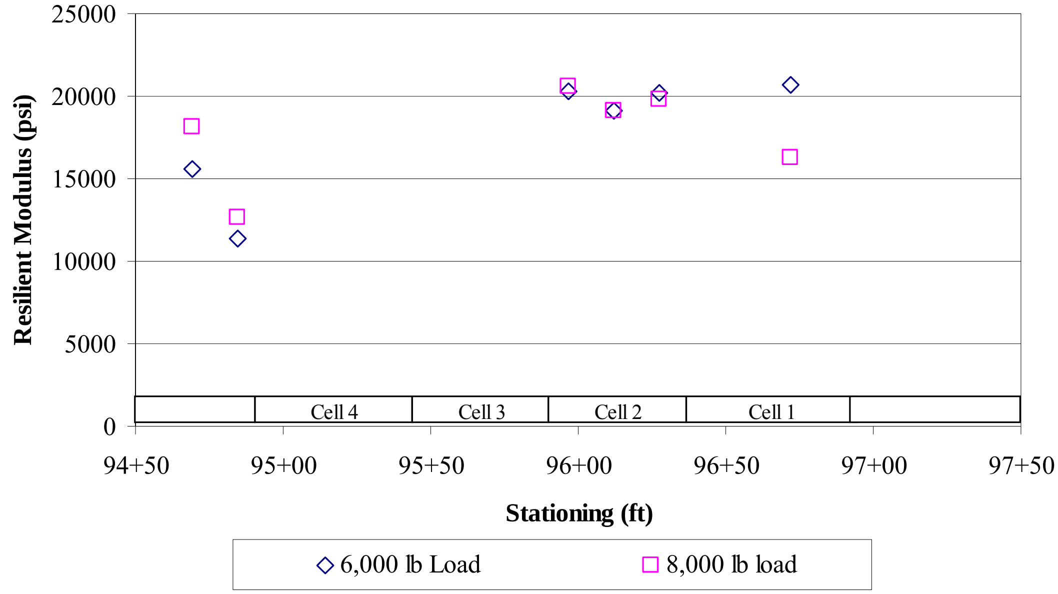

Figure 3.18 Backcalculated resilient modulus of subbase and backfill.

The average resilient modulus of the subbase and backfill near Cell 4 is 14,400 psi with a standard deviation of 3,060 psi and the average resilient modulus for Cells 1 and 2 is 19,500 with a standard deviation of 1,450 psi. The deflections from Figure 3.17 measured directly under the load plate and 36 in away from the applied load are summarized in Figure 3.18. The deflection directly under the applied load provides an indication of the stiffness of the upper layers in the pavement structure while the deflection measured further away from the applied load gives an indication of the stiffness of the lower layers. Figure 3.19 shows the deflections measured 36 inches away from the applied load to be relatively constant while the deflections measured directly under the applied load show greater variability. This indicates the lower layers have a relatively constant resilient modulus but the resilient modulus of the upper layers varies. Table 3.7 contains the average resilient modulus of each pavement layer.

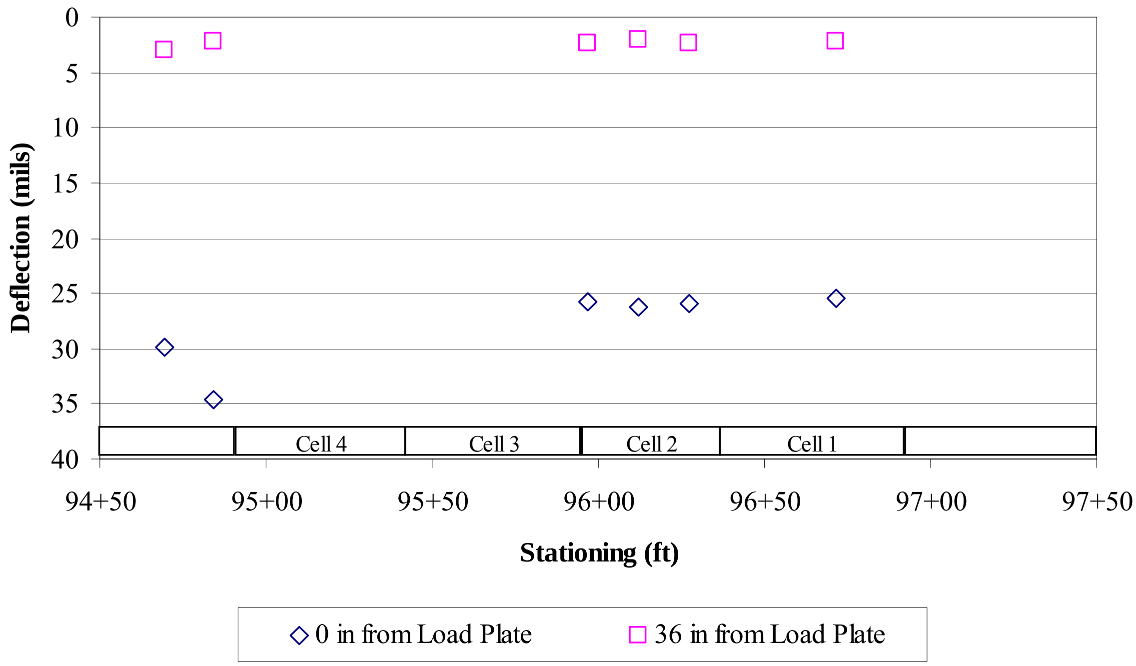

Figure 3.19 Deflections measured on top of the ATPB .

Table 3.7 Stiffness of each pavement layer.

Layer	Stiffness
PCC slab @ 28 days	4,600,000 psi
ATPB @ 53 °F	348,000
2A Subbase and Backfill	19,500 psi
Subgrade	4,500 psi

3.3.4 PCC Pavement

Paving took place on the morning of August 16, 2004 beginning at approximately 6:15 a.m. The design thickness of the PCC layer is 12 inches, although cores taken from the instrumented section showed actual thicknesses ranging from 12 to 14 inches. A summary of slab thicknesses throughout the test section is presented in Chapter 6 of this report. The concrete was produced by Stone and Company. It was mixed at a portable plant located approximately five miles east of the project site in Export, Pennsylvania and was delivered to the site via front-discharge mixer trucks, as shown in Figure 3.20.

Figure 3.20 Concrete truck delivering fresh concrete to site.

The eastbound pavement was previously placed so only the westbound lane was being paved on August 16. The curb and gutter was tied onto this outside lane at a later date. The Gomaco paver ran off a single string-line. During paving, great care was taken to protect the sensors located throughout the slab from damage associated with the paving equipment. Prior to the passing of the paver, fresh concrete was mounded around each sensor installation by hand and then consolidated using a flexible shaft vibrator. This procedure can be seen in Figure 3.21.

After the paver passed, transverse tining was performed, as shown in Figure 3.22, and a curing compound from W.R. Meadows, Inc., was applied to the surface. Sawing of the joints began at approximately 5:00 PM that evening. The joints were sawed to a depth of 1/3 the slab thickness.

Tests pertaining to the quality of ride for Construction Section B01 were performed following construction of the PCC layer and it was determined that diamond grinding would be required over several sections in order to eliminate surface roughness. In order to maintain consistent sensor depths below the original pavement elevation, diamond grinding was prohibited in the Smart Pavement section.

Figure 3.21 Concrete was hand placement around the sensors.

Figure 3.22 Application of transverse tining.

3.4 MIXTURE DESIGN

The purpose of the following section is to characterize the material properties of the PCC used for the Smart Pavement project. Properties such as water-cement-ratio, aggregate gradation, and chemical composition of the cement affect early age strength gain in concrete. Data for PCC material properties was obtained from the PENNDOT “Batcher Mixer Slip” completed August 16, 2004 at 5:05 AM, approximately one hour prior to construction.

The cementitious materials included Type I cement manufactured by St. Lawrence Cement’s Mississauga, Ontario plant as well as ground granulated blast furnace slag from Holcim Inc. in Wierton, West Virginia. A chemical analysis conducted by St. Lawrence Cement reveals the composition detailed in Table 3.8. Physical properties and compressive strengths, also evaluated by St. Lawrence Cement, are summarized in Table 3.9 and 3.10 respectively.

Table 3.8 Chemical analysis of cement loaded into rail cars.

Component	Percent	Component	Percent
LCl	2.30	Insoluble (previous month)	0.29
SiO_2	19.65	CO_2	1.51
Al_2O_3	5.48	Limestone	4.0
Fe_2O_3	2.21	$CaCO_3$ in Limestone	66.6
CaO	61.76	**Mineralogical Composition**	**Percent**
MgO	2.42	C_3S	42.44
SO_3	4.15	C_2S	24.33
Total Alkali	0.92	C_3A	10.77
Free Lime	0.84	C_4AF	6.73

Table 3.9 Chemical analysis of cement loaded into rail cars.

Residue	8.4 %
Blaine	1953 ft^2/lbs
Air Content	7.3 %
Initial Set (min)	119 minutes
Auto Expansion (previous month)	0.06 %
Sulfate Expansion	0.013 %
False Set	72.2 %

Table 3.10 Compressive strength of cement as measured by St. Lawrence Cement.

Age (days)	Strength (psi)
1	2993
3	4155
7	4953
28 (previous month)	6138

The course aggregate, AASHTO No. 57, consisted primarily of limestone and came from Hanson Aggregates PMA in Whitney, Pennsylvania. The fine aggregate, PENNDOT Spec. Type A, came from their South Buffalo Township, Pennsylvania branch. Gradations for the fine and coarse aggregates can also be found in Tables 3.11 and 3.12, respectively. The "Batcher Mixer Slip" indicated that loss by washing for the fine aggregate was 1.20%, while the loss by washing for the coarse aggregate was 1.22%.

Table 3.11 Gradation of fine aggregate used in the PCC.

Fine Aggregate	
Sieve Size	**Percent Passing**
3/8"	100
#4	100
#8	76
#16	57
#30	45
#50	23
#100	6

Table 3.12 Gradation of coarse aggregate used in the PCC.

Coarse Aggregate -- Limestone	
Sieve Size	**Percent Passing**
1 ½"	100
1"	99
½"	36
#4	2
#8	2

The mixture design had a water-to-cementicious ratio (w/cm) of 0.36 based on the "Batcher Mixer Slip." Air entrainment and water reducing admixtures supplied by Axim Concrete Technologies were also used. A summary of the mixture design can be found in Table 3.13.

Table 3.13 PCC mixture design for Smart Pavement test section.

Material	Specific Gravity	Absorption	Batch Weight (per yd^3)
Type I Cement (St. Lawrence)	3.15	n/a	382 lbs
Ground Granulated Blast Furnace Slag (Holcim)	2.89	n/a	206 lbs
Fine Aggregate (Hanson, PENNDOT Spec. Type A)	2.61	1.15 %	1248 lbs
Coarse Aggregate (Hanson, AASHTO No. 57)	2.68	0.5 %	1881 lbs
Air Entrainment – Catexol 360 (Axim)	n/a	n/a	5.7 oz
Water Reducer – Catexol 100N (Axim)		n/a	17 oz
Water Content (City Water)	1	n/a	286 lbs

3.5 INSTRUMENTATION AND DATA ACQUISITION

This chapter will provide background information on the sensors and data collection equipment used to characterize the early age stress response of the JPCP to environmental stresses. Information pertaining to the installation technique employed for each sensor will be covered in addition to an explanation of the data acquisition and monitoring system utilized. The latter section of this chapter will present the layout of the test section and provide an overview of the locations where each sensor was installed.

3.5.1 Sensor Overview

To determine the response of the slab to environmental loads, the response of the slab, as well as the climatic conditions within the structure, must be monitored. For this reason, environmental sensors were installed to document the temperature and moisture gradients that develop throughout the depth of the slab. A weather station was also installed on site so that ambient conditions could be recorded. The weather station records air temperature, relative humidity and wind speed every fifteen minutes. All of this data is fed into the automated data acquisition system that will be discussed further at the end of this chapter. A description of the environmental sensors selected is provided below.

3.5.1.1 Temperature Sensor Thermocouples, pictured in Figure 3.23, were selected for measuring temperature throughout the pavement structure. For the Smart Pavement project, 60 thermocouples were installed at four locations (two in the corner of the slab and two at midpanel).

Figure 3.23 Temperature sensor installation.

Type T thermocouple wire from Omega Engineering was used. The thermocouple wire contains two dissimilar metals, copper and constantan. When a junction is formed between these two metals, a small but unique voltage is produced. Since this voltage is approximately linear with temperature, a relationship can be established. Prior to installation, the ends of the thermocouple wire were spliced and soldered, creating a junction at the end of the wire. These wire ends were then mounted to wooden dowels at various depths, as shown in Figure 3.23. The opposite ends of the thermocouples were wired to 3 separate 25-channel Campbell AM25T multiplexors. The AM25T, as shown in Figure 3.24, is wired to a Campbell CR23X datalogger.

Figure 3.24 AM25T thermocouple multiplexor, (www.campbellsci.ca/CampbellScientific/Catalogue/AM25T.html, June 2005).

3.5.1.2 Concrete Moisture Sensors In order to measure moisture levels within the concrete, 24 Sensirion SHT75 relative humidity and temperature sensors were installed in Cell 4. Procedures developed at the University of Illinois at Urbana-Champaign for the use of these sensors in concrete applications were followed (Grasely and et al., 2003). At Illinois, the sensors were used successfully in laboratory concrete embedment applications; however, a reliable procedure for the use of these sensors in large-scale field research applications had not been developed prior to the Smart Pavement Project. The SHT75 sensor is a relatively small (approximately 0.75 in by 0.25 in by 0.125 in) and cost effective means of measuring relative humidity in concrete. The module, pictured in Figure 3.25, utilizes a capacitive polymer sensing element to measure relative humidity and a band gap temperature sensor to measure temperature.

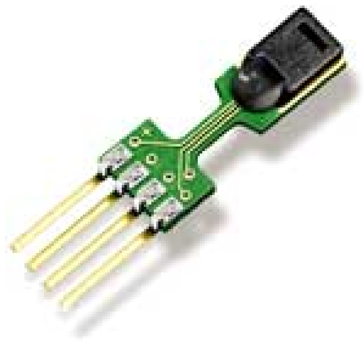

Figure 3.25 Sensirion SHT75 Relative Humidity and Temperature Sensor, (www.sensirion.com, June 2005).

The sensors are pre-calibrated with built-in correction coefficients. Communication to and from the sensor is accommodated by four connector pins, which supply power, receive clock instructions, and transmit temperature and relative humidity data.

In order to collect data in the field, the SHT75 must be wired to a data-collection system. For this purpose, a BasicX24 Microcontroller kit was programmed to retrieve data from the sensor. These relatively inexpensive microcontroller kits, pictured in Figure 3.26, include a wall power transformer, a 9-pin serial download cable, programming software for the microcontroller chip, and a development board, which can accommodate up to 15 Sensirion sensors.

Figure 3.26 BasicX24 microcontroller development kit, (www.basicx.com/Products/BX-24/bx24devkit.htm, June 2005).

A data interface program developed at the University of Illinois by Z. C. Grasley and D. A. Lange was used to communicate measurement intervals to the microcontroller. This program, created using Labview 7, also allows for real-time viewing of the data in graphical format while storing temperature and relative humidity information in a user-selected file location.

To protect the sensor from direct exposure to the concrete mixture, a sensor housing system developed by Grasley and Lange was employed. For protection, the sensor is inserted into a plastic cylindrical tube. In most cases an ordinary plastic pen tube will accommodate the sensor. The end of the tube is sealed with a circular GORE™ membrane vent. These vents act to protect the sensor from exposure to cement particles and excessive water exposure, while allowing the passage of water vapor for accurate humidity readings.

The membrane can be sealed to the cylindrical plastic enclosure using ordinary superglue. However, it is recommended to do this at least twenty-four hours prior to inserting the sensor because vapors given off from the adhesive may diffuse into the polymeric layers of the sensor, leading to unexpected errors in sensor offsets and sensitivity. After gluing, for additional support, the Gore™ Membrane Vents were tightly sealed around the circumference of the plastic enclosures using zip-ties. The opposite end of the tube is sealed using rubber electricians tape and an electricians waterproofing sealant. Similar to the thermocouples, the moisture sensors are attached to wooden dowels at given depths. The final result, shown in Figure 3.27, is a cost-effective, less invasive means of measuring PCC relative humidity then other options evaluated.

Figure 3.27 Installation of relative humidity sensors.

3.5.1.3 Static Strain Sensors The PCC response to static loads generated is measured with vibrating wire (VW) strain gages. These gages were installed at various depths and locations within the PCC panels. For purposes of this thesis, the following critical strain locations will be analyzed: the midpanel, the longitudinal edges, the transverse edge, and the corners of the panel.

For the Smart Pavement project, Geokon Model 4200 vibrating wire concrete embedment strain gages were used. The gages operate on the vibrating wire principle. A steel cable is tensioned between two metal end blocks. When the gage is embedded in concrete and concrete deformations take place, these end blocks move relative to one another. The movement of these end blocks influences the degree of tension in the steel cable. This tension in the cable is quantified by an electromagnetic coil, which measures the cable's resonant frequency of vibration upon being plucked. The sensor is also equipped with a thermistor so that corrections for temperature can be made.

Figure 3.28 shows a typical VW strain gage configuration that was employed at the Smart Pavement study near the longitudinal centerline joint. This configuration consists of two rows of gages, one located near the top and one near the bottom of the PCC slab.

Figure 3.28 Static strain gage installation.

The gages were installed similar to the PCC thermocouple and moisture sensors. Sensors were attached to wooden dowels at given depths. These depths were meticulously checked to ensure proper depth and alignment upon PCC paving.

Data from static strain gages is collected and stored on a Campbell CR10X datalogger for the Cell 3 VW gages and a Campbell CR23X datalogger for the Cell 4 VW gages. Additional components required to read the vibrating wire strain gages of the Smart Pavement project include Campbell AVW4 vibrating wire interfaces and Campbell 16-channel AM16/32 multiplexers, which are shown in Figure 3.29. The AVW4 interface contains circuitry that allows for frequency measurements taken from the strain gages to be read as voltage by the datalogger. The AM16/32 expands the number of channels that can be wired to the datalogging equipment, allowing for a multitude of sensors to be read.

Figure 3.29 Accessories for collecting data from the vibrating wire strain gages, (http://www.campbellsci.ca, June 2005).

3.5.2 Sensor Locations

The following section provides an overview of the locations of each of the sensors discussed in subsequent chapters. This section is divided into two components. The first component discusses the general layout of the test sections. The second component describes the location of the sensors within these sections.

3.5.2.1 Layout of the Test Sections Static strain gages, moisture sensors, and thermocouples were installed in sets of slabs (panels) referred to as "cells." There are a total of four cells consisting of three panels each in the Smart Pavement study. The cells are labeled 1 through 4, with numbers increasing in the westward direction. Cells 1 and 2 measure seasonal dynamic loading and Cells 3 and 4 measure both static and environmental loading. The sensors in Cells 1 and 2 are of the same type, quantity, depth, and location. The same is true for Cells 3 and 4 with the exception that Cell 4 also contains environmental monitoring sensors. Static and environmental sensors were installed in Cells 3 and 4 and will therefore be the focus of this study.

While the sensor arrangements in these two sets of cells are repetitive, there is one key variable that sets them apart. Cells 2 and 3 are unrestrained by dowel and tie bars (see Figure 3.7) while Cells 1 and 4 contain dowels and tie bars. One of the key research objectives is to investigate the effects of the restraint condition induced by the dowel and tie bars on pavement response. Non-instrumented transition panels act to isolate the two unrestrained cells (Cells 2 and 3) from the restrained cells (Cells 1 and 4). Of the 14 panels that comprise the instrumentation section, twelve were instrumented with the remaining two acting as transition panels between the restrained and unrestrained sections. See Figure 3.30.

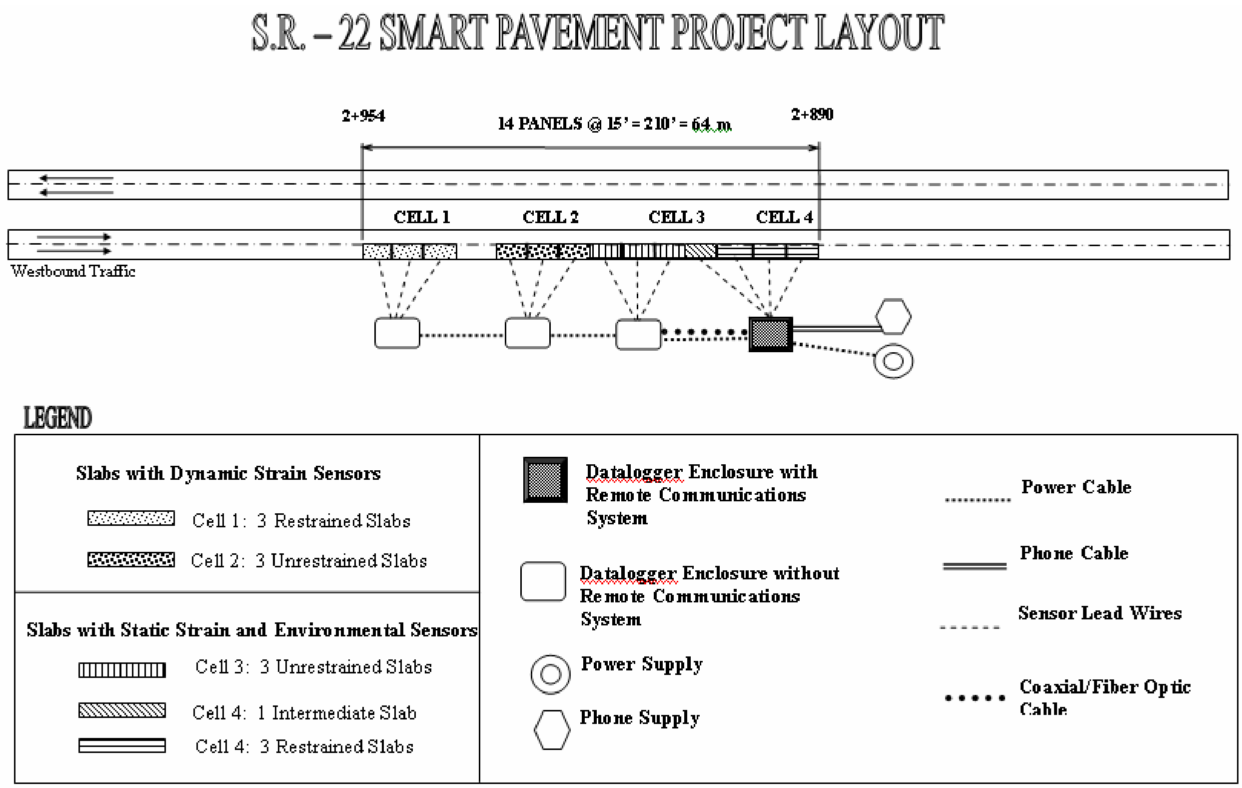

Figure 3.30 Layout of the Smart Pavement section.

Prior to installation, the performance of each sensor was tested at the University of Pittsburgh's Pavement Mechanics and Materials Lab to ensure that they met manufacturer specifications. The sensors were then installed in each of the 4 cells and wired to a set of datalogging equipment specific to that cell. A total of over three miles of wire was used to connect all the sensors into the dataloggers. The dataloggers for each cell are housed within protective enclosures that were constructed directly adjacent the instrumented panels and approximately twelve feet away from the edge of the curb. Electricity is provided for each of these enclosures and phone service is provided for the enclosures for Cells 3 and 4. A schematic of the general sensor layout, enclosure arrangement, and wiring is provided in Figure 3.30.

A summary of the sensors used to characterize early age environmental stress response, including quantity and location is provided in Table 3.14.

Table 3.14 Summary of Environmental and Static Strain Sensors.

Sensor Type	Sensor Name	Qty.	Measurement	Cell
Environmental	Thermocouple	60	Temperature	4
Environmental	Moisture Sensor	24	Relative Humidity	4
Static Strain	Vibrating Wire Strain Gage	156	Static Strain	3, 4

3.5.2.2 Environmental and Static Sensor Locations The layout of the climatic and static load sensors contained in Cells 3 and 4 is shown in Figure 3.31. The typical dimensions are shown in Figure 3.32. The surveyed coordinates can be found in Appendix A, along with a diagram outlining sensor locations within the test section. Note that the static strain gages are oriented both longitudinally and transversely. Longitudinally oriented static strain gages measure static strains occurring in the longitudinal direction of the panel. Transversely oriented static strain gages measure static strains across the transverse direction of the panel.

In order to capture thermal and moisture gradients at locations throughout the slab area, thermocouples and moisture sensors are located at both the midpanel and slab corners in Cell 4.

Figure 3.31 also shows the locations of the elevation rods used for taking surface profile measurements. The dashed lines in Figure 3.31 show the directions along the slab where these measurements were performed. The role of surface profile measurements will be discussed in Chapter 5. Not shown in the figure are gage studs, which were imbedded in the corners of the slabs to measure the joint widths.

The planned depths of the sensors in Cells 3 and 4 are shown in Figure 3.33. Note that the static strain gages and moisture sensors are located in the PCC layer only. Thermocouples occur throughout the entire depth of the pavement structure to capture both daily and seasonal temperature variations.

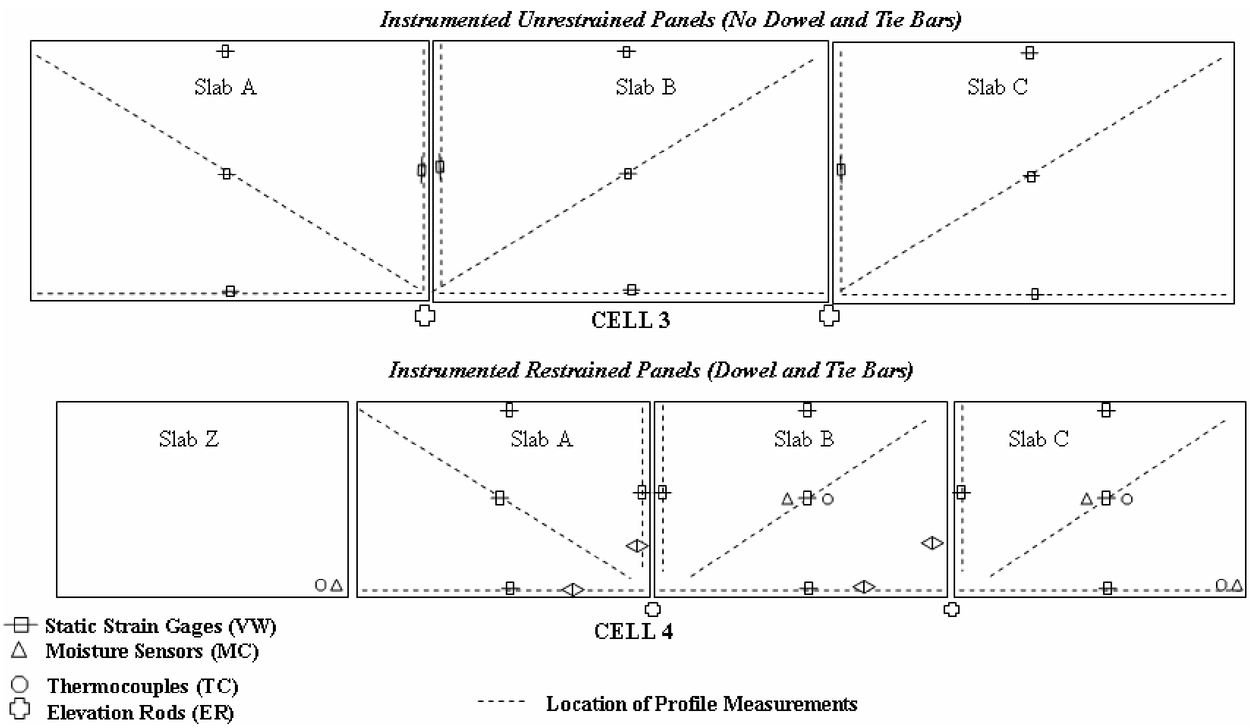

Figure 3.31 Location of static strain gages, environmental sensors, TDR sensors, and static pressure cells.

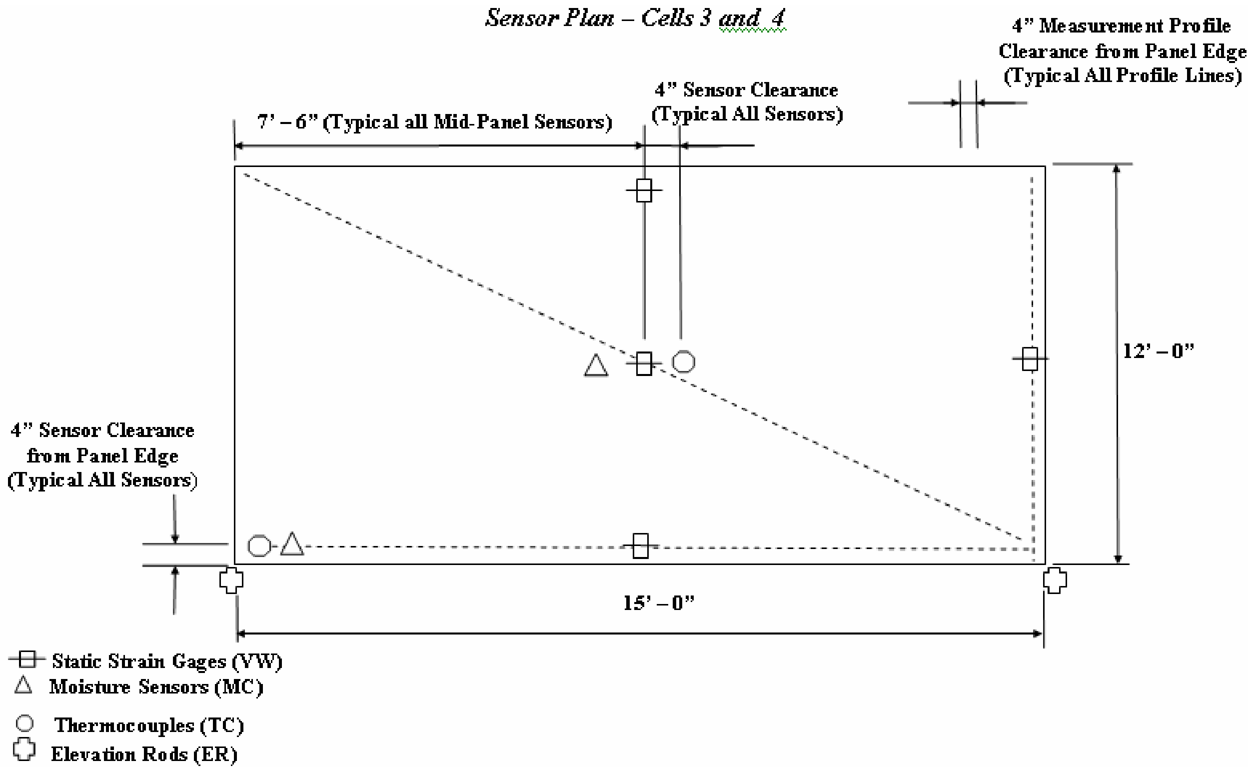

Figure 3.32 Typical dimensions of static strain gages and environmental sensors.

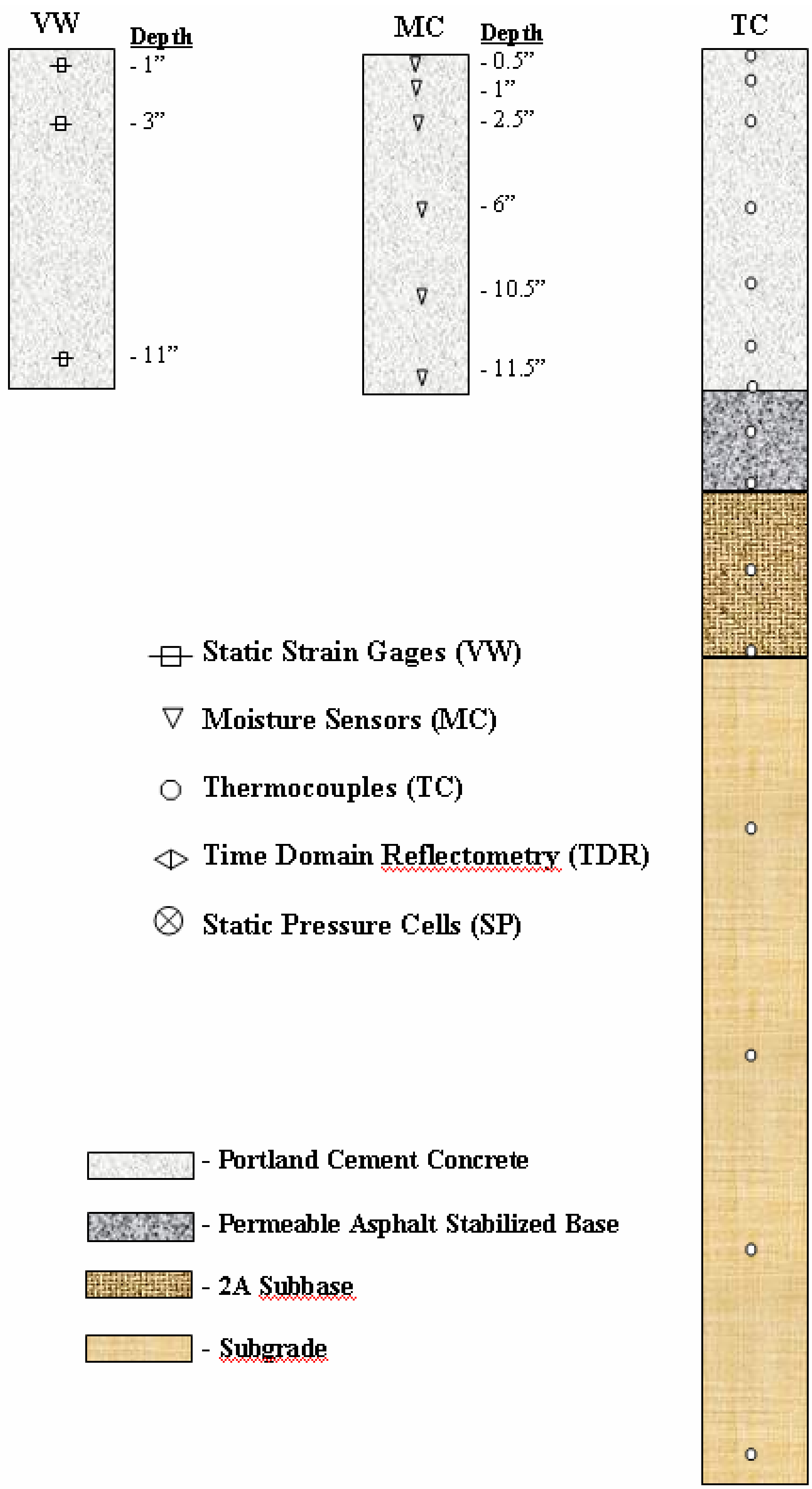

Figure 3.33 Depths of sensors in cell 3 and cell 4.

3.5.3 Automated Data Acquisition Layout

Data for the Smart Pavement project is collected both on manual and automated systems. Manual data collection is performed for the dynamic sensors in Cells 1 and 2, while automated data collection takes place for the static and environmental sensors in Cells 3 and 4. The manual data collection system is utilized during seasonal load response testing so that data collection can be triggered for known load magnitudes and locations. The automated data collection system has been collecting data from the time of paving and continues to collect data at predetermined time intervals. The following section will describe the automated data collection system of Cells 3 and 4.

For the static load and environmental sensors of Cells 3 and 4, an automated data collection system, shown in Figure 3.34, was developed.

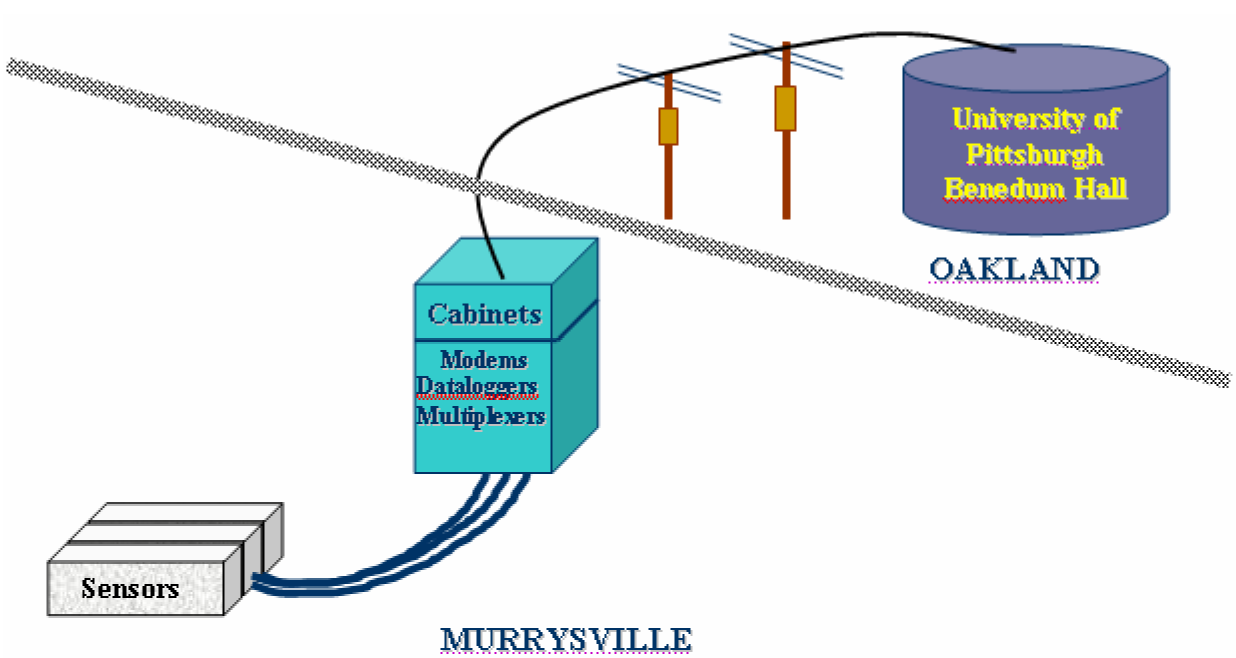

Figure 3.34 Automated data collection system for the static and environmental sensors.

Under this system, the embedded sensors are wired to multiplexors, which are wired to dataloggers. The dataloggers automatically retrieve data at given time intervals. For the Smart Pavement project, data for all sensors is collected every 15 minutes, with the exception of the TDRs. Data is collected from the TDRs once every 24 hours. Once per day, the data collected on the CR10X datalogger in Cell 3 and the CR23X datalogger in Cell 4 is sent via telephone modems to a computer database located at the University of Pittsburgh. The data collected every 24 hours for each datalogger is appended to the end of the existing data files. This data communication process is repeated daily and checked for validity and backed-up weekly.

4.0 PCC CLIMATIC DATA ANALYSIS

The following chapter provides an analysis of the climatic data collected at the Smart Pavement site. The climatic conditions at the time of paving can greatly affect the performance of the slab. Climatic conditions are also important when characterizing the effects of curling. Ambient conditions were measured in the field using the on-site weather station. Thermal and moisture gradients were captured using thermocouples and moisture sensors embedded throughout the depth of the pavement. The early age response of the pavement structure to these gradients is highly sensitive to the ambient conditions and this section will therefore present the findings from the climatic data analysis and its influence on slab response.

4.1 VALIDATION OF TEMPERATURE MEASUREMENTS

All embedded thermocouples were replicated in the event of individual sensor failure and to insure the accuracy of each sensor. Sensor locations and coordinates can be found in Appendix A. Two sets of thermocouples were installed at midpanel and two at the edge of the slab throughout the depth of the pavement structure. Data from each pair of replicated sensors was directly compared as a means of validating sensor accuracy. Figure 4.1 shows the temperature at various depths within the pavement structure for the replicated sensors at the approximate time of set and the time the transverse joints cracked. The sensors correlated very well.

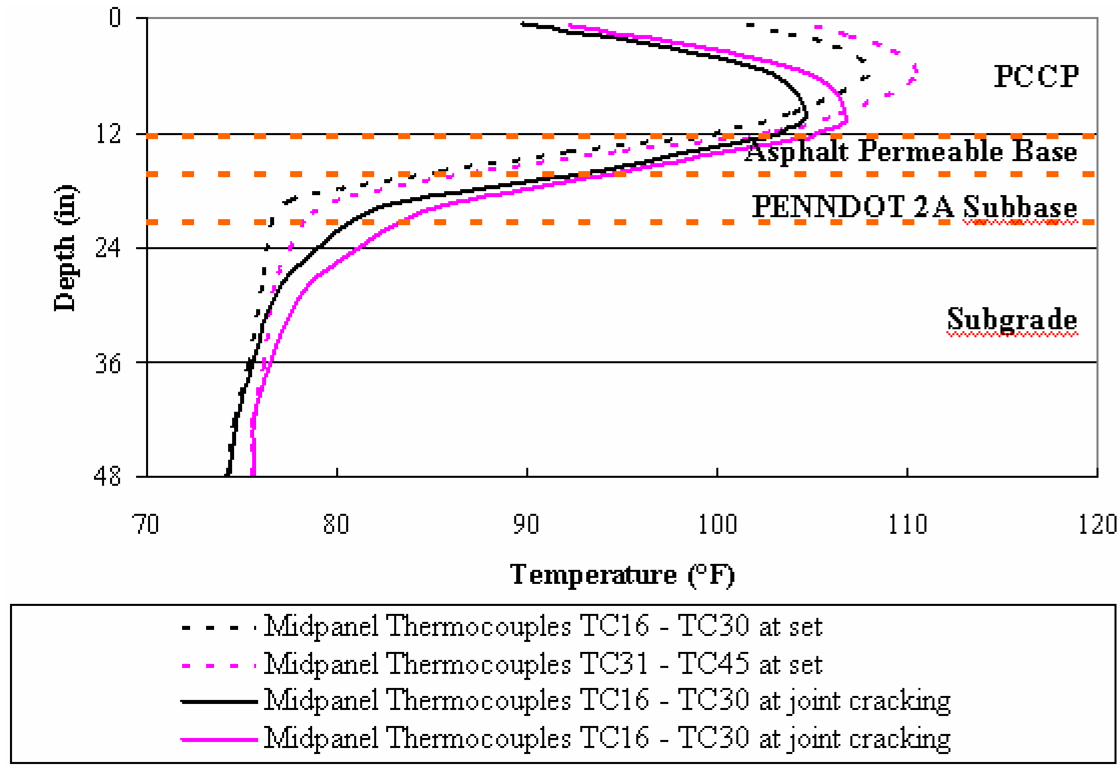

Figure 4.1 Temperature gradients measured at midpanel in two separate slabs when the concrete set and when the joints cracked.

The same evaluation was performed on the thermocouples installed along the edge of the slab. The temperature gradients in Figure 4.2 show thermocouples 46 through 60 are giving temperatures about 3 to 5 degrees higher than the temperatures provided by thermocouples 1 through 15. The temperature gradients match much more closely for the data collected on October 31, 2005, as shown in Figure 4.3. The curb and gutter was tied on after the paving of the westbound lane was performed. Therefore the edges of the slab and the base were exposed to the ambient climatic conditions. The curb and gutter were constructed before October 31, thereby creating more uniform conditions between the sensor groups. The survey data revealed that thermocouples 1 through 15 are located approximately 13 inches from the edge of the slab while thermocouples 46 through 60 were located just over 9 inches from the edge. It appears that this difference in distance from the edge is influential before the curb and gutter are attached but are not significant once the curb and gutter has been placed.

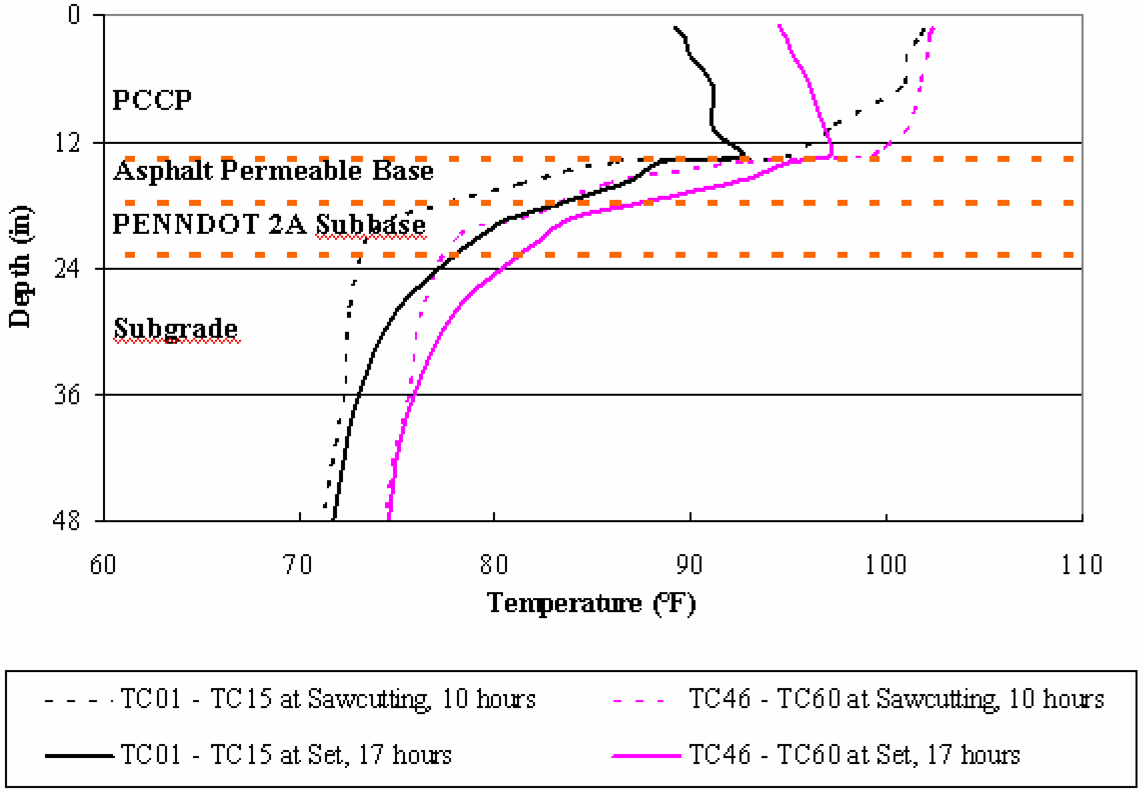

Figure 4.2 Temperature gradients measured at the slab edge in two separate slabs when the concrete set and when the joints were being sawed.

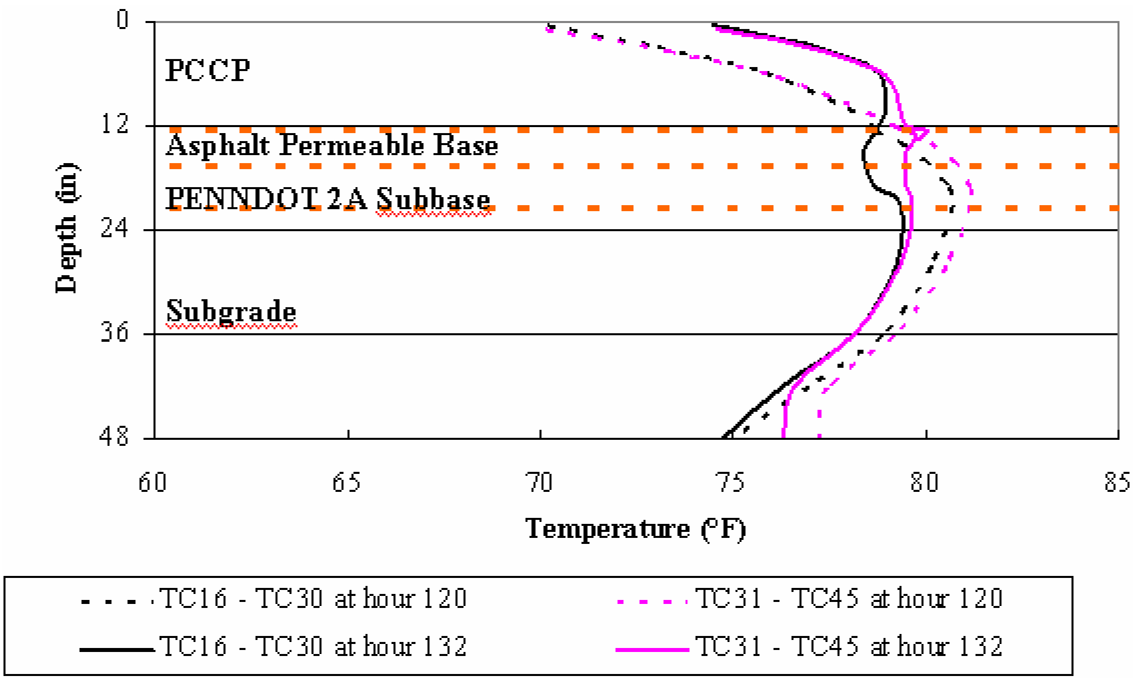

Figure 4.3 Temperature gradients measured at the slab edge in two separate slabs on October 31st, 2005, after the curb and gutter was constructed.

4.2 BUILT-IN CONSTRUCTION CURLING AND WARPING

Temperature gradients throughout the pavement structure are affected by both seasonal and daily environmental conditions. The top of the pavement is affected predominantly by daily environmental changes while the bottom varies more seasonally. Positive gradients force the edges and corners of the pavement downwards thereby increasing support in these locations and decreasing the support at the center of the slab. Corner and edge loads may result in decreased deflections under these conditions because the contact area and/or pressure between the slab and the underlying layer is increased. Negative gradients force the corners and edges of the pavement upwards and the center of the pavement downwards, thereby reducing support at the corners while increasing it at midpanel, this results in decreased midpanel deflections and increased corner and edge deflections.

The slab dose not generally lie flat when a temperature/moisture gradient is not present because the concrete slab typically sets with a temperature gradient present, resulting in permanent deformation. The temperature gradient present at the time the concrete sets is referred to as the construction gradient, as discussed above. The magnitude of the construction gradient is influenced by the time of the day at which the concrete is placed and by the daily fluctuations in the ambient temperature. The construction gradient is a required input for the 2002 Guide for the Design of New and Rehabilitated Pavement Structures but there currently is not good data available to define what this input should be with any level of confidence.

Figure 4.5 shows the temperature distribution throughout the pavement and sublayers at the time of paving, when the concrete set, and when the joints cracked. The estimated time of set of 10 hours was based on static strain data. This was also about the same time the joints were sawed. Figure 4.4 shows strain versus change in temperature. The set time was defined as the time that strain began to develop with changes in temperature.

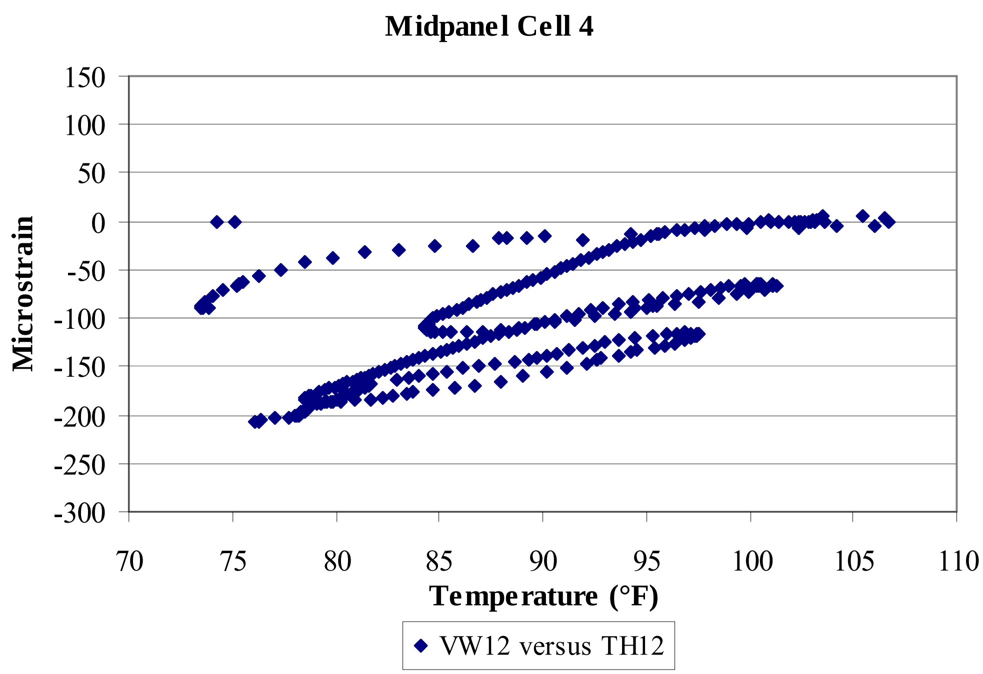

Figure 4.4 Strain versus temperature at midpanel in Cell 4 for the first 72 hrs after paving.

At the time of set, there was a 0.7 °F/in. gradient at the edge of the slab and practically no gradient at midpanel. However, since the gradient is not linear, identifying the gradient as zero does not do justice to the larger internal temperature differentials present at the time of set, as seen in Figure 4.5. The moisture sensors showed the moisture content throughout the depth of the slab to be at 100 percent relative humidity, indicating a built-in moisture gradient was not of concern for this pavement. It should be noted that the moisture sensor closest to the pavement surface was 1/2 inch below the surface. The relative humidity at the surface or a very short distance below may have been less than 100 percent.

The joints cracked approximately 17 to 19 hours after paving. At this time there was a large negative gradient of about -1.0 °F/in, as shown in Figure 4.6, which produced enough stress to crack the slab.

Figures 4.6 and 4.7 show the temperature distribution at midpanel and the edge of the slab, respectively. These graphs illustrate the fact that the temperature distribution throughout the slab is not uniform so the deformation produced by the temperature gradients in the slab will not be symmetrical. The temperature generated within the slab is a function of the boundary conditions. The slab is cast along a pre-existing slab on one side (centerline edge) and the other edge (lane/shoulder edge) is exposed to ambient conditions since the curb and gutter were constructed after the lane was paved. At midpanel, the heat will be retained more than at the lane/shoulder edge where the slab is exposed to the cooler evening temperatures throughout the depth of the pavement. This is why the edge of the pavement will be approximately the same temperature throughout the depth of the slab. A hypothetical depiction of the spatial distribution of the temperature throughout the slab is provided in Figure 4.8.

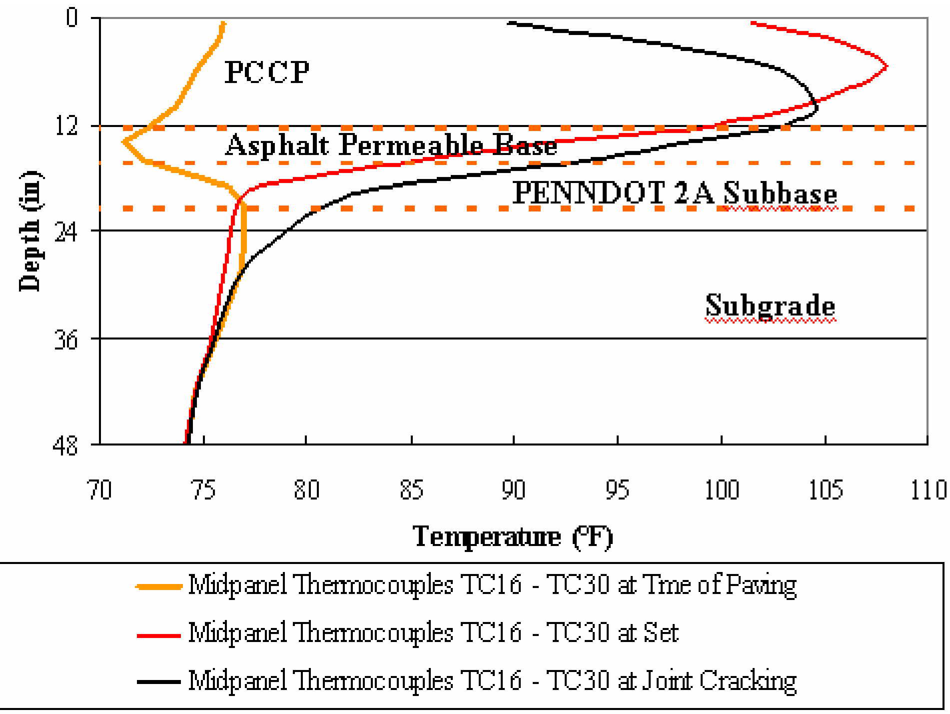

Figure 4.5 Temperature distribution throughout the depth of the pavement structure at midpanel.

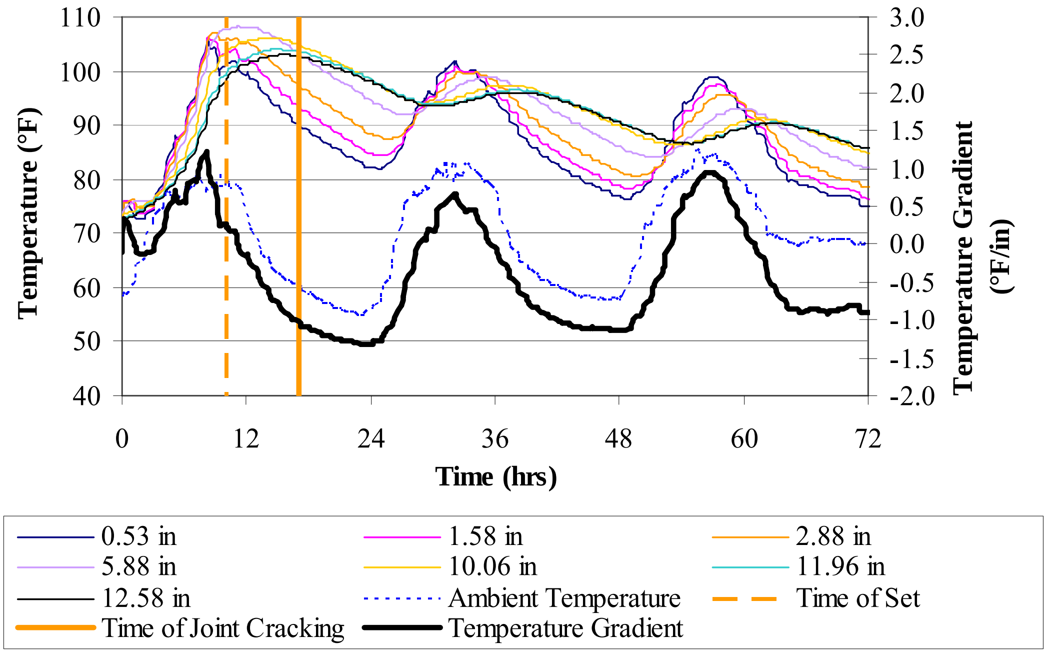

Figure 4.6 Midpanel temperature distribution within the concrete slab compared to ambient temperature and temperature moment.

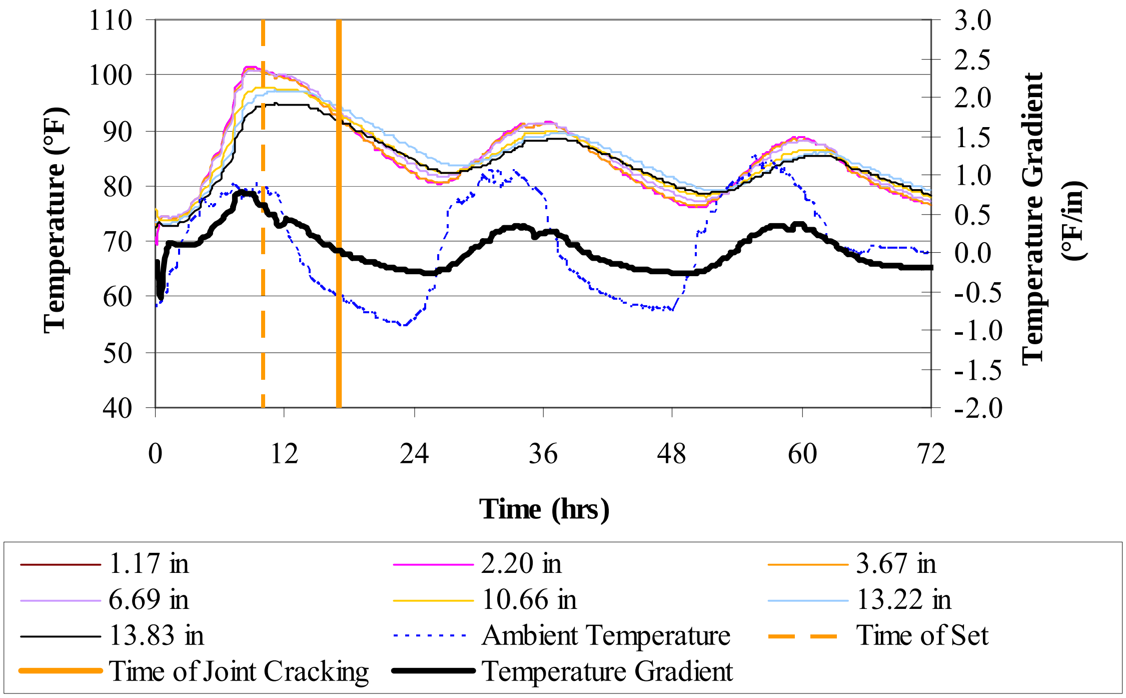

Figure 4.7 Edge temperature distribution within concrete slab compared to ambient temperature and temperature moment.

Figures 4.9 and 4.10 illustrate more clearly the difference between gradients at midpanel and at the edge. It is apparent that the midpanel is subject to more dramatic temperature swings during the day. These larger swings result in the development of larger gradients at the midpanel. As shown in Figures 4.9 and 4.10, even adding on the curb and gutter does not completely negate of the effect between the temperatures at the edge of the slab and at midpanel.

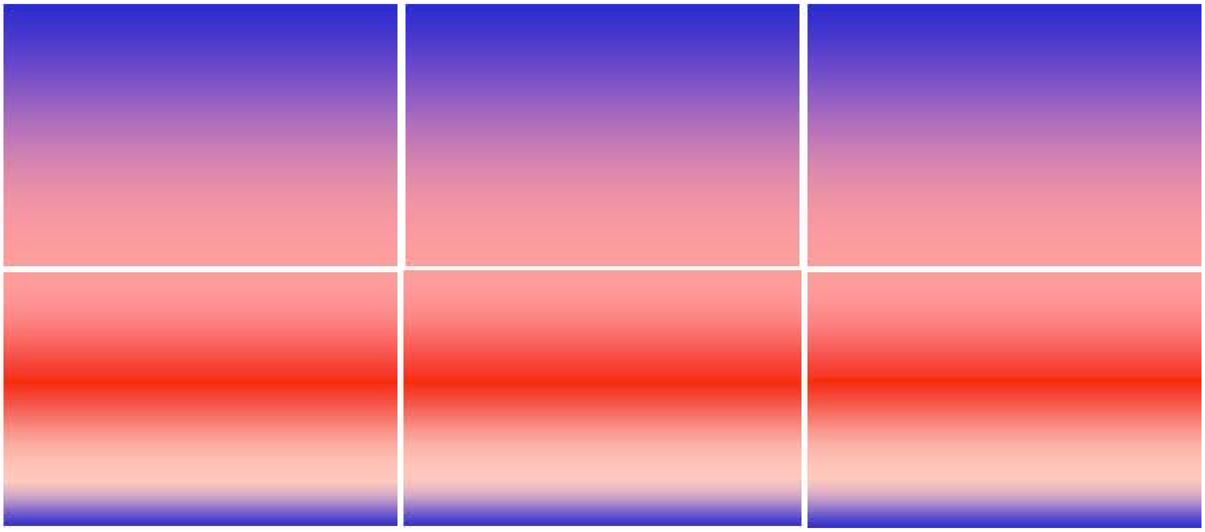

Figure 4.8 Representation of the spatial temperature distribution within slab when the concrete set.

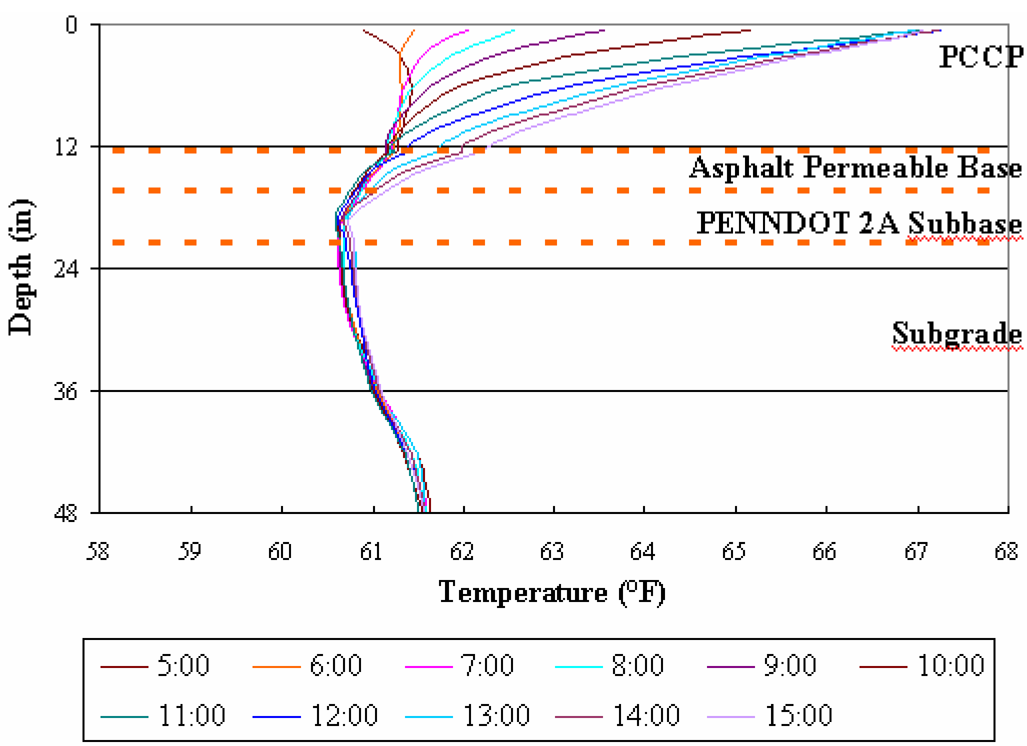

Figure 4.9 Temperature gradient at the midpanel during a 10- hour period on October 31, 2005.

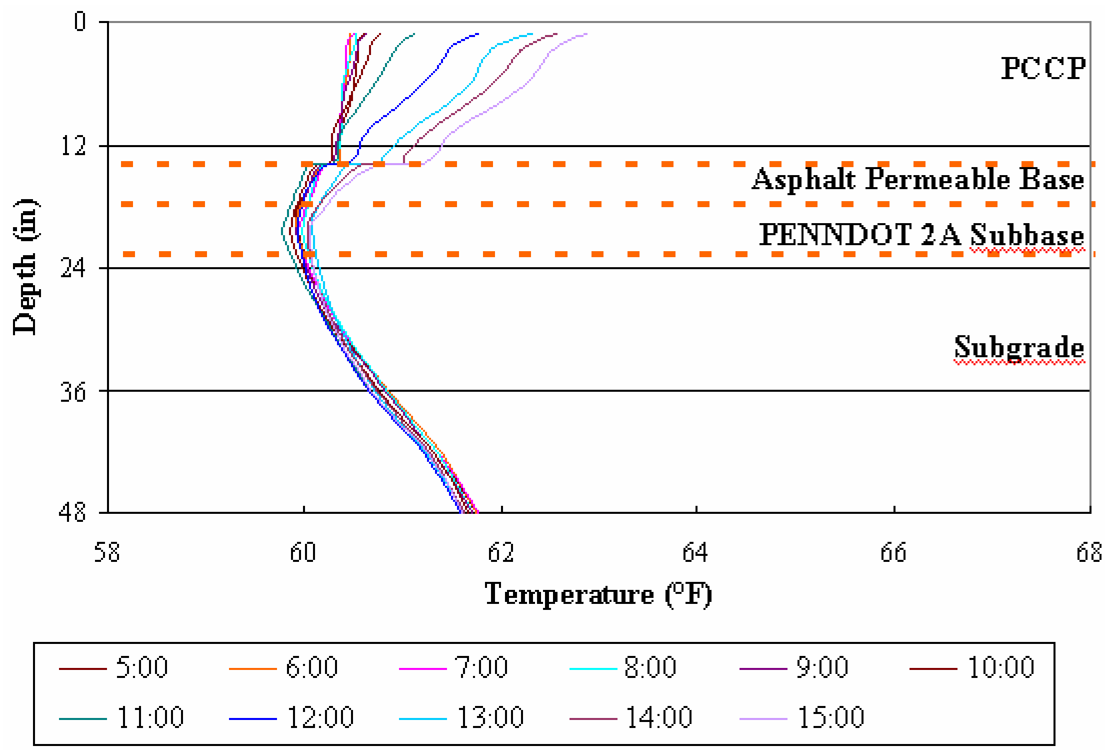

Figure 4.10 Temperature gradient at the edge during a 10- hour period on October 31, 2005.

4.3 AMBIENT TEMPERATURE CONDITIONS

The ambient conditions at the Smart Pavements were collected from the time of paving (August 2004) through July 2005. Seasonal changes in temperature have a significant effect on temperatures within the pavement. These seasonal changes in pavement temperature profiles effect the stress distributions in pavements throughout the year.

Ambient and embedded thermocouple data collected from the latter part of August to the beginning of July are shown in Figure 4.11. The data includes average monthly, average monthly high, and average monthly low air temperatures. Monthly averages were also provided for the temperature gradient measured throughout the depth of the slab and weighted average slab temperature.

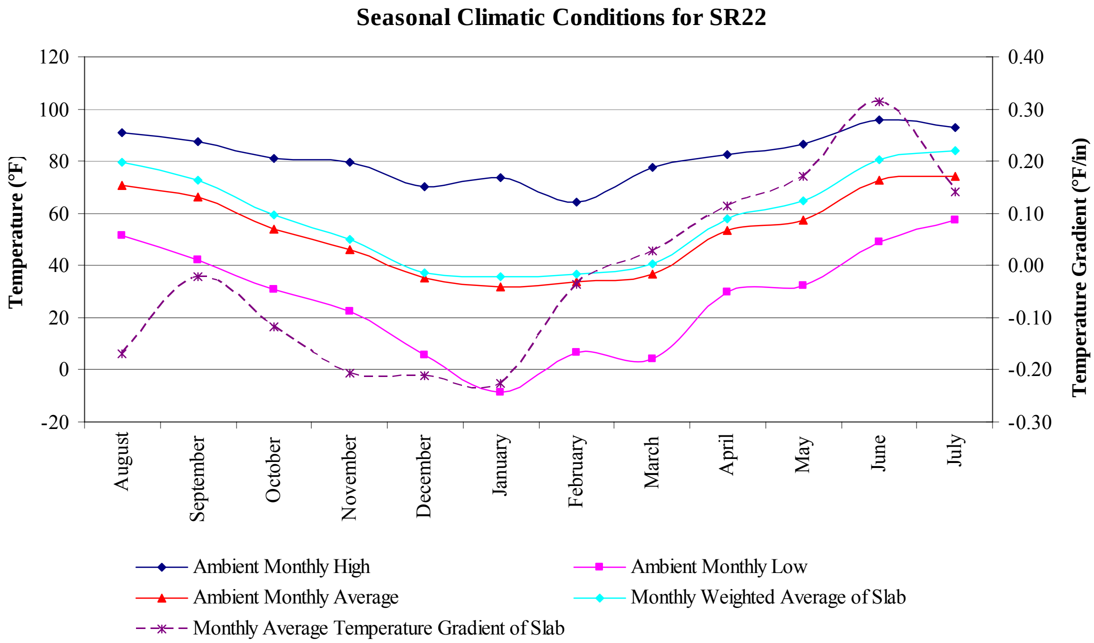

Figure 4.11 Seasonal temperature conditions at the Smart Pavement site.

Notice that the temperature conditions are typical for that of a region experiencing four distinct seasons. The monthly average temperature reaches a low in the winter (January) and reaches a high in the summer (June). It is important to note that only partial data was available in for the months of July and August. As expected, monthly average slab temperature matches the average monthly ambient temperature very closely. Another important aspect of Figure 4.11 worth noting is that the monthly average temperature gradient reaches a minimum in January, while reaching a maximum in June, indicating the strong relationship between seasonal temperature gradient and ambient conditions. Histograms summarizing monthly ambient temperature, monthly weighted average slab temperature, and monthly temperature gradient are given in Appendix B of this report. The effect of these seasonal temperature patterns on PCC strain response will be evaluated in Chapter 6 of this report.

4.4 PCC MOISTURE CONTENT

Variations in moisture throughout the concrete slab depth causes warping of the slab. The moisture distribution throughout the slab was measured directly using moisture sensors. A detailed analysis of the contribution of moisture to strain within the concrete was also conducted and is presented in Chapter 6.

Moisture content was continuously monitored within the concrete at varying depths using relative humidity sensors. Some communication problems with the data acquisition system led to gaps in the data. A sample of the moisture date measured over a four day period between 300 to 460 hours after paving is shown in Figure 4.12. The dotted lines represent sensors near the surface, the dashed lines represent sensors near mid-depth and the solid lines represent sensors located near the bottom of the slab. The temperature fluctuations are smaller at lower depths in the slab. The influence of temperature on relative humidity is apparent in that the deeper the sensor is embedded in the slab, the smaller the magnitude of the fluctuations in the humidity readings. No rain events were recorded during the period shown, so fluctuations in humidity are primarily due to changes in temperature and drying of the pavement surface. As can be seen in Figure 4.12, the moisture content in the concrete is still quite high throughout the depth of the slab.

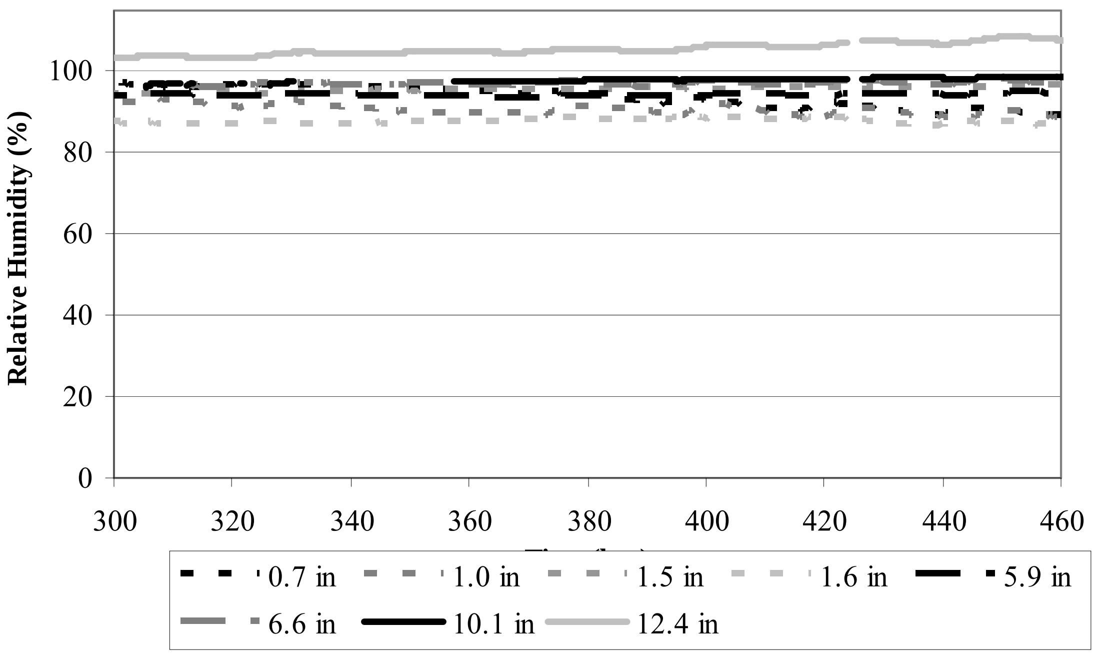

Figure 4.12 Relative humidity at varying depths in the concrete 300 to 460 hours after paving.

Figure 4.13 shows the moisture distribution throughout the depth of the slab. The relative humidity of the concrete near the surface of the slab is lower then at the bottom of the slab. The exposure to the ambient heat and wind near the surface of the slab reduces the humidity. The moisture content in the concrete is also influenced by rain events. Rain events can increase the relative humidity near the surface and bottom of the slab. This requires continuous rain over a sustained period of time. The moisture content at the bottom of the slab will then increase as the base becomes saturated.

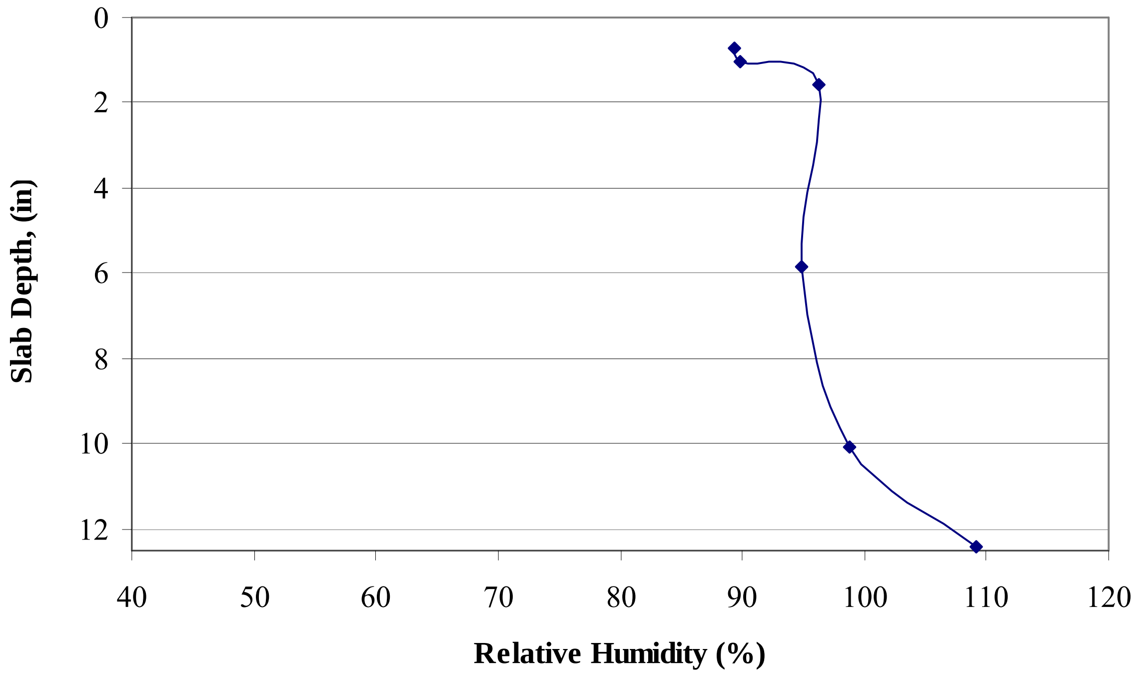

Figure 4.13 Moisture distribution throughout the depth of the concrete.

5.0 CURLING AND WARPING ANALYSIS

5.1 SURFACE PROFILE MEASUREMENTS

In order to quantify the effect of early-age (first 72 hours) and seasonal effects of curling and warping on PCC pavements, surface profile measurements are taken. These profile measurements capture the shape of the slab under various temperature and moisture gradients. In order to measure the surface profiles of slabs experiencing thermal and moisture gradients, an instrument called a dipstick, manufactured by Face Construction Technologies, Inc. was utilized. The dipstick pictured in Figure 5.1, is a highly sensitive device that measures difference in elevation between successive points along a PCC surface. When walked across a PCC slab, relative elevations of the slab profile, and hence curling and warping can be measured. Surface profiles were measured along designated lines across the slab in the longitudinal, diagonal, and transverse directions, as outlined in Figure 5.2.

Figure 5.1 Dipstick used to measure surface profiles.

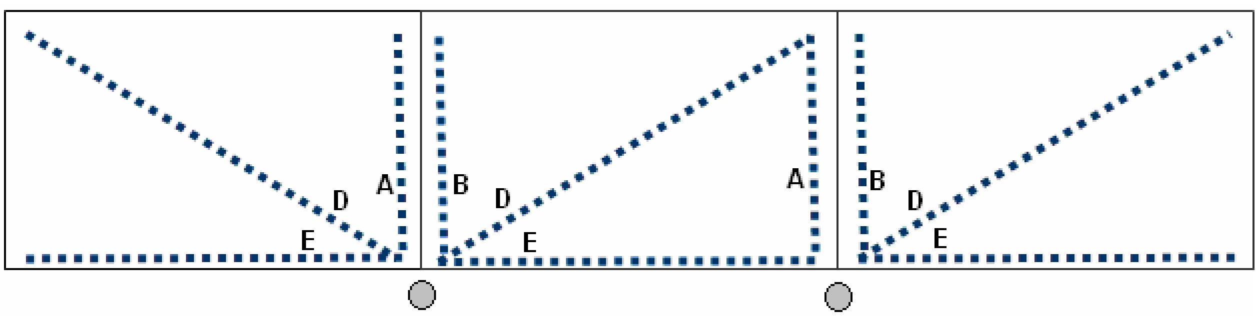

Figure 5.2 Locations where surface profiles were measured.

Note the two circular objects located near the transverse joints along the shoulder in Figure 5.2. These objects represent the tops of invar rods which were placed in the ground at a depth of approximately 12 feet. The top of this rod, pictured in Figure 5.3, maintains a constant elevation throughout the year and is thus used as a benchmark for all slab profile measurements. In order to ensure the consistency of these reference elevations, the upper portions of the invar rods were encased in grease-filled polyvinylchloride (PVC) tubing to protect the rods from the expansive stresses induced by frost exposure. The elevation of the top of the rods was determined by the District 12 survey crew. Initiating each dipstick run off from the top of the rod allows all relative elevations measured with the dipstick to be tied into actual elevations.

Figure 5.3 Top of invar rod.

5.2 TEMPERATURE MOMEMT

The temperature gradients described earlier are calculated simply by dividing the temperature at the top and the bottom of the pavement by the distance between them. The shortcoming of this method is that it provides a linear relationship while non-linear gradients are known to exist in the pavement. In order to account for the non-linear temperature gradients, the parameter "temperature moment" developed by Janssen and Snyder (2000) will be used. The temperature moment was developed so that a nonlinear gradient can be defined using a single parameter. Figure 5.4 graphically summarizes the derivation of temperature moment for any given period of time within the concrete pavement. It is important to remember that a positive linear gradient will produce a negative temperature moment and therefore a negative linear gradient produces a positive temperature moment.

$$\textit{Temperature Moment} = \Sigma(A_i \ \mathrm{x} \ r_i)/D$$

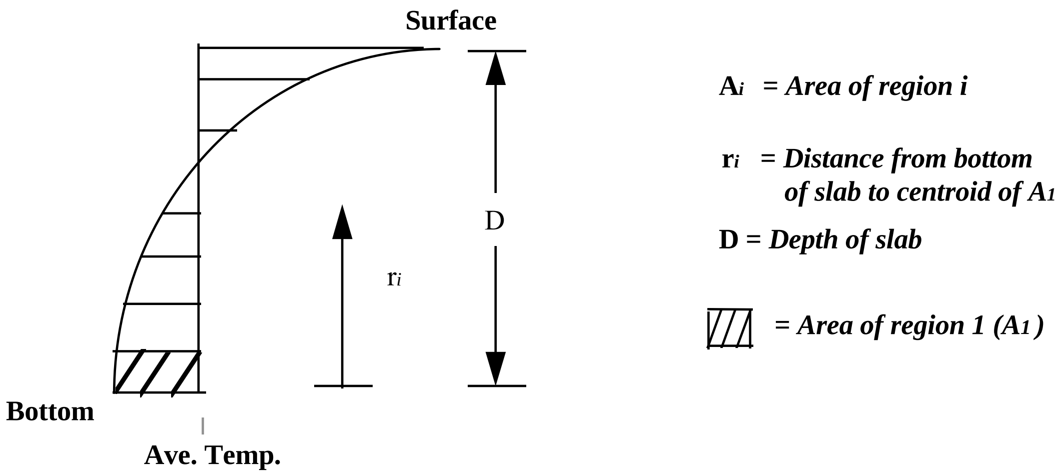

Figure 5.4 Graphical method for showing the temperature moment calculations (Vandenbossche, 2003).

5.3 SURFACE PROFILE MEASUREMENTS

The dipstick was able to provide a dynamic representation of the concrete slab surface profile as daily temperature moments caused it to curl. The main focus of this analysis was to evaluate the curling response to different joint conditions, in particular between those with and without dowel and tie bars. Note that imperfections in the slab were taken into account by zeroing each profile based on the time the concrete set. The set time occurred between 5:00 PM to 9:00 PM when there was almost no gradient in the slab. The temperature moment at the time of set was less than 50 ^{o}F-in^{2}. All profile measurements discussed below were made prior to the placement of the curb and gutter.

Representative slab profiles measured in the diagonal, longitudinal, and transverse direction are shown in Figures 5.5 through 5.10. Each figure contains profiles measured at different times of the day. The diagonal profiles are in Figures 5.5 and 5.6, the longitudinal profiles are in Figures 5.7 and 5.8 and the transverse profiles are in Figures 5.9 and 5.10 for both unrestrained and restrained slabs. All profiles were measured within the first week after paving.

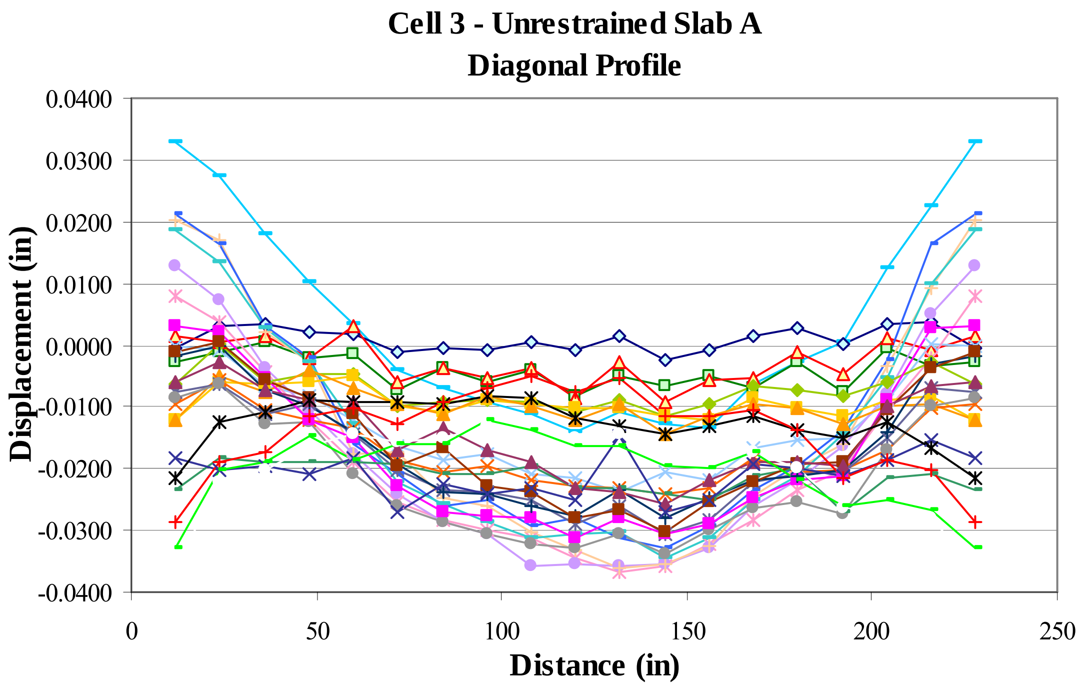

Figure 5.5 Diagonal profiles measured on Slab A in the unrestrained cell.

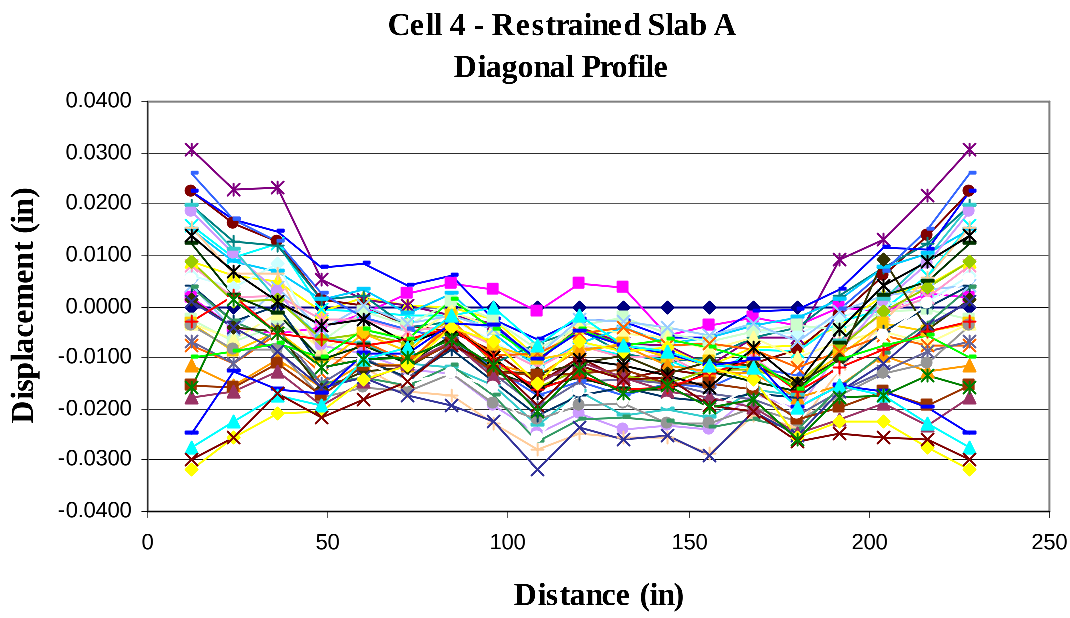

Figure 5.6 Diagonal profiles measured on Slab A in the restrained cell.

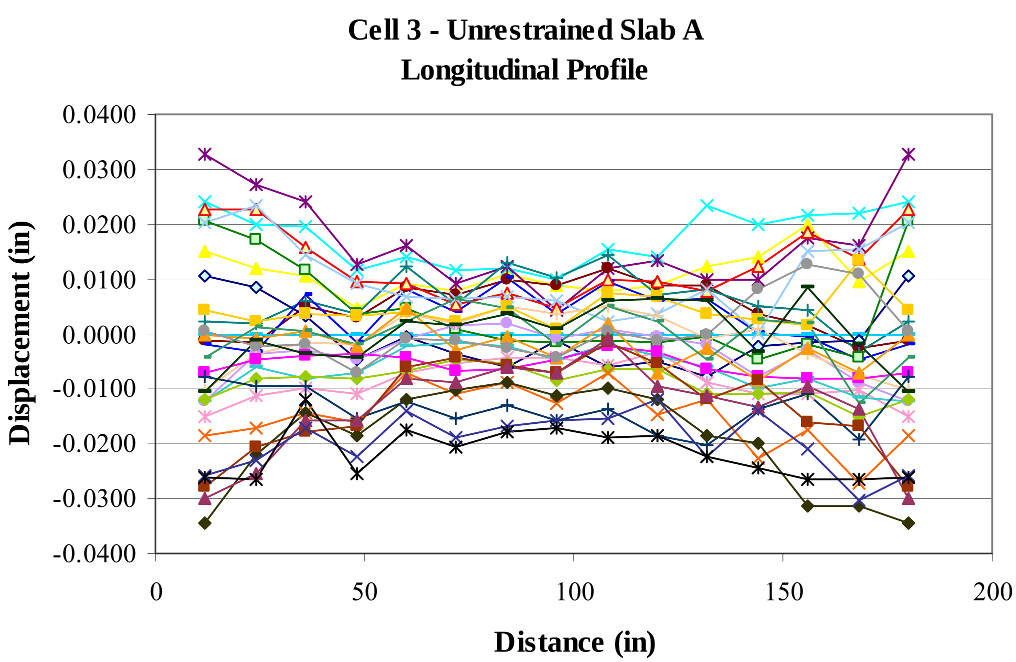

Figure 5.7 Longitudinal profiles measured on Slab A in the unrestrained cell.

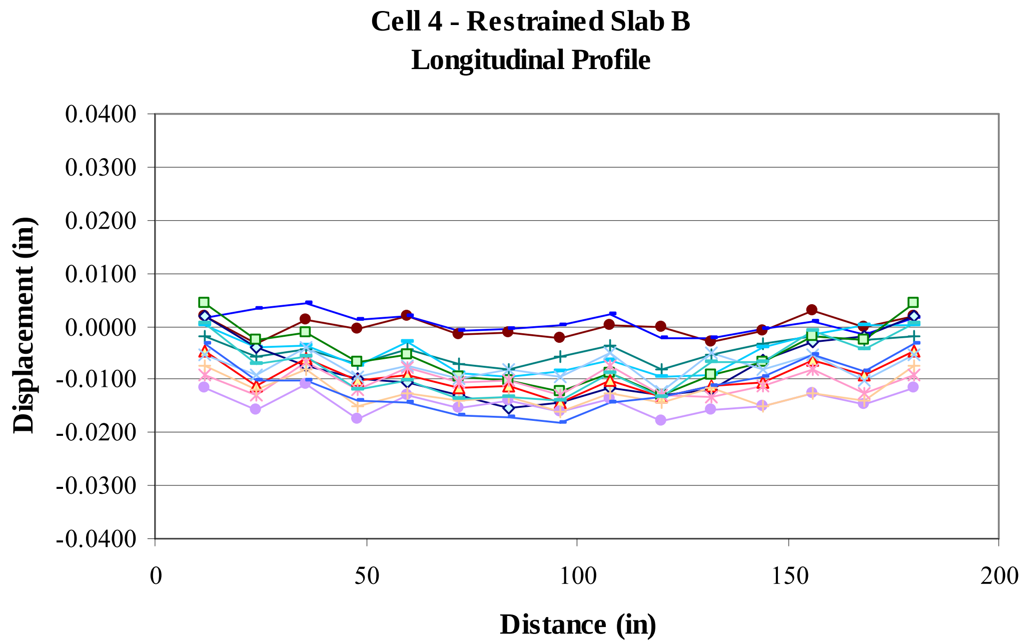

Figure 5.8 Longitudinal profiles measured on Slab B in the restrained cell

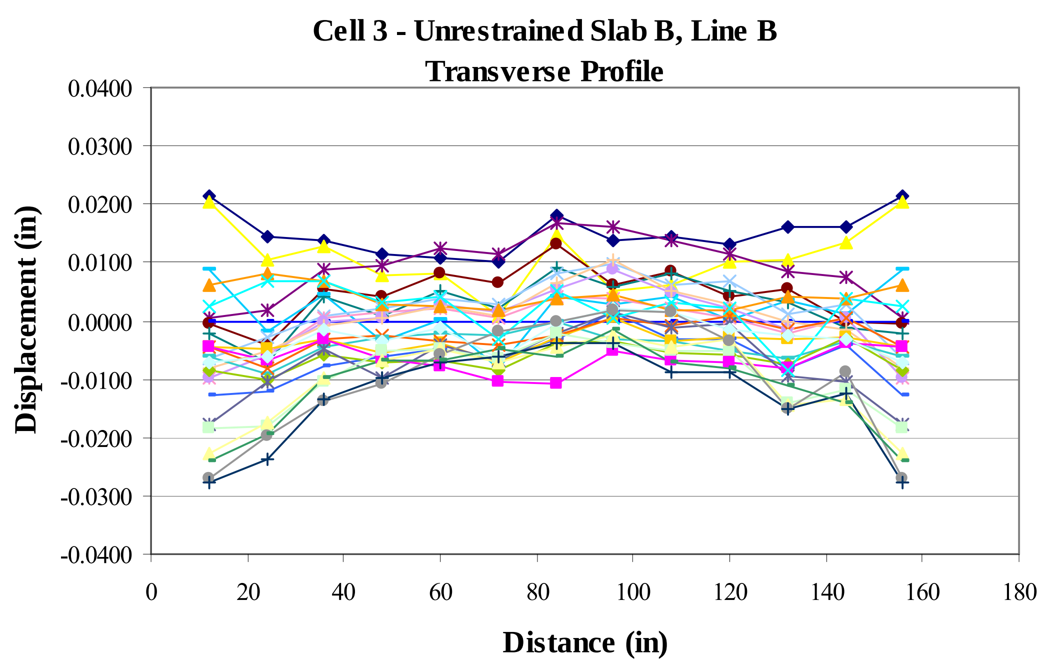

Figure 5.9 Transverse profiles measured on Slab B in the unrestrained cell.

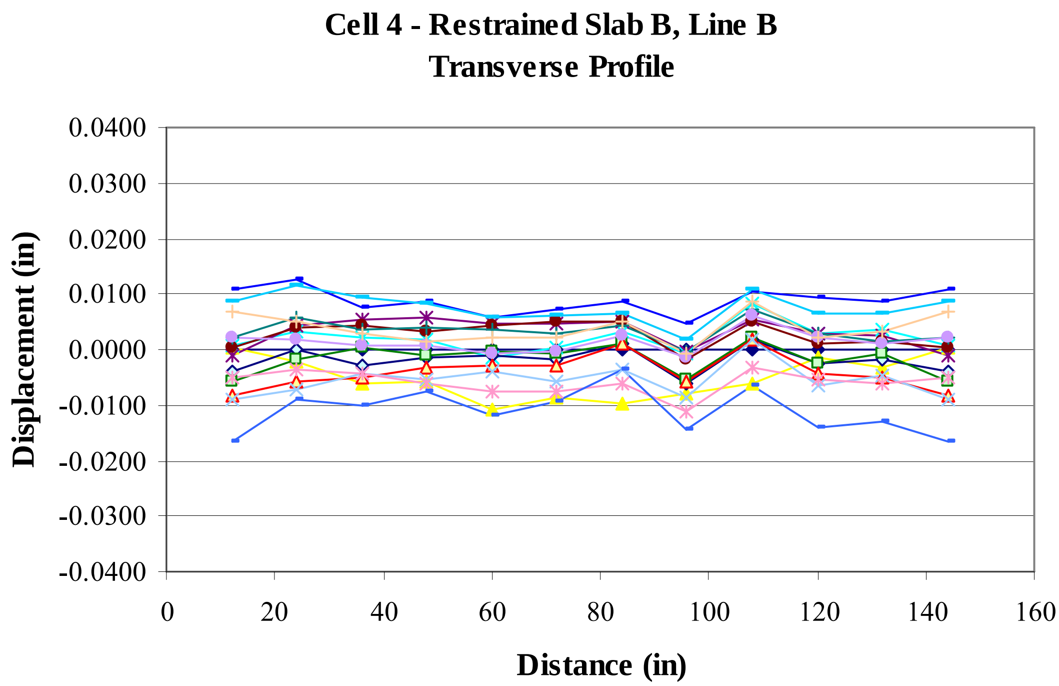

Figure 5.10 Transverse profiles measured on Slab B in the restrained cell.

Profiles measured across the diagonal of the slab were similar for unrestrained and restrained slabs. The longitudinal profiles showed the greatest difference between unrestrained and restrained slabs. The reason for this could draw from the fact that during the time period for which the profiles were measured, there was no curb adjacent to the longitudinal joint so the restraint conditions were the same for both cells. Since the edge of the slab was exposed to the ambient climatic conditions, temperature gradients did not develop within the slab along the edge. This could be another reason why the curvature in the longitudinal profile was small. In the transverse direction, the profiles of the unrestrained slabs exhibit slightly more movement at the edges.

As would be expected, the maximum displacement for the unrestrained slab was substantially higher than the restrained slab. The movement of the end of an unrestrained slab as a result of curling and warping can be as much as twice as high compared to the restrained slab.

A displacement of zero or less indicates the slab is in contact with the base. A portion of the slab is always in contact with the base when looking at the diagonal profiles in Figures 5.5 and 5.6. Figures 5.7 through 5.10 show that many times the edge of the slab will be completely unsupported in both the transverse and longitudinal directions. This is true for both the restrained and unrestrained slabs.

Another trend seen in Figures 5.5 through 5.10 is that the movement of the slab as a whole is far less for the restrained slabs than the unrestrained slabs. This is indicated by the more tightly grouped profiles depicted in the displacements graphs for the restrained slabs compared to the unrestrained slabs. The restraint provided by the dowels at the transverse joint greatly reduces the curvature at the end of the slab. Part of this can also be attributed to the fact that fewer measurements were made for the restrained slabs and the gradients were not as high when the measurements were made.

5.4 CURVATURE BEFORE AND AFTER THE JOINTS CRACK

The curvature for each profile was calculated by fitting a second order polynomial to the measured profile. The curvature of the polynomial was then calculated one foot into the slab from the shoulder. By combining the profile data with the temperature moment derived from the midpanel thermocouples, the relationship between slab curvature and temperature moment was defined. Plots of curvature versus temperature moment for all profiles measured within the initial 72 hours after paving are provided in the proceeding sections.

The response of the slab to temperature gradients before and after the joints crack is quite different, as would be expected because the effective slab length is substantially larger. Figure 5.11 shows the curvature calculated for profiles measured before and after the joints cracked for Slab A in the unrestrained cell. The curvature calculated before the joints cracked (shown as solid circles) are well below the best fit line of all of the data points. In all cases except when the temperature moment is quite high, curvature calculated before cracking will be less than curvature calculated after cracking by a factor of two. With the curvatures before cracking removed, the coefficient of determination increased from 0.86 to 0.93.

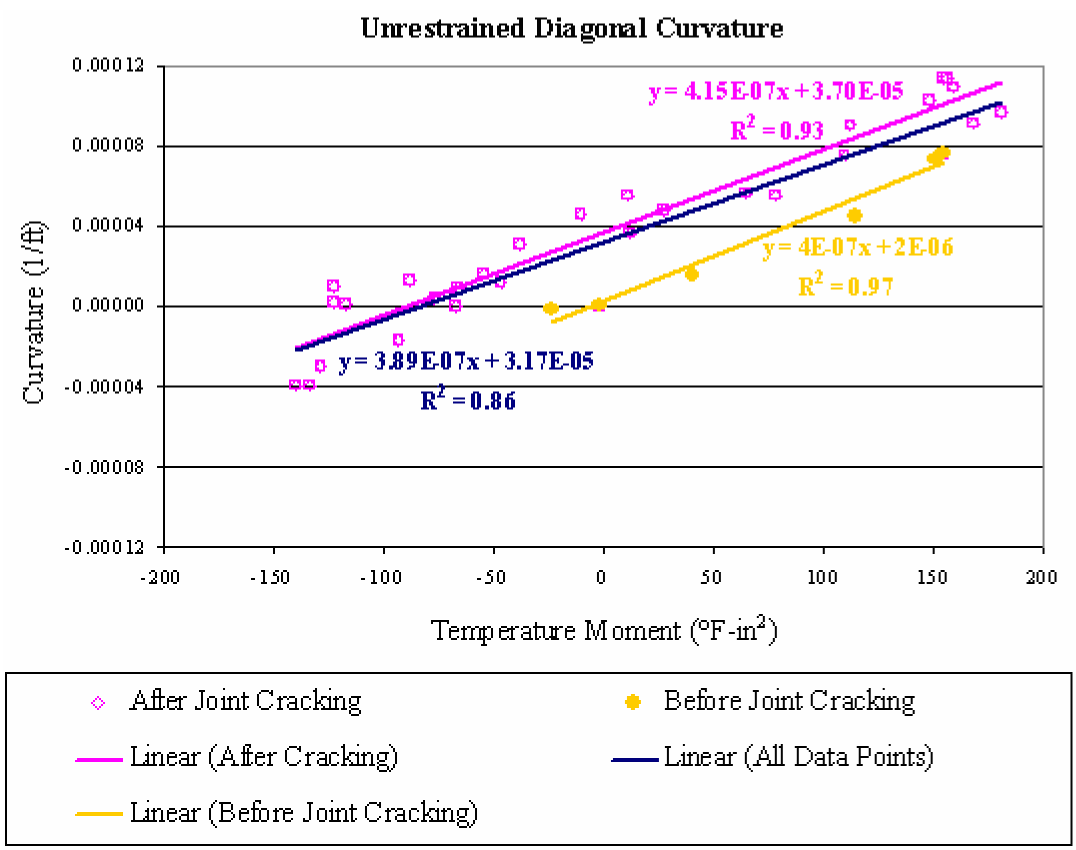

Figure 5.11 Relationship between temperature moment and curvature before and after joint cracking for the diagonal profiles of the unrestrained cell.

5.5 EFFECT OF TEMPERATURE ON SLAB CURVATURE

Figures 5.12 through 5.17 illustrate the relationship between curvature and temperature moment. The curvatures for the diagonal profiles measured for the unrestrained and restrained slabs are provided in Figure 5.12 and 5.13, respectively. Curvatures calculated for the transverse and longitudinal profiles are summarized in Figures 5.14 and 5.15 and Figures 5.16 and 5.17, respectively. Only the curvatures calculated for the profiles measured after the slab cracked were used to generate the plots.

In this analysis, the slope of the line indicates the rate of increase in curvature with an increase in temperature moment. The slopes of the restrained profiles are on average 7 percent less than those of the unrestrained. The maximum curvatures for the restrained slab are also substantially less than the unrestrained. This can be observed best for the diagonal profiles since in the longitudinal and transverse directions for the restrained cell, few profiles were measured during occurrences of high temperature moments. The reduction in curvature for the restrained slab provides an indication of the stress that develops within the slab when this curvature is restrained.

Another notable aspect found for the transverse joints is that the increase in curvature with increasing temperature moment (slope of the line) for restrained transverse joints seems to be more uniform than the unrestrained joints. In the restrained joints, shown in Figure 5.17, the transverse profile of line A of Slab A and the profile of line B of Slab B are measured on opposing sides of the joint while the profile of line A of Slab B and the profile of line B of Slab C are also measured on opposite sides of a joint. Overall, the slopes seem similar, despite the lack of data for higher temperature moments. Looking at the transverse profiles measured on opposite sides of the unrestrained joints, profiles measured along the joint between Slabs B and C exhibit a larger slope than the profiles measured along the transverse joint between Slabs A and B. The difference between the curvatures along the two joints is the result of the joint cracking pattern. The joint between Slabs A and B cracked first and was a wider crack than the crack at the joint between Slabs B and C. The larger crack opening results in less restraint and therefore a greater amount of curvature will develop for equivalent gradients.

The y-intercept is dependant on the time the slab set and the resulting curvature set into the slab. This will be a function of the time each slab was paved, the temperature gradients that developed throughout the day and the restraint conditions. The largest built in curvature measured along the diagonal for the restrained and unrestrained slabs was 4.08×10^{-5} 1/ft and 4.54×10^{-5} 1/ft, respectively. The average built in curvature for the restrained slabs was 3.37×10^{-5} 1/ft with a standard deviation of 8.64×10^{-6} 1/ft. The average built in curvature for the unrestrained slabs was 4.05×10^{-5} 1/ft with a standard deviation of 4.65×10^{-6} 1/ft.

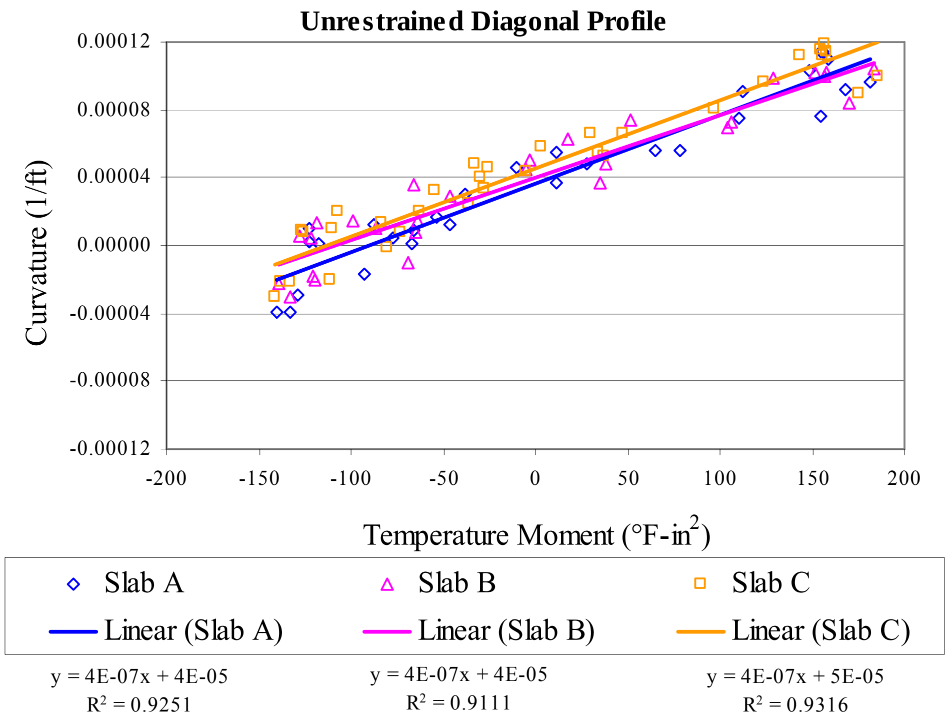

Figure 5.12 Temperature moment versus curvature for unrestrained diagonal profiles.

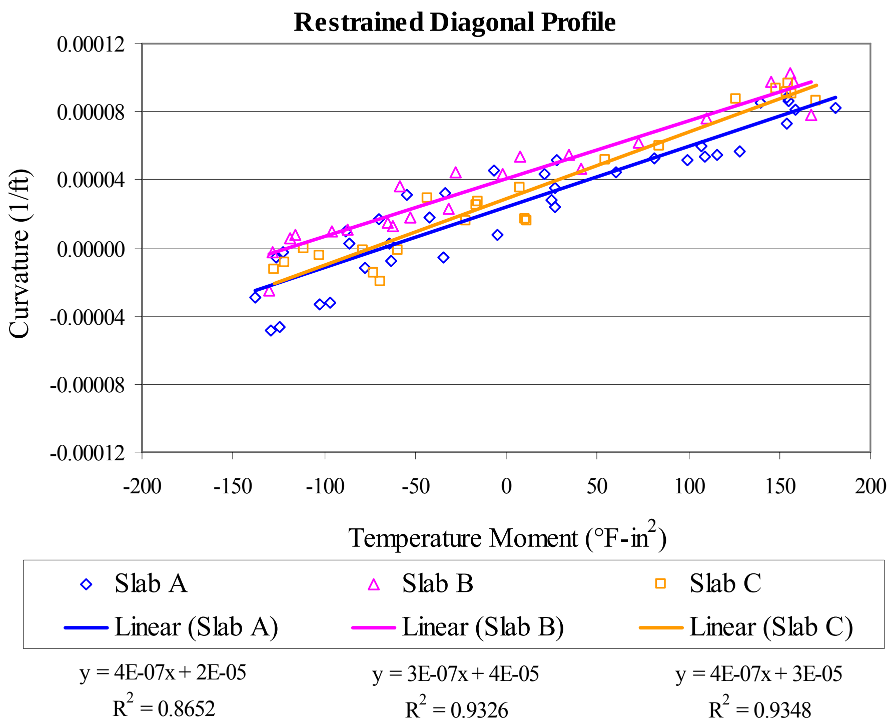

Figure 5.13 Temperature moment versus curvature for restrained diagonal profiles.

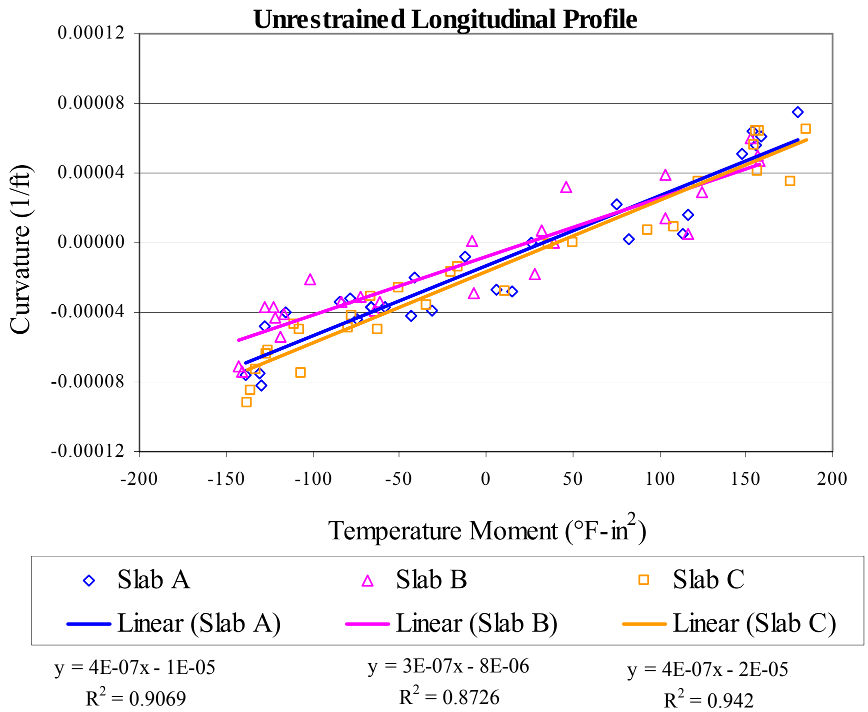

Figure 5.14 Temperature moment versus curvature for unrestrained longitudinal profiles.

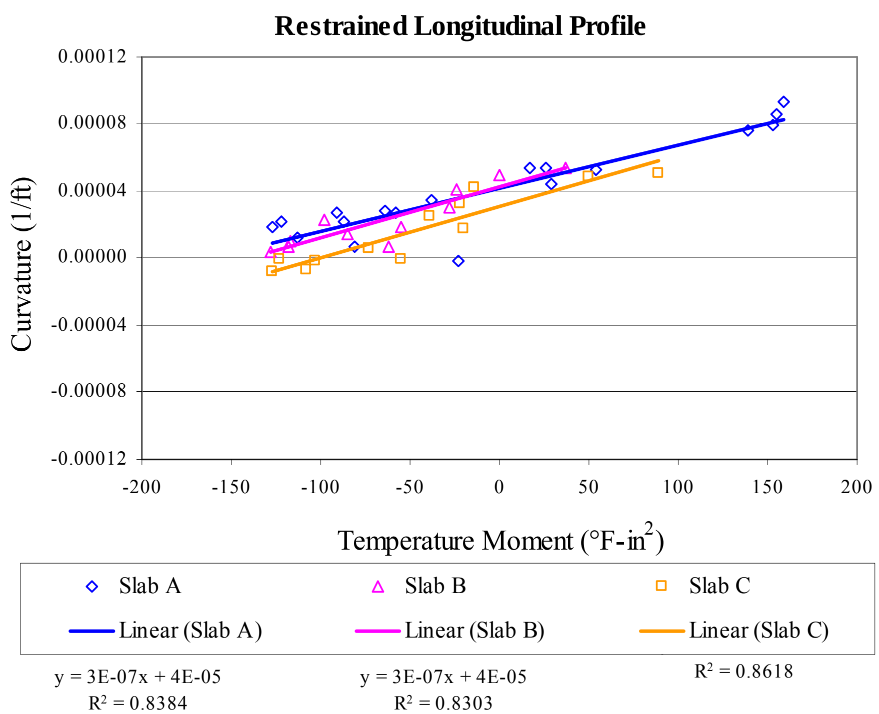

Figure 5.15 Temperature moment versus curvature for restrained longitudinal profiles.

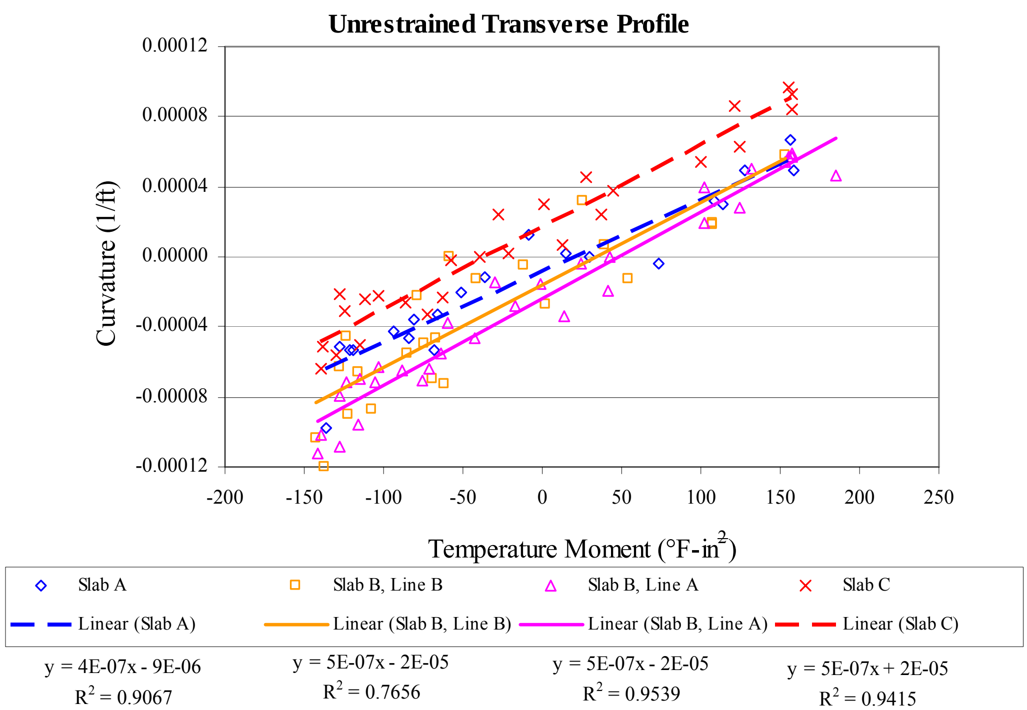

Figure 5.16 Temperature moment versus curvature for unrestrained transverse profiles.

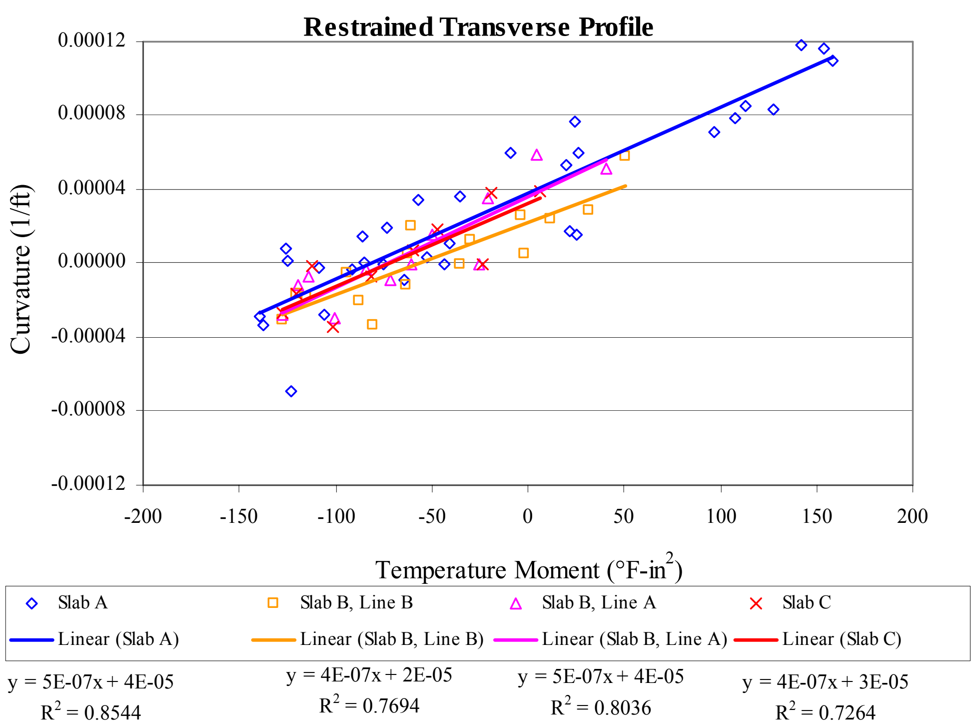

Figure 5.17 Temperature moment versus curvature for restrained transverse profiles.

5.6 APPLICATION OF EDGE TEMPERATURE MOMENTS

The temperature moments in the preceding figures were all based on the midpanel thermocouples. Since the longitudinal profile was measured along the edge of the slab, the relationship between temperature moments calculated using the thermocouples along the edge of the slab was evaluated. The temperature moment versus curvature plots for the edge thermocouple are provided in Figure 5.18 for the unrestrained slabs and Figure 5.19 for the restrained slabs. It is apparent by the substantial reduction in the coefficient of determination, the relationship between temperature moment calculated using the thermocouples at the edge and curvature is not nearly as strong as when using the thermocouples at midpanel to calculate temperature moment. This reveals that the response of the slab along the longitudinal edge is controlled by the temperature of the slab at midpanel more so than the edge. The restrained cell seems to correlate to the edge temperature moment even less than the unrestrained.

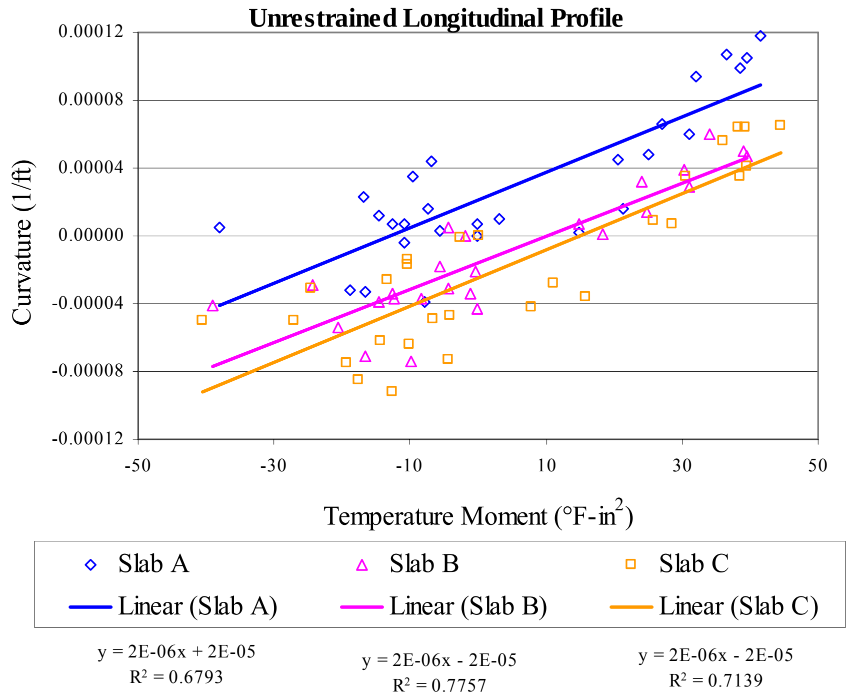

Figure 5.18 Temperature moment versus curvature for the longitudinal profiles based on edge temperature moments for the unrestrained cell.

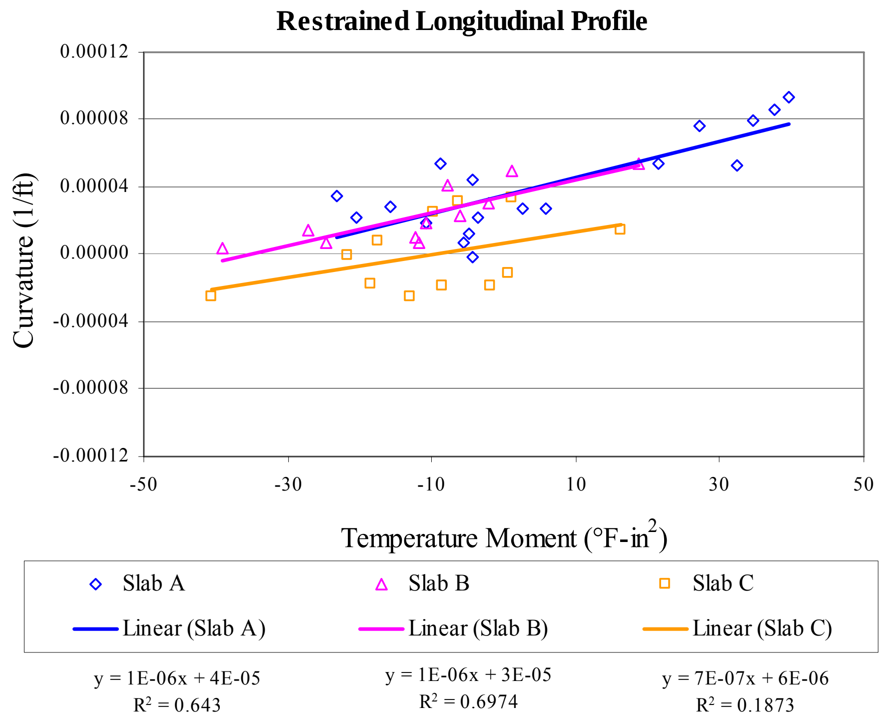

Figure 5.19 Temperature moment versus curvature for the longitudinal profiles based on edge temperature moments for the restrained cell.

5.7 CONCLUSION

The surface profiles give insight into the response of the pavement to environmental loads, in particular temperature. The temperature moment at the time of set was less than 50 ^{o}F-in^{2}. Since the concrete set at a time when little gradient or temperature moment was present, a full range of curvatures both positive and negative can be seen in the profiles. The largest built in curvature measured along the diagonal for the restrained and unrestrained slabs was 4.08×10^{-5} 1/ft and 4.54×10^{-5} 1/ft, respectively. The average built in curvature for the restrained slabs was 3.37×10^{-5} 1/ft with a standard deviation of 8.64×10^{-6} 1/ft. The average built in curvature for the unrestrained slabs was 4.05×10^{-5} 1/ft with a standard deviation of 4.65×10^{-6} 1/ft.

The unrestrained slabs curled more dramatically with a much larger maximum displacement than the restrained slabs. The increase in curvature with increase in temperature moment was 7 percent higher for the unrestrained slabs compared to the restrained slabs. The restrained slab profiles are also grouped much more closely together, indicating that the slabs moved much less along the entire length of the profile. In the longitudinal and transverse directions for both restrained and unrestrained slabs, the profiles indicated that the edges sometimes become completely unsupported.

Taking into account the curvature of the slabs, it was observed that the slabs respond differently to temperature moments before and after setting. Looking at the difference between slab restraint conditons, the unrestrained slabs curled much more under the same temperature moment than the restrained slabs. Along the transverse joint for the doweled slabs, the relationship between curvature and temperature moment was very similar. This indicates that the dowel bars create more uniform conditions where they are present. Also, the unrestrained slabs exhibited greater curvature at joints with wider cracks.

6.0 PCC STATIC STRAIN DATA ANALYSIS

6.1 STRAIN DATA OVERVIEW

The following section provides an analysis of the stress and strain response of the JPCP panels of Cells 3 and 4 to environmental loads. Vibrating wire strain gage data collected through the first ten months after paving (August 2004 through June 2005) will be analyzed to interpret seasonal strain behavior with respect to three separate conditions: location with respect to joint proximity, depth within slab, and level of restraint applied to the slab. Strain response of JPCP is significantly influenced by all three of these factors. The layout of the Smart Pavement project, as discussed in Chapter 3, can accommodate such analysis. Strain data at the top (1 in from the surface) and bottom of the slab (1 in from the base) and at several locations within slab for both restrained and unrestrained slabs were analyzed. Gage locations are described below and shown in Figure 6.1.

- adjacent to the lane/shoulder joint at midpanel oriented in the longitudinal direction
- at midpanel oriented in the longitudinal
- adjacent to the centerline joint at midpanel oriented in the longitudinal
- adjacent to the transverse joint in the center of the lane oriented in the transverse direction
- adjacent to the lane/shoulder joint corner oriented in the longitudinal, transverse, and diagonal directions

- adjacent to the centerline joint corner oriented in the longitudinal, transverse, and diagonal directions

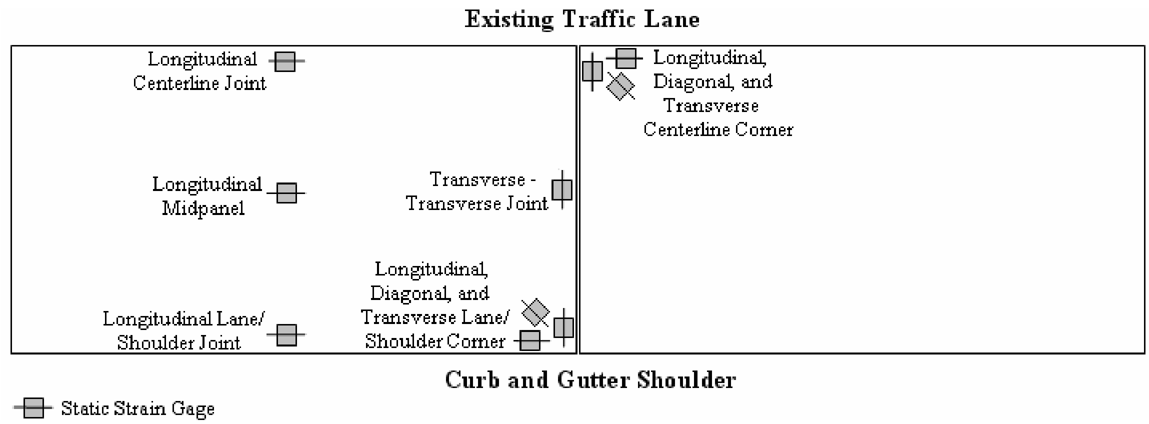

Figure 6.1 Summary of vibrating wire strain gage locations within the panel.

In order to obtain comparable representative data from both the restrained and unrestrained cells, it was desired to find panels within each cell with similar thicknesses. Data from survey measurements taken of the PCC slab following construction was used to determine the thickness of the slab at various locations. A summary of the survey data, along with a layout of the sensor locations can be found in Appendix B of this report. Figure 6.2 provides a summary of the surveyed depths:

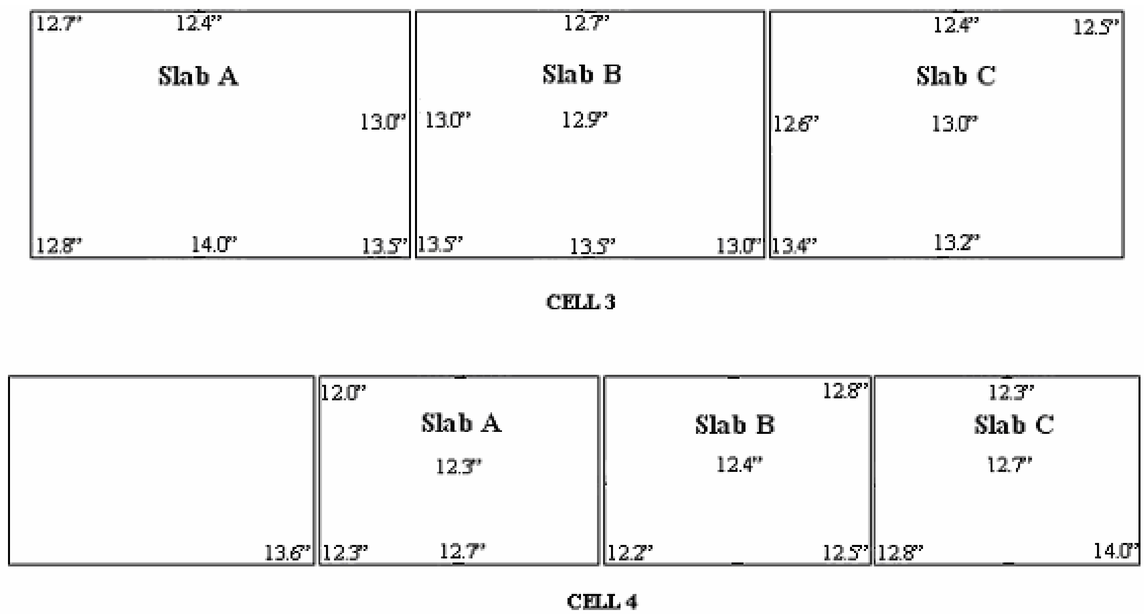

Figure 6.2 Surveyed slab thicknesses for Cells 3 and 4.

Based on these thicknesses, it was determined that Slab A of Cell 3 and Slab C of Cell 4 were quite similar. Strain data from these two slabs was chosen to represent panels in their respective cells.

Creep and fluctuations in moisture and temperature in the concrete will affect the measured strains. Equation (6-1) accounts for the thermal, moisture, and creep contributions towards concrete strain, also referred to as *actual strain*.

$$\mu_{m,c,t} = (R_1 - R_0)B + (T_1 - T_0)(C_1) \qquad \textit{(6-1)}$$

where:

$\mu_{m,c,t}$ = strain influenced by creep, moisture, and temperature changes

R_0 = raw strain at time$_0$ (initial concrete set)

R_1 = raw strain at time$_1$

T_0 = temperature at $time_0$

T_1 = temperature at $time_1$

C_1 = thermal coefficient of expansion of steel in strain gage

= 6.78 microstrain/°F

B = batch calibration factor (provided by the manufacturer)

As mentioned in Chapters 4 and 5, the time of set was approximately 10 hours after paving. The set time was used to determine the initial strain in the concrete. Figure 4.4 illustrates the early age relationship between strain and temperature in Cell 4. Equation (6-1) was utilized in the development of this relationship, thereby including the effect of temperature on the total strain in the concrete. Before the concrete sets, the concrete experiences large changes in temperature with little to no change in strain, as shown in Figure 4.4. The concrete began to experience more uniform changes in strain with changes in temperature at about 4:30 PM in Cell 3 and 4:45 PM in Cell 4 (Cell 3 was paved prior to Cell 4). This correlates to a concrete set time beginning approximately 10 hours after initial paving.

6.2 STRAIN RESPONSE *(FIRST 72 HOURS AFTER PAVING)*

The static strain gages are used to measure deformation caused by moisture and temperature changes. Stress will not develop if the slab is free to deform when changes in temperature and moisture occur. It is when this deformation is restrained that stresses develop. The deformation is restrained primarily by the friction between the bottom of the slab and the base, the dowel and tie bars, and the weight of the slab itself. The following section provides an analysis of the strain measured during the first 72 hours after paving, a time period when the concrete gains a large portion of its strength. Strain will be investigated with respect to depth, location and restraint within the JPCP. This section will also utilize strain data to evaluate strain continuity across joints.

6.2.1 The Influence of Depth, Location, and Restraint on Strain *(First 72 Hours After Paving)*

Figures 6.3 and 6.4 compare strain measured at four different locations within unrestrained slabs during the first 72 hours after paving. As shown in the figures, readings were taken at two different depths, 1 in and 11 in below the pavement surface. Both graphs show the largest strain to be measured along the transverse joint. This is because with the absence of a curb and gutter, there is no restriction on movement from the outside portion of the slab. The longitudinal strain along the centerline exhibits the lowest strain in both cases, since movement is restrained by the presence of the eastbound lane. The magnitude of the strain decreases with increasing slab depth. This indicates the bond between the base and the bottom of the slab is sufficient to restrain slab deformation. Also, the temperature fluctuations at the bottom of the slab are less than at the top of the slab.

Similar comparisons were performed for the restrained slabs. See Figures 6.5 and 6.6. The largest strain was measured along the transverse joint in the transverse direction and the smallest strain was found along the centerline joint in the longitudinal direction. Strains measured at the bottom of the slab were lower than the strains measured at the top of the slab for the restrained slabs, as was seen for the unrestrained slabs.

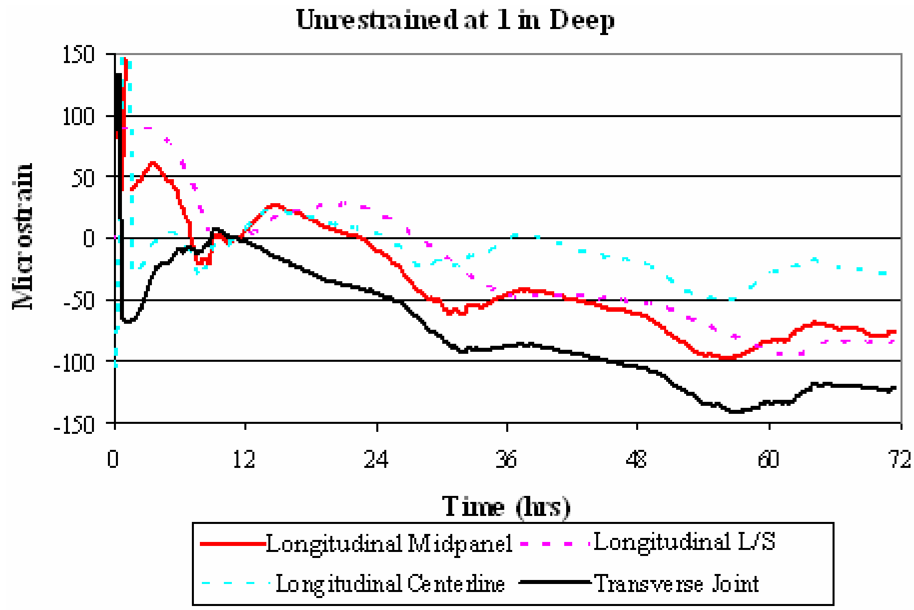

Figure 6.3 Strain in the unrestrained cell at a depth of 1 in.

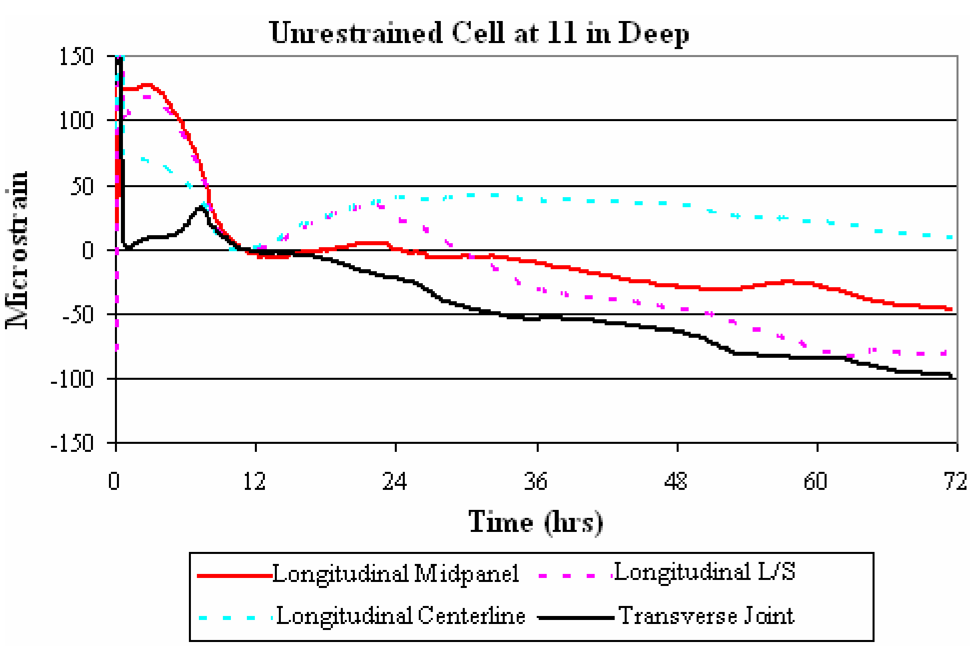

Figure 6.4 Strain in the unrestrained cell at a depth of 11 in.

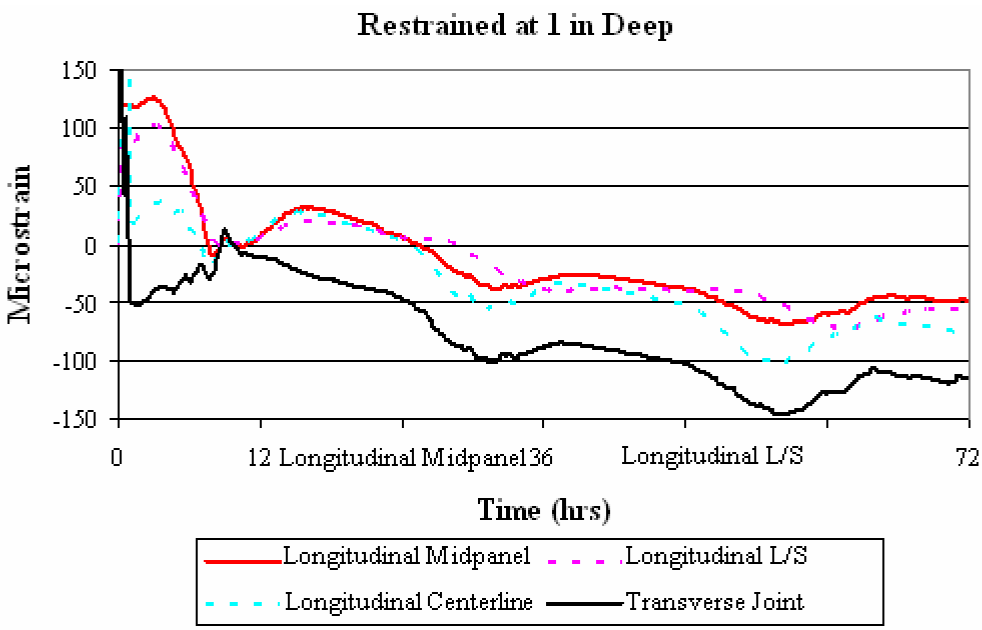

Figure 6.5 Strain in the restrained cell at a depth of 1 in.

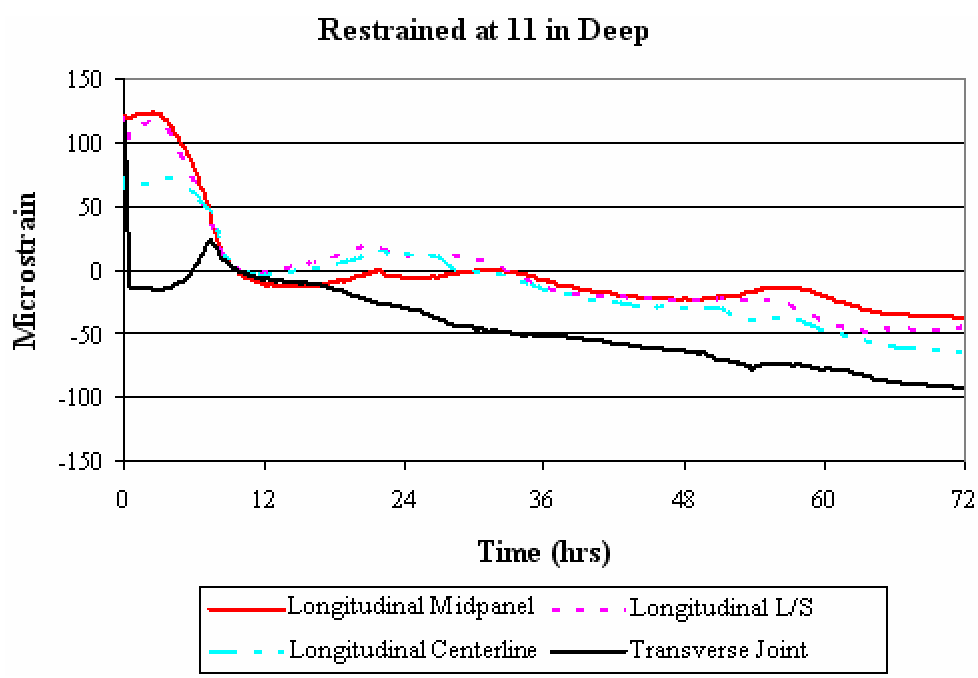

Figure 6.6 Strain in the restrained cell at a depth of 11 in.

In comparing the strains measured in the restrained slabs with those in the unrestrained slabs, the spatial variation in the magnitude of measured strain was greater for the unrestrained slab compared to the restrained slab. The strains appear more uniform across the slab for the restrained slabs. In general, the strains for the restrained slab appear to be lower than for the unrestrained slab. This can be attributed to the fact that the slab is tied to the previously constructed eastbound lane. The stiffness of the concrete in the eastbound lane would be higher than the concrete in the westbound lane since this analysis is looking at strains measured within the first 72-hours after paving the westbound lane.

6.2.2 Uniformity of Strain on Opposing Sides of Transverse Joint *(First 72 Hours After Paving)*

In order to evaluate the uniformity of the strain on opposing sides of a transverse joint, strain measured in the corner adjacent to the L/S joint on both the approach and leave side of the transverse joint were compared. This comparison is made to determine how uniform strain is throughout the pavement section. Strains measured in the longitudinal, diagonal, and transverse directions are depicted in Figures 6.7 and 6.8. Little difference is seen in the magnitude of the strain between unrestrained and restrained cell along the transverse joint. This most likely is due to the fact the curb and gutter have not yet been constructed so the restraint conditions along the L/S joint are similar. Both the figures show a good correlation between strains measured on opposite sides of the joint but in the same direction. There is a slight discrepancy between the diagonal strains in the restrained slabs. Since the longitudinal and transverse strains are similar, this is most likely the result of the orientation of the diagonal sensor on the approach side installed in a slightly more transverse direction, thus producing readings similar to the transverse sensors.

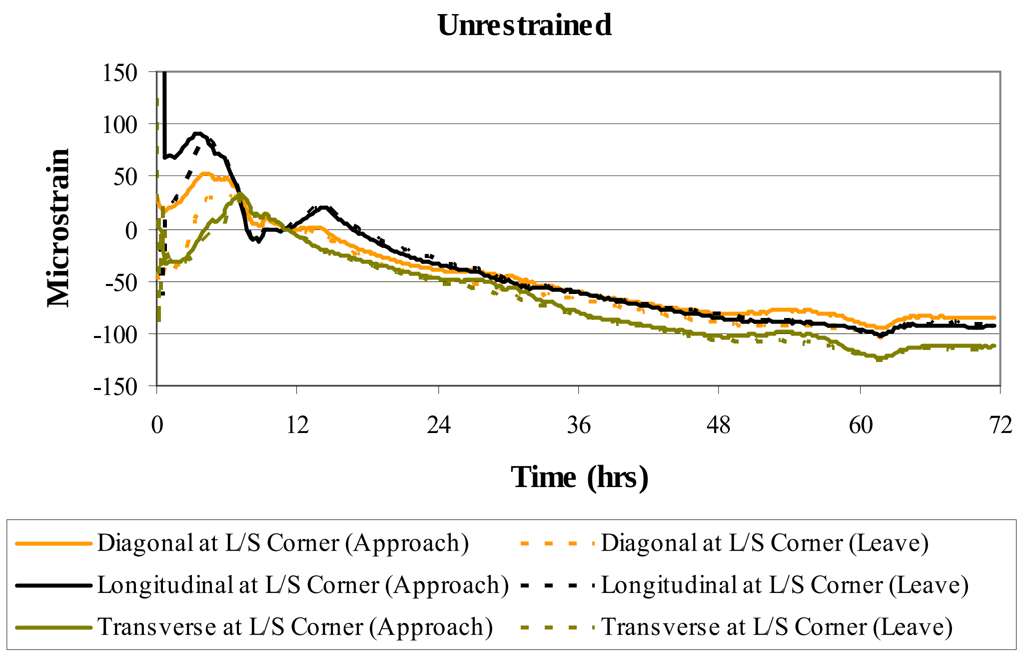

Figure 6.7 Strain in the corner adjacent to the L/S joint on both the approach and leave side of the transverse joint of unrestrained slabs.

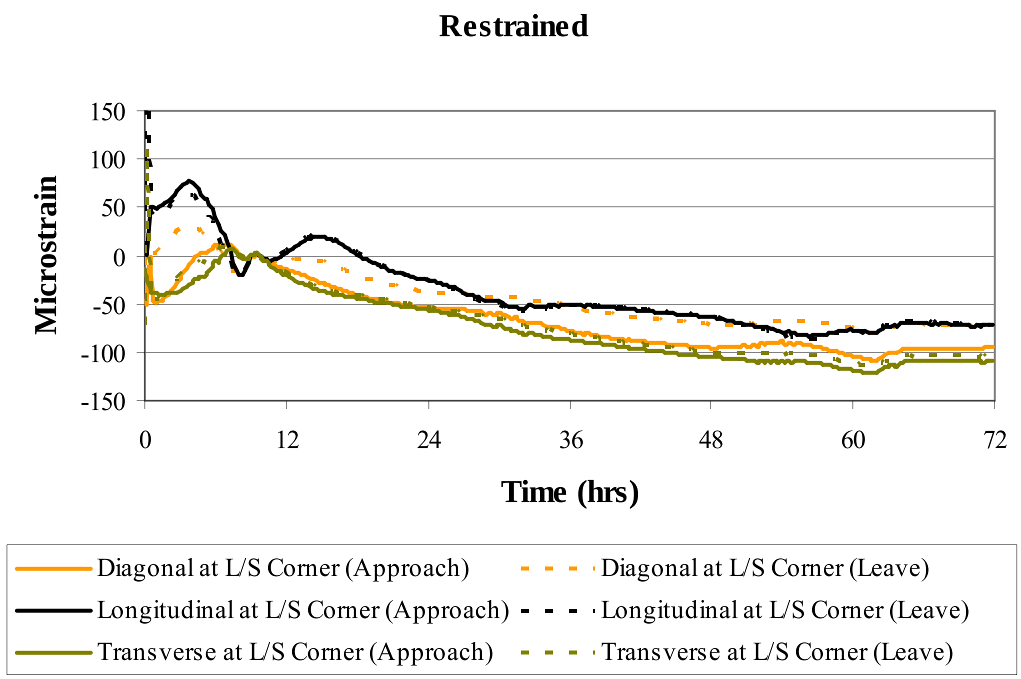

Figure 6.8 Strain in the corner adjacent to the L/S joint on both the approach and leave side of the transverse joint of restrained slabs.

6.2.3 Strains at the Centerline and the Lane/Shoulder Joint *(First 72 Hours After Paving)*

Figures 6.9 and 6.10 show the strains measured in the corner along the L/S joint and in the corner along the centerline joint. These strains were measured adjacent to the same transverse joint to eliminate possible discrepancies that could be attributed to differences in joint width. For the unrestrained cell, Figure 6.9 shows that the strain in all directions is similar on the L/S side. Restraint associated with the boundary conditions was limited since no curb and gutter is present and the crack at the joint was quite wide. At the centerline, the strain in the transverse direction is similar to that in the opposing corner near the L/S joint. However, in the longitudinal direction the strain is lower due to the restraint imposed by the existing eastbound lane. The restraint in the longitudinal direction also affected the strain measured along the diagonal. The decrease in strain between that measured in the transverse direction compared to the longitudinal and diagonal directions along the centerline joint was about 50 microstrain. This correlates to a stress of 180 psi. Strains measured in the restrained slabs, shown in Figure 6.10 exhibited a very similar response.

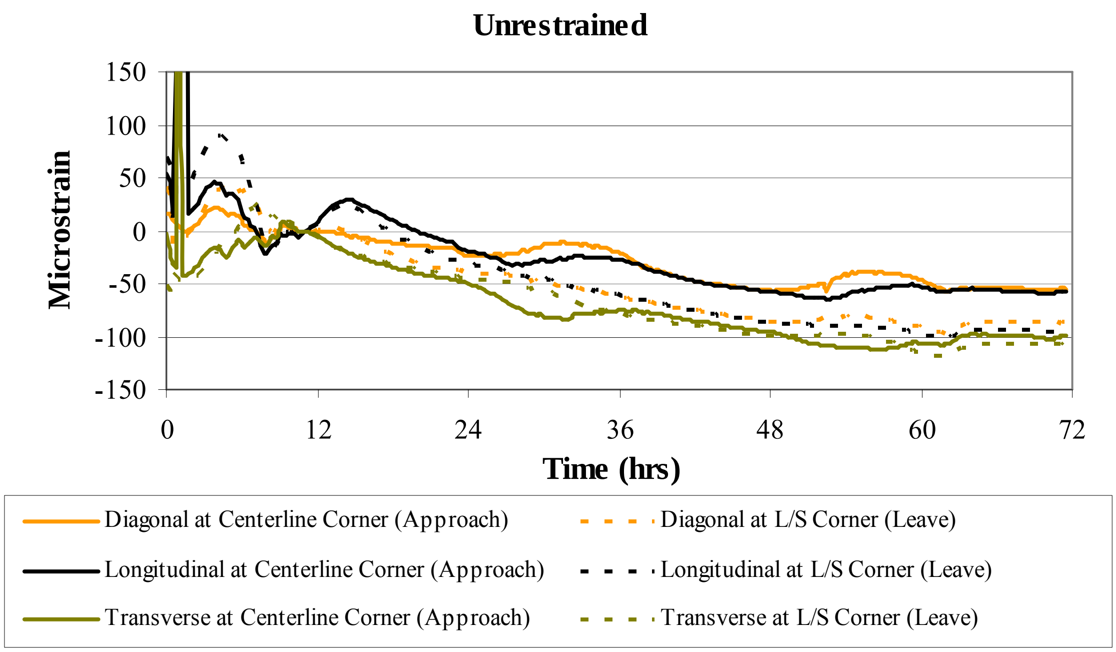

Figure 6.9 Strains measured in the corner along the L/S and in the corner along the centerline joint for unrestrained slabs.

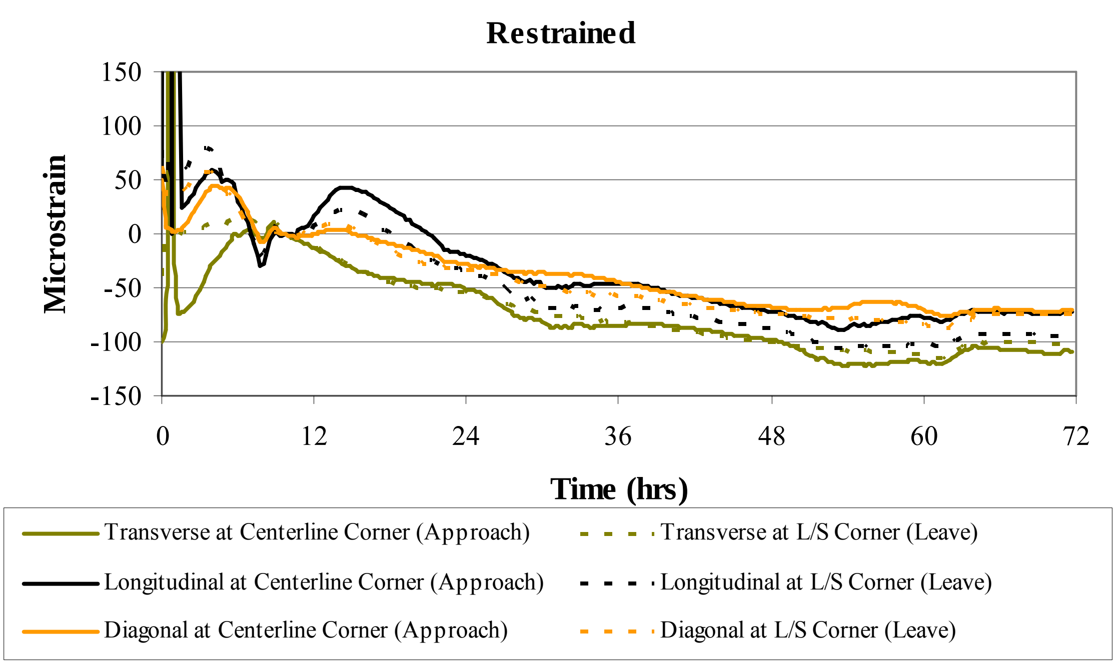

Figure 6.10 Strains measured in the corner along the L/S and in the corner along the centerline joint for restrained slabs.

6.2.4 Effect of Crack Width on Strain *(First 72 Hours After Paving)*

When the joints cracked after sawing, the relative width of the crack was recorded. The strains measured in the corner near joints with different crack widths were compared to evaluate the effect of joint width on the measured strains. Figure 6.11 compares strains measured in the corner near the centerline and adjacent to a transverse joint with a wide crack and a transverse joint with a narrow crack. The strains were similar regardless of crack width with the exception of that measured along the diagonal direction. This is probably a result of the final orientation that the gage was restrained at, as previously mentioned.

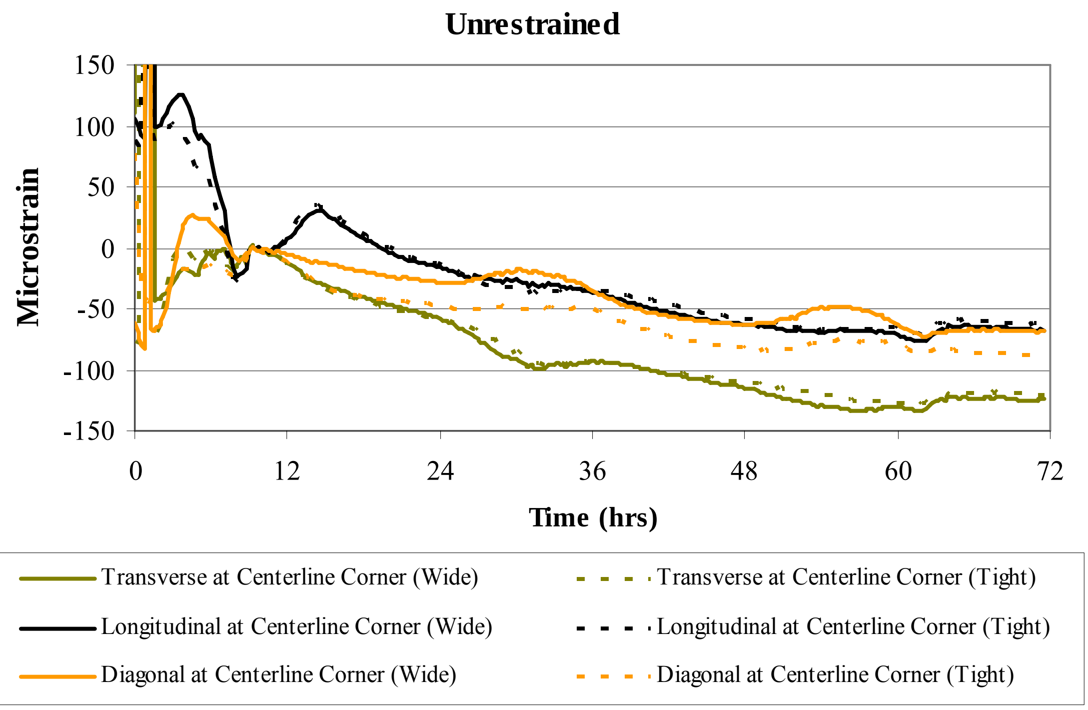

Figure 6.11 Strain at the centerline of two different joints for unrestrained slabs.

6.3 SEASONAL STRAIN RESPONSE *(FIRST TEN MONTHS AFTER PAVING)*

This section explores the variation in strain throughout the depth of JPCP slabs through seasonal temperature and moisture fluctuations. The graphed strain for this analysis includes strain induced by temperature, moisture and creep, and like the 72-hour strain investigated in Section 2 of this chapter, is based on equation (6-1). As a pavement undergoes changes in thermal and moisture conditions, the strain response between the top and bottom of the slab can be quite different. Diurnal and seasonal factors such as nonuniform drying shrinkage throughout the depth of the slab, subgrade temperature and moisture, ambient air conditions, and frictional restraint at the PCC/base interface can contribute to significant differences in the strain, and hence stress, response between the top and bottom of JPCP slabs.

6.3.1 Seasonal Variation in Strain With Respect to Depth, Location, and Restraint *(First Ten Months After Paving)*

As evidenced by Figure 6.12, the strain measured in October, shortly (2 months) after construction, is negative at the top and bottom of the slab. This can be explained by the fact that the temperature throughout the depth of the slab at the time of set is higher than the slab temperatures typically encountered during the month of October (refer to Figure 4.11). As the overall ambient temperature decreases, the length of the slab decreases. Another interesting observation is that the strain at the top of the unrestrained slab is greater than that at the bottom. This phenomenon can be attributed to the higher degree of drying shrinkage that takes place at the surface compared to the bottom of the slab. The daily fluctuations in temperature throughout the depth of the slab can also be seen in Figure 6.13.

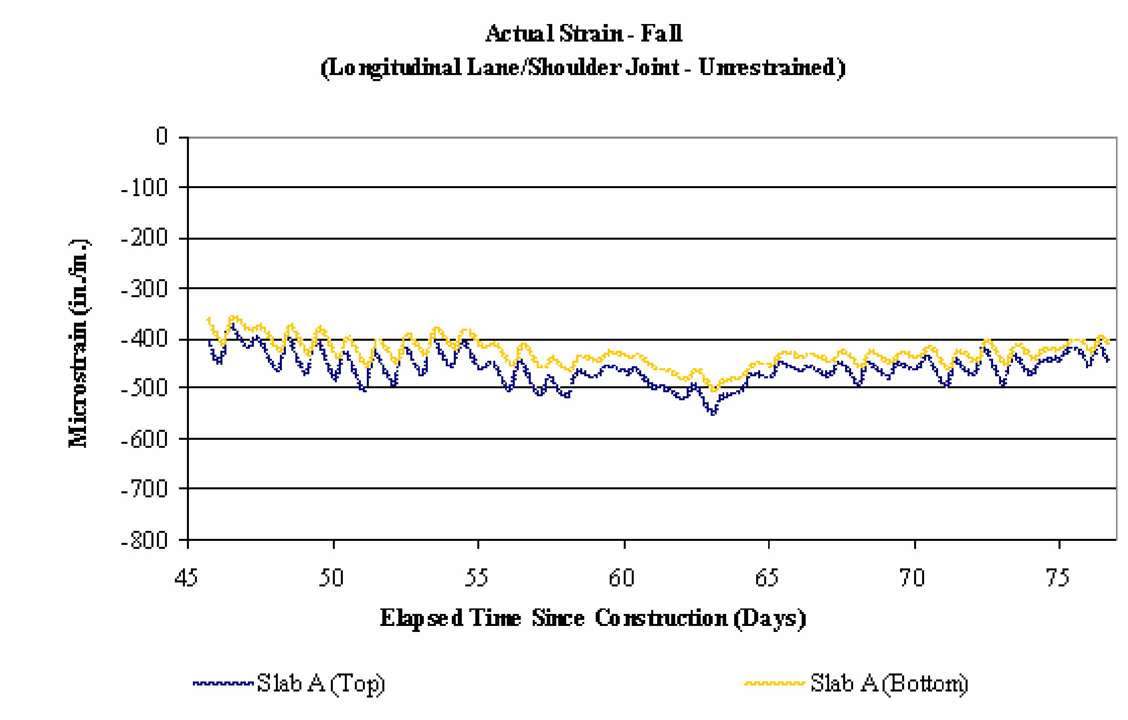

Figure 6.12 Static strain measured in the fall along the lane/shoulder joint for an unrestrained slab.

As ambient temperatures drop in the winter (refer to Figure 4.11), the measured strains become increasingly negative as indicated by Figure 6.13. The average strain in the fall was around -450 microstrain while the average strain in the winter was -600 microstrain. The diurnal temperature swings also decrease in the winter due to prevailing seasonal temperature patterns and the length of daylight hours. This fact is reflected in Chapter 4, for which Figure 4.11 shows that the average thermal gradient in the concrete is at a minimum in the winter. The resulting response is a decrease in diurnal strain fluctuations when comparing strains measured in the fall (Figure 6.12) with those measured in the winter (Figure 6.13). The drying shrinkage at the surface of the slab also appeared to be slightly higher in the winter than the fall. Factors contributing to this are the humidity in the winter is lower and there are fewer precipitation events. Plus, a substantial amount of drying shrinkage will occur the first 90 days after paving.

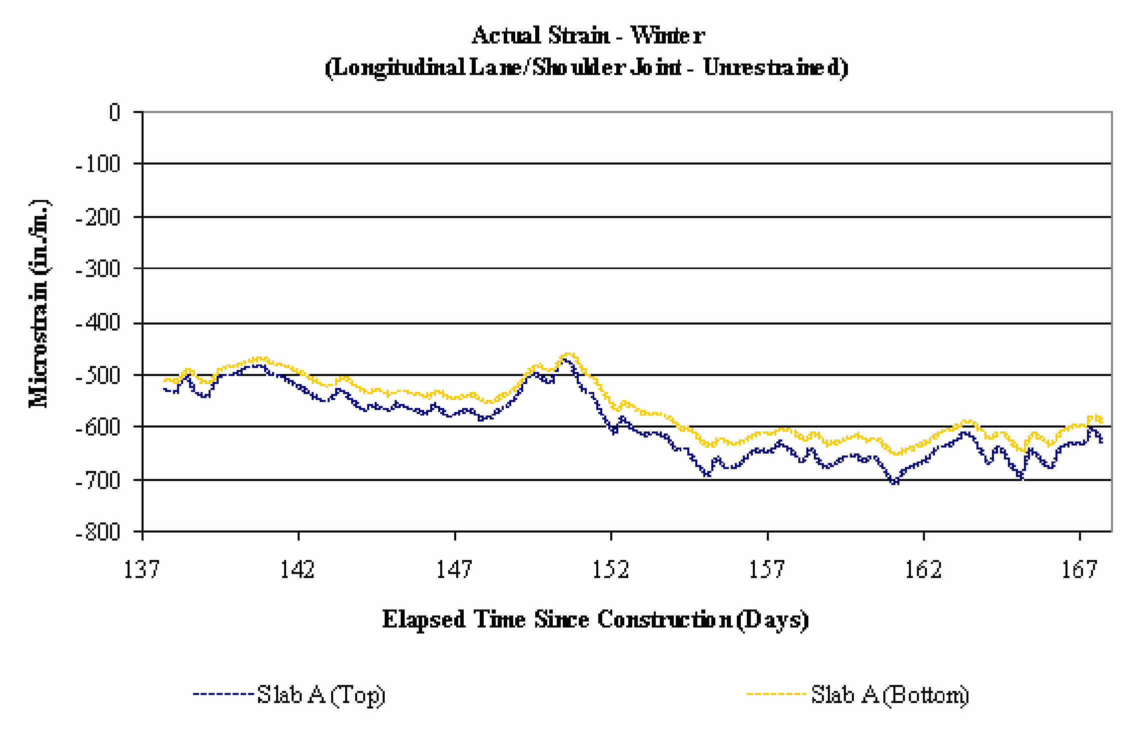

Figure 6.13 Static strain measured in the winter along the lane/shoulder joint for an unrestrained slab.

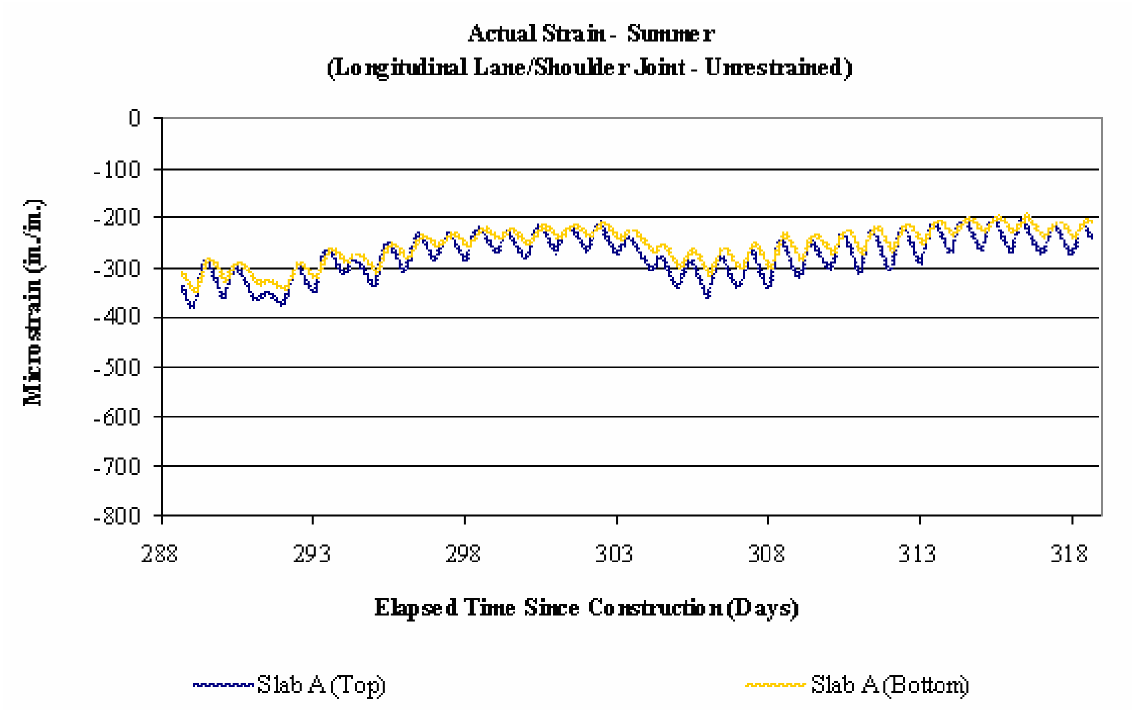

Figure 6.14 Static strain measured in the summer along the lane/shoulder joint for an unrestrained slab.

Strains measured in the summer (June) are shown in Figure 6.14. The ambient temperatures increase during the spring and summer. This resulted in a decrease in the average strain from -600 microstrain in the winter to -250 microstrain in the spring and early summer. Figure 6.14 shows that the daily strain fluctuations are also much larger in the summer than in the winter (Figure 6.13). The reason for this can be contributed to the fact that there are higher temperature fluctuations in the spring and summer as is reflected in Figure 4.11 of Chapter 4. These temperature fluctuations are much larger on the surface than the bottom of the slab and this is reflected in the larger strain fluctuations measured on the surface of the slab.

This behavior was found to be quite similar for restrained slabs. Figure 6.15 shows the strain at the top and bottom of a restrained slab over the same time period during the winter.

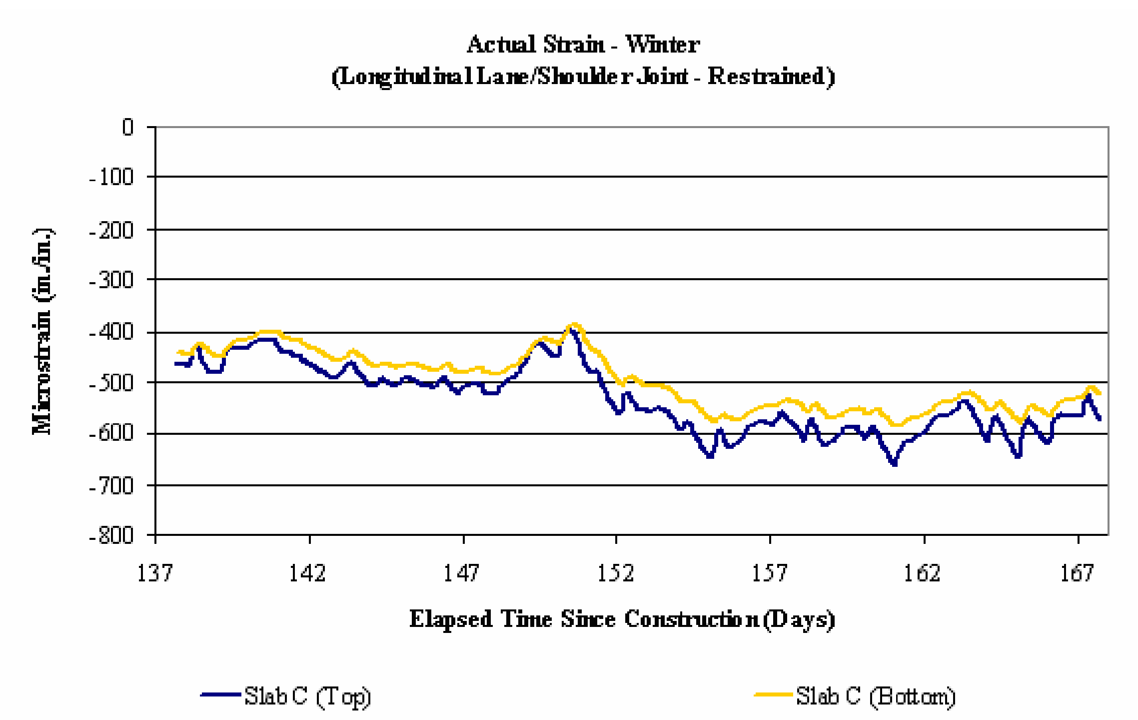

Figure 6.15 Static strain measured in the winter along the lane/shoulder joint for a restrained slab.

Comparing Figures 6.15 and 6.13, it appears that restraint has negligible influence on strain differentials between the top and bottom of the slab in the longitudinal direction. While the overall strain is predominantly less for the restrained slabs, the disparity between strains throughout the depth of the slab is comparable to that of an unrestrained slab. A compilation of seasonal static strain response at the tops and bottoms of restrained and unrestrained slabs can be found in Appendix C.

6.3.2 Seasonal Variation in Strain with Respect to Position within Slab and Level of Restraint

The final two parameters that will be investigated are position within the slab and level of restraint. For this analysis, pavement temperatures measured in the field were plotted against the corresponding strains. The level of restraint was quantified through the thermal strain rate (TSR). The thermal strain rate, similar to the thermal coefficient, was defined by plotting strain versus temperature and then performing a linear regression analysis. The slope of this line is defined as the thermal strain rate. Differences in the TSR provide an indication of the level of restraint present at each location. Strains measured in the spring (April) were chosen for this analysis. Figure 4.11 in Chapter 4 shows the range of temperatures experienced for a particular location within in a slab is greatest in the spring. These large variations in temperatures provide a greater range of data points over which to make a more accurate evaluation of the TSR.

Figure 6.16 shows the distribution of strain across the top of an unrestrained slab. As expected, the overall strain at the centerline joint is the smallest due to restraint provided by the adjacent slab. The largest strain was measured adjacent to the lane/shoulder joint in the longitudinal direction. The TSR at the centerline was the largest and the TSR at the lane/shoulder joint was the smallest. Figure 6.17 shows the same trends for a restrained slab.

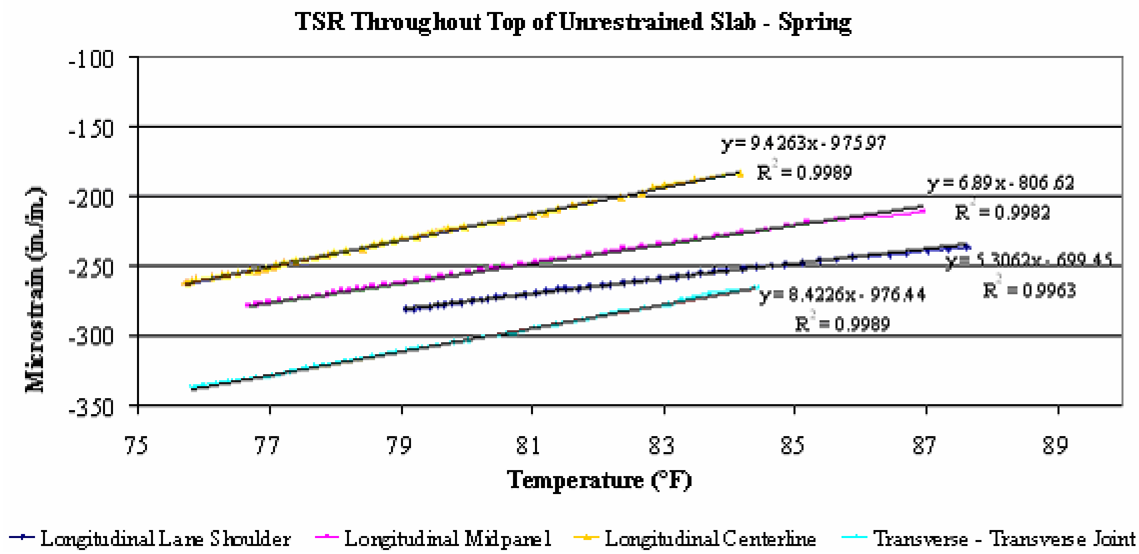

Figure 6.16 Temperature vs. strain measured at the top of an unrestrained slab.

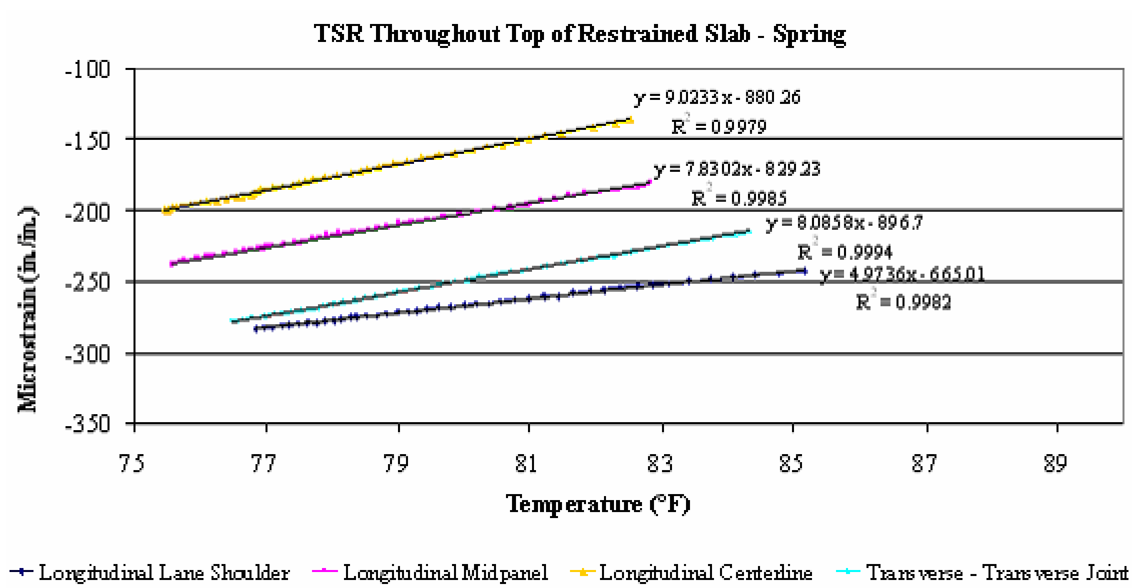

Figure 6.17 Temperature vs. strain measured at the top of a restrained slab.

Figures 6.18 and 6.19 show the distribution of strain at the bottom of the slab. It is evident that overall strains are less at the bottom of the slab than at the top for both restrained and unrestrained slabs. This is due to the frictional resistance provided by the base material and the higher moisture content at the bottom of the slab compared to the top.

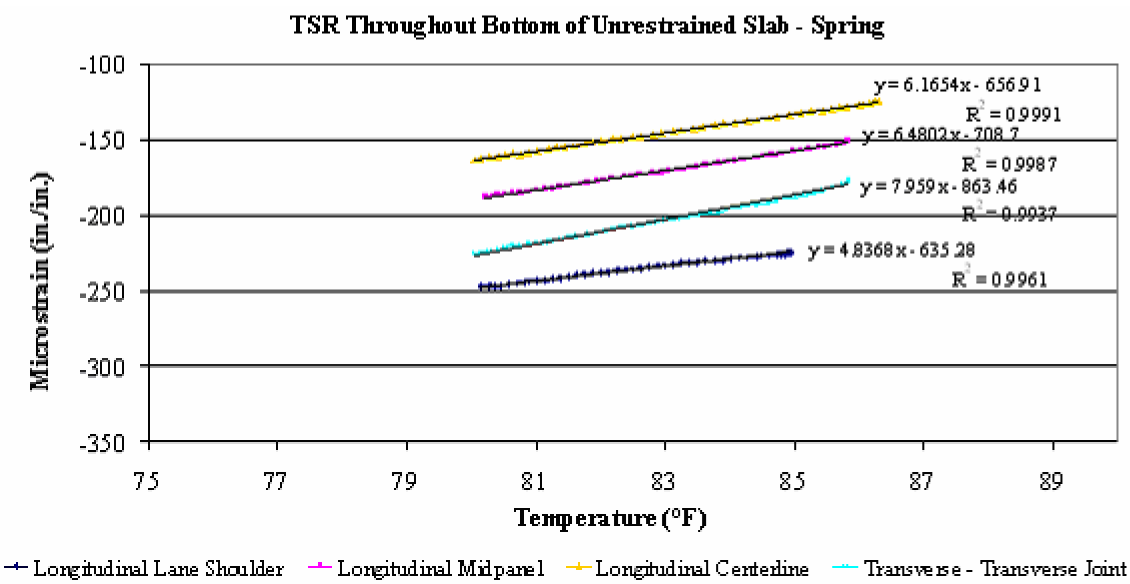

Figure 6.18 Temperature vs. strain measured at the bottom of an unrestrained slab.

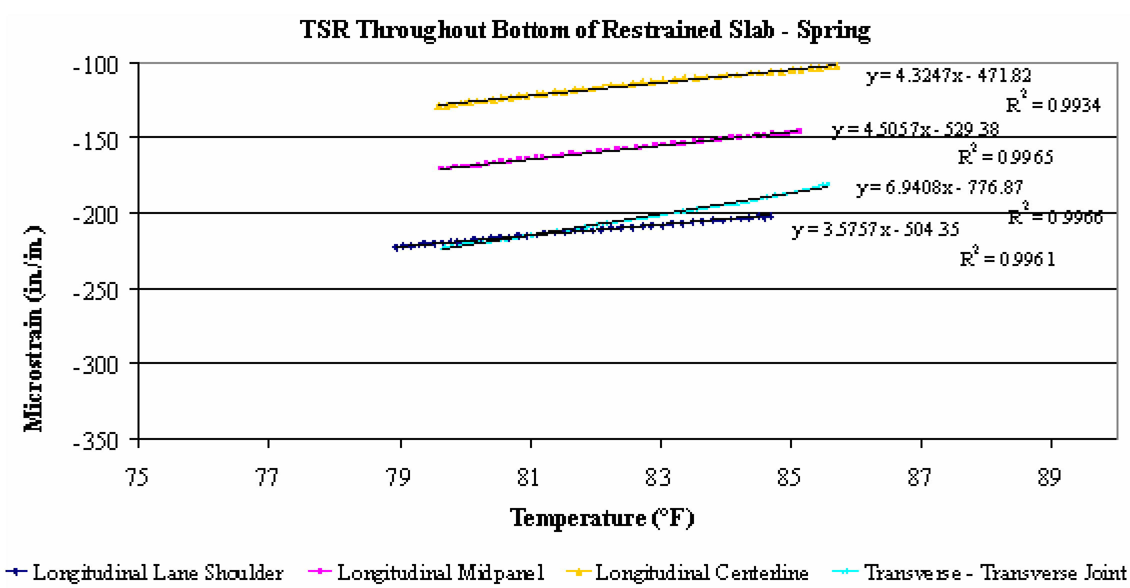

Figure 6.19 Temperature vs. measured strain at the bottom of a restrained slab.

Tables 6.15 and 6.16 summarize the TSR values obtained from Figures 6.16 through 6.19. Table 6.15 summarizes the difference in strain for each location at the top of the slab while Table 6.16 summarizes the difference in strain for each location at the bottom of the slab. From Table 6.15, it can be seen that the reduction in strain with changes in temperature at locations near the joint is approximately 0.34 to 0.41 microstrain/^{o}F. This indicates the dowel and tie bars do restrain thermal deformation in the slab. The opposite effect is apparent at midpanel, with a higher rate of strain with changes in temperature occurring at midpanel for the restrained slabs. Restraint creates a redistribution of strain concentrations in which strain is reduced at locations near the joints, but is increased at locations further away from the joints.

Table 6.15 Summary of thermal strain rates at the top of the slab.

Summary of Restraint for Top Sensors				
	TSR (in./in./°F)			
Restraint Condition	Longitudinal Lane/Shoulder	Longitudinal Midpanel	Longitudinal Centerline	Transverse Transverse Joint
Unrestrained	5.31E-06	6.89E-06	9.43E-06	8.43E-06
Restrained	4.97E-06	7.83E-06	9.02E-06	8.09E-06
Difference	3.40E-07	-9.40E-07	4.10E-07	3.40E-07

Table 6.16 Summary of thermal strain rates at the bottom of the slab.

Summary of Restraint for Bottom Sensors				
	TSR (in./in./°F)			
Restraint Condition	Longitudinal Lane/Shoulder	Longitudinal Midpanel	Longitudinal Centerline	Transverse Transverse Joint
Unrestrained	4.84E-06	6.48E-06	6.17E-06	7.96E-06
Restrained	3.58E-06	4.51E-06	4.32E-06	6.94E-06
Difference	1.26E-06	1.97E-06	1.85E-06	1.02E-06

From Table 6.16 it is evident that restraint has a greater effect on slab movement at the bottom of the slab than at the top. The design thickness of the slab was 12 inches but the as-built thicknesses were up to 14 inches. The dowel and tie bars were most likely located closer to the bottom of the slab than the top. This would produce a higher level of restraint near the bottom of the slab. At locations of joints the difference in restraint between restrained and unrestrained slabs is 3 to 4.5 times greater for bottom sensors than for top sensors. As with the top of the slab, the difference between restrained and unrestrained slabs at the midpanel location is the greatest.

6.4 EFFECTS OF DRYING SHRINKAGE AND CREEP ON STRAIN

The following section provides a look at the effects of drying shrinkage and creep on strain at locations within the slab throughout the year. Drying shrinkage and creep are isolated from thermal strain in this analysis using equation (6-2):

$$\mu_{m,c} = (R_1 - R_0)B + (T_1 - T_0)(C_1 - C_2) \qquad \textit{(6-2)}$$

where:

$\mu_{m,c}$ = strain influenced by creep and moisture changes

R_0 = raw strain at $time_0$ (initial concrete set)

R_1 = raw strain at $time_1$

T_0 = temperature at $time_0$

T_1 = temperature at $time_1$

C_1 = thermal coefficient of expansion of steel in strain gage

=6.78 microstrain/°F

C_2 = thermal coefficient of expansion of the concrete

=5.71 microstrain /°F (measured in the laboratory)

B = batch calibration factor (provided by the manufacturer)

Note that this equation is similar to equation (6-1); however, the effects of thermal strain are removed by subtracting out the thermal expansion of the concrete. Figure 6.20 provides a direct comparison between the contributions of temperature, moisture and creep, moisture and creep and temperature to strain development. The strains in Figure 6.20 are the average of strains measured from three different slabs.

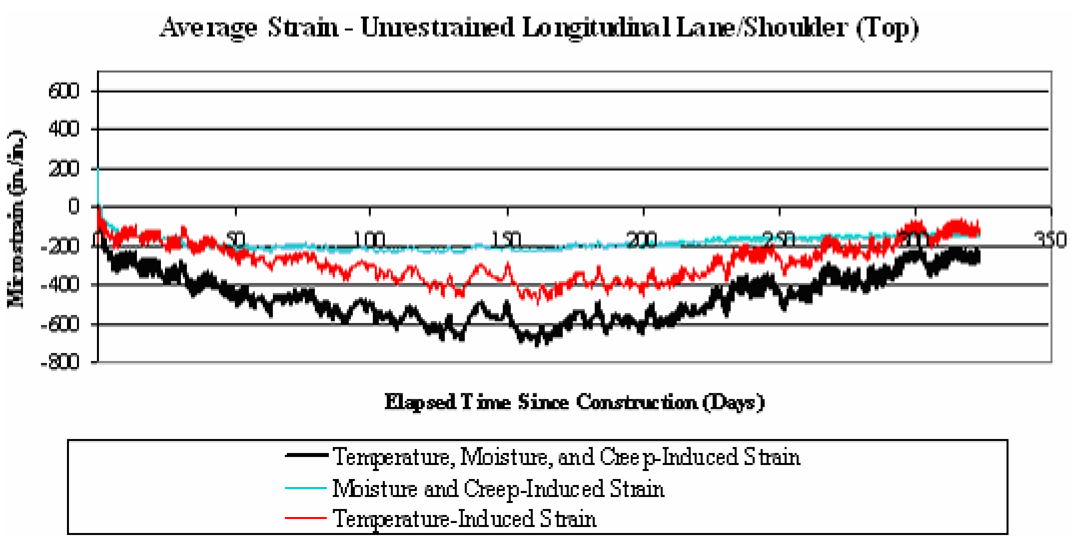

Figure 6.20 Contribution of temperature, creep, and drying shrinkage on total strain.

Note that temperature has the greatest effect on strain throughout the year. From the time of paving, the thermal strain follows the seasonal ambient temperature trend (refer to Figure 4.11) and the magnitude of strain steadily increased until reaching a maximum in the winter. The strain decreases as the ambient temperatures increase in the spring and summer.

Drying shrinkage is typically less than thermal strain. From Figure 6.20, thermal strain was found to be twice as high as the drying shrinkage the first winter after paving. Drying shrinkage is influenced by relative humidity, but unlike temperature, relative humidity does not experience pronounced diurnal fluctuations.

6.4.1 Analysis of Drying Shrinkage and Creep *(First Ten Months After Paving)*

Figures 6.21 through 6.24 show drying shrinkage for various locations at the top and bottom of restrained and unrestrained slabs. Figures 6.21 and 6.22 show strains in the unrestrained slabs while 6.24 and 6.25 show strains in the restrained slabs.

Comparing Figures 6.21 and 6.22 it can be observed that overall strain in the top sensors is greater than that at the bottom. The effect of drying shrinkage is greatest at the top due to the fact that it receives greater exposure to the open air, and is hence more susceptible to evaporation. The noticeably greater strains observed at the bottom of the transverse joint appear to be the result of moisture infiltration through the transverse joints.

Variations in drying shrinkage not only occur through the depth of the slab but also across the surface of the slab. Drying shrinkage is the lowest at midpanel where its exposure to the air is limited to the surface of the slab. Drying shrinkage was the highest along the lane/shoulder joint because the tied curb and gutter was not constructed until a few weeks after the lane was paved. This left the face of the slab exposed to the wind and the ambient conditions and therefore a lager amount of drying shrinkage occurred. Less drying shrinkage occurred along the transverse joint early on compared to the lane/shoulder joint because its exposure to wind and the ambient climatic conditions was less. The tied centerline joint had even less exposure to wind than the transverse joint and therefore the drying shrinkage was less than that found at the transverse joint but higher than that at midpanel.

Similar trends were found for the restrained slabs as were found for the unrestrained slabs. See Figures 6.23 and 6.24. In general, the drying shrinkage increases drastically the first 50 days after paving. The increase in drying shrinkage continues through the winter months but then begins do decrease during the spring when precipitation events occur more frequently. This gradual lessening of drying shrinkage (reversible drying shrinkage) can be seen in Figures 6.21 through 6.24 in the range of 150 to 250 days after paving. This phenomenon makes it possible to determine the magnitude of reversible shrinkage that will occur throughout the slab. The drying shrinkage along the centerline was closer to the drying shrinkage at midpanel more so for the restrained slabs than the unrestrained slabs. This is because the tie bars keep the centerline joint tight and reduce the exposure to the ambient air and wind.

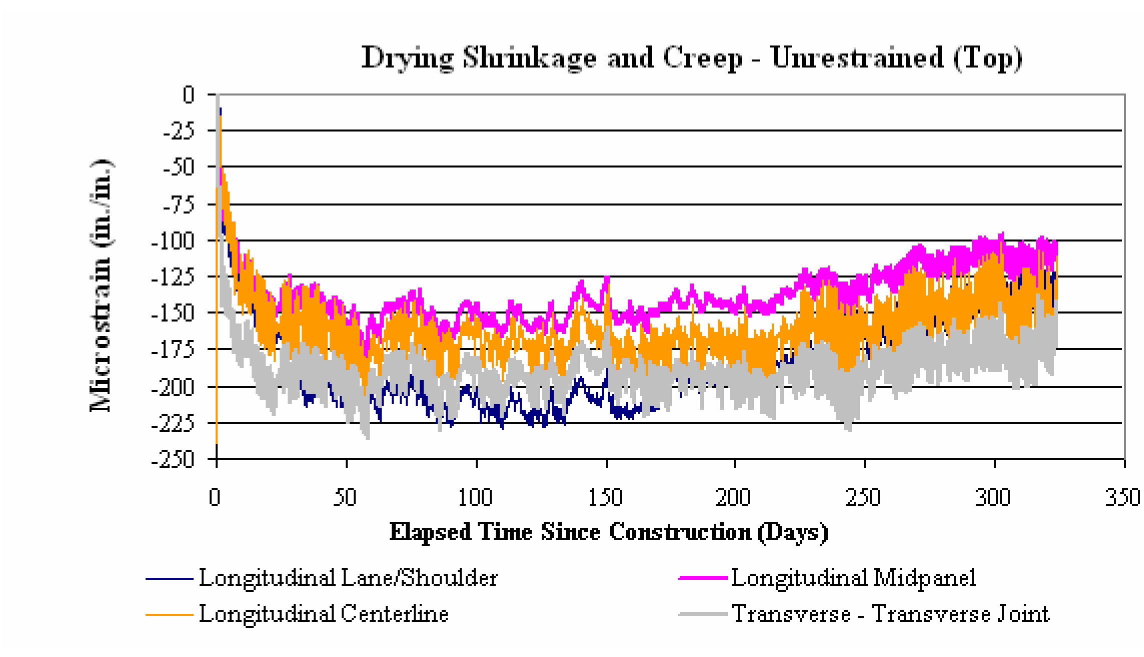

Figure 6.21 Drying shrinkage and creep at locations throughout the top of an unrestrained slab.

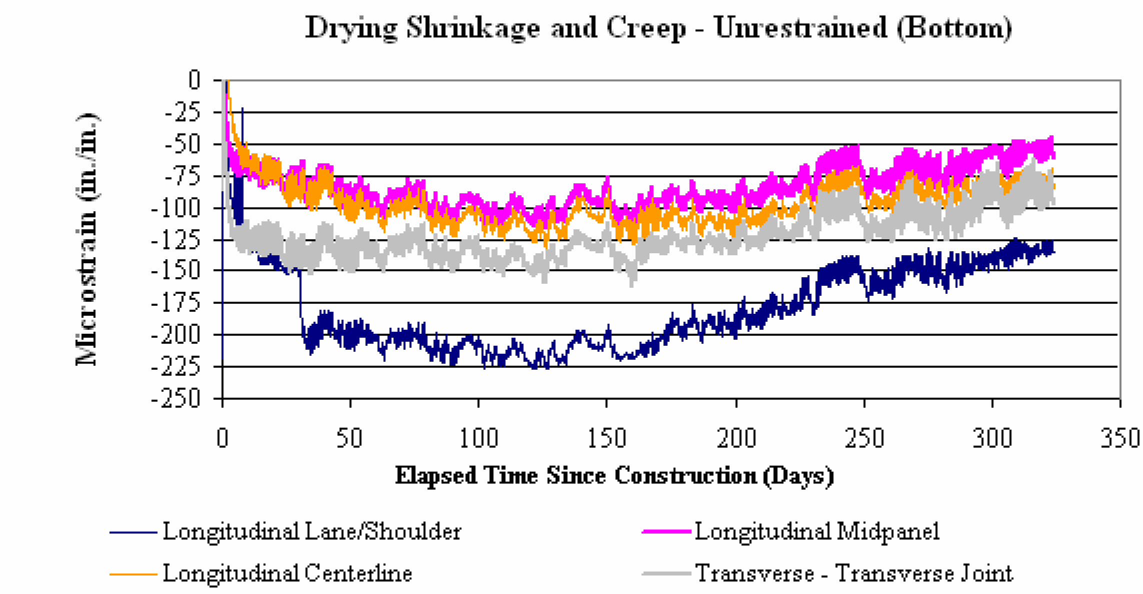

Figure 6.22 Drying shrinkage and creep at locations throughout the bottom of an unrestrained slab.

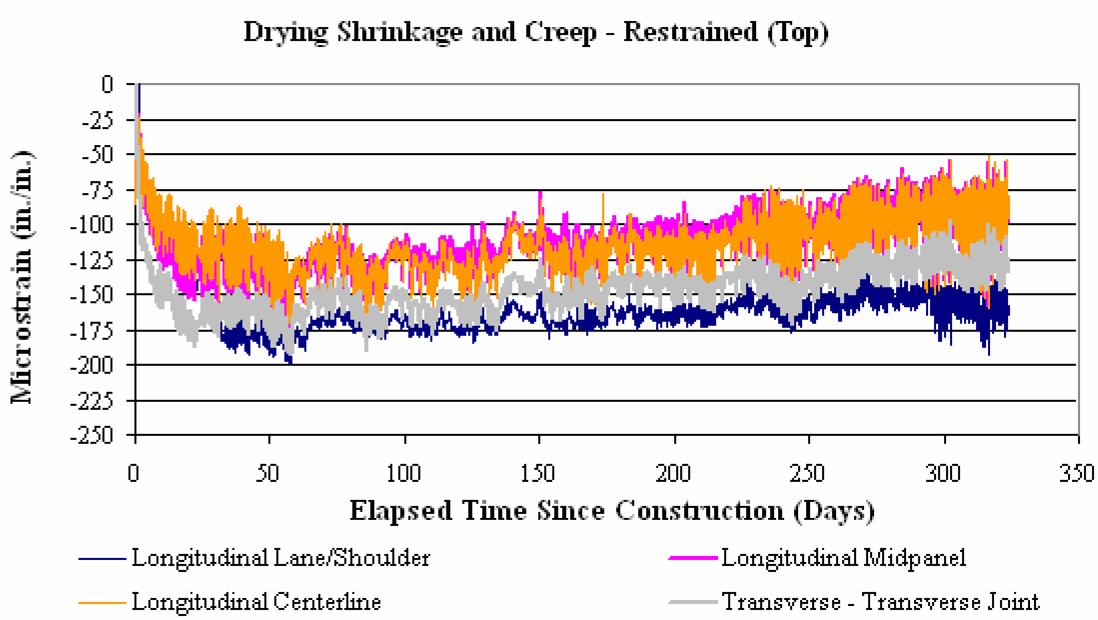

Figure 6.23 Drying shrinkage and creep at locations throughout the top of a restrained slab.

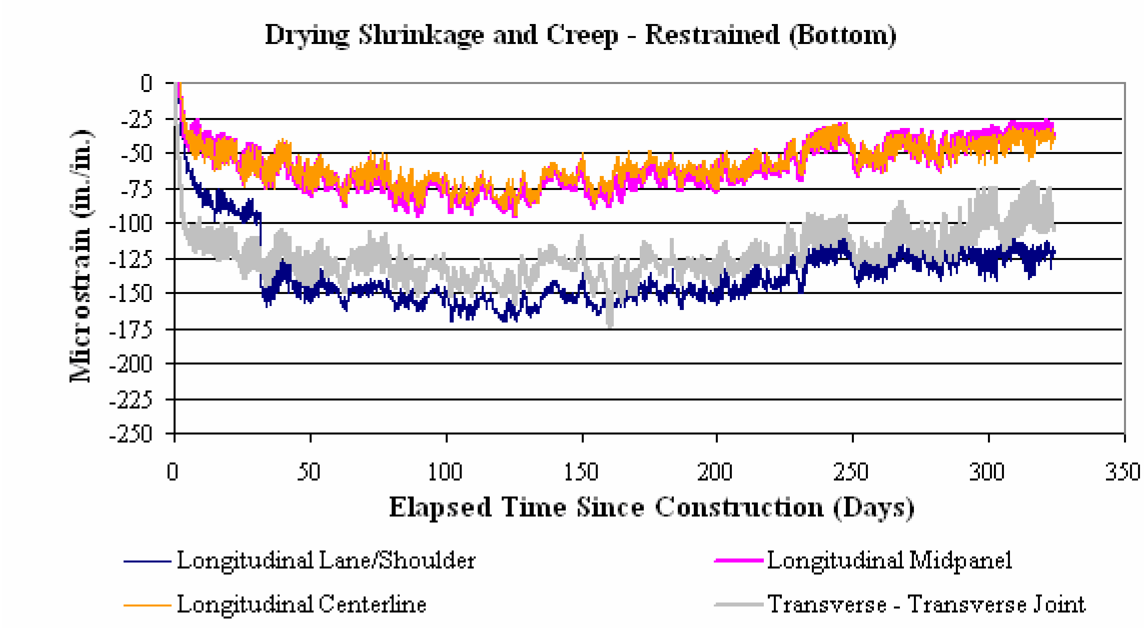

Figure 6.24 Drying shrinkage and creep at locations throughout the bottom of a restrained slab.

Looking at the longitudinal lane/shoulder strain in Figures 6.22 and 6.24 it can be seen that construction of the concrete curb and gutter caused a significant increase in strain. Figure 6.25 shows the strain around the time the concrete curb and gutter was constructed. Notice that the sudden increase in strain follows a similar pattern to that when the pavement was initially constructed. It is not clear why this substantial increase in strain developed. Based on an analysis of the strain and temperature data at this time, it was observed that the curb and gutter were constructed on September 13, the morning of the 28th day after initial paving.

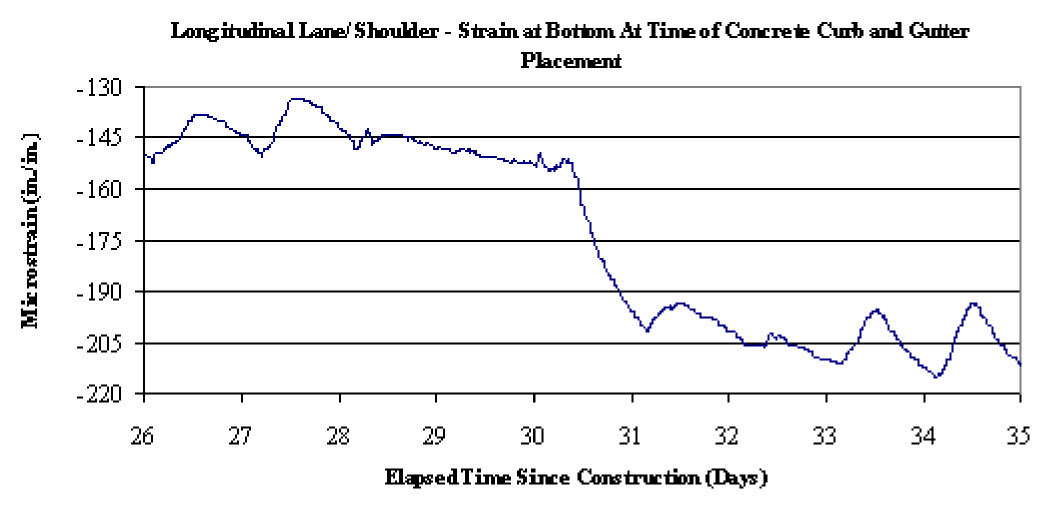

Figure 6.25 Drying shrinkage and creep at the time the curb and gutter were constructed.

7.0 RECOMMENDATIONS AND CONCLUSIONS

For this research project a section of JPCP was heavily instrumented with environmental sensors. From the time of paving in August 2004, the test section has been monitored using thermocouples, moisture sensors, static strain gages, and an on-site weather station.

The effects of these environmental conditions on the JPCP in terms of curling and warping was quantified by taking profile measurements of the slab. The results of the surface profile measurements were used to determine a relationship between curvature in the slab and temperature moment, a single parameter used to quantify nonlinear temperature gradients throughout the depth of the concrete. Several factors that affect the relationship between curling and temperature moment were investigated, including restraint and time of concrete set. The surface profile analysis was followed by an in-depth look at the variation in strain within the slab.

An analysis of the measured strains was conducted by looking at data collected during the first 72 hours after paving as well as data collected throughout the four seasons following paving. Parameters that influence strain within a slab such as depth, location and level of restraint were investigated.

Several conclusions concerning the early-age behavior of JPCP under environmental loads were reached. The following section provides a summary of these conclusions.

7.1 CONCLUSIONS

The following conclusions were made based on the results of this study:

1. Temperatures generated within JPCP slabs are a function of the boundary conditions. Larger gradients will tend to develop at midpanel then along the lane/shoulder joint when the curb and gutter or a shoulder is not placed at the same time the lane is paved. The leads to nonsymmetrical built-in curvature (Section 4.2).
2. Slabs respond differently to temperature gradients before and after the transverse joints crack since the slab length is effectively decreased after the joints begin to crack (Section 5.4).
3. Unrestrained slabs curl more dramatically with a much larger maximum displacement than restrained slabs. The curvature was 7 percent larger for the unrestrained slabs compared to the restrained slabs (Section 5.5).
4. Unrestrained slabs exhibited greater curvature at joints with wider cracks. Larger crack openings result in less restraint and therefore a greater amount of curvature will develop for equivalent gradients (Section 5.5).
5. Strains in JPCP slabs adjacent to the centerline are smaller than those adjacent to the lane/shoulder joint. The restraint provided by the existing slab inhibits movement of the new slab (Section 6.2.1).
6. The magnitude of strain in JPCP slabs decreases with increasing slab depth since the frictional restraint provided by the base layer restricts movement. Also, the

temperature fluctuations at the bottom of the slab are less than at the top of the slab (Section 6.2.1)

7. Spatial variation in the magnitude of measured strain across a given slab depth is less for restrained slabs compared to unrestrained slabs. The strains appear more uniform across the slab for the restrained slabs (Section 6.2.1).
8. Overall strains for restrained slabs are lower than the unrestrained slabs. This is predominately due to the fact that the restrained slab is tied to a previously constructed lane so the deformation due to drying shrinkage in the newly constructed lane is reduced (Section 6.2.1).
9. Strains at transverse and longitudinal joints are slightly larger in magnitude when the crack at the joint is wide compared to a narrow crack because there is more allowable movement before the joint locks up (Section 6.2.4).
10. As the ambient temperatures drop in the winter, the magnitude of strain measured increases. Increases in drying shrinkage also occur. The average strain in the fall was around -450 microstrain while the average strain in the winter was -600 microstrain (Section 6.3.1).
11. Diurnal strain fluctuations are at their lowest in the winter. This is due to the prevailing seasonal temperature patterns and the length of daylight hours (Section 6.3.1).
12. The reduction in strain with changes in temperature between the restrained and unrestrained slabs at locations near the joints is approximately 0.34 to 0.41 microstrain/^{o}F. Restraint creates a redistribution of strain concentrations in which

strain is reduced at locations near the joints, but is increased at locations further away from the joints (Section 6.3.2).

13. Restraint has a greater effect on slab movement at the bottom of the slab than at the top. At locations along the joints, the difference in the rate of strain with changes in temperature between restrained and unrestrained slabs is 3 to 4.5 times greater for bottom sensors than for top sensors (Section 6.3.2).
14. Drying shrinkage is lowest at midpanel where its exposure to the air is limited to the surface of the slab. Drying shrinkage is higher at exposed edges of the slab due to increased surface exposure to ambient conditions and wind (Section 6.4.1).
15. Drying shrinkage increases drastically during the first 50 days after paving. The increase in drying shrinkage continues through the winter months but then begins to decrease during the spring when rain events occur more frequently (Section 6.4.1).
16. The drying shrinkage along the centerline was more similar to the drying shrinkage at midpanel for the restrained slab compared to the unrestrained slab. This is because the tie bars keep the centerline joint tight and reduce the exposure to the ambient air and wind (Section 6.4.1).

7.2 RECOMMENDATIONS

The following recommendations have been made from the conclusions reached in this research study:

1. Further research is needed to understand the distribution of stresses in JPCP slabs. The strain data from this study can be utilized in the calibration of finite element models to

accurately predict magnitude and distribution of stress. Based on this research the following JPCP variables can be analyzed:

a. temperature and moisture gradients
b. restraint provided by dowel bars, tie bars, aggregate interlock, and base layer friction
c. crack width
d. slab depth
e. location within slab with reference to type and location of discontinuities (joints)

2. Further research is also needed in understanding the stress contribution from drying shrinkage as well as means of reducing these stresses through improved construction methods.
3. Validate current drying shrinkage models using the field data collected on SR-22.
4. Validate current models used to evaluate environmental loads using the field data collected on SR-22.

APPENDIX A

SENSOR LAYOUT AND SURVEY COORDINATES

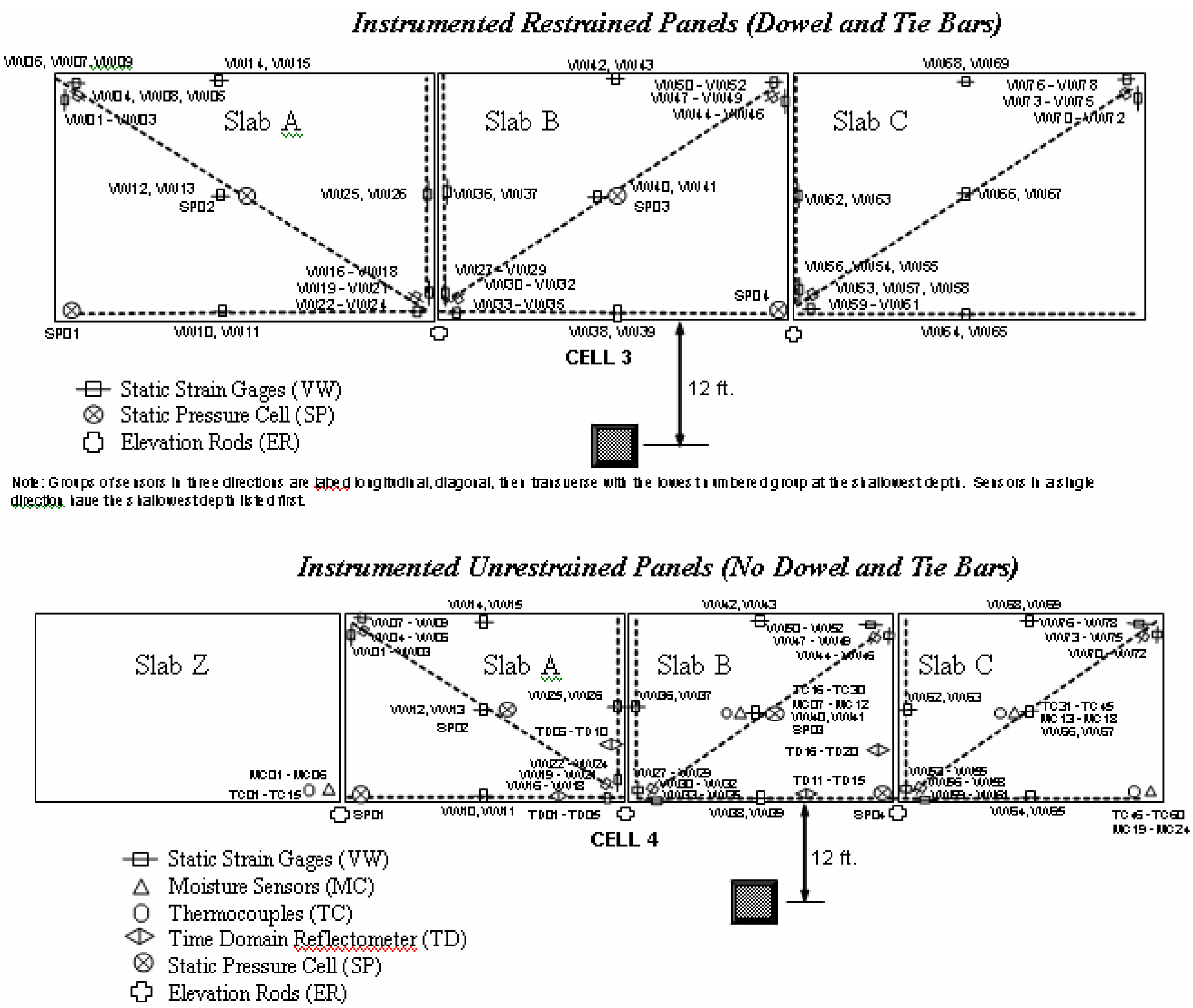

Figure A.1 Static strain gage and environmental sensor for Cells 3 and 4.

Table A.17 Survey coordinates for each sensor and the top and bottom of the slab and at the same location.

Sensor ID	Slab	Northing	Easting	Elevation
04TC46 - CONC	C	3021.6928	7019.9956	283.4082
04TC46	C	3021.6921	7019.9973	283.3803
04TC47	C	3021.6725	7019.9968	283.3591
04TC48	C	3021.6386	7020.0045	283.3194
04TC49	C	3021.6417	7020.0168	283.2394
04TC50	C	3021.6255	7020.0155	283.1417
04TC51	C	3021.6176	7020.0091	283.0809
04TC52	C	3021.6195	7020.0107	283.0663
GROUND	C	3021.6193	7020.0113	283.0555
04TC31 - CONC	C	3019.3651	7021.7635	283.4735
04TC31	C	3019.3640	7021.7664	283.4531
04TC32	C	3019.3674	7021.7756	283.4264
04TC33	C	3019.3642	7021.7830	283.3890
04TC34	C	3019.3607	7021.7922	283.3146
04TC35	C	3019.3712	7021.7956	283.2109
04TC36	C	3019.3664	7021.7962	283.1695
04TC37	C	3019.3797	7021.7817	283.1695
GROUND	C	3019.3869	7021.8047	283.1600
04TC16 - CONC	B	3018.1699	7026.0228	283.5419
04TC16	B	3018.1686	7026.0269	283.5284
04TC17	B	3018.1681	7026.0282	283.5019
04TC18	B	3018.1676	7026.0430	283.4688
04TC19	B	3018.1588	7026.0440	283.3925
04TC20	B	3018.1594	7026.0506	283.2863
04TC21	B	3018.1703	7026.0448	283.2381
04TC22 + GROUND	B	3018.1879	7026.0265	283.2225
04TC01 - CONC	A	3017.8751	7033.1279	283.6201
04TC01	A	3017.8735	7033.1318	283.5905
04TC02	A	3017.8676	7033.1443	283.5643
04TC03	A	3017.8615	7033.1574	283.5268
04TC04	A	3017.8506	7033.1036	283.4502
04TC05	A	3017.9033	7033.1555	283.3494
04TC06	A	3017.8540	7033.0968	283.2843
04TC07 + GROUND	A	3017.8520	7033.1644	283.2688
04MC01 - CONC	A	3017.8473	7033.2695	283.6215
04MC01	A	3017.8478	7033.2686	283.5820
04MC02	A	3017.8400	7033.2852	283.5809
04MC03	A	3017.8701	7033.2762	283.5226
04MC04	A	3017.8270	7033.3215	283.4532
04MC05	A	3017.8295	7033.3161	283.3562
04MC06	A	3017.8235	7033.3101	283.3065
GROUND	A	3017.8139	7033.3075	283.2811
04MC07 - CONC	B	3018.3010	7025.4829	283.5337
04MC07	B	3018.2991	7025.4877	283.5292
04MC08	B	3018.3054	7025.4710	283.5190

04MC09	B	3018.2933	7025.5017	283.4714
04MC10	B	3018.2941	7025.4538	283.3976
04MC11	B	3018.2901	7025.5105	283.2997
04MC12	B	3018.2756	7025.4628	283.2349
GROUND	B	3018.2756	7025.4774	283.2120
04MC13 - CONC	B	3019.5434	7021.1462	283.4605
04MC13	C	3019.5423	7021.1489	283.4421
04MC14	C	3019.5562	7021.1219	283.4343
04MC15	C	3019.5321	7021.1544	283.3868
04MC16	C	3019.5526	7021.1010	283.3116
04MC17	C	3019.5316	7021.1381	283.2050
04MC18	C	3019.5395	7021.1175	283.1614
GROUND	C	3019.5322	7021.1356	283.1391
04MC19 - CONC	C	3021.6386	7020.1357	283.4089
04MC19	C	3021.6390	7020.1342	283.3735
04MC20	C	3021.6439	7020.1103	283.3624
04MC21	C	3021.6264	7020.1520	283.3128
04MC22	C	3021.6198	7020.1596	283.2431
04MC23	C	3021.6257	7020.1678	283.1423
04MC24	C	3021.6406	7020.1108	283.0912
GROUND	C	3021.6397	7020.1128	283.0507
04VW64 - CONC	C	3021.1815	7021.8103	283.4360
04VW64	C	3021.1826	7021.8083	283.3988
04VW65	C	3021.1789	7021.7957	283.1261
04VW66 - CONC	C	3019.4501	7021.3996	283.4660
04VW66	C	3019.4497	7021.4014	283.4338
04VW67	C	3019.4562	7021.4054	283.1720
04VW68 - CONC	C	3017.7996	7020.8257	283.5046
04VW68	C	3017.7989	7020.8275	283.4796
04VW69	C	3017.7771	7020.9027	283.2204
04VW62 - CONC	C	3018.8639	7023.4255	283.4997
04VW62	C	3018.8643	7023.4243	283.4721
04VW63	C	3018.8676	7023.4340	283.2084
04VW38 - CONC	B	3019.8401	7026.3418	283.5046
04VW38	B	3019.8396	7026.3429	283.4826
04VW39	B	3019.8238	7026.3122	283.2144
04VW40 - CONC	B	3018.1770	7025.7995	283.5409
04VW40	B	3018.1791	7025.7955	283.5147
04VW41	B	3018.1855	7025.7999	283.2599
04VW42 - CONC	B	3016.5251	7025.2452	283.5653
04VW42	B	3016.5243	7025.2473	283.5445
04VW43	B	3016.5079	7025.2505	283.2884
04VW36 - CONC	B	3017.5702	7027.8626	283.5684
04VW36	B	3017.5701	7027.8636	283.5518
04VW37	B	3017.5689	7027.8665	283.2814
04VW25 - CONC	A	3017.5056	7028.0954	283.5731
04VW25	A	3017.5063	7028.0947	283.5474
04VW26	A	3017.4895	7028.1040	283.2880

04VW10 - CONC	A	3018.5920	7030.6383	283.5746
04VW10	A	3018.5929	7030.6363	283.5422
04VW11	A	3018.5790	7030.6336	283.2825
04VW12 - CONC	A	3016.9087	7030.1418	283.6069
04VW12	A	3016.9081	7030.1425	283.5788
04VW13	A	3016.9116	7030.1544	283.3131
04VW14 - CONC	A	3015.2177	7029.6541	283.6433
04VW14	A	3015.2169	7029.6571	283.6178
04VW15	A	3015.2361	7029.6636	283.3532
04SP01 - CONC	A	3017.7824	7032.3364	283.6113
04SP01	A	3017.7831	7032.3354	283.3000
04SP02 - CONC	A	3016.6660	7030.0869	283.6136
04SP02	A	3016.6649	7030.0897	283.3003
04SP03 - CONC	B	3017.9598	7025.7463	283.5477
04SP03	B	3017.9581	7025.7507	283.2340
04SP04 - CONC	B	3020.1119	7024.3994	283.4802
04SP04	B	3020.1124	7024.3980	283.1637
03SP04 - CONC	B	3014.8914	7042.0036	283.7738
03SP04	B	3014.8899	7042.0066	283.4397
03SP03 - CONC	B	3012.7597	7043.3119	283.8361
03SP03	B	3012.7607	7043.3100	283.5249
03SP02 - CONC	A	3011.4323	7047.6652	283.9143
03SP02	A	3011.4341	7047.6619	283.5900
03SP01 - CONC	A	3012.5028	7049.9052	283.9121
03SP01	A	3012.5010	7049.9082	283.5861
02DP04 - CONC	C	3011.6296	7052.6847	283.9529
02DP04	C	3011.6307	7052.6830	283.6403
02DP03 - CONC	C	3011.1181	7054.3136	283.9845
02DP03	C	3011.1186	7054.3130	283.6673
02DP02 - CONC	B	3010.8633	7055.1958	283.9968
02DP02	B	3010.8645	7055.1937	283.6859
02DP01 - CONC	B	3010.2155	7057.3025	284.0375
02DP01	B	3010.2155	7057.3026	283.7262
01DP04 - CONC	C	3006.2315	7070.1209	284.2731
01DP04	C	3006.2288	7070.1207	283.9342
01DP03 - CONC	C	3005.6960	7071.8710	284.3065
01DP03	C	3005.6968	7071.8714	283.9558
01DP02 - CONC	B	3005.4189	7072.7352	284.3243
01DP02	B	3005.4166	7072.7338	283.9625
01DP01 - CONC	B	3003.4073	7079.1404	284.4472
01DP01	B	3003.4064	7079.1373	284.0841
04VW70 - CONC	C	3018.5272	7019.0975	283.4718
04VW70	C	3018.5278	7019.0979	283.4745
04VW71	C	3018.5343	7019.1078	283.4498
04VW72	C	3018.5751	7019.0631	283.4665
04VW73	C	3018.5354	7019.1551	283.3324
04VW74	C	3018.5854	7019.1282	283.2989
04VW75	C	3018.5937	7019.0660	283.3221
04VW76	C	3018.5371	7019.1717	283.2067

04VW77	C	3018.5889	7019.1388	283.1824
04VW78	C	3018.6041	7019.0727	283.1969
GROUND	C	3018.5451	7019.0272	283.1587
04VW53 - CONC	C	3020.4603	7023.6009	283.4629
04VW53	C	3020.4588	7023.6031	283.4253
04VW54	C	3020.4145	7023.5980	283.4065
04VW55	C	3020.3978	7023.6371	283.4140
04VW56	C	3020.4993	7023.6094	283.3324
04VW57	C	3020.4253	7023.5848	283.3209
04VW58	C	3020.3943	7023.6578	283.3201
04VW59	C	3020.4756	7023.6035	283.1773
04VW60	C	3020.4211	7023.5741	283.1632
04VW61	C	3020.3854	7023.6583	283.1657
GROUND	C	3020.4650	7023.6930	283.1372
04VW44 - CONC	B	3017.2399	7023.5231	283.5381
04VW44	B	3017.2416	7023.5183	283.4986
04VW45	B	3017.2633	7023.5327	283.4883
04VW46	B	3017.3015	7023.5008	283.4969
04VW47	B	3017.2290	7023.5219	283.4282
04VW48	B	3017.2665	7023.5422	283.4067
04VW49	B	3017.3231	7023.4585	283.4174
04VW50	B	3017.2638	7023.5449	283.2599
04VW51	B	3017.3006	7023.5068	283.2411
04VW52	B	3017.3175	7023.4545	283.2418
GROUND	B	3017.2413	7023.4023	283.2139
04VW27 - CONC	B	3019.1286	7028.1047	283.5295
04VW27	B	3019.1273	7028.1076	283.4910
04VW28	B	3019.1223	7028.1192	283.4743
04VW29	B	3019.0976	7028.1749	283.4761
04VW30	B	3019.1729	7028.1162	283.4196
04VW31	B	3019.0823	7028.1235	283.3996
04VW32	B	3019.0650	7028.1755	283.4140
04VW33	B	3019.1771	7028.1230	283.2430
04VW34	B	3019.1174	7028.0897	283.2552
04VW35	B	3019.0718	7028.2029	283.2561
GROUND	B	3019.1188	7028.2247	283.2191
04VW16 - CONC	A	3018.9293	7028.9022	283.5476
04VW16	A	3018.9302	7028.9001	283.5029
04VW17	A	3018.8926	7028.8772	283.4893
04VW18	A	3018.9105	7028.8115	283.4985
04VW19	A	3018.9349	7028.9109	283.4217
04VW21	A	3018.8934	7028.8061	283.4135
04VW22	A	3018.9479	7028.9208	283.2780
04VW23	A	3018.8738	7028.8886	283.2581
04VW24	A	3018.8914	7028.7961	283.2649
GROUND	A	3018.9836	7028.8182	283.2250
04VW01 - CONC	A	3014.8823	7031.4901	283.6689
04VW01	A	3014.8818	7031.4926	283.6314

04VW02	A	3014.9136	7031.5113	283.6106
04VW03	A	3014.9106	7031.5618	283.6237
04VW04	A	3014.8673	7031.4435	283.5599
04VW06	A	3014.9223	7031.5746	283.5412
04VW07	A	3014.8473	7031.4400	283.4156
04VW08	A	3014.9538	7031.5122	283.3958
04VW09	A	3014.9048	7031.5850	283.4015
GROUND	A	3014.8236	7031.5627	283.3641
03VW68 - CONC	C	3012.6134	7038.4834	283.7901
03VW68	C	3012.6132	7038.4849	283.7642
03VW69	C	3012.6302	7038.4400	283.5009
GROUND	C	3012.6553	7038.4764	283.4750
03VW66 - CONC	C	3014.2870	7038.9499	283.7566
03VW66	C	3014.2847	7038.9549	283.7252
03VW67	C	3014.3163	7038.9633	283.4599
GROUND	C	3014.3267	7038.9892	283.4216
03VW64 - CONC	C	3015.9642	7039.4601	283.7257
03VW64	C	3015.9647	7039.4594	283.6755
03VW65	C	3015.9977	7039.5116	283.4113
GROUND	C	3016.0056	7039.4959	283.3900
03VW62 - CONC	C	3013.6867	7041.0708	283.7916
03VW62	C	3013.6872	7041.0702	283.7557
03VW63	C	3013.6582	7041.0317	283.4976
GROUND	C	3013.6598	7041.0935	283.4722
03VW42 - CONC	B	3011.3193	7042.8548	283.8676
03VW42	B	3011.3181	7042.8583	283.8338
03VW43	B	3011.3518	7042.8400	283.5726
GROUND	B	3011.3469	7042.8718	283.5449
03VW40 - CONC	B	3012.9820	7043.3684	283.8252
03VW40	B	3012.9821	7043.3673	283.8034
03VW41	B	3013.0183	7043.3390	283.5281
GROUND	B	3013.0235	7043.3627	283.4986
03VW38 - CONC	B	3014.6610	7043.8807	283.7927
03VW38	B	3014.6602	7043.8825	283.7555
03VW39	B	3014.7009	7043.8515	283.4792
GROUND	B	3014.7101	7043.8715	283.4495
03VW36 - CONC	B	3012.3606	7045.4098	283.8674
03VW36	B	3012.3599	7045.4116	283.8212
03VW37	B	3012.3858	7045.4658	283.5753
GROUND	B	3012.3641	7045.4029	283.5383
03VW25 - CONC	A	3012.3004	7045.6030	283.8692
03VW25	A	3012.2993	7045.6053	283.8285
03VW26	A	3012.3171	7045.6492	283.5757
GROUND	A	3012.3057	7045.6654	283.5420
03VW14 - CONC	A	3010.0088	7047.2061	283.9394
03VW14	A	3010.0066	7047.2108	283.9056
03VW15	A	3010.0034	7047.2507	283.6516
GROUND	A	3010.0213	7047.2064	283.6239

03VW12 - CONC	A	3011.6930	7047.6903	283.9077
03VW12	A	3011.6908	7047.6942	283.8647
03VW13	A	3011.7103	7047.6926	283.6034
GROUND	A	3011.6406	7047.7071	283.5751
03VW10 - CONC	A	3013.3728	7048.2532	283.8766
03VW10	A	3013.3734	7048.2525	283.8257
03VW11	A	3013.3425	7048.2304	283.5611
GROUND	A	3013.3190	7048.2396	283.5249
03VW70 - CONC	C	3013.3466	7036.6757	283.7581
03VW70	C	3013.3488	7036.6714	283.7238
03VW71	C	3013.4042	7036.6601	283.7121
03VW72	C	3013.4136	7036.6053	283.6974
03VW73	C	3013.3326	7036.6743	283.6247
03VW74	C	3013.3963	7036.6793	283.6110
03VW75	C	3013.4388	7036.6176	283.5954
03VW76	C	3013.3211	7036.6804	283.4876
03VW77	C	3013.3838	7036.6915	283.4749
03VW78	C	3013.4324	7036.6189	283.4696
GROUND	C	3013.3519	7036.5632	283.4396
03VW53 - CONC	C	3015.2766	7041.2339	283.7583
03VW53	C	3015.2761	7041.2351	283.7016
03VW54	C	3015.2268	7041.2377	283.6971
03VW55	C	3015.1989	7041.2582	283.6789
03VW56	C	3015.2842	7041.2416	283.6218
03VW57	C	3015.2439	7041.2214	283.6164
03VW58	C	3015.2000	7041.2952	283.6059
03VW59	C	3015.3019	7041.2217	283.4650
03VW60	C	3015.2414	7041.1980	283.4632
03VW61	C	3015.2122	7041.3065	283.4570
GROUND	C	3015.2677	7041.3429	283.4175
03VW44 - CONC	B	3012.0409	7041.0746	283.8354
03VW44	B	3012.0415	7041.0731	283.7995
03VW45	B	3012.0738	7041.0993	283.7805
03VW46	B	3012.0983	7041.0368	283.7841
03VW47	B	3011.9999	7041.0917	283.7190
03VW48	B	3012.1058	7041.0941	283.7115
03VW49	B	3012.1038	7041.0341	283.7196
03VW50	B	3011.9914	7041.0862	283.5734
03VW51	B	3012.0823	7041.0957	283.5676
03VW52	B	3012.1095	7041.0284	283.5507
GROUND	B	3012.0103	7040.9971	283.5219
03VW27 - CONC	B	3013.9641	7045.6341	283.8303
03VW27	B	3013.9644	7045.6335	283.7792
03VW28	B	3013.9057	7045.6157	283.7735
03VW29	B	3013.9025	7045.6765	283.7693
03VW30	B	3013.9932	7045.6382	283.6890
03VW31	B	3013.9339	7045.6201	283.6814
03VW32	B	3013.9350	7045.7041	283.6762

03VW33	B	3013.9857	7045.6394	283.5449
03VW34	B	3013.9188	7045.6180	283.5179
03VW35	B	3013.8810	7045.6876	283.5224
GROUND	B	3013.9586	7045.7312	283.4885
03VW16 - CONC	A	3013.7099	7046.4085	283.8451
03VW16	A	3013.7114	7046.4056	283.7855
03VW17	A	3013.6752	7046.3651	283.7745
03VW18	A	3013.6880	7046.3029	283.7638
03VW19	A	3013.7419	7046.3769	283.6873
03VW21	A	3013.6922	7046.2871	283.6826
03VW22	A	3013.7450	7046.3769	283.5480
03VW23	A	3013.6681	7046.3492	283.5332
03VW24	A	3013.6768	7046.2848	283.5240
GROUND	A	3013.7740	7046.3042	283.5033
03VW01 - CONC	A	3009.6266	7049.0574	283.9692
03VW01	A	3009.6257	7049.0597	283.9210
03VW02	A	3009.6762	7049.0684	283.9071
03VW03	A	3009.6818	7049.1367	283.9204
03VW04	A	3009.6325	7049.0055	283.8386
03VW06	A	3009.6702	7049.1479	283.8284
03VW07	A	3009.6316	7049.0038	283.6907
03VW08	A	3009.6807	7049.0451	283.6764
03VW09	A	3009.6722	7049.1472	283.6881
GROUND	A	3009.5633	7049.1092	283.6457
01CE01 - CONC	A	3001.9494	7084.9360	284.5526
01CE01	A	3001.9489	7084.9319	284.5307
01CE02	A	3001.9109	7084.9242	284.1976
GROUND	A	3001.9149	7084.9785	284.1906
01CE03 - CONC	A	3001.6992	7084.8628	284.5564
01CE03	A	3001.6993	7084.8621	284.5214
01CE04	A	3001.6802	7084.8475	284.1996
GROUND	A	3001.6699	7084.9391	284.1889
01CE05 - CONC	A	3001.4171	7084.7774	284.5648
01CE05	A	3001.4172	7084.7793	284.5322
01CE06	A	3001.4180	7084.7753	284.2050
GROUND	A	3001.4107	7084.8232	284.1922
01CE07 - CONC	A	3001.1947	7084.7152	284.5709
01CE07	A	3001.1946	7084.7140	284.5382
01CE08	A	3001.1799	7084.7047	284.2158
GROUND	A	3001.1822	7084.8075	284.2028
01CE09 - CONC	A	3001.9816	7084.8124	284.5504
01CE09	A	3001.9813	7084.8119	284.5226
01CE10	A	3001.9815	7084.8143	284.1989
GROUND	A	3002.0326	7084.9068	284.1824
01CE11 - CONC	A	3002.0576	7084.5333	284.5420
01CE11	A	3002.0534	7084.5355	284.5223
01CE12	A	3002.0400	7084.5433	284.1874
GROUND	A	3002.1489	7084.5072	284.1719

01CE13 - CONC	A	3002.1507	7084.2926	284.5387
01CE13	A	3002.1501	7084.2860	284.5120
01CE14	A	3002.1274	7084.2944	284.1804
GROUND	A	3002.1756	7084.3068	284.1678
01CE15 - CONC	A	3002.2107	7084.0541	284.5380
01CE15	A	3002.2105	7084.0524	284.5112
01CE16	A	3002.1969	7084.0656	284.1797
GROUND	A	3002.2614	7084.0886	284.1687
01CE17 - CONC	A	3002.4538	7083.1957	284.5195
01CE17	A	3002.4538	7083.1973	284.4973
01CE18	A	3002.4540	7083.1989	284.1547
GROUND	A	3002.4328	7083.2935	284.1477
01CE19 - CONC	A	3002.3244	7083.1609	284.5224
01CE19	A	3002.3240	7083.1573	284.4978
01CE20	A	3002.3205	7083.1653	284.1548
GROUND	A	3002.3048	7083.2719	284.1519
01CE21 - CONC	A	3002.1660	7083.1178	284.5258
01CE21	A	3002.1661	7083.1195	284.5028
01CE22	A	3002.1662	7083.1208	284.1596
GROUND	A	3002.1504	7083.2077	284.1496
01CE23 - CONC	A	3002.0199	7083.0819	284.5294
01CE23	A	3002.0196	7083.0792	284.5099
01CE24	A	3002.0192	7083.0745	284.1674
GROUND	A	3002.0063	7083.1794	284.1581
01CE25 - CONC	A	3001.8751	7083.0345	284.5344
01CE25	A	3001.8753	7083.0373	284.5188
01CE26	A	3001.8755	7083.0384	284.1737
GROUND	A	3001.8688	7083.1363	284.1631
01CE27 - CONC	B	3003.2763	7080.6141	284.4708
01CE27	B	3003.2756	7080.6111	284.4470
01CE28	B	3003.2628	7080.6246	284.1083
GROUND	B	3003.2545	7080.6696	284.1012
01CE29 - CONC	B	3003.0494	7080.5407	284.4750
01CE29	B	3003.0498	7080.5426	284.4576
01CE30	B	3003.0174	7080.5529	284.1164
GROUND	B	3003.0157	7080.6150	284.1079
01CE31 - CONC	B	3002.7896	7080.4694	284.4782
01CE31	B	3002.7897	7080.4693	284.4609
01CE32	B	3002.7675	7080.4579	284.1208
GROUND	B	3002.7719	7080.5437	284.1126
01CE33 - CONC	B	3002.5594	7080.3879	284.4836
01CE33	B	3002.5601	7080.3926	284.4706
01CE34	B	3002.5269	7080.3886	284.1306
GROUND	B	3002.5300	7080.4557	284.1230
01CE35 - CONC	B	3003.3243	7080.4881	284.4652
01CE35	B	3003.3222	7080.4793	284.4414
01CE336	B	3003.3251	7080.4956	284.1069
GROUND	B	3003.3842	7080.5241	284.0964

01CE37 - CONC	B	3003.3979	7080.2415	284.4636
01CE37	B	3003.3972	7080.2388	284.4379
01CE38	B	3003.4043	7080.2151	284.1059
GROUND	B	3003.4556	7080.2579	284.0966
01CE39 - CONC	B	3003.4703	7079.9925	284.4563
01CE39	B	3003.4714	7079.9968	284.4348
01CE40	B	3003.4738	7079.9974	284.0962
GROUND	B	3003.5230	7080.0023	284.0897
01CE41 - CONC	B	3003.5468	7079.7414	284.4549
01CE41	B	3003.5460	7079.7390	284.4252
01CE42	B	3003.5550	7079.7433	284.0901
GROUND	B	3003.6166	7079.7486	284.0740
01CE43 - CONC	B	3003.8137	7078.8532	284.4354
01CE43	B	3003.8142	7078.8545	284.4078
01CE44	B	3003.8013	7078.8684	284.0795
GROUND	B	3003.8266	7078.9362	284.0682
01CE45 - CONC	B	3003.6731	7078.7932	284.4381
01CE45	B	3003.6723	7078.7909	284.4104
01CE46	B	3003.6535	7078.8382	284.0803
GROUND	B	3003.6735	7078.9077	284.0688
01CE47 - CONC	B	3003.5370	7078.7517	284.4421
01CE47	B	3003.5369	7078.7512	284.4217
01CE48	B	3003.5265	7078.7740	284.0825
GROUND	B	3003.5135	7078.8795	284.0711
01CE49 - CONC	B	3003.3997	7078.7193	284.4449
01CE49	B	3003.3988	7078.7164	284.4281
01CE50	B	3003.3863	7078.7454	284.0872
GROUND	B	3003.3409	7078.8351	284.0827
01CE51 - CONC	B	3003.2605	7078.6757	284.4497
01CE51	B	3003.2614	7078.6790	284.4309
01CE52	B	3003.2407	7078.7104	284.0936
GROUND	B	3003.1906	7078.8050	284.0806
02CE01 - CONC	A	3008.7431	7063.1968	284.1341
02CE01	A	3008.7421	7063.1977	284.1072
02CE02	A	3008.7416	7063.1981	283.8441
GROUND	A	3008.7140	7063.2746	283.8356
02CE03 - CONC	A	3008.5110	7063.1420	284.1393
02CE03	A	3008.5105	7063.1424	284.1180
02CE04	A	3008.5135	7063.1418	283.8426
GROUND	A	3008.4872	7063.2193	283.8324
02CE05 - CONC	A	3008.2892	7063.0452	284.1381
02CE05	A	3008.2859	7063.0482	284.1160
02CE06	A	3008.2727	7063.0476	283.8457
GROUND	A	3008.2369	7063.1226	283.8354
02CE07 - CONC	A	3008.0206	7062.9761	284.1516
02CE07	A	3008.0206	7062.9761	284.1338
02CE08	A	3007.9979	7062.9612	283.8502
GROUND	A	3007.9969	7063.0358	283.8397

02CE09 - CONC	A	3008.7786	7063.0631	284.1304
02CE09	A	3008.7808	7063.0613	284.1058
02CE10	A	3008.7771	7063.0664	283.8438
GROUND	A	3008.8444	7063.0536	283.8316
02CE11 - CONC	A	3008.8645	7062.8058	284.1281
02CE11	A	3008.8671	7062.8036	284.0963
02CE12	A	3008.8593	7062.7935	283.8334
GROUND	A	3008.8816	7062.8509	283.8226
02CE13 - CONC	A	3008.9513	7062.5526	284.1243
02CE13	A	3008.9516	7062.5523	284.1005
02CE14	A	3008.9520	7062.5519	283.8308
GROUND	A	3009.0151	7062.5613	283.8179
02CE15 - CONC	A	3009.0249	7062.3026	284.1203
02CE15	A	3009.0253	7062.3023	284.0989
02CE16	A	3009.0064	7062.3079	283.8268
GROUND	A	3009.0617	7062.3242	283.8204
02CE17 - CONC	A	3009.2678	7061.4456	284.1048
02CE17	A	3009.2656	7061.4479	284.0845
02CE18	A	3009.2768	7061.4610	283.8193
GROUND	A	3009.2523	7061.5538	283.8080
02CE19 - CONC	A	3009.1193	7061.3970	284.1065
02CE19	A	3009.1231	7061.3931	284.0832
02CE20	A	3009.1240	7061.4145	283.8140
GROUND	A	3009.0959	7061.5110	283.8058
02CE21 - CONC	A	3008.9919	7061.3431	284.1080
02CE21	A	3008.9880	7061.3471	284.0847
02CE22	A	3008.9962	7061.3665	283.8178
GROUND	A	3008.9657	7061.4619	283.8019
02CE23 - CONC	A	3008.8266	7061.2969	284.1104
02CE23	A	3008.8286	7061.2948	284.0973
02CE24	A	3008.8238	7061.3207	283.8218
GROUND	A	3008.8113	7061.4225	283.8115
02CE25 - CONC	A	3008.7177	7061.2639	284.1130
02CE25	A	3008.7159	7061.2660	284.0956
02CE26	A	3008.7014	7061.2737	283.8242
GROUND	A	3008.6666	7061.3544	283.8120
02CE27 - CONC	B	3010.0910	7058.7968	284.0549
02CE27	B	3010.0913	7058.7966	284.0280
02CE28	B	3010.0793	7058.8109	283.7678
GROUND	B	3010.0634	7058.8650	283.7523
02CE29 - CONC	B	3009.8446	7058.7358	284.0598
02CE29	B	3009.8449	7058.7354	284.0325
02CE30	B	3009.8364	7058.7460	283.7661
GROUND	B	3009.8226	7058.8004	283.7564
02CE31 - CONC	B	3009.5971	7058.6656	284.0665
02CE31	B	3009.5949	7058.6683	284.0367
02CE32	B	3009.6004	7058.6680	283.7634
GROUND	B	3009.5710	7058.7401	283.7582

02CE33 - CONC	B	3009.3688	7058.6029	284.0696
02CE33	B	3009.3702	7058.6010	284.0482
02CE34	B	3009.3656	7058.6016	283.7701
GROUND	B	3009.3356	7058.6892	283.7613
02CE35 - CONC	B	3010.1207	7058.6766	284.0575
02CE35	B	3010.1242	7058.6726	284.0228
02CE36	B	3010.1313	7058.6697	283.7659
GROUND	B	3010.1883	7058.6967	283.7494
02CE37 - CONC	B	3010.2167	7058.4163	284.0529
02CE37	B	3010.2182	7058.4147	284.0242
02CE38	B	3010.1982	7058.4314	283.7529
GROUND	B	3010.2387	7058.4502	283.7461
02CE39 - CONC	B	3010.2813	7058.1706	284.0465
02CE39	B	3010.2840	7058.1675	284.0195
02CE40	B	3010.2674	7058.1619	283.7516
GROUND	B	3010.1968	7058.2490	283.7430
02CE41 - CONC	B	3010.3522	7057.9186	284.0366
02CE41	B	3010.3500	7057.9214	284.0148
02CE42	B	3010.3313	7057.9448	283.7489
GROUND	B	3010.2970	7058.0058	283.7399
02CE43 - CONC	B	3010.6189	7057.0288	284.0241
02CE43	B	3010.6206	7057.0269	284.0028
02CE44	B	3010.6149	7057.0515	283.7308
GROUND	B	3010.5887	7057.1418	283.7205
02CE45 - CONC	B	3010.4836	7056.9888	284.0265
02CE45	B	3010.4820	7056.9907	284.0044
02CE46	B	3010.4847	7056.9976	283.7370
GROUND	B	3010.4568	7057.0792	283.7230
02CE47 - CONC	B	3010.3301	7056.9615	284.0299
02CE47	B	3010.3305	7056.9611	284.0090
02CE48	B	3010.3343	7056.9622	283.7361
GROUND	B	3010.3119	7057.0399	283.7226
02CE49 - CONC	B	3010.1804	7056.9260	284.0342
02CE49	B	3010.1800	7056.9264	284.0116
02CE50	B	3010.1879	7056.9157	283.7363
GROUND	B	3010.1672	7057.0008	283.7296
02CE51 - CONC	B	3010.0307	7056.8676	284.0358
02CE51	B	3010.0288	7056.8704	284.0132
01CE52	B	3010.0188	7056.8846	283.7389
GROUND	B	3010.0039	7056.9587	283.7298

APPENDIX B

MONTHLY AMBIENT TEMPERATURE, WEIGHTED AVERAGE SLAB TEMPERATURE, AND SLAB TEMPERATURE GRADIENT

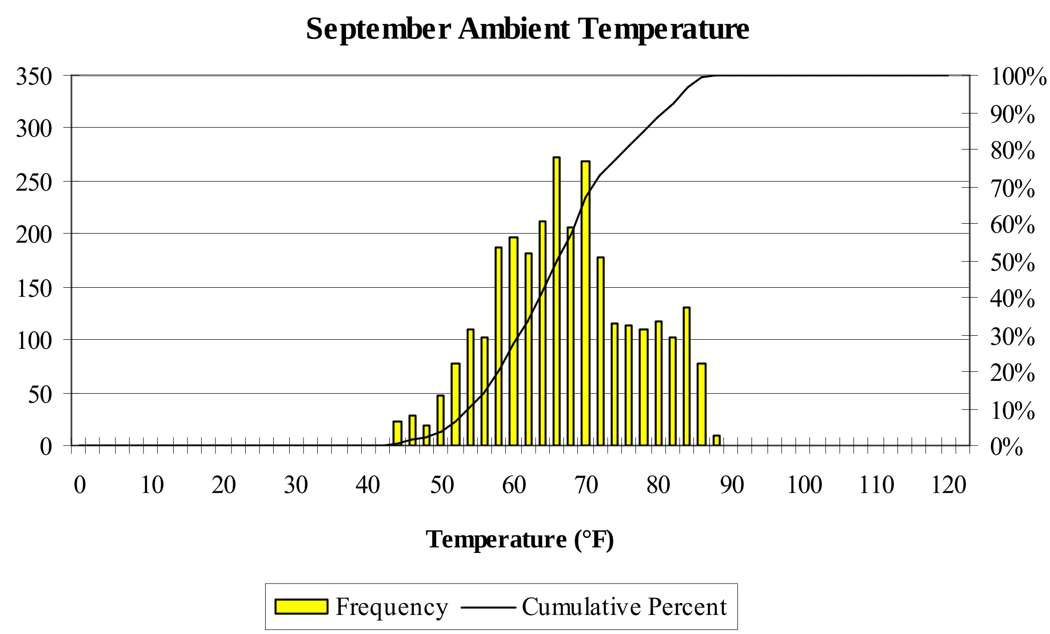

Figure B.1 Ambient temperature distribution during September at the Smart Pavement site.

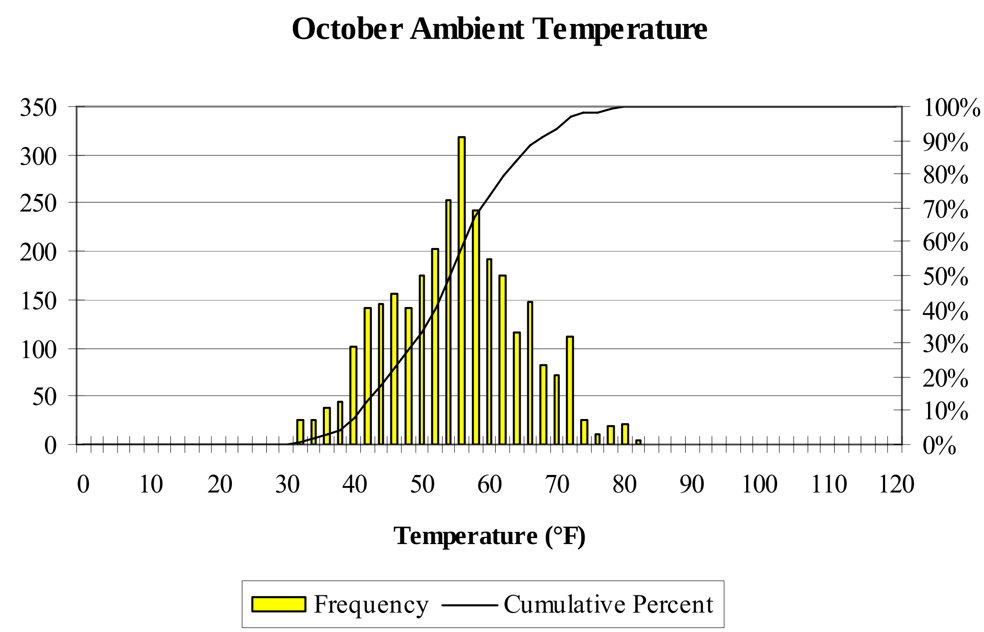

Figure B.2 Ambient temperature distribution during October at the Smart Pavement site.

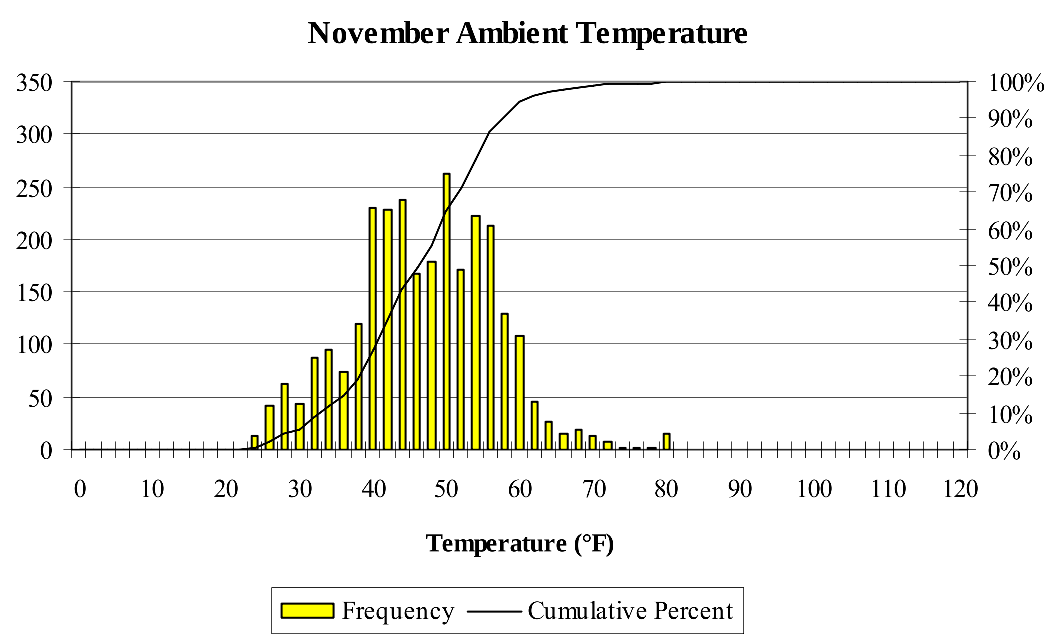

Figure B.3 Ambient temperature distribution during November at the Smart Pavement site.

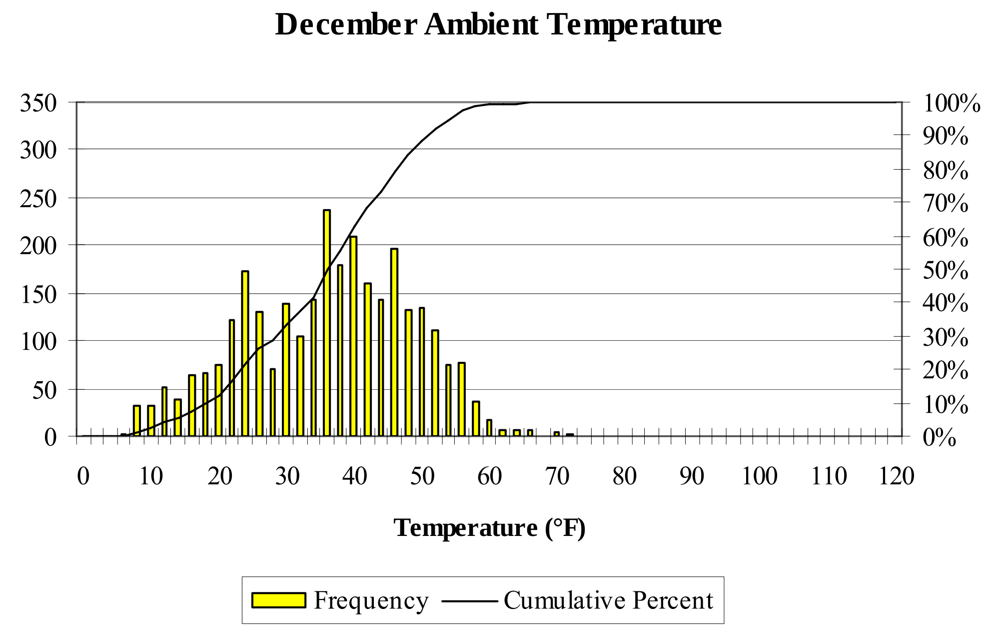

Figure B.4 Ambient temperature distribution during December at the Smart Pavement site.

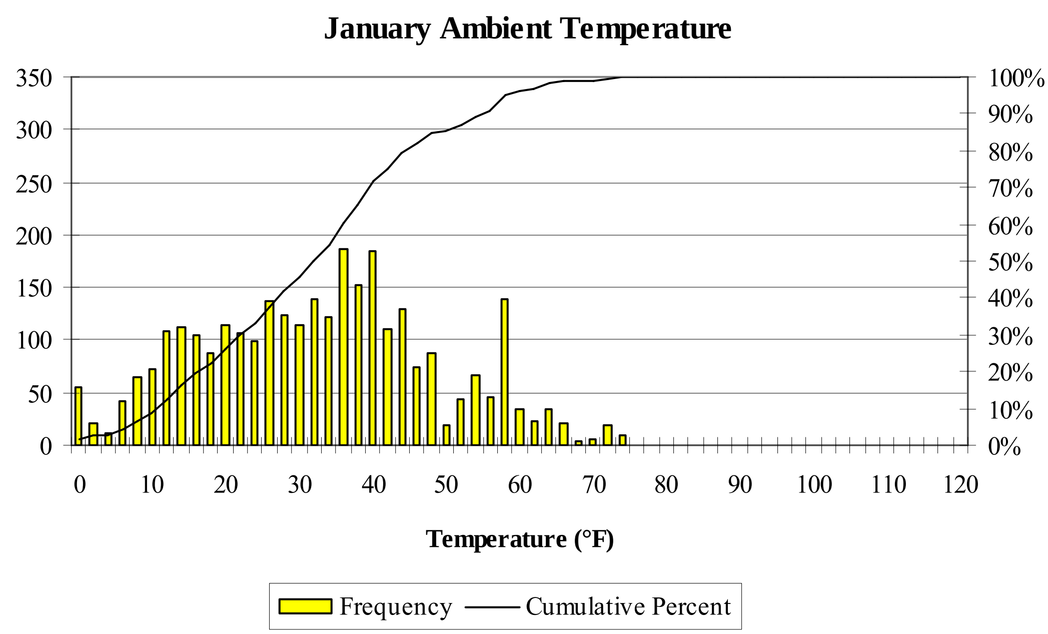

Figure B.5 Ambient temperature distribution during January at the Smart Pavement site.

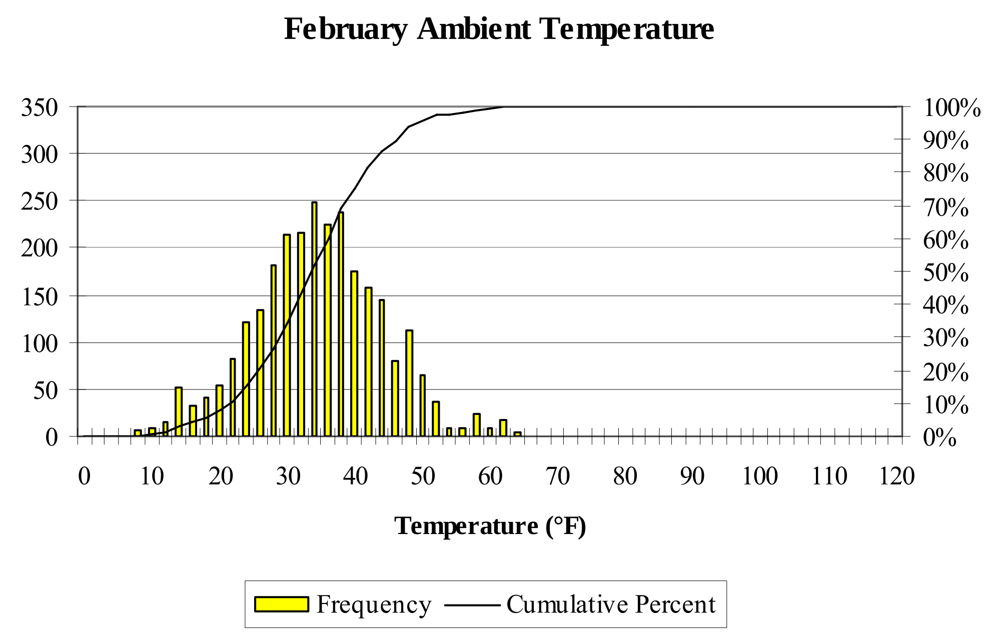

Figure B.6 Ambient temperature distribution during October at the Smart Pavement site.

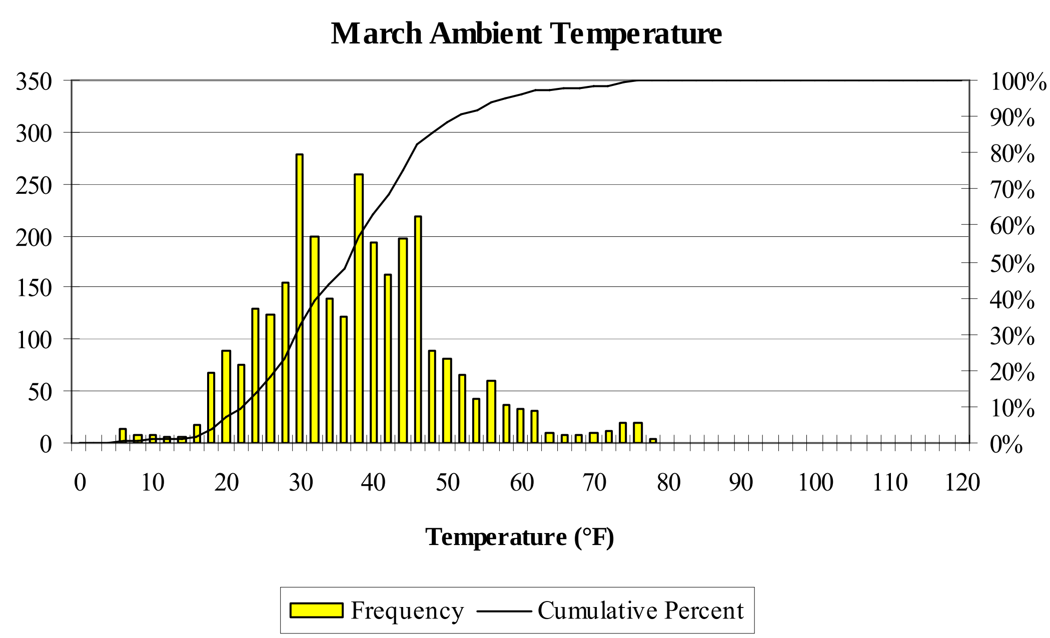

Figure B.7 Ambient temperature distribution during March at the Smart Pavement site.

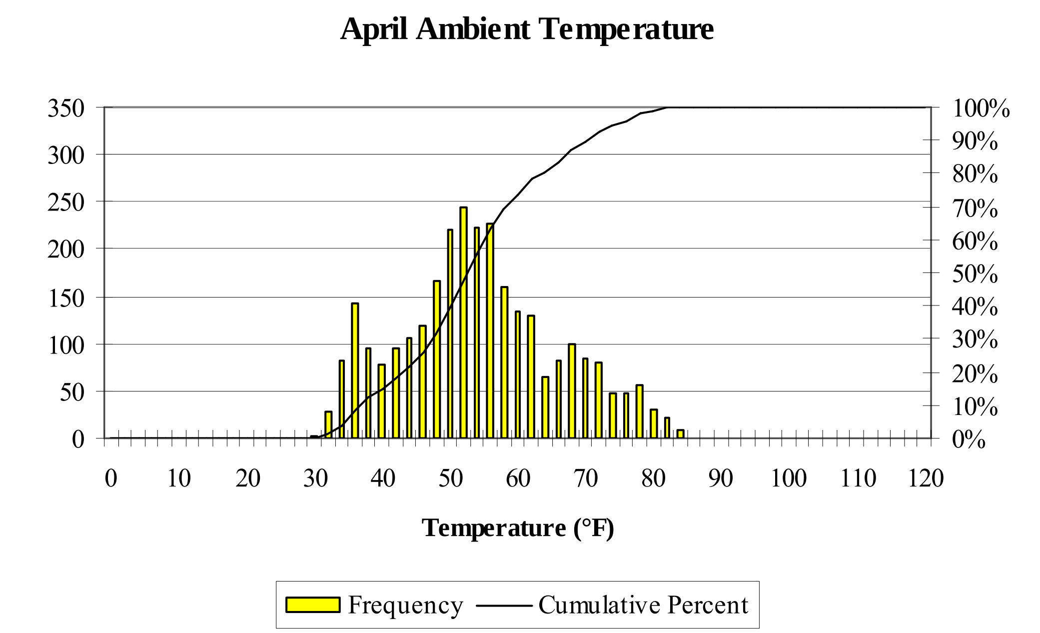

Figure B.8 Ambient temperature distribution during April at the Smart Pavement site.

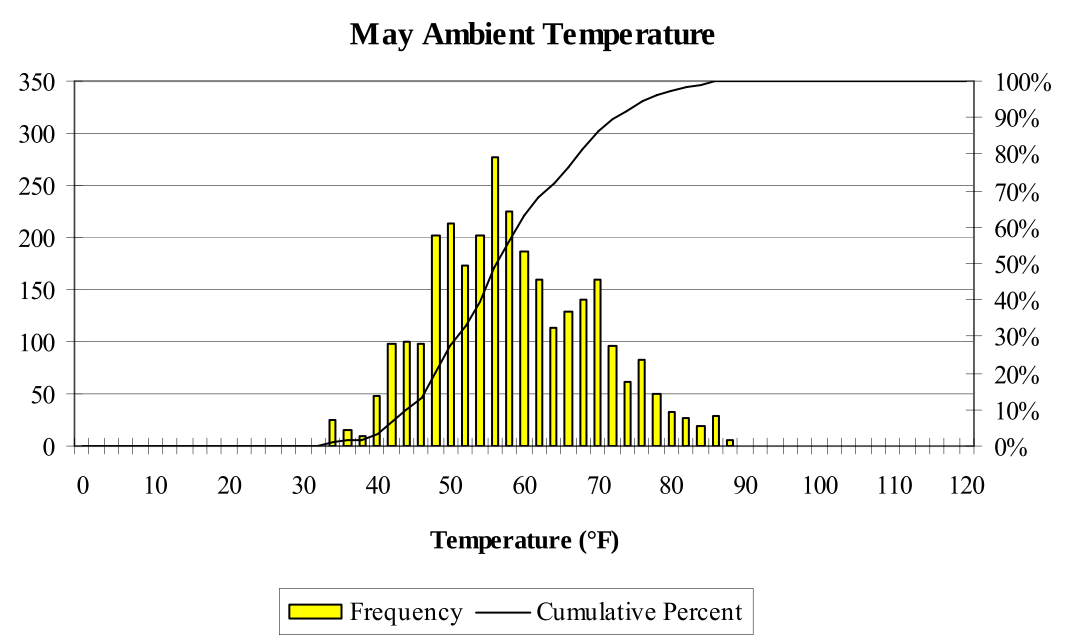

Figure B.9 Ambient temperature distribution during May at the Smart Pavement site.

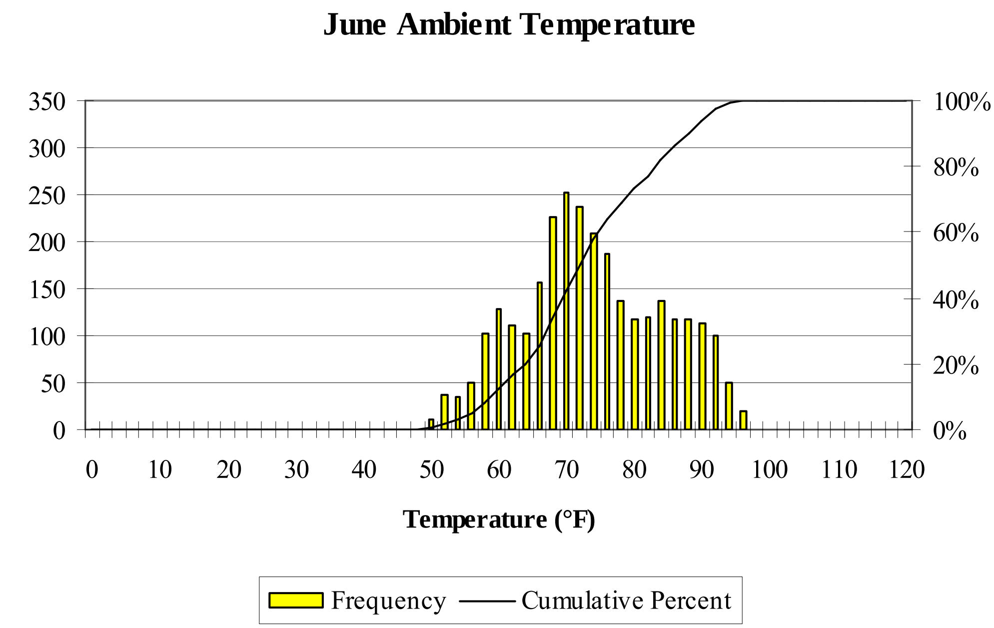

Figure B.10 Ambient temperature distribution during June at the Smart Pavement site.

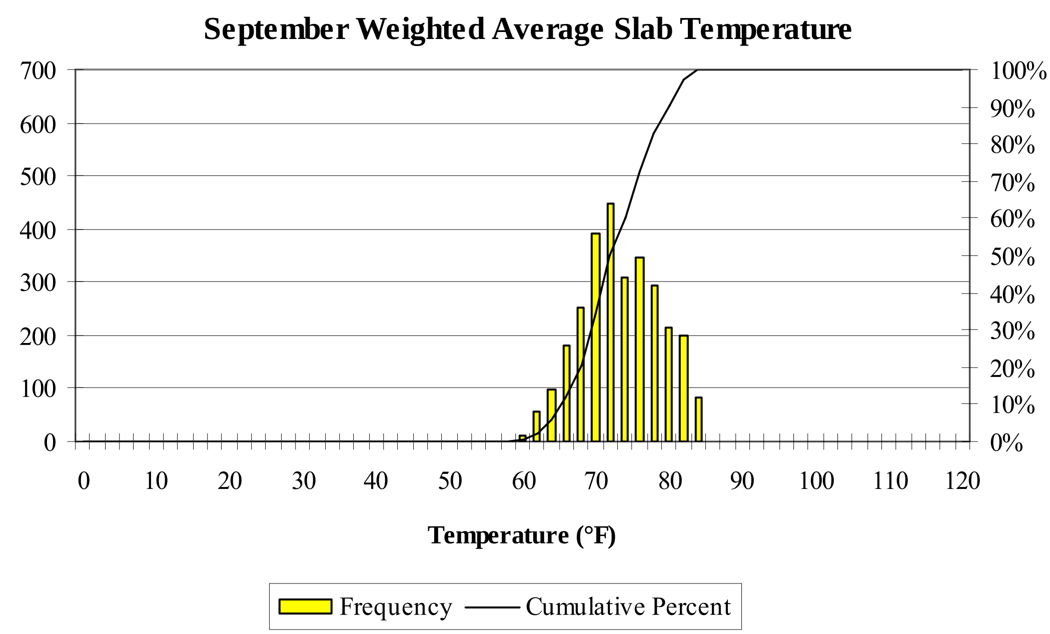

Figure B.11 Weighted average slab temperature during September at the Smart Pavement Site.

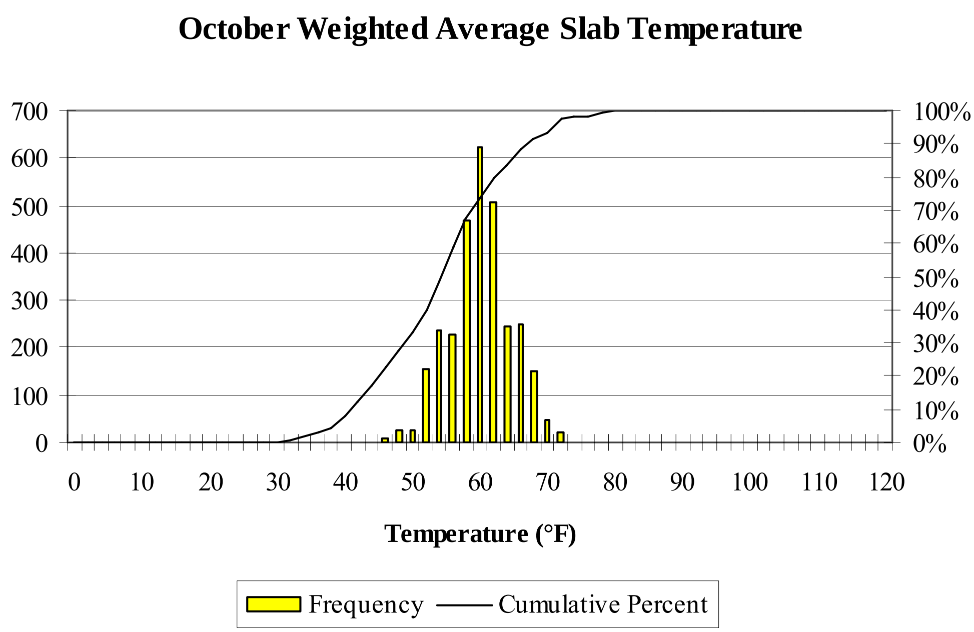

Figure B.12 Weighted average slab temperature during October at the Smart Pavement Site.

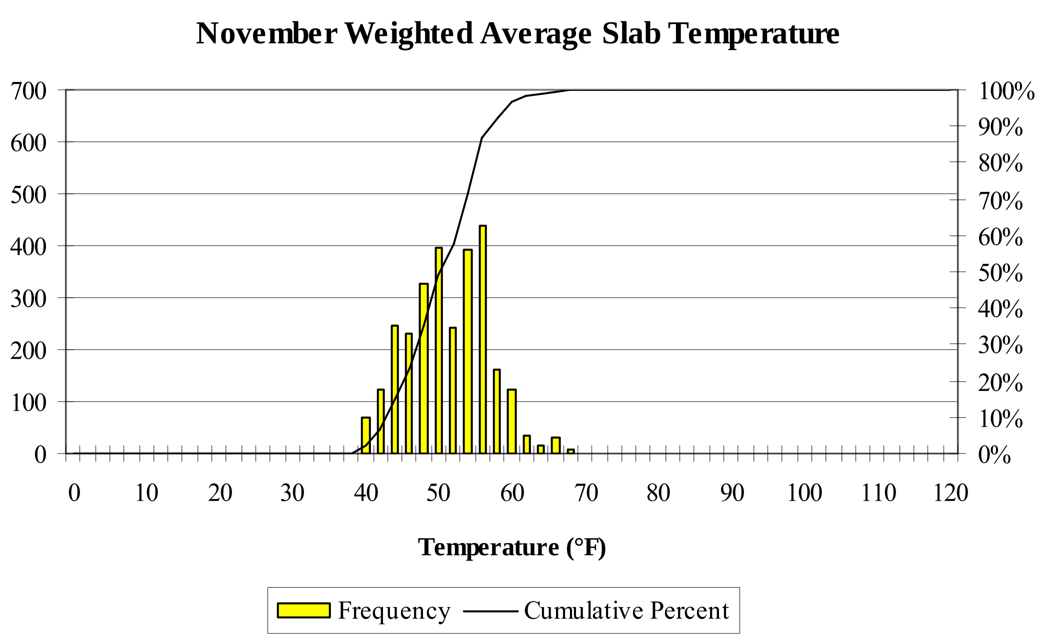

Figure B. 13 Weighted average slab temperature during November at the Smart Pavement Site.

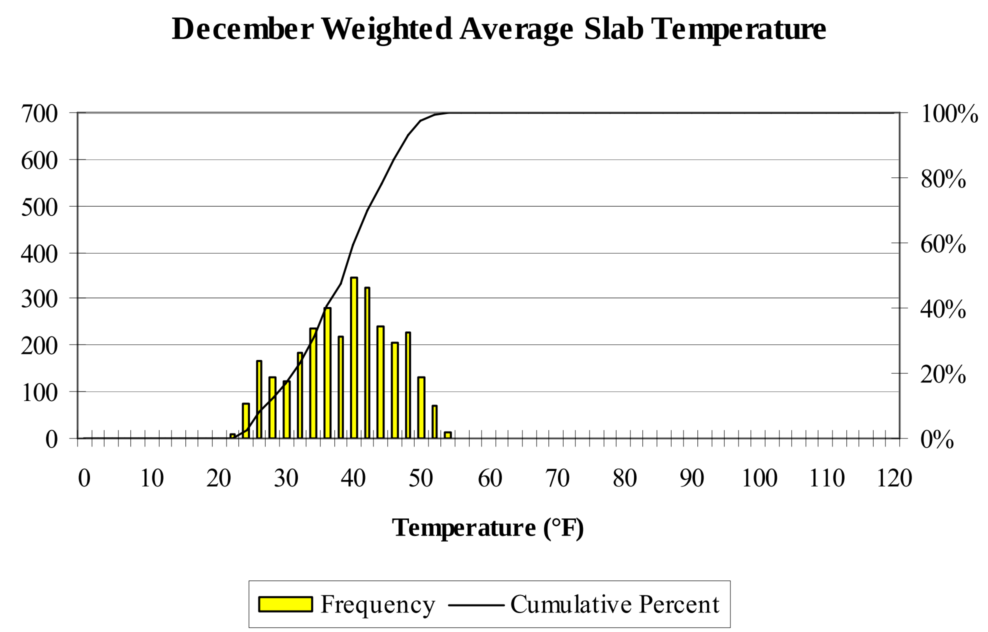

Figure B.14 Weighted average slab temperature during December at the Smart Pavement Site.

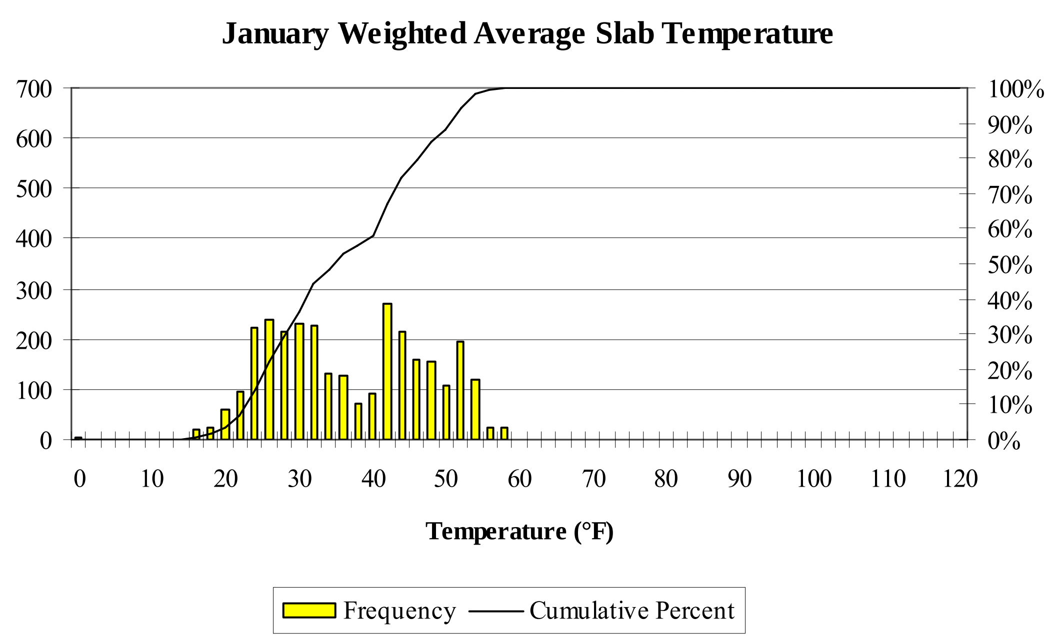

Figure B.15 Weighted average slab temperature during January at the Smart Pavement Site.

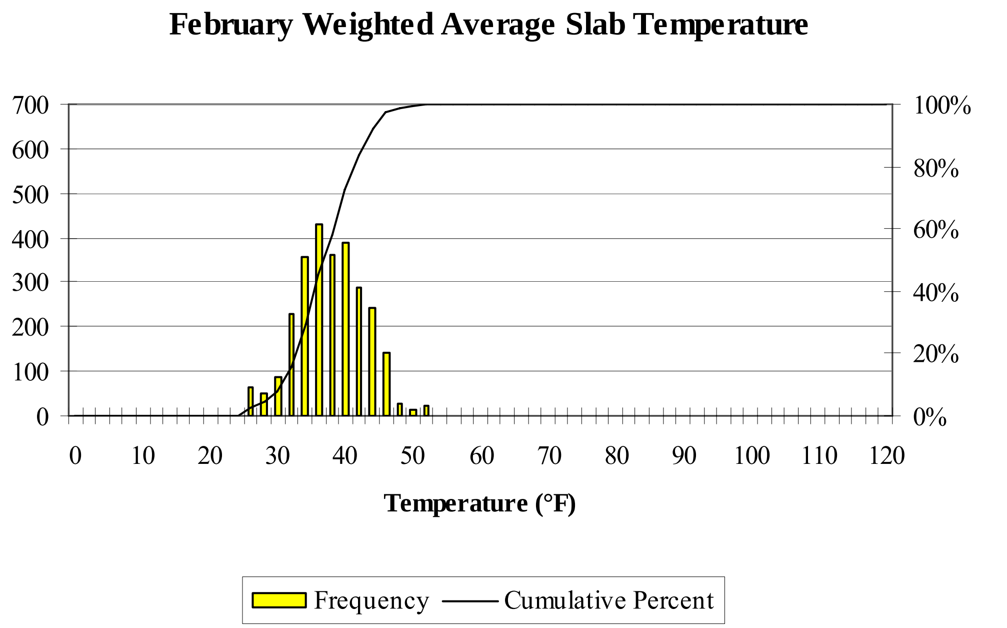

Figure B.16 Weighted average slab temperature during February at the Smart Pavement Site.

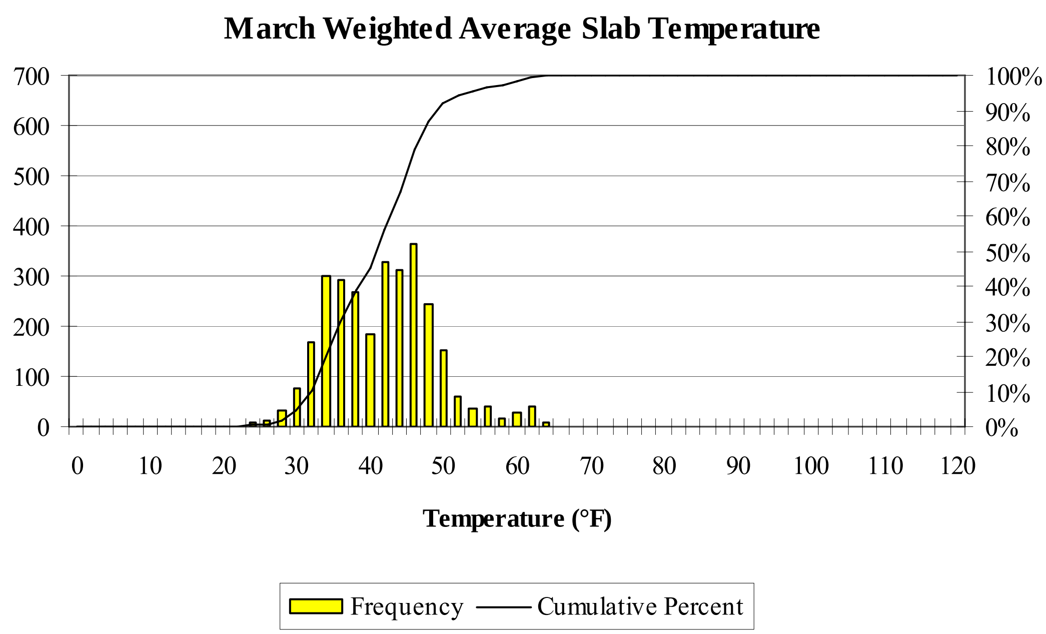

Figure B.17 Weighted average slab temperature during March at the Smart Pavement Site.

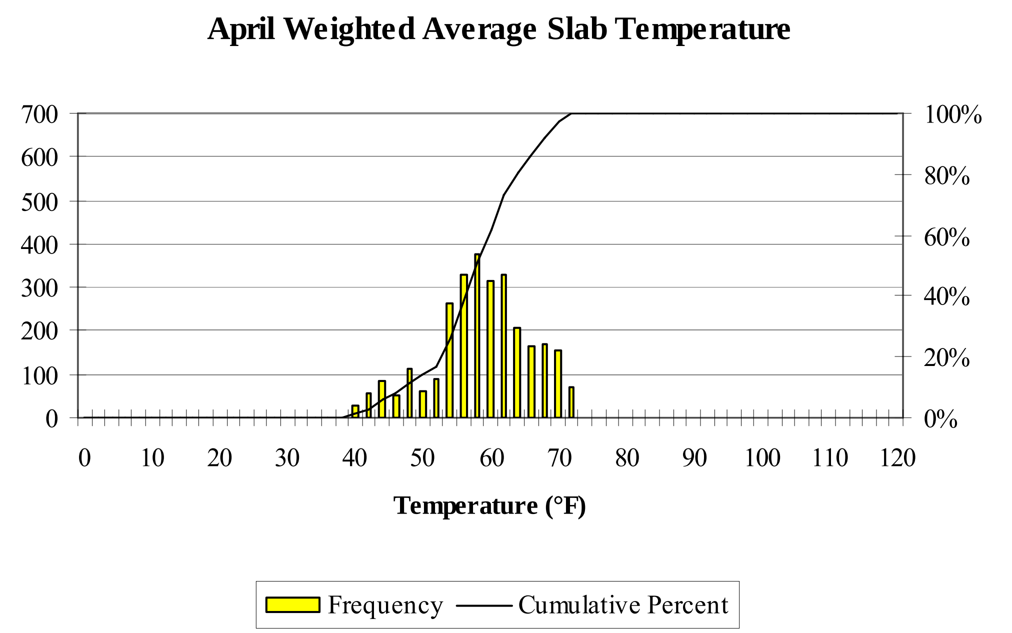

Figure B.18 Weighted average slab temperature during April at the Smart Pavement Site.

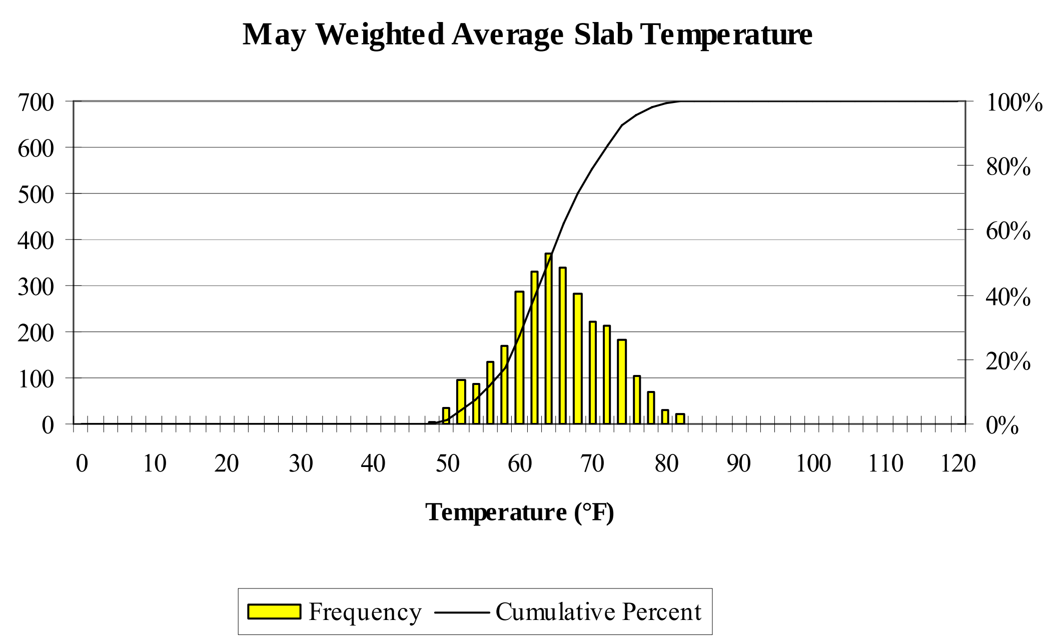

Figure B.19 Weighted average slab temperature during May at the Smart Pavement Site.

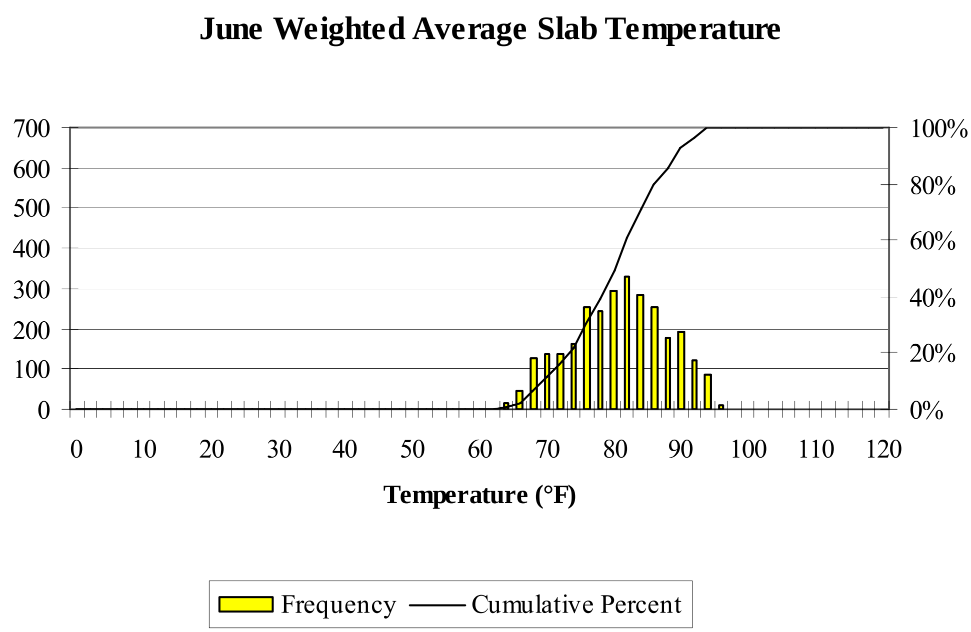

Figure B.20 Weighted average slab temperature during June at the Smart Pavement Site.

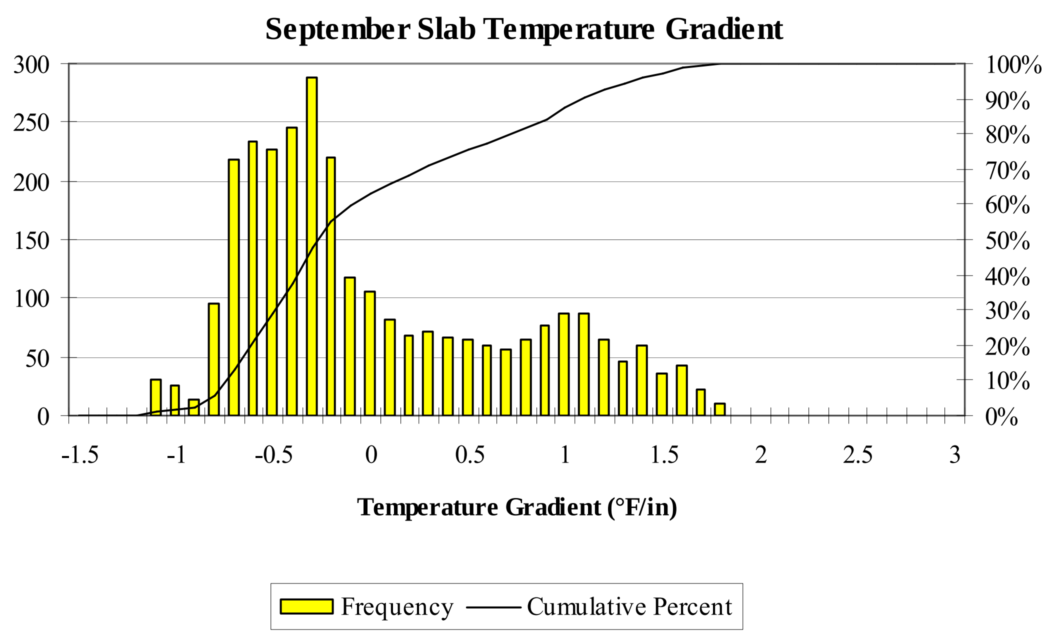

Figure B.21 Temperature gradient frequency distribution during September at the Smart Pavement Site.

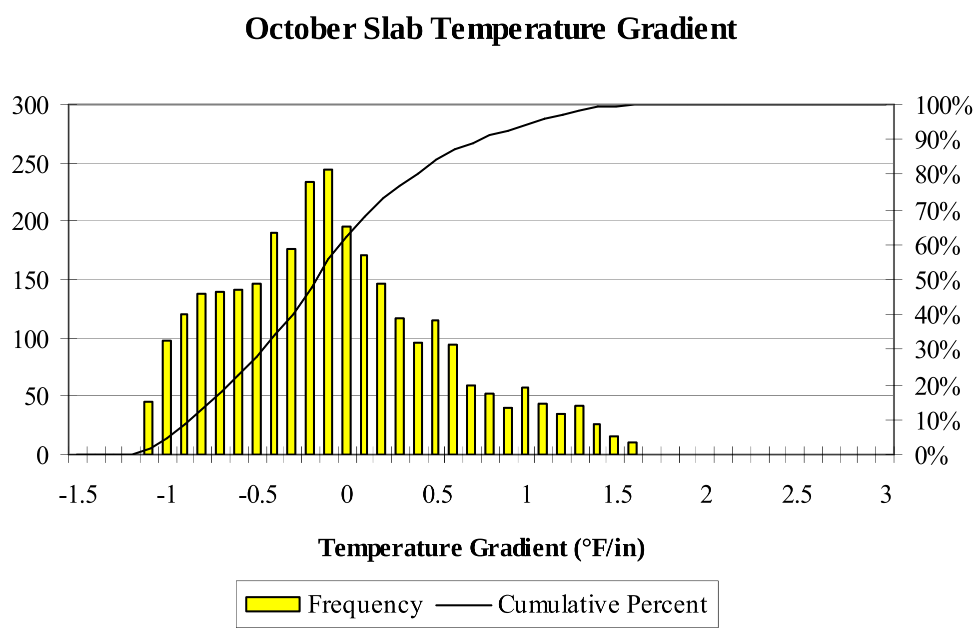

Figure B.22 Temperature gradient frequency distribution during October at the Smart Pavement Site.

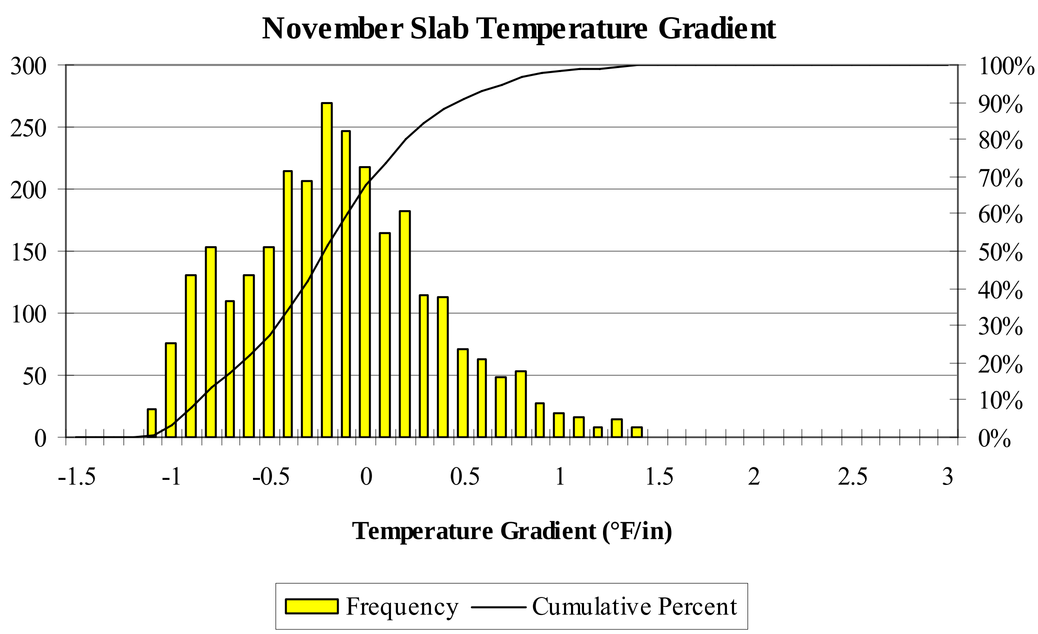

Figure B.23 Temperature gradient frequency distribution during November at the Smart Pavement Site.

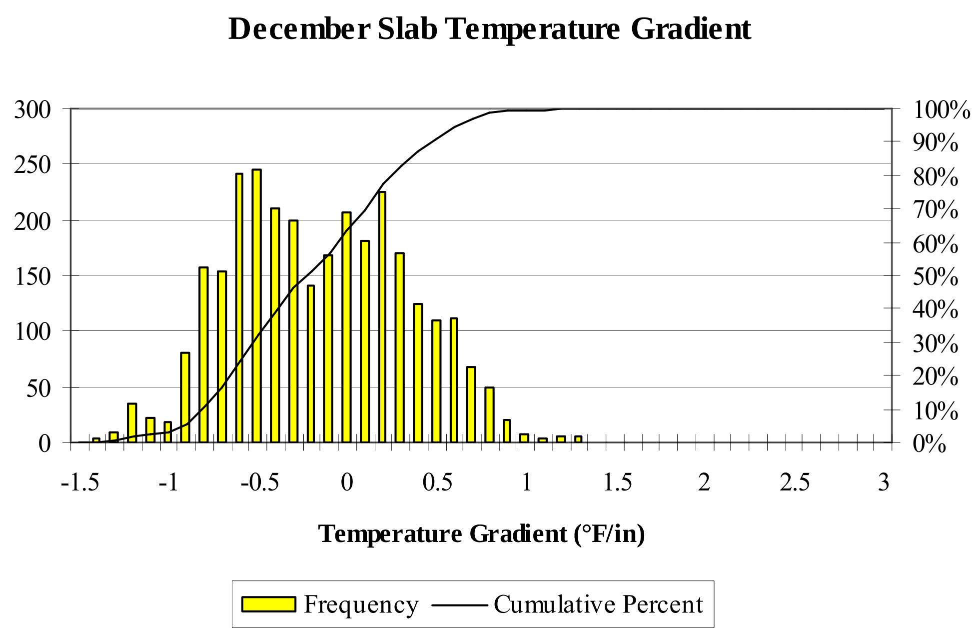

Figure B.24 Temperature gradient frequency distribution during December at the Smart Pavement Site.

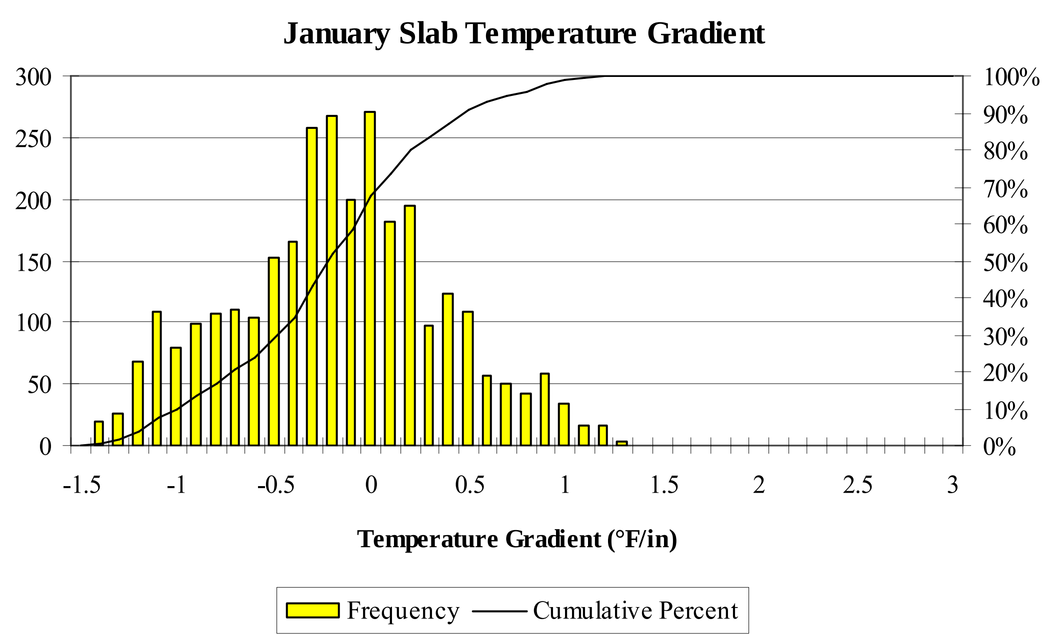

Figure B.25 Temperature gradient frequency distribution during January at the Smart Pavement Site.

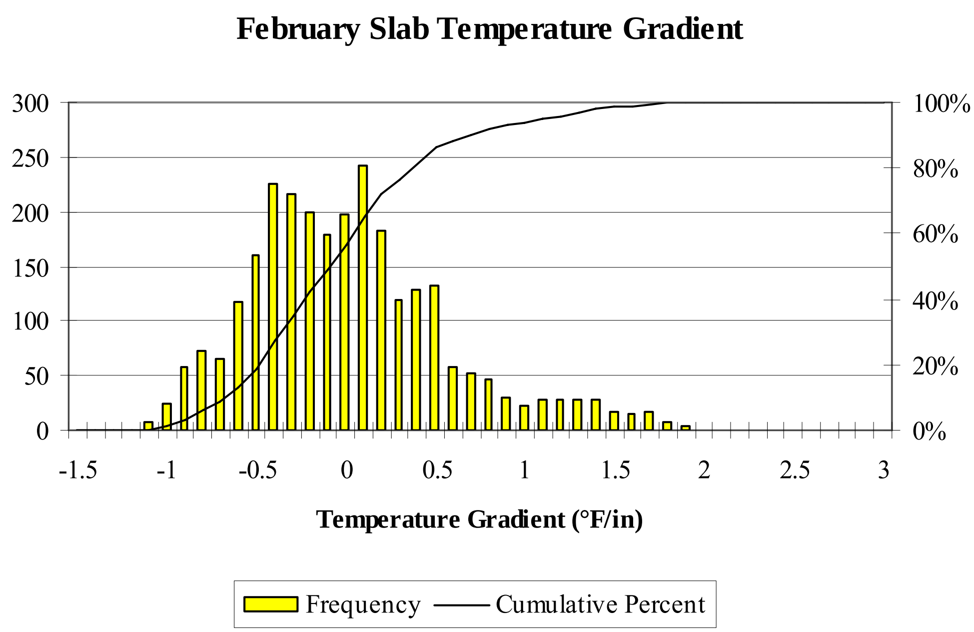

Figure B.26 Temperature gradient frequency distribution during February at the Smart Pavement Site.

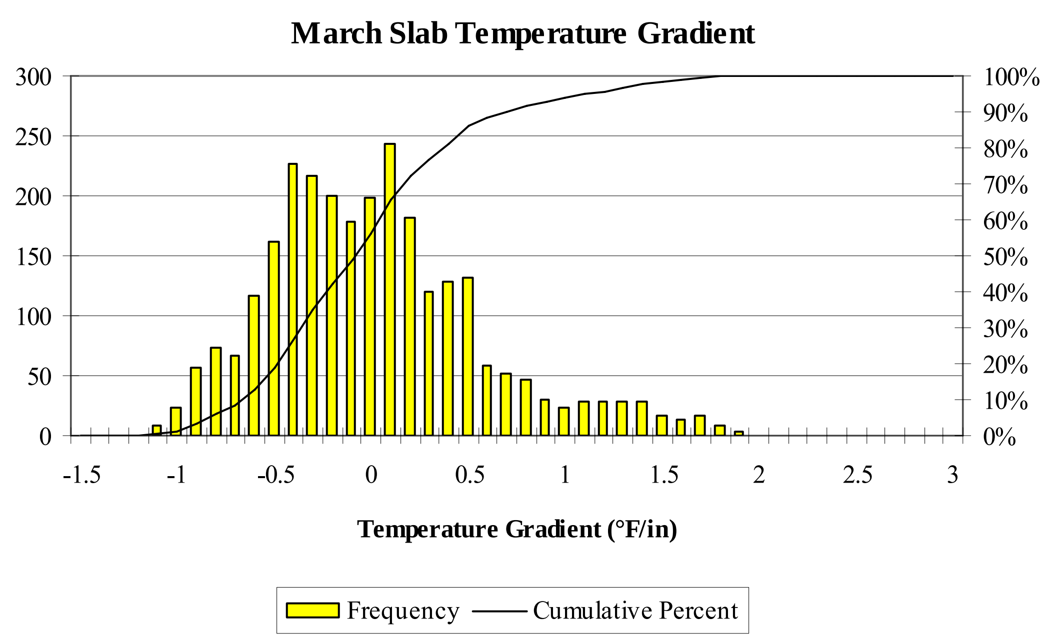

Figure B.27 Temperature gradient frequency distribution during March at the Smart Pavement Site.

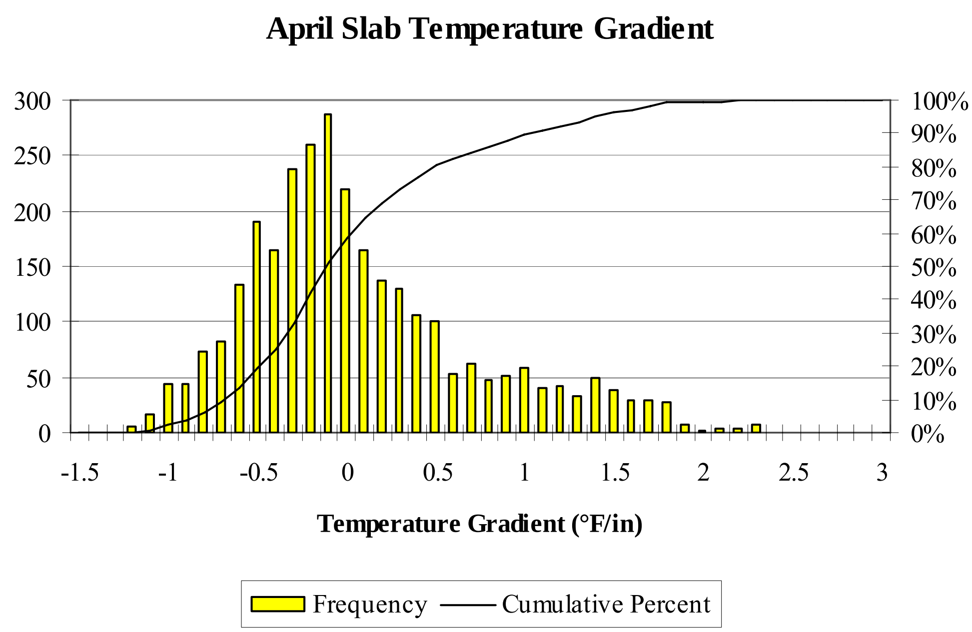

Figure B.28 Temperature gradient frequency distribution during April at the Smart Pavement Site.

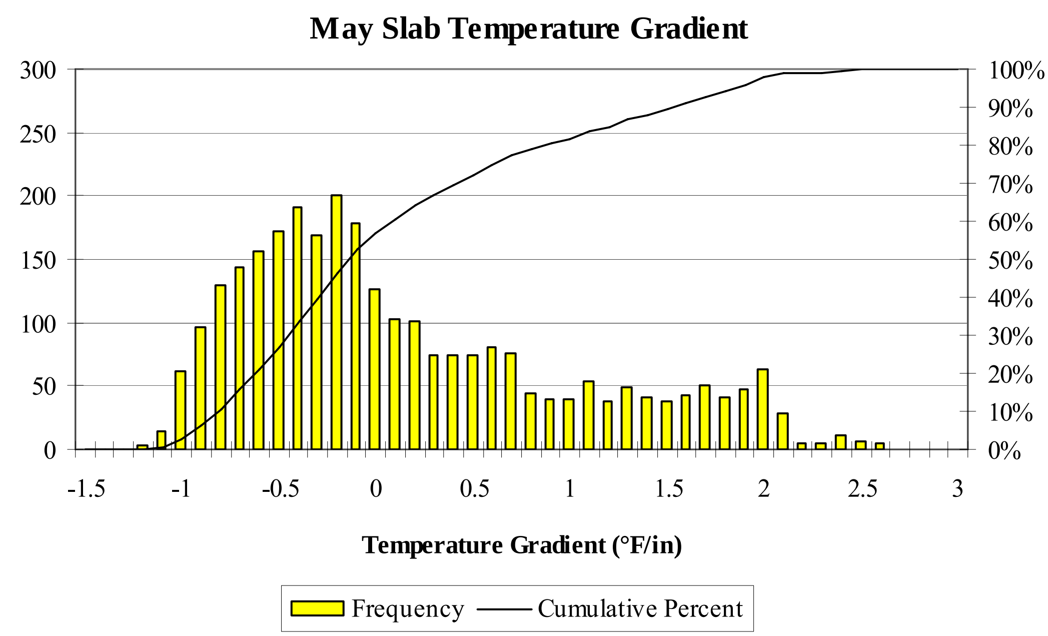

Figure B.29 Temperature gradient frequency distribution during May at the Smart Pavement Site.

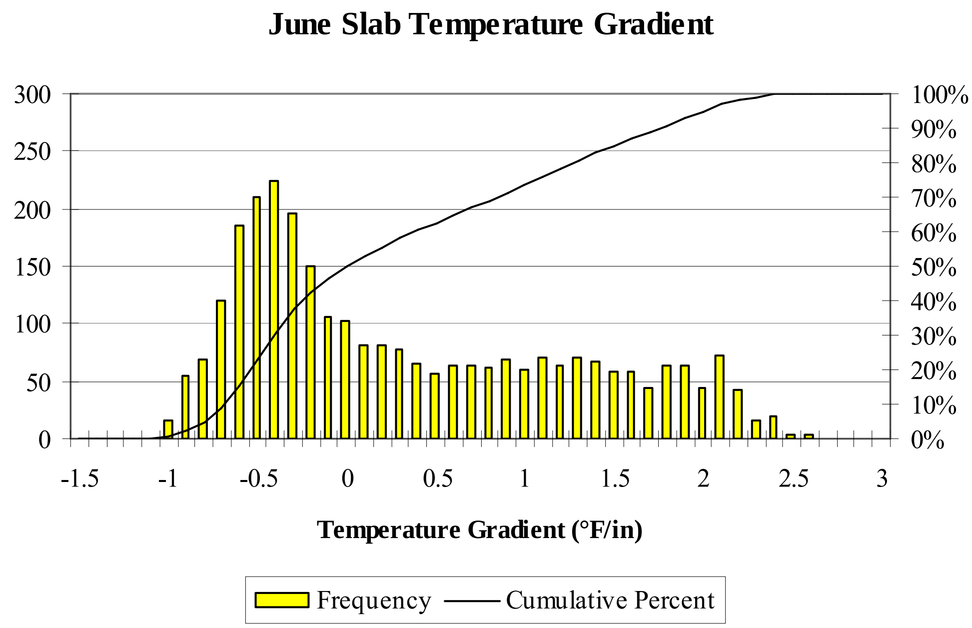

Figure B.30 Temperature gradient frequency distribution during June at the Smart Pavement Site.

APPENDIX C

SEASONAL STRAIN FOR RESTRAINED AND UNRESTRAINED SLABS

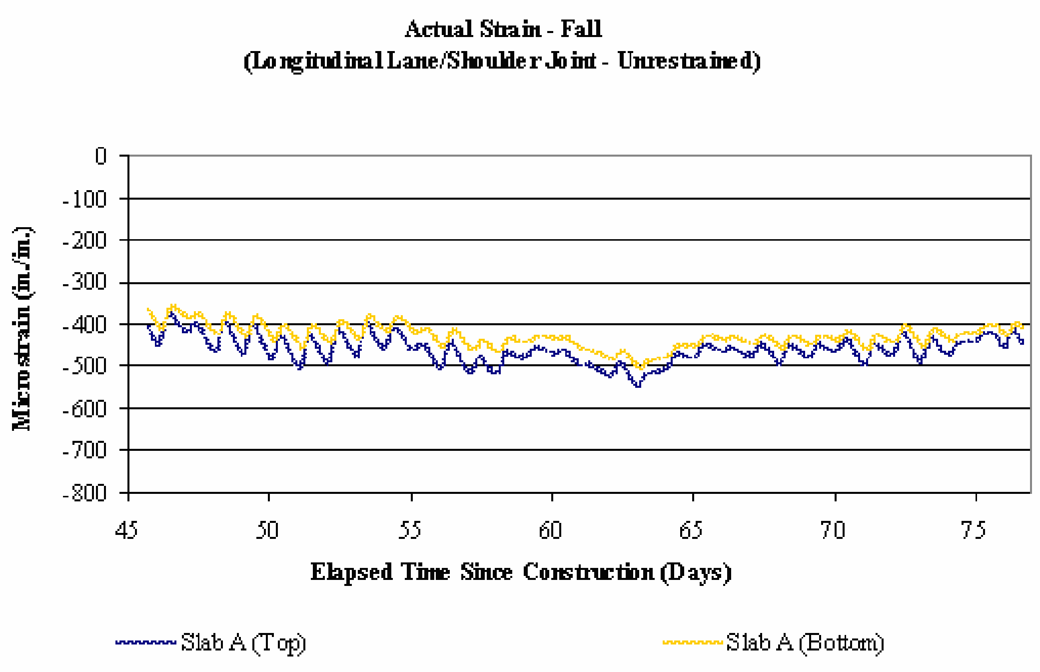

Figure C.1 Strain 1 in from the top and 1 in from the bottom of an unrestrained slab measured near the lane/shoulder joint in the fall.

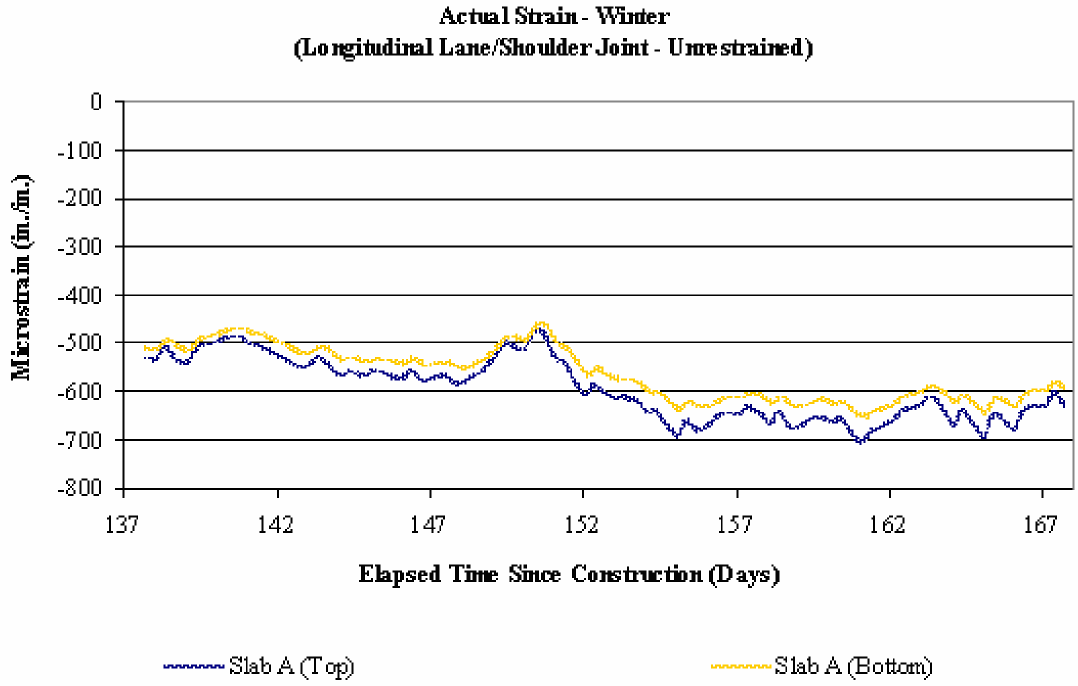

Figure C.2 Strain 1 in from the top and 1 in from the bottom of an unrestrained slab measured near the lane/shoulder joint in the winter.

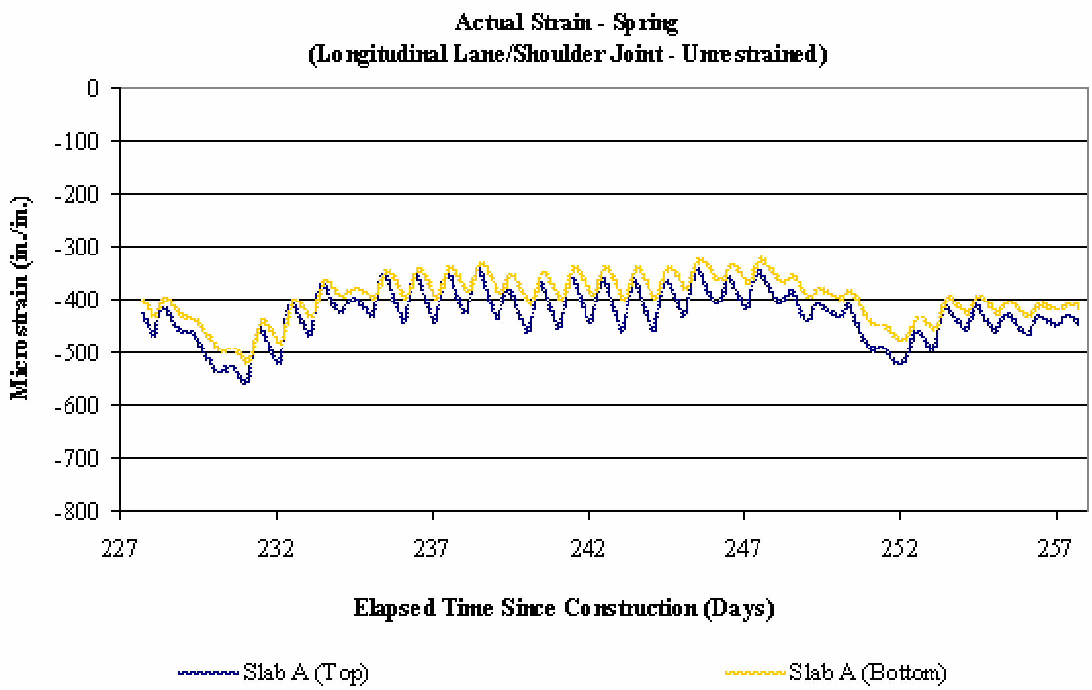

Figure C.3 Strain 1 in from the top and 1 in from the bottom of an unrestrained slab measured near the lane/shoulder joint in the spring.

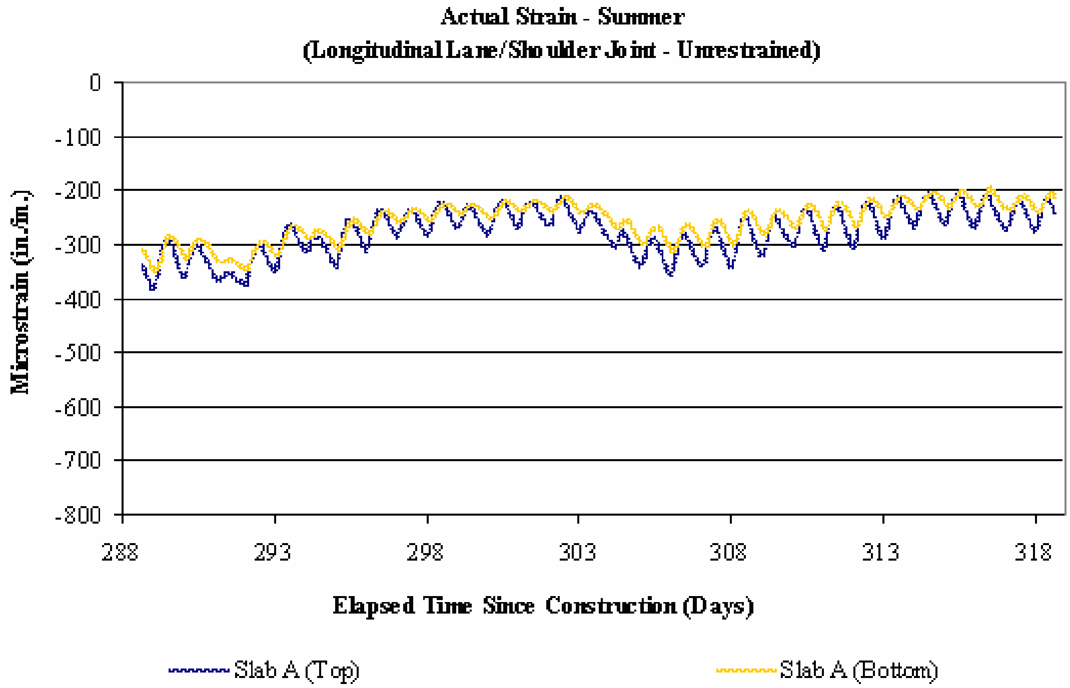

Figure C.4 Strain 1 in from the top and 1 in from the bottom of an unrestrained slab measured near the lane/shoulder joint in the summer.

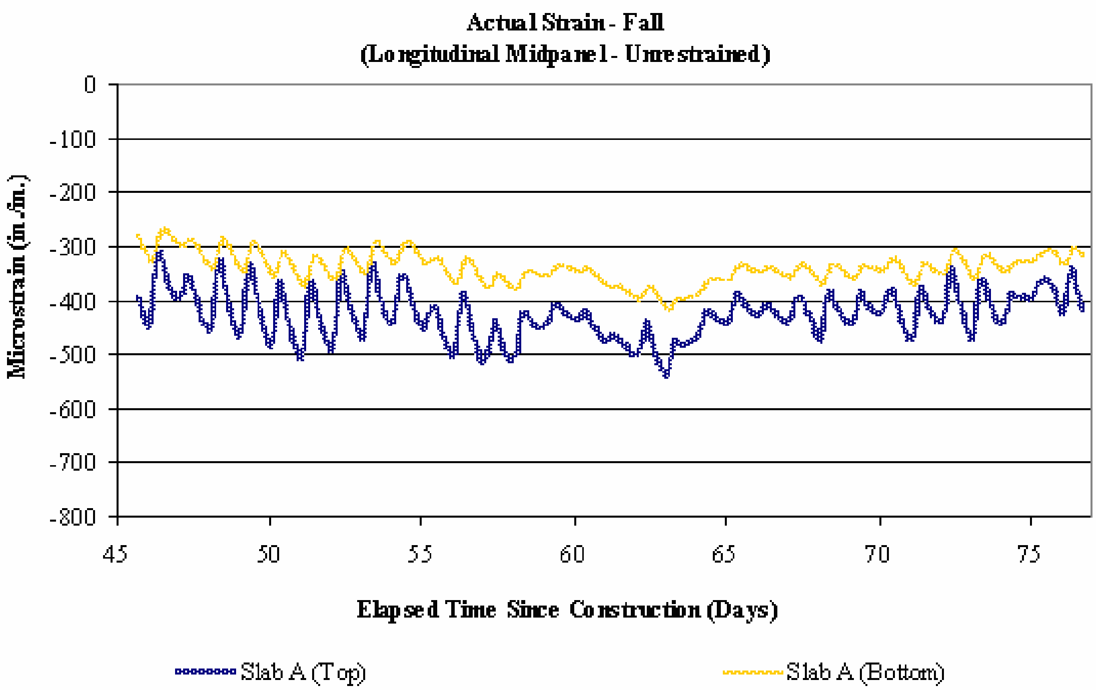

Figure C.5 Strain 1 in from the top and 1 in from the bottom of an unrestrained slab measured near midpanel in the fall.

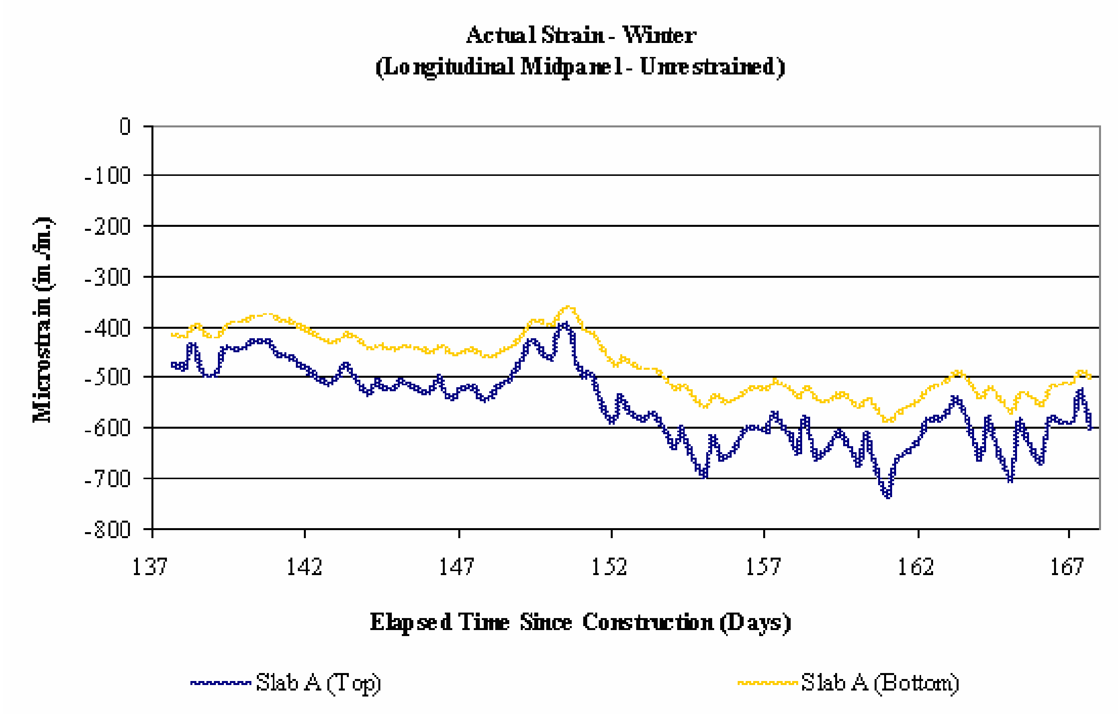

Figure C.6 Strain 1 in from the top and 1 in from the bottom of an unrestrained slab measured near midpanel in the winter.

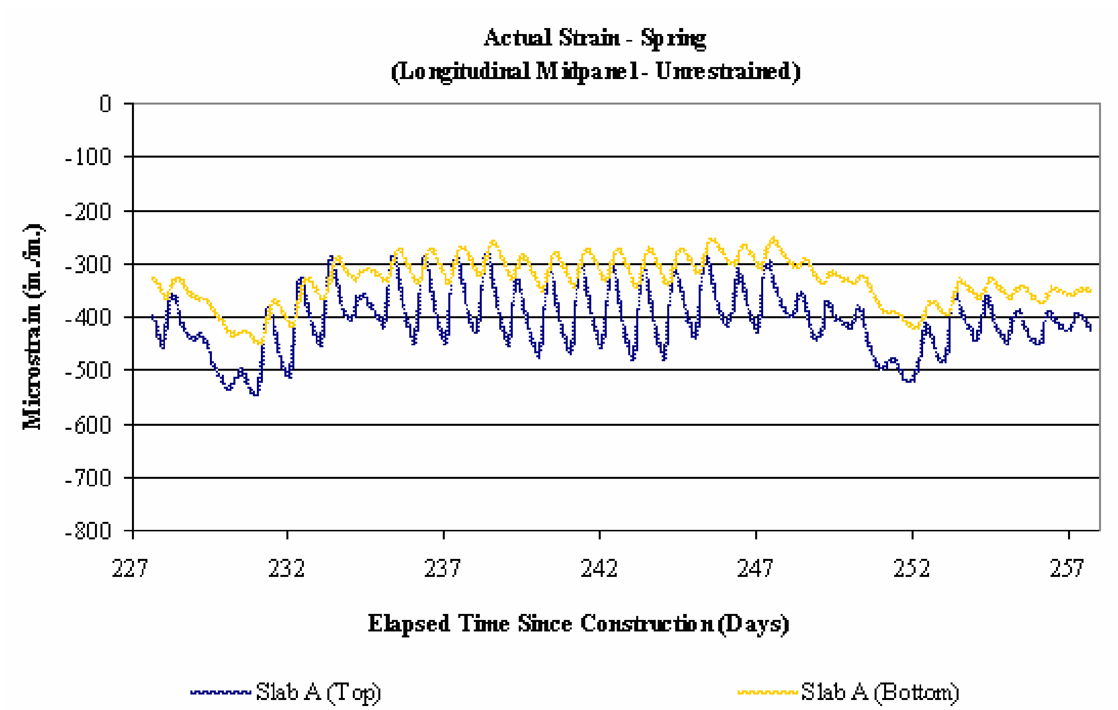

Figure C.7 Strain 1 in from the top and 1 in from the bottom of an unrestrained slab measured near midpanel in the spring.

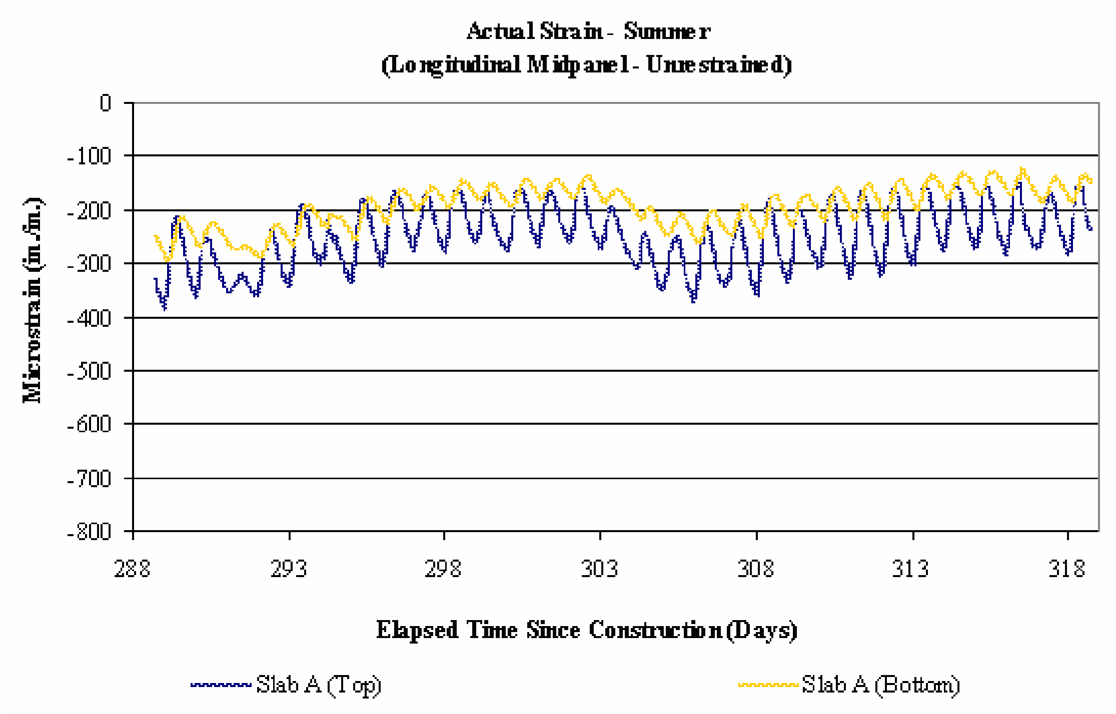

Figure C.8 Strain 1 in from the top and 1 in from the bottom of an unrestrained slab measured near midpanel in the summer.

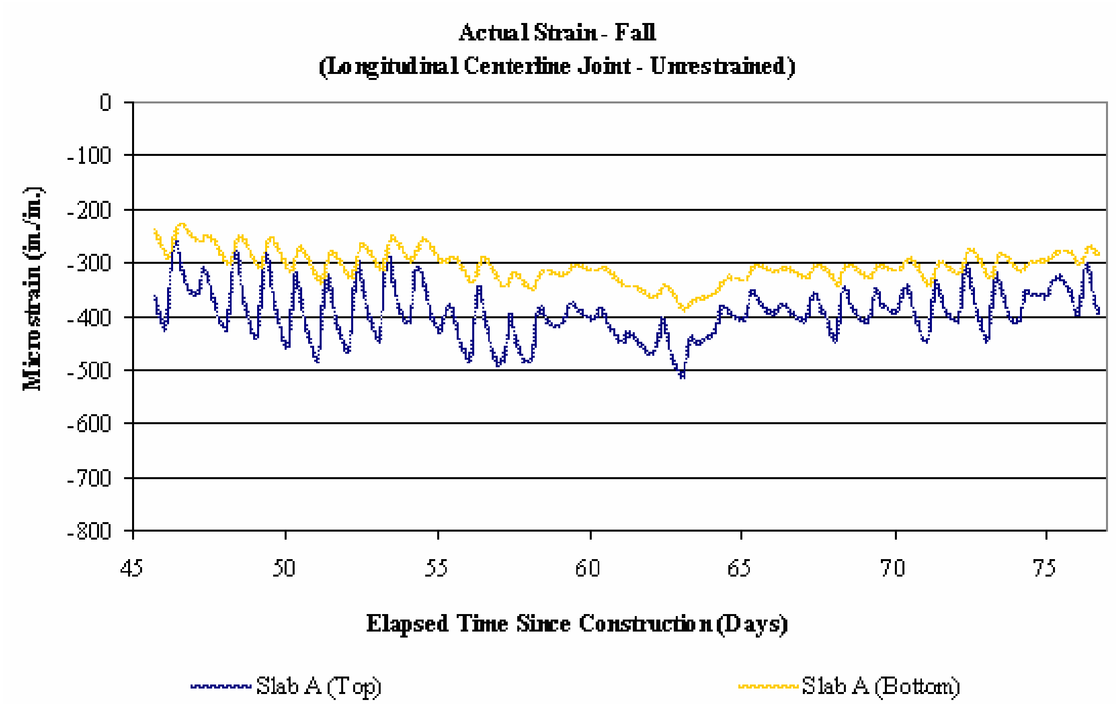

Figure C.9 Strain 1 in from the top and 1 in from the bottom of an unrestrained slab measured near the centerline joint in the fall.

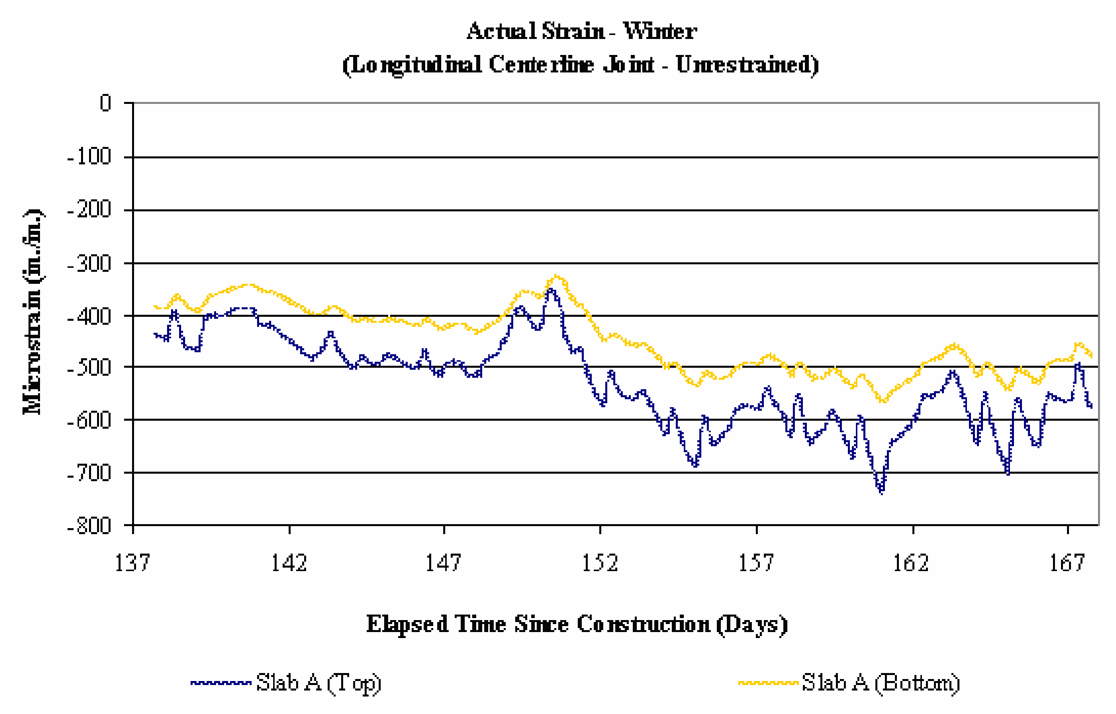

Figure C.10 Strain 1 in from the top and 1 in from the bottom of an unrestrained slab measured near the centerline joint in the winter.

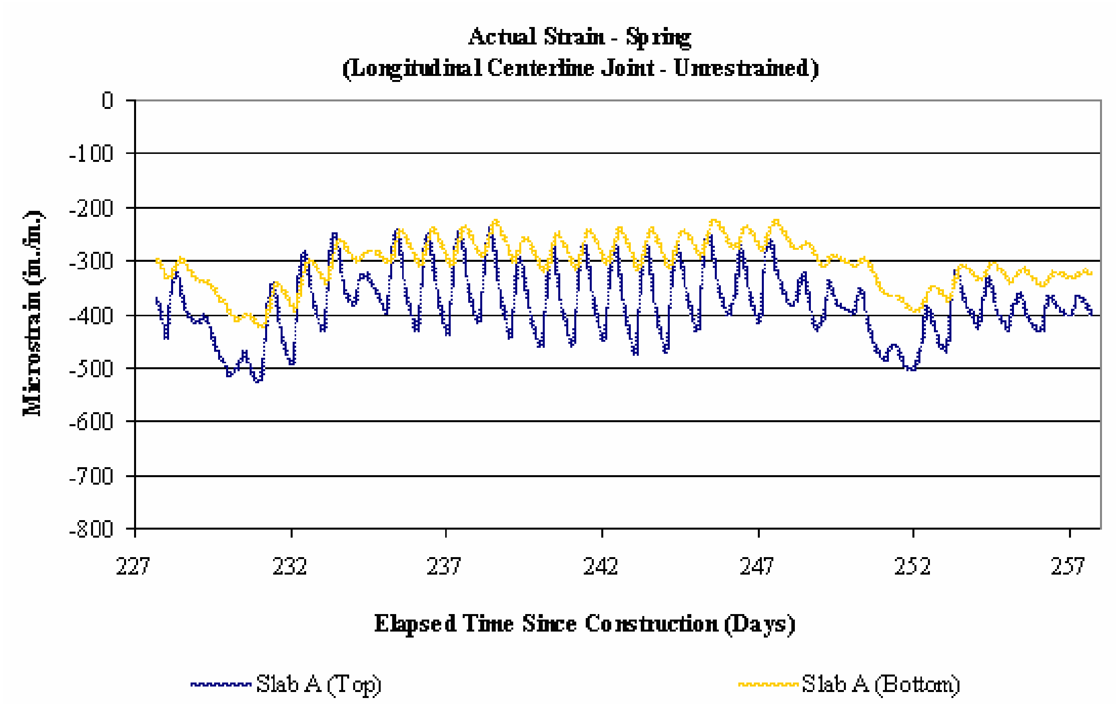

Figure C.11 Strain 1 in from the top and 1 in from the bottom of an unrestrained slab measured near the centerline joint in the spring.

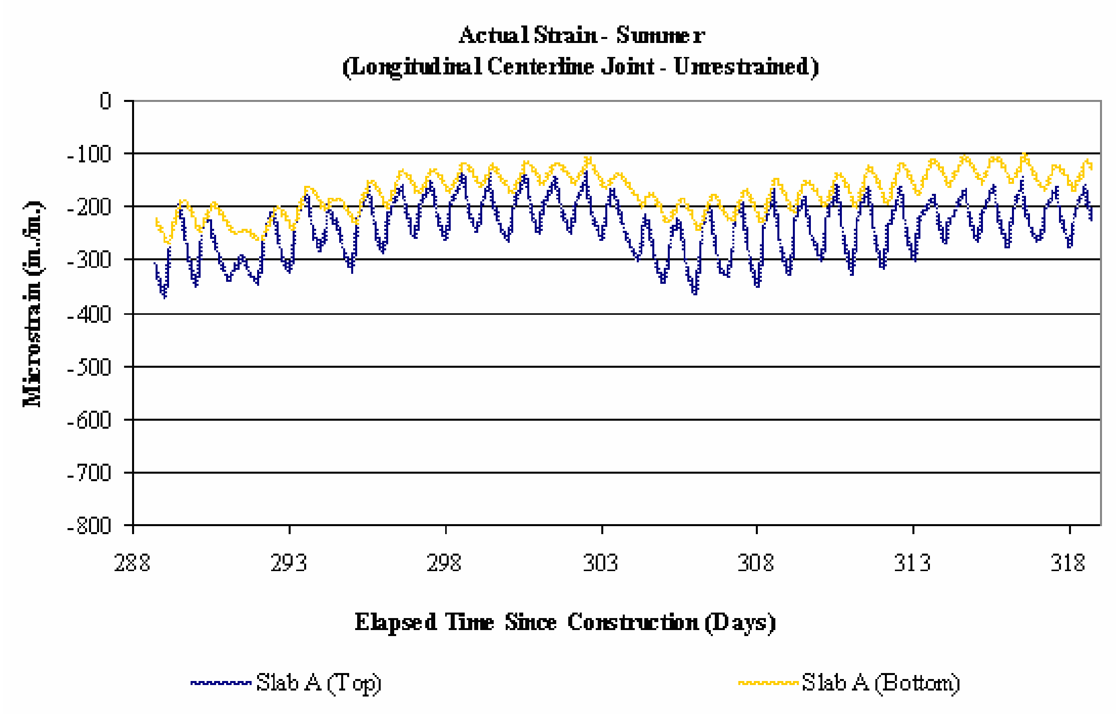

Figure C.12 Strain 1 in from the top and 1 in from the bottom of an unrestrained slab measured near the centerline joint in the summer.

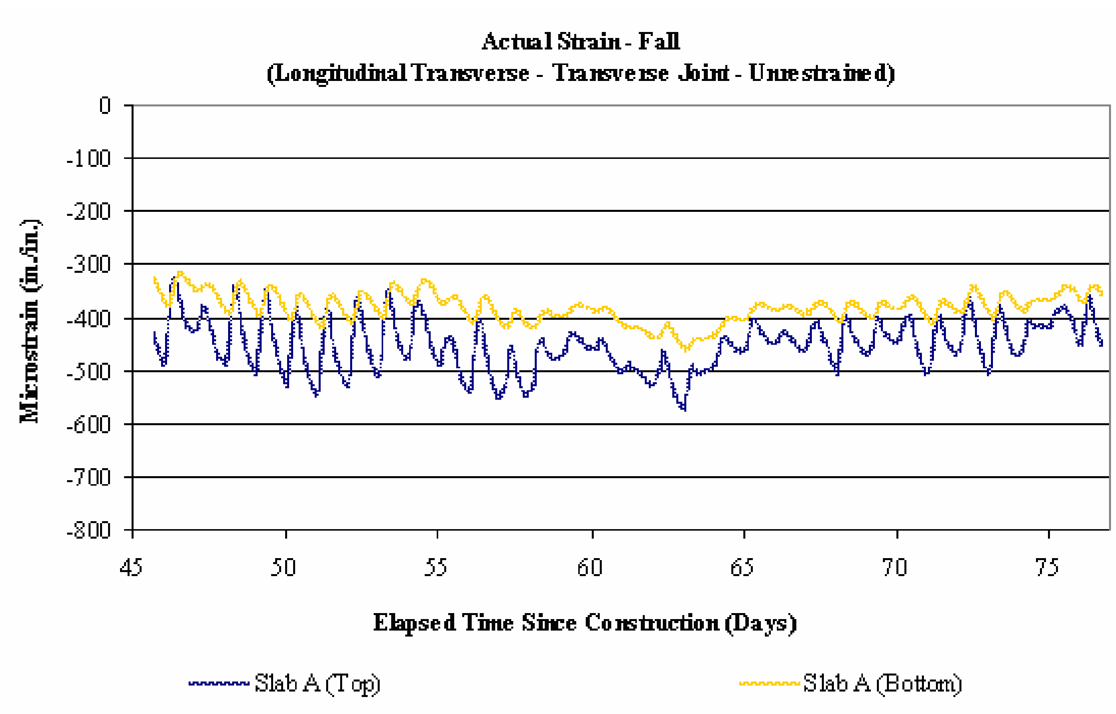

Figure C.13 Strain 1 in from the top and 1 in from the bottom of an unrestrained slab measured near the transverse joint in the fall.

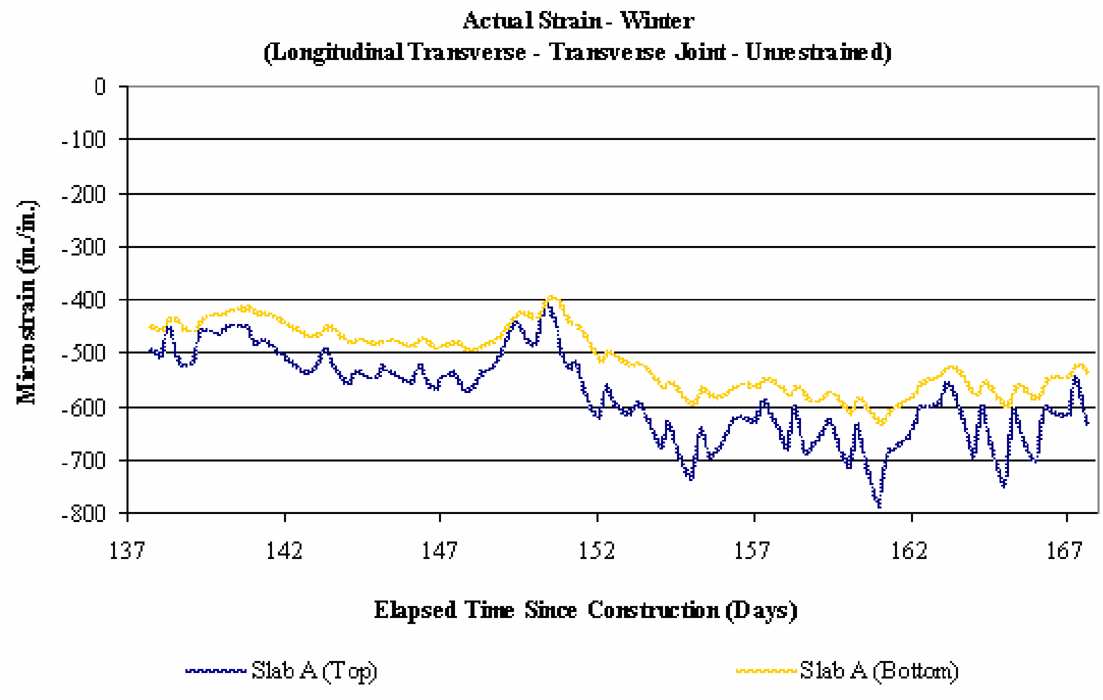

Figure C.14 Strain 1 in from the top and 1 in from the bottom of an unrestrained slab measured near the transverse joint in the winter.

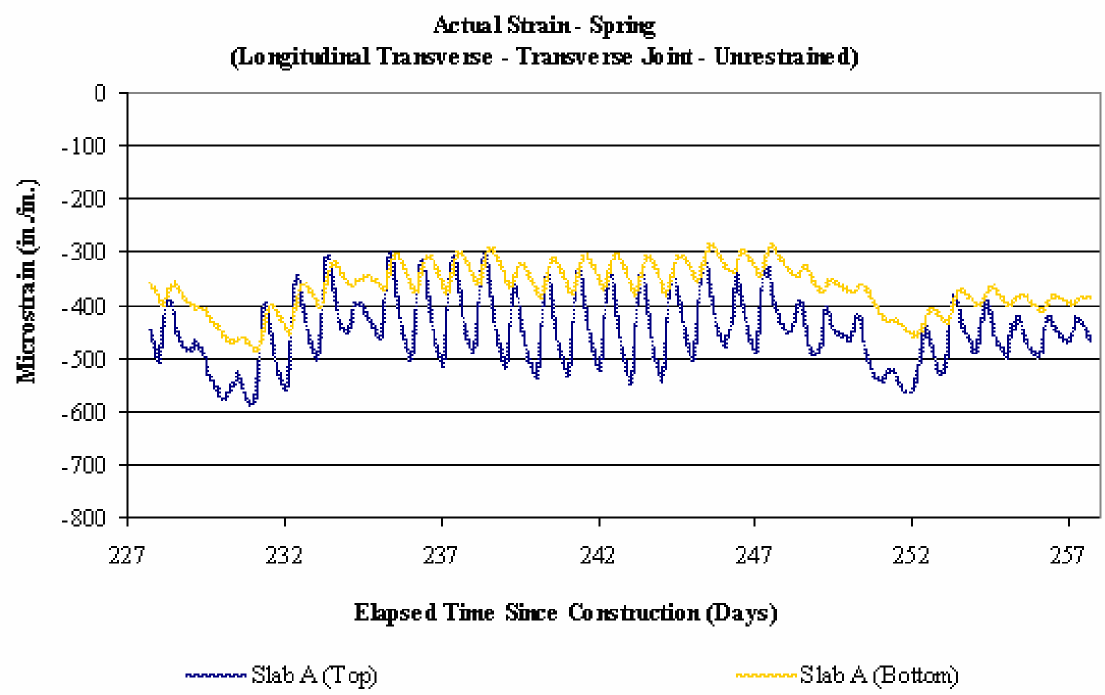

Figure C.15 Strain 1 in from the top and 1 in from the bottom of an unrestrained slab measured near the transverse joint in the spring.

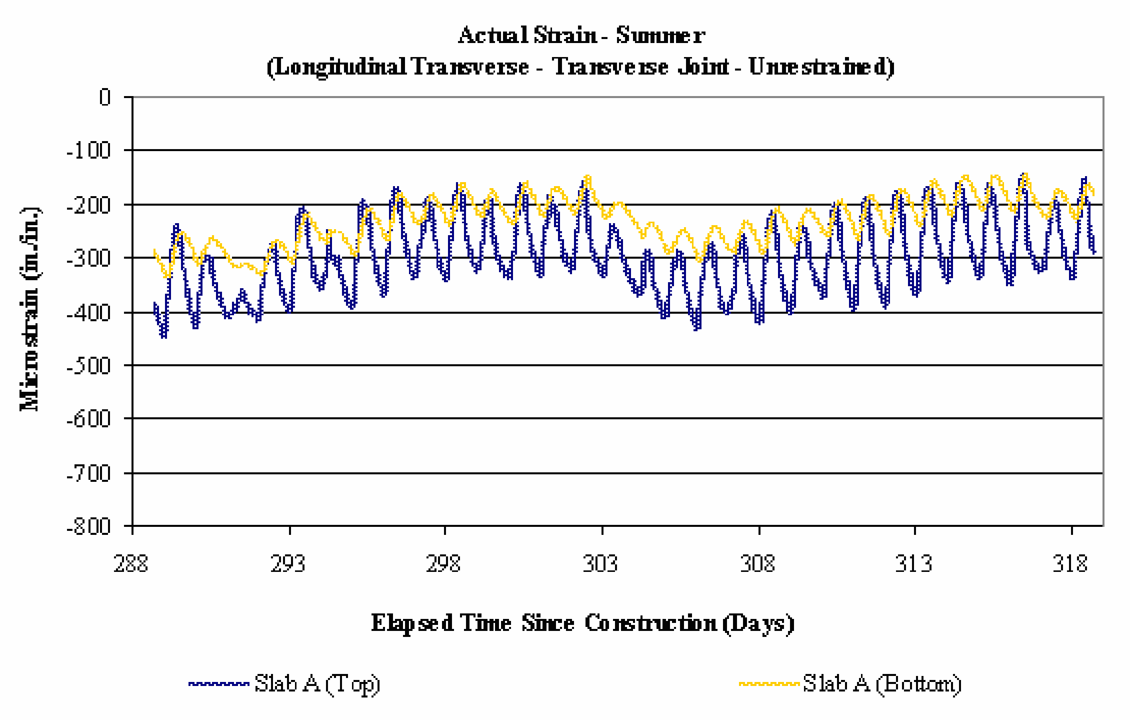

Figure C.16 Strain 1 in from the top and 1 in from the bottom of an unrestrained slab measured near the transverse joint in the summer.

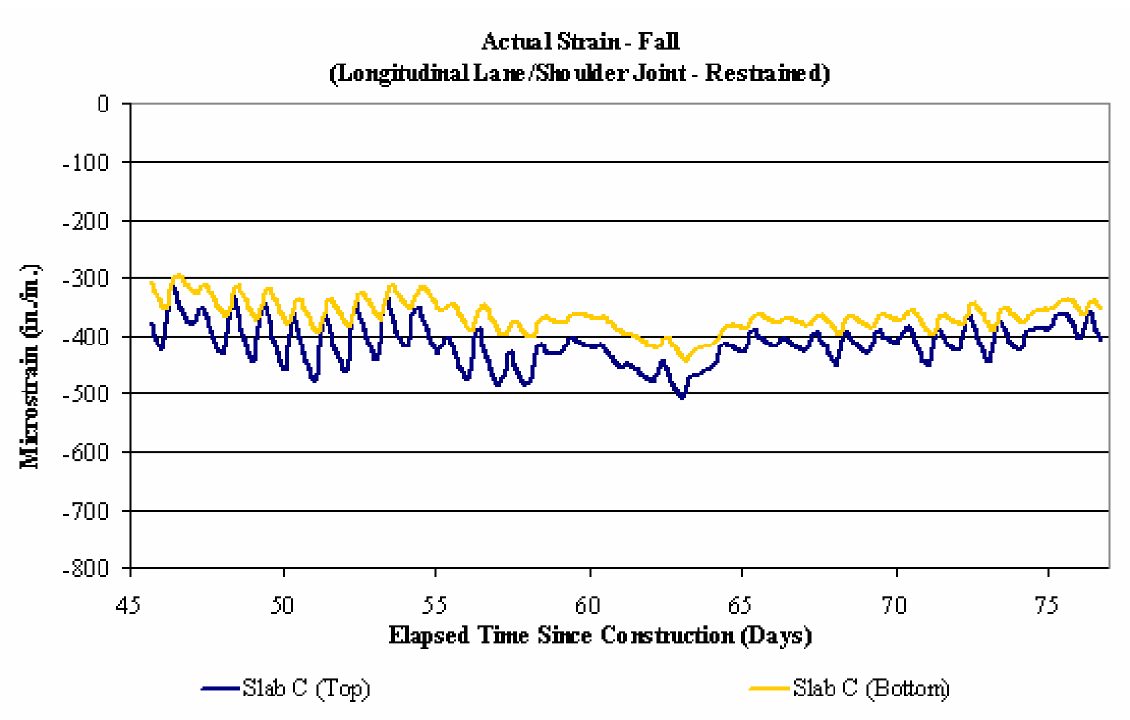

Figure C.17 Strain 1 in from the top and 1 in from the bottom of an unrestrained slab measured near the lane/shoulder joint in the fall.

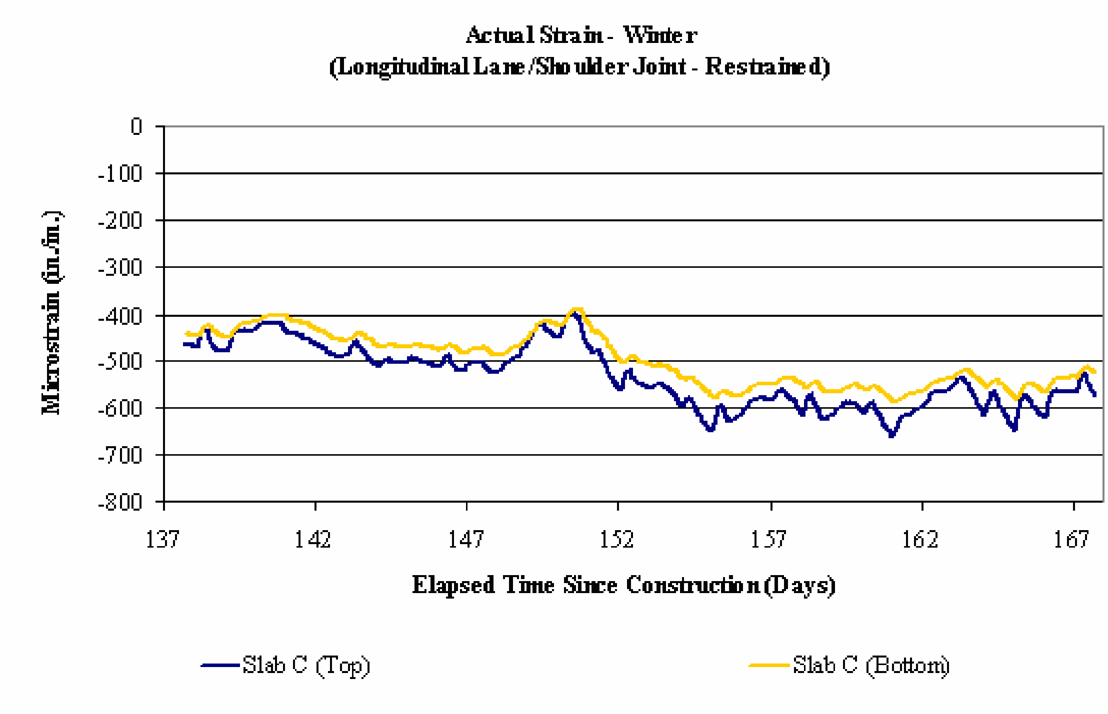

Figure C.18 Strain 1 in from the top and 1 in from the bottom of an unrestrained slab measured near the lane/shoulder joint in the winter.

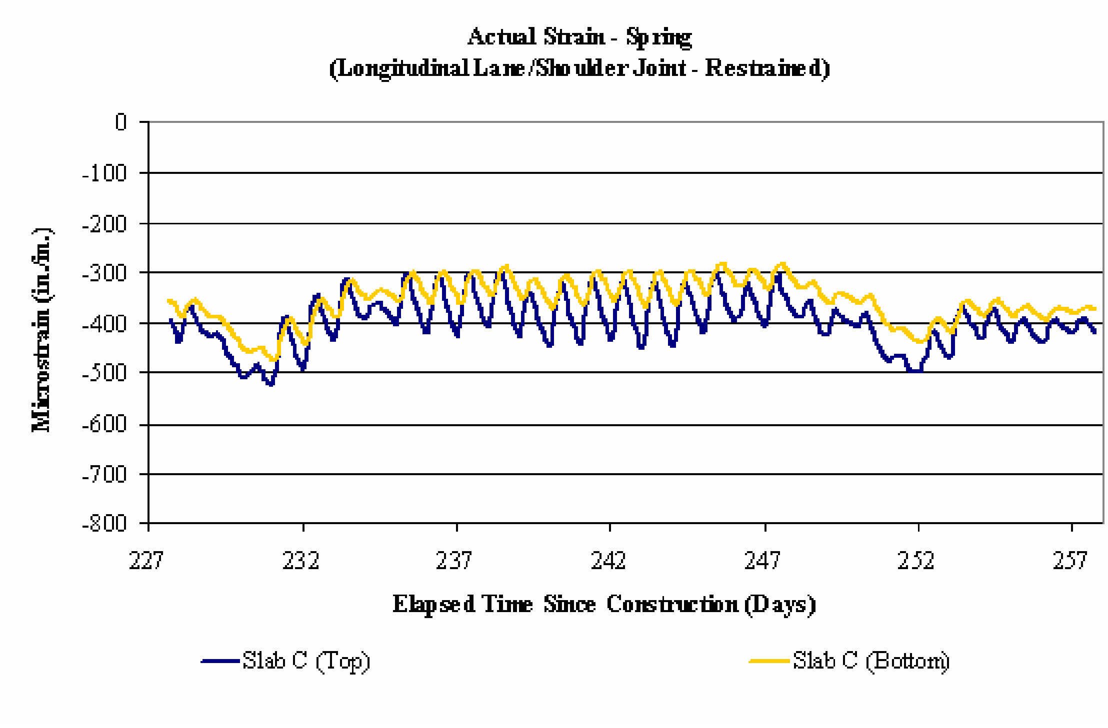

Figure C.19 Strain 1 in from the top and 1 in from the bottom of an unrestrained slab measured near the lane/shoulder joint in the spring.

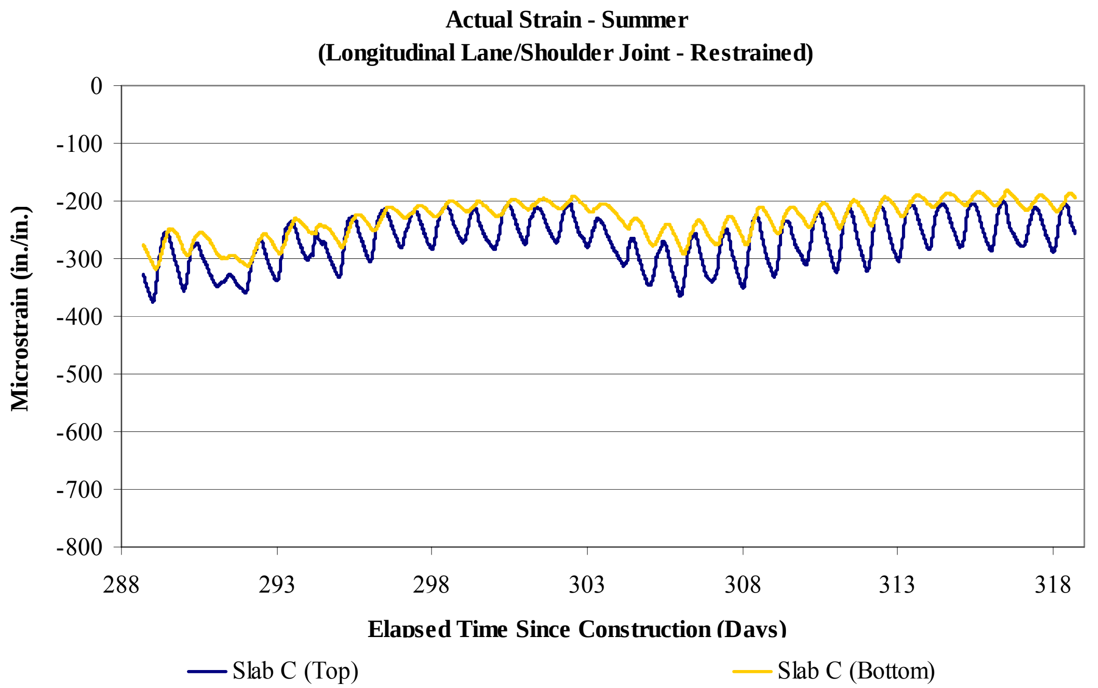

Figure C.20 Strain 1 in from the top and 1 in from the bottom of an unrestrained slab measured near the lane/shoulder joint in the summer.

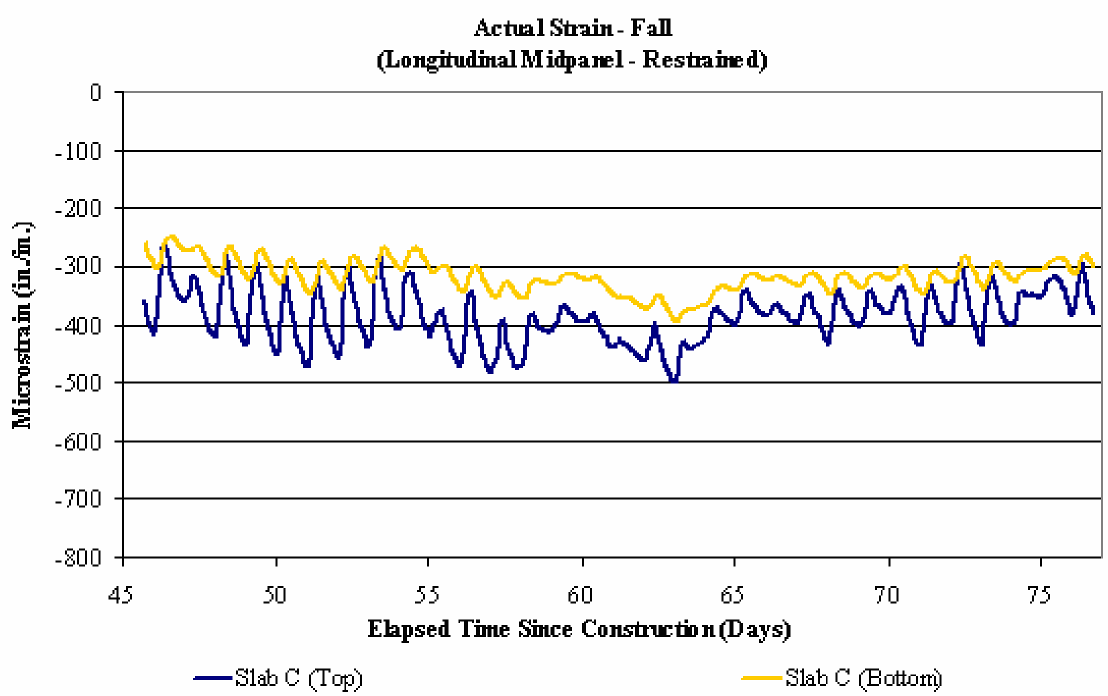

Figure C.21 Strain 1 in from the top and 1 in from the bottom of an unrestrained slab measured near midpanel in the fall.

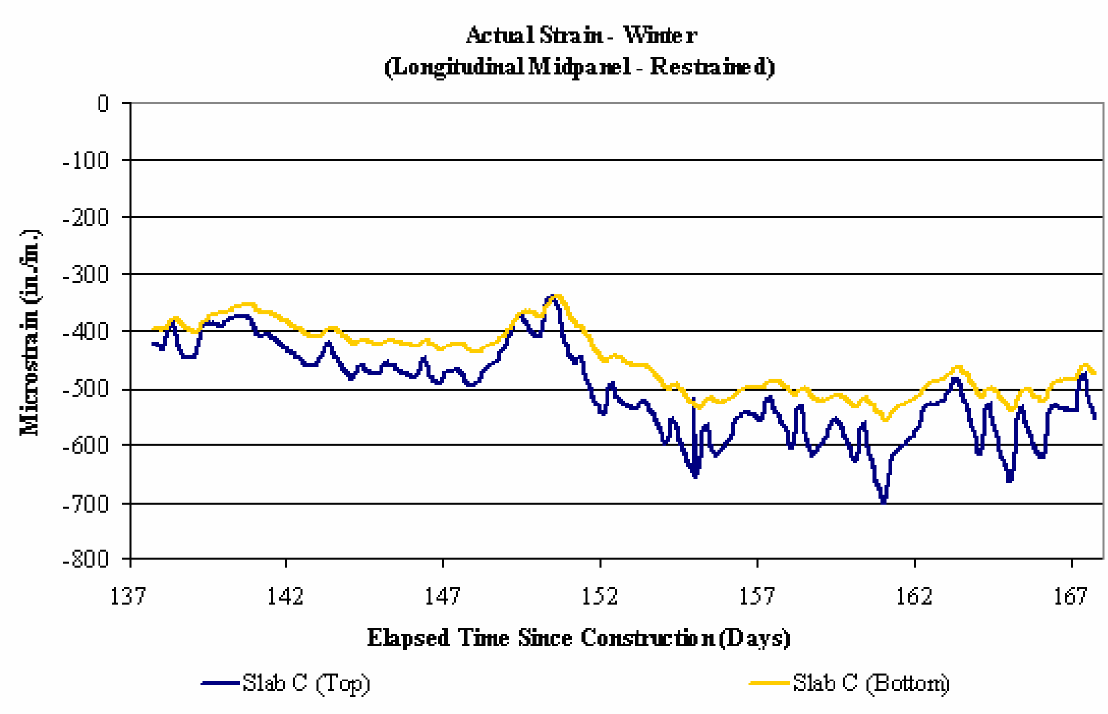

Figure C.22 Strain 1 in from the top and 1 in from the bottom of an unrestrained slab measured near midpanel in the winter.

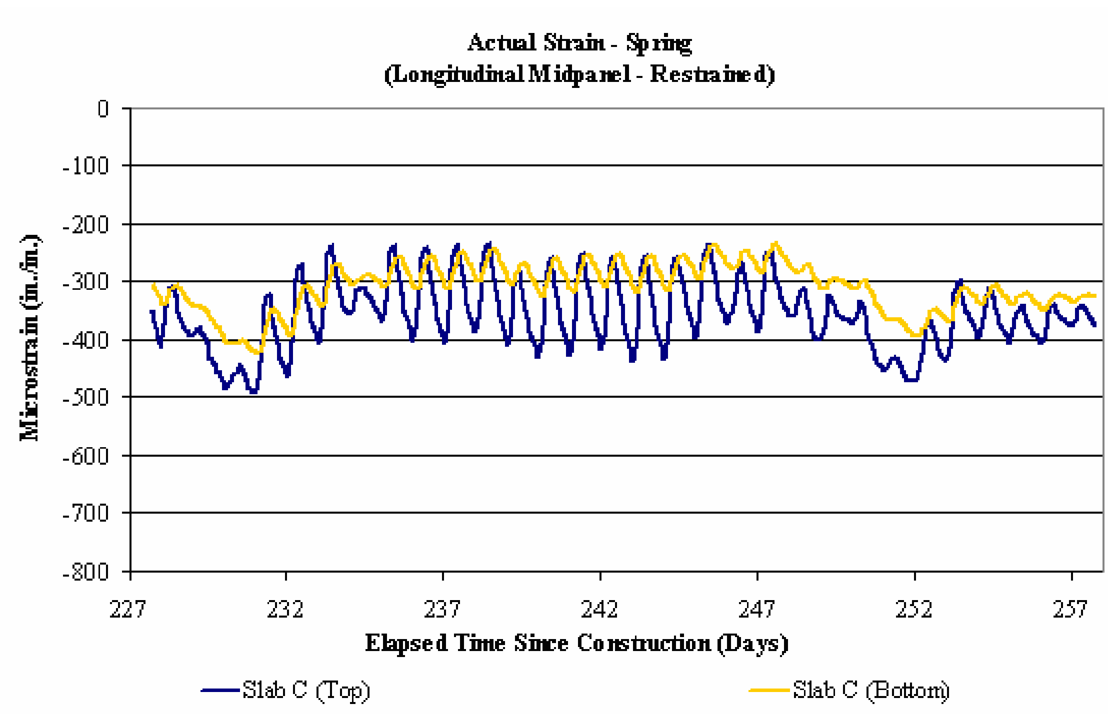

Figure C.23 Strain 1 in from the top and 1 in from the bottom of an unrestrained slab measured near midpanel in the spring.

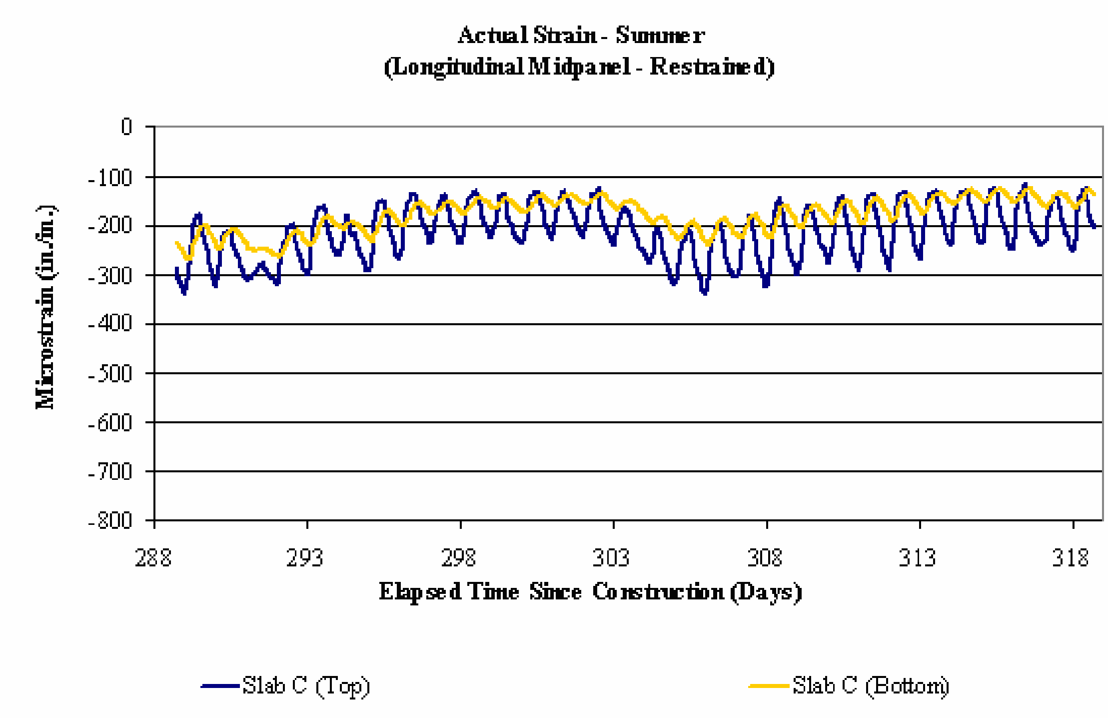

Figure C.24 Strain 1 in from the top and 1 in from the bottom of an unrestrained slab measured near midpanel in the summer.

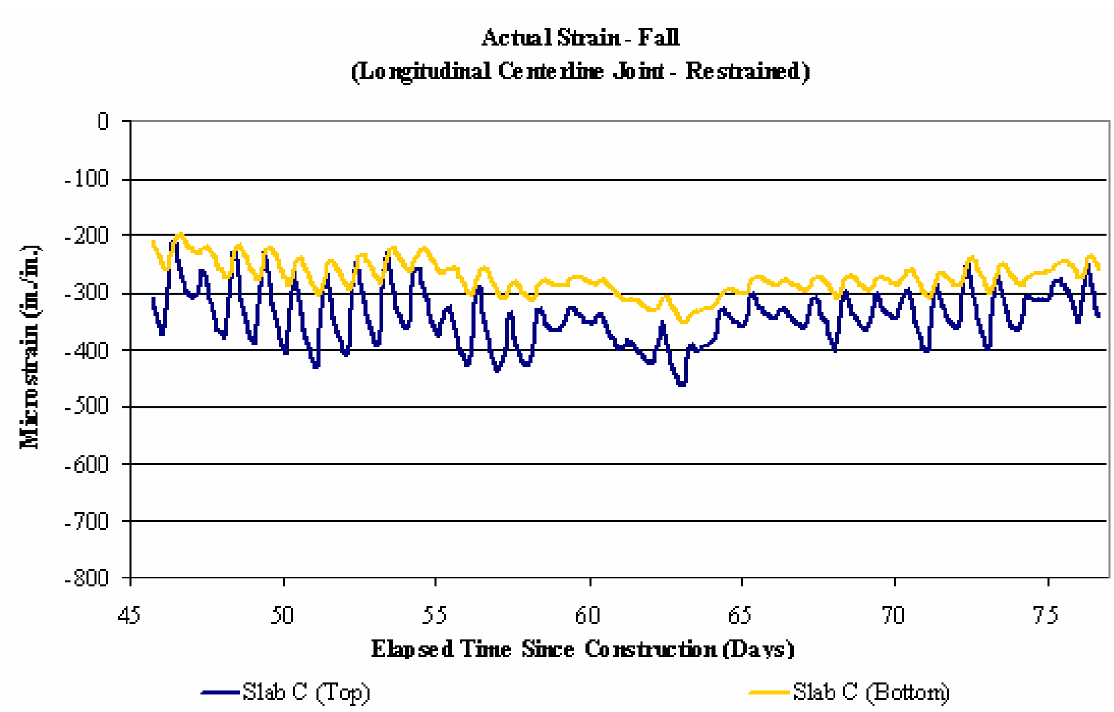

Figure C.25 Strain 1 in from the top and 1 in from the bottom of an unrestrained slab measured near the centerline joint in the fall.

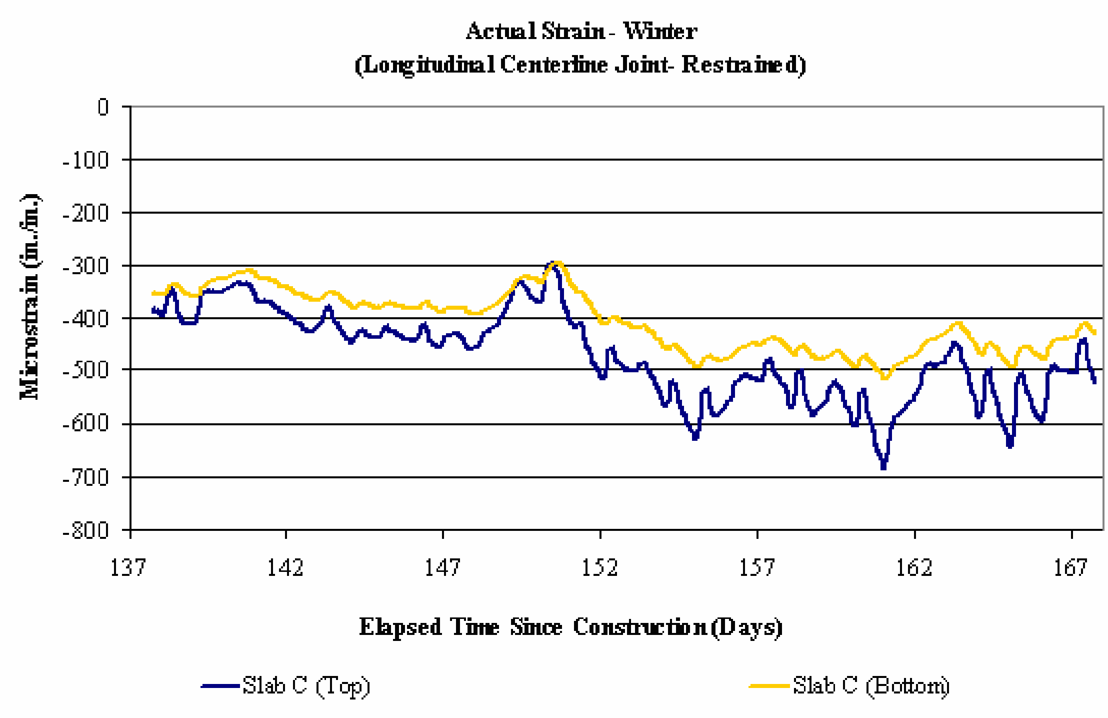

Figure C.26 Strain 1 in from the top and 1 in from the bottom of an unrestrained slab measured near the centerline joint in the winter.

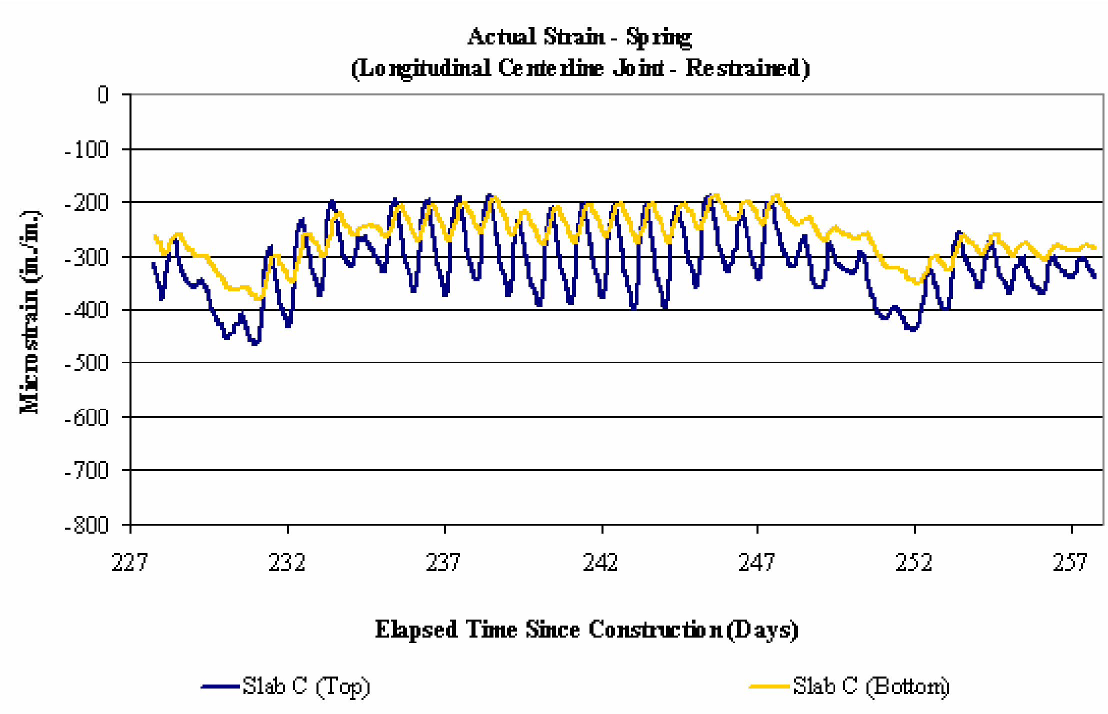

Figure C.27 Strain 1 in from the top and 1 in from the bottom of an unrestrained slab measured near the centerline joint in the spring.

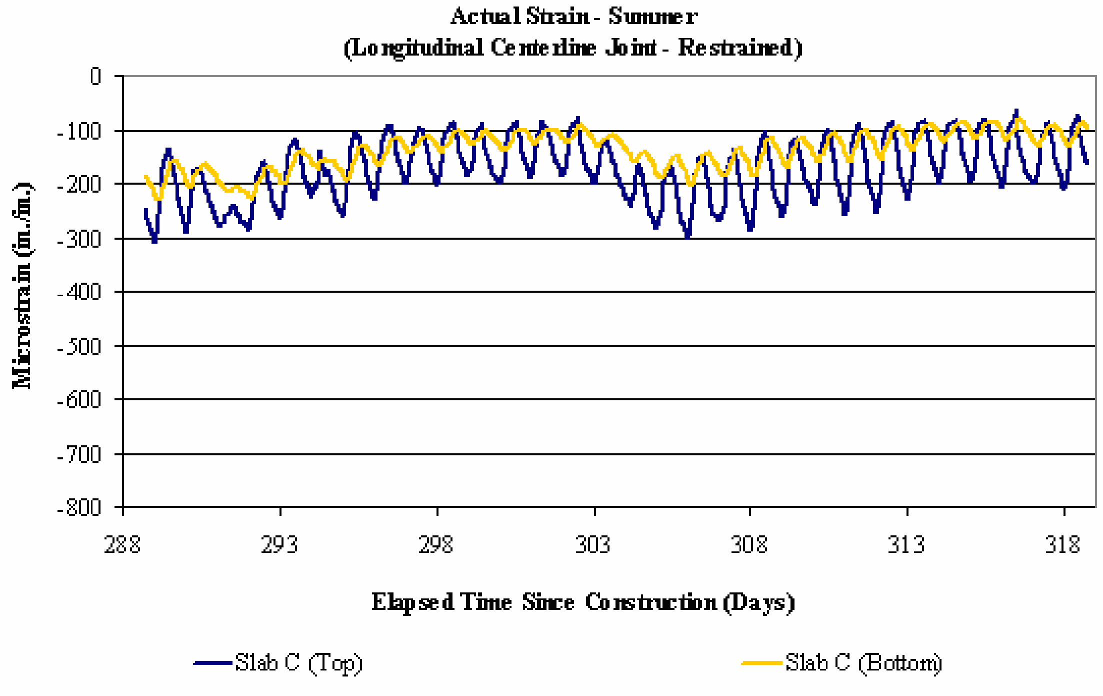

Figure C.28 Strain 1 in from the top and 1 in from the bottom of an unrestrained slab measured near the centerline joint in the summer.

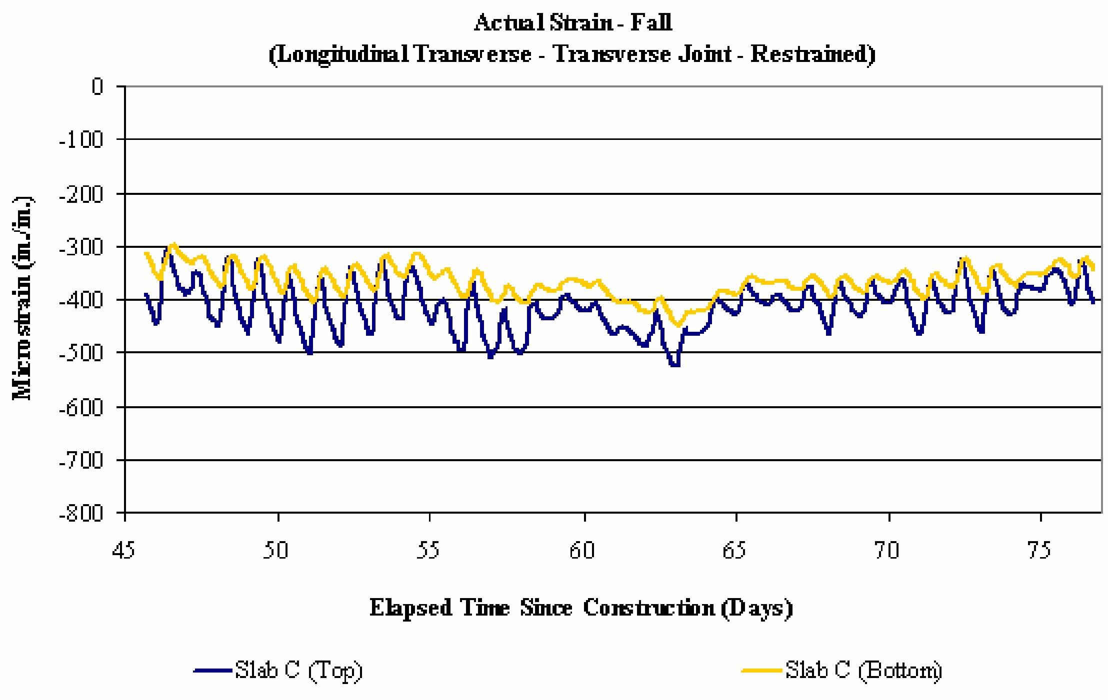

Figure C.29 Strain 1 in from the top and 1 in from the bottom of an unrestrained slab measured near the transverse joint in the fall.

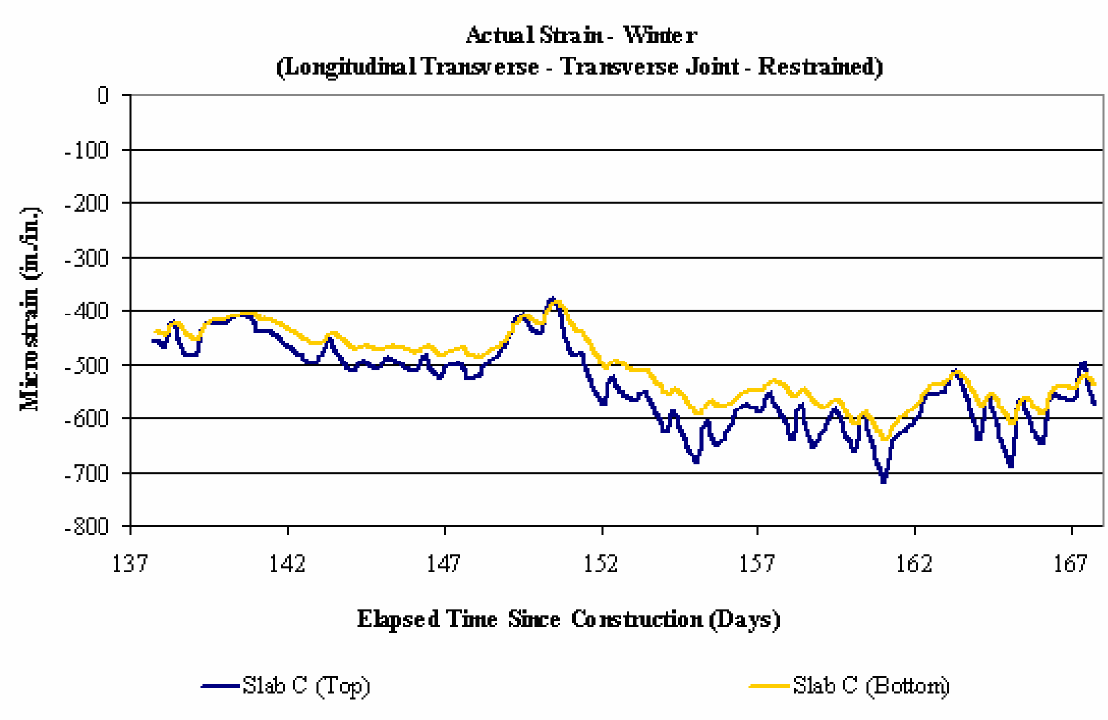

Figure C.30 Strain 1 in from the top and 1 in from the bottom of an unrestrained slab measured near the transverse joint in the winter.

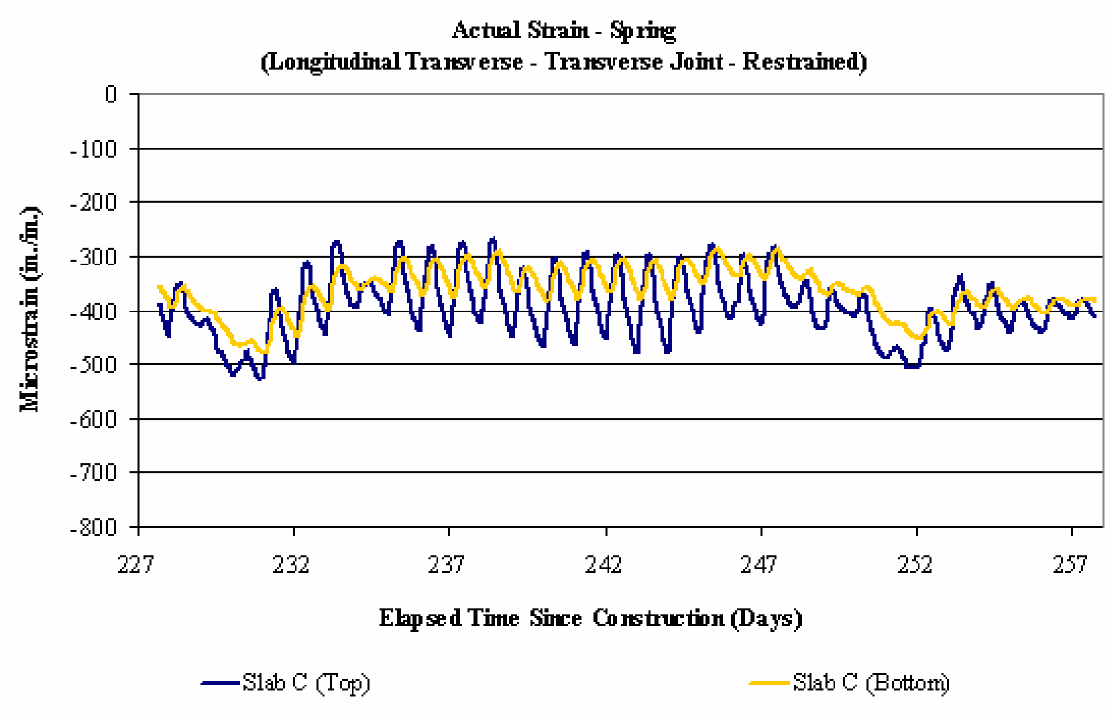

Figure C.31 Strain 1 in from the top and 1 in from the bottom of an unrestrained slab measured near the transverse joint in the spring.

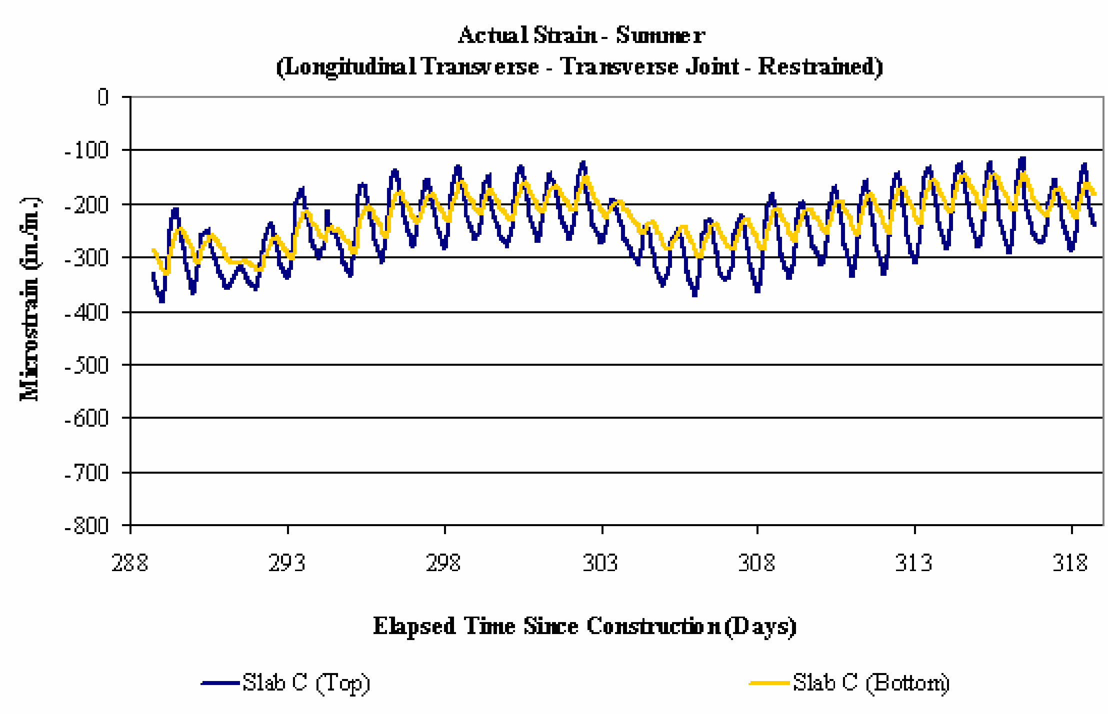

Figure C.32 Strain 1 in from the top and 1 in from the bottom of an unrestrained slab measured near the transverse joint in the summer.

BIBLIOGRAPHY

Davids, W.G. (2001), "3D Finite Element Study on Load Transfer at Doweled Joints in Flat and Curled Rigid Pavements," *International Journal of Geomechanics,* Vol. 1, Issue 3, July 2001, pp. 309-323.

Guo, E.H. and Marsey, W. (2001), "Verification of Curling in PCC Slabs at FAA National Airport Pavement Test Facility," *Advancing Airfield Pavements,* Aug. 5-8, 2001, Chicago, IL, Ed. W.G. Buttlar and J.E. Naughton. Reston, VA: ASCE, 2001, pp. 15-29.

Huang, Y.H. (1993), *Pavement Analysis and Design*, New Jersey: Prentice Hall.

Ionnides, A.M. and Hammons, M.I. (1996), "A Westergaard-Type Solution for the Edge Load Transfer Problem," *Transportation Research Record 1525,* Transportation Research Board, Washington D.C.,1996, pp. 28-34.

Ioannides, A.M., Thompson, M.R., and Barenberg, E.J. (1985), "Finite Element Analsyis of Slab-on-Grade Using a Variety of Support Models," *3rd International Conference on Concrete Pavement Design and Rehabilitation*, Purdue University, West Lafayette, IN.

Janssen, D. J. and M. B. Snyder, 2000. "The Temperature-Moment Concept for Evaluating Pavement Temperature Data. Technical Note." *Journal of Infrastructure Engineering, Vol. 6, No. 2.* American Society of Civil Engineers. Reston, VA, June 2000. pp. 81-83.

Grasley, Z.C., Lange, D.A., and D'Ambrosia, M.D. (2003), "Internal Relative Humidity and Drying Stress Gradients in Concrete," *Proceedings of Engineering Conferences International*, Advances in Cement and Concrete IX, Copper Mountain, CO, 2003.

Hall, K. T., M. I. Darter, T. E. Hoerner and L. Khazanovich, *LTPP Data Analysis-Phase I, Validation of Guidelines for k-Value Selection and Concrete Pavement Performance Prediction*, Technical Report FHWA-RD-96-198, Washington, DC, 1997.

Kelleher, K. and Larson R.M. (1989), "The Design of Plain Doweled Jointed Concrete Pavement," *4th International Conference on Concrete Pavement Design and Rehabilitation,* Purdue University, West Lafayette, IN.

Kennedy, J.C. and Everhart D.R. (1998), "Warping and Curling of Rigid Pavements, A Mechanstic Approach Implemented in UMPAD," *Final Report to Turner-Fairbank Highway Research Center: Work Order Number BAT-94-019, TWR No. 6*, June 1998.

Mirambell, E. (1990), "Temperature and Stress Distributions in Plain Concrete Pavements Under Thermal and Mechanical Loads," *Proceedings*, Second International Workshop on the Design and Rehabilitation of Concrete Pavements, Sigüenza, Spain.

Rao, S. and Roesler, J.R. (2005), "Characterizing Effective Built-In Curling from Concrete Pavement Field Measurements," *Journal of Transportation Engineering,* Vol. 4, April 2005, pp. 320-327.

Shoukry, S.N. and William, G.W. (2001), "3D Finite Element Analysis of Temperature-Induced Stresses in Dowel Jointed Concrete Pavements," *International Journal of Geomechanics*, Vol. 1, Issue 3, July 2001, pp. 291-307.

Vandenbossche, J.M. (2003), *Interpreting Falling Weight Deflectometer Results for Curled and Warped Portland Cement Concrete Pavements*, University of Minnesota, Minneapolis, MN.

Vandenbossche, J.M., Schmidt, S.K., Rao, C.B., Holt, E.E., Taflin, J.W., & Barenberg, E.J. (2002), "Early and Long-Term Effects of Curling and Warping on Jointed Concrete Pavement", *Federal Highway Administration Contract DTFH61-95-C-00021*, Ed. S.L. Marvinney, D.J. Janssen and M.B. Snyder, Washington, D.C., November 2002.

Yoder, E.J. and Witzcak, M.W. (1975), *Principles of Pavement Design,* 2nd edition. New York: John Wiley and Sons.